Title

Elucidating design principles for chromenylium-based polymethine dyes for improved in vivo shortwave infrared imaging

Author

Spearman, Anthony

Publication Date

2024

Peer reviewed|Thesis/dissertation

UNIVERSITY OF CALIFORNIA

Los Angeles

Elucidating design principles for chromenylium-based polymethine dyes for improved *in vivo* shortwave infrared imaging

A dissertation submitted in partial satisfaction of the

requirements for the degree Doctor of Philosophy

in Chemistry

by

Anthony Lee Roy Spearman

2024

ABSTRACT OF THE DISSERTATION

Elucidating design principles for chromenylium-based polymethine dyes for improved *in vivo* shortwave infrared imaging

by

Anthony Lee Roy Spearman

Doctor of Philosophy in Chemistry

University of California, Los Angeles, 2024

Professor Ellen May Sletten, Chair

Optical imaging has been a vital tool in chemical biology for elucidating biological processes. Traditionally, light in the visible (VIS; 400–700 nm) and near-infrared (NIR; 700–1000 nm) regions of the electromagnetic spectrum has been harnessed for various imaging applications. Recently, it has been shown that light in the shortwave infrared (SWIR; 1000–2000 nm) possesses numerous advantages over the aforementioned regions, such as enhanced contrast and resolution. Numerous classes of SWIR contrast agents have been developed in the past couple of years. These range from inorganic materials such as single-walled carbon nanotubes, quantum dots, conjugated polymers, and rare earth doped nanoparticles, as well as organic, small molecule fluorophores. A small molecule scaffold of choice comes in the form of polymethine dyes. Presently, several SWIR-emissive polymethine dyes have been designed and used for real-time *in vivo* imaging

applications. However, only a handful of SWIR-absorbing polymethines with sufficient molecular brightness have been developed. The work in this dissertation outlines efforts towards better understanding design principles for chromenylium-based polymethine dyes, in order to design improved SWIR-absorbing contrast agents.

Chapter One is a perspective on relevant polymethine design principles and introduces early flavylium-based polymethine dyes and their SWIR imaging potential.

In Chapter Two, we elucidated flavylium and chromenylium structure-property relationships that allowed us to modulate λ_{max} and Φ_F through heterocycle modifications. This insight led to a handful of fluorophores matched to commercial NIR and SWIR laser lines, allowing us to perform real-time, excitation-multiplexed SWIR *in vivo* imaging. Through this work, up to 4 dyes could be orthogonally excited and imaged with video framerates.

In Chapter Two, we noted that modifications at the 2-position influenced Φ_F but sought to gain further insight. In Chapter Three, we sought to understand these effects with additional 2-position modifications, considering molecular parameters such as steric effects and substituent electronics. These efforts allowed us to identify additional 2-position substituents that could red-shift λ_{max} or directly improve Φ_F.

Previously, we dealt only with pentamethine and heptamethine chromenylium dyes for imaging. However, fundamental polymethine design principles led us to investigate longer chain derivatives. In Chapter Four, we developed red-shifted nonamethine chromenylium dyes. These dyes are the brightest fluorophores at their bandgaps to date. For the first time, we demonstrated excitation-multiplexed, 2-color imaging with small molecule fluorophores using only SWIR excitation.

Finally in Chapter Five, we embarked on another flavylium structure-property investigation, this time combining 7-position modifications seen in Chapter Two and 2-position modifications seen in Chapter Three. Additionally, we synthesized and characterized pentamethine analogues of these fusion flavylium dyes. This work helped us understand the additive effects of these modifications.

The dissertation of Anthony Lee Roy Spearman is approved.

Justin R. Caram

Patrick G. Harran

R. Michael van Dam

Ellen May Sletten, Committee Chair

University of California, Los Angeles

2024

This dissertation is dedicated to my parents, Julia and Larry, my grandmother Jessie, and my late grandparents, Antonio, Lee, and Flo

TABLE OF CONTENTS

LIST OF FIGURES

CHAPTER ONE

CHAPTER TWO

CHAPTER THREE

CHAPTER FOUR

LIST OF SCHEMES

CHAPTER TWO

CHAPTER THREE

CHAPTER FOUR

CHAPTER FIVE

LIST OF TABLES

CHAPTER TWO

CHAPTER THREE

CHAPTER FOUR

CHAPTER FIVE

ACKNOWLEDGEMENTS

First, I would like to thank my PhD Advisor Ellen Sletten. This was quite the journey - filled with many hardships and obstacles, but with your mentorship and guidance (and especially your patience) I was able to grow, both as a chemist and an individual. I truly thank you for everything. With you at the helm, I know the future of the lab is secure. I would also like to thank my committee members: Professor Justin Caram, Professor Patrick Harran, and Professor Mike van Dam. Additionally, I also extend thanks to Professor Hosea Nelson and Professor Neil Garg for both being incredible role models.

Next, I would like to thank the legendary members of the Sletten lab that came before me. To my original graduate student mentor Maly, thank you for teaching me so much when I joined the group. You trained me well and I owe you for showing me the ropes (and also for answering questions I had - no matter how dumb). Also, thank you for all the hours you helped by looking over slides or listening to my practice presentations. Know that I tried my best to pay it forward, but I don't think I was ever able to be as good a mentor as you were. Next, I'd like to thank my former 4224 fume hood and desk neighbor Anna; you kept me sharp in lab and also helped me learn much in my first year for my classes and during practice quals prep. Even indirectly, I learned a lot from watching you present at journal club and group meetings. I will always admire your mastery of the field and your ability to communicate. Thank you to former lab dad Joe. You taught me the delicate balance of getting work done while still knowing when to relax. One day I know we'll pull off one of the many "get rich quick schemes" the Panda Thursday crew came up with (just not *two shorts*). Lastly, thank you for reminding me that "It does get easier". To Monica and Gina, thank you for being great friends who also helped me refine my skills as a synthetic chemist.

Thanks for the constant cat therapy with Gumbo and Wumbo – and later with Miso. Thank you for showing me all the best restaurants in Sawtelle and the tastiest KBBQ a grad student could afford. Along with Joe and Irene, we created many precious memories that I will never forget. One day we all have to reunite and try our hand at bar trivia once again. To Margeaux, I don't think a more well-rounded individual has ever existed in Sletten lab history. Thank you for all of your advice and feedback, which helped me grow tremendously, both in designing experiments and putting together talks. I hope you are doing well because you deserve greatness. To Rachael and Dan, thank you for showing me all around LA, I'll never forget all the fun we had, whether it was out in the city or staying in at y'all's apartment. Both of you also helped me grow in grad school; Rachael, you taught me more biology than I ever thought I'd be able to learn (which really helped me during my 2nd year talk) and Dan, you showed me that there were always more experiments that I could be doing - the grind never stops. I'd also like to thank all the former postdocs that helped me develop as a researcher. To Jon, Heidi, and Shang, thank you all for helping me get into shape for my candidacy exam and for also serving as role models of what a successful chemist looks like. Thank you to Daniel Turner for all of their help and positivity while serving as my undergraduate mentee. You are a rockstar chemist in your own right, who has long surpassed me – keep on thriving and good luck with your graduate studies. And to Irene, there aren't enough words to express how thankful I am for your existence. You are someone that perseveres time and time again, no matter how hard the fight is – no matter what life throws at you – and no matter how much weight is put upon you. You truly were the glue that held the group together during its most critical transition. You are like a big sister to me, and I will always be eternally grateful for every single way you helped me and all the moments we shared. Thank you.

To all of you, I hope our paths cross again – and sorry for being reclusive at times.

I would now like to acknowledge Cesar Garcia, my former labmate/roommate/housemate and the only member in the lab within my cohort. Cesar, know that you will always be a brother to me. We fought long and hard in these trenches together and (assuming we got the "good ending") we finally, FINALLY, finished the battle. I'll never forget when I first met you in Westwood when you were jogging to the gym, our silent battles for highest yields or cleanest NMRs once you joined SWIR team, and all the video games we played together. We also had unforgettable moments working in the lab late at night, taking turns blasting music on the 4224 speaker. Once we managed to endure practice quals and pass our candidacy exams during the *COVID-19 Pandemic of 2020*, our bond was solidified. You joke that after COVID, "Prime Cesar" was no more, but in my eyes you only grew further. Where I began to give into despair, you held on with pure determination and grit. I will always admire your tenacity, even if something is impossible, you do it – because it has to get done. Consistency and reliability are some of your greatest strengths and nobody will ever crank out Flav7 derivatives like you. I could not have possibly finished this program without you and your positive influence. So, thank you for everything my friend, I look forward to getting into mischief with you in the future.

I also need to thank lab members that joined after me. Thank you to Joseph Garcia for holding it down on the 5th floor. Congratulations on *actually* being the lab's first Dr. Garcia (sorry Cesar). I swear we will go to Mom's (or any equivalent venue) one day fellow king, but also if you ever want to dive together again just let me know. Thank you to the current lab leaders: Quintashia and Kait. You both are excellent chemists and will achieve success without a doubt. Quintashia, thank you for keeping me honest often (flashbacks to bandgap discussions) but also for genuinely caring for my well-being and reminding me who I am. Kait, thank you for all of your support throughout the years and for putting up with my horrible puns and all my venting. Looking forward

to more snaps of young Bug – so long as you're prepared for more snaps of Eve. To Emily, keep on fighting the good fight. You know I see myself in you, but you are 100x better. Keep the legacy of SWIR team alive and make the mice (with Eric) shine as bright as you. Thank you for being a dear friend, I'll cherish the late-night hangs we had (along with Ethan). To Helen, thanks for all the endless riffing in 4224, the bit never dies with hue (or was it cue?). Even on my worst days you never failed to put a smile on my face. I'll miss our trips to the vending machines (but not as much as hosting H+C trivia events with you). It's up to you to keep the positive vibes in 4224 going. (Also tell Matt I thank him for all the hours we spent gaming together – and best of luck to both of you next year and the years to come). To Prairie, thank you for being the tender soul that you are. I appreciate your warmth and the kindness you extend to the people you care about. I'll never forget your cinnamon-related shenanigans (though there is one I wish I could…). Also, I will always have your surprise birthday shirt to remember you by. To Paige, thank you for also serving as a positive force within the lab and much like Helen, also remaining committed to the bit. If Joseph and I do ever go to Mom's again, you will certainly be invited. To Eric, the boba king, we had some good times indeed. Thank you for all your help with the projects and always answering my foolish questions. When you get back to med school, teach them the power of the SWIR. Also please let me know if you ever want to grind some OSM together, I'm ready. To Katie, thanks for being extremely chill 24/7. I hope you find success because you absolutely deserve it. Also, good luck with the solvent system, and may the solvent gods treat you well. To Ethan, thank you for helping me de-stress (and get in shape) with all the jogs we went on, though they were slightly countered by all the food we ate at Hop Woo. Hold on to the stories of Sletten lab past and pass down new stories to the next generation. You've matured into a fine chemist in your own right, just keep it pushing. And remember that "the game is the game, always". To Devon, your skills are

now complete. I have no doubt you're going to effect great change in the group in the years to come. There are times when it may not be easy, but I know you can do it, 5th year Devon will be a force to be reckoned with. Finally, best of luck to Jesus, Luigi and Kai. Thank you for all the good (albeit brief) times we had together. You are all amazing people.

I would also like to thank some people within my cohort. To Dan Curet, Nik Theopold, Milauni Mehta, and Austin Bailey, thank you for being such great friends to me throughout the trials and tribulations of grad school. We survived our early years together, working on problem sets and cramming for mid-terms and we always made sure to celebrate just as hard. I wish you all the best in your future endeavors.

Finally, I'd like to briefly thank some of my friends and family. Thank you to my parents for all their love and support. I know I've been away for many years now but it's almost over. To my sister Lauren, thank you for all of your local support, as you were the only family I had in California. You helped me get through some of my darkest times. Thank you to Kelly Wong and Erika Ramirez for their support during troubled times as well. Also, thank you to Richard, George, and Alex for playing DDR with me at D&B for a time – I hope we can step on arrows together in the future. Thanks to my former cat Celeste and current cat Eve for the love and affection they gave me. Finally, I'd like to thank Biko, Janais, Cristina, Thomas, Erik, Kevin, David, and Byron for keeping me as sane as possible during this phase of my life.

To those that went unnamed but still helped me these past couple of years, know that I thank you from the bottom of my heart.

Chapter One is an unpublished perspective on polymethine dyes written by Spearman.

Chapter Two is a version of Cosco, E. D.; Spearman, A. L.; Ramakrishnan, S.; Lingg, J. G. P.; Saccomano, M.; Pengshung, M.; Arús, B. A.; Wong, K. C. Y.; Glasl, S.; Ntziachristos, V.; Warmer, M. McLaughlin, R. R.; Bruns, O. T.*; Sletten, E. M.* Shortwave Infrared Polymethine Fluorophores Matched to Excitation Lasers Enable Non-Invasive, Multicolour in Vivo Imaging in Real Time. *Nat. Chem.* **2020**, *12*, 1123–1130. Cosco, Spearman, Ramakrishnan, Lingg, Saccomano, Pengshung, Arús, Wong, Glasl, Warmer and McLaughlin contributed to experimental work. Cosco, Sletten and Bruns contributed to writing.

And, Cosco, E. D.; Arus, B. A.; Spearman, A. L.; Atallah, T. L.; Lim, I.; Leland, O. S.; Caram, J. R.; Bischof, T. S. Bruns, O. T.*; Sletten, E.M.* Bright chromenylium polymethine dyes enable fast, four-color *in vivo* imaging with shortwave infrared detection. *J. Am. Chem. Soc.* **2021**, *143*, 6836-6846. Cosco, Arus, Spearman, Atallah, Lim, Lelang, Caram, and Bischof contributed to experimental work. Cosco, Sletten, and Bruns contributed to writing.

Chapter Three is a version of an unpublished work Spearman, A. L.; Turner, D. W.; Kimpton, I.; Garcia, C. A.; Lopez, S. A.; Sletten, E. M.* Exploring Structure-Property Relationships of Chromenylium-Based Shortwave Infrared Polymethine Dyes (*Manuscript in preparation*). Spearman, Turner, Kimpton, Garcia, and Lopez contributed to experimental work. Spearman and Sletten contributed to writing.

Chapter Four is a version of Spearman, A. L.; Lin, E. Y.; Mobley, E. B.; Chmyrov, A.; Turner, D.; Garcia, C.; Bui, K.; Rowlands, C.; Bruns, O.; Sletten, E. M.* High-resolution multicolor shortwave infrared in vivo imaging with chromenylium nonamethine dyes. *ChemRxiv.* **2024**, DOI: 10.26434/chemrxiv-2024-dxdr9. Spearman, Lin, Mobley, Chmyrov, Turner, Garcia, and Bui, Rowlands, and Bruns contributed to experimental work. Spearman and Sletten contributed to writing.

Chapter Five is a version of an unpublished work Spearman, A. L.; Turner, D. W.; Alde, L.; Sletten, E. M.* Designer Fusion Flavylium Polymethine Dyes for Understanding Flavylium Dye Structure-Property Relationships (*Manuscript in preparation*). Spearman, Turner, and Alde contributed to experimental work. Spearman and Sletten contributed to writing.

Throughout these studies, I was supported by UCLA (Charlene and Ralph Bauer Award, Jim and Barbara Tsay Excellence in Second Year Research Award, Senior Foote Fellow Award) and the National Institutes of Health (F31 Predoctoral Fellowship).

BIOGRAPHICAL SKETCH

Education

University of California-Los Angeles
M.S. in Chemistry (2020)

Southern Methodist University
May 2018
Major: Chemistry (B.A.)
Minor: Japanese, Biomedical Anthropology, Asian Studies

Research Experience

University of California, Los Angeles (Department of Chemistry & Biochemistry)
2018 - 2024
Advisor: Dr. Ellen Sletten

Southern Methodist University (Department of Chemistry)
2017 - 2018
Advisor: Prof. Alexander Lippert

Selected Honors:

SMU Engaged Learning Fellow (2017-2018)
Ford Foundation Fellowship Honorable Mention (2020)
Senior Foote Graduate Fellow (2021)
Jim & Barbara Tsay Endowed Graduate Student Award (2021)
NIH F31 Predoctoral Fellowship (2021-2023)
UCLA Ralph & Charlene Bauer Graduate Student Award (2022)
Chemists Association Dissertation Award (2023)

Publications:

1. Cosco, E.D.; **Spearman, A.L.**; Ramakrishnan, S.; Lingg, J.G.P.; Saccomano, M.; Pengshung, M.; Arús, B. A.; Wong, K.C.Y.; Glasl, S.; Ntziachristos, V.; Warmer, M. McLaughlin, R.R.; Bruns, O.T.; Sletten, E.M. "Shortwave infrared polymethine fluorophores matched to excitation lasers enable non-invasive, multicolour *in vivo* imaging in real time." *Nat. Chem.* **2020**, *12*, 1123-1130.
2. Cosco, E.D.; Arús, B.A.; **Spearman, A. L.**; Atallah, T. L.; Leland, O.S.; Caram, J.R.; Bischof, T.S.; Bruns, O.T.; Sletten, E.M. "Bright chromenylium polymethine dyes enable fast, four-color *in vivo* imaging with shortwave infrared detection." *J. Am. Chem. Soc.* **2021,** *143*, 6836–6846**.**
3. **Spearman, A.L.**; Lin, E.Y.; Mobley, E.B.; Chmyrov, A.; Turner, D.; Garcia, C.; Bui, K.; Rowlands, C.; Bruns, O.; Sletten, E.M. High-resolution multicolor shortwave infrared in vivo imaging with chromenylium nonamethine dyes. *ChemRxiv.* **2024**, DOI: 10.26434/chemrxiv-2024-dxdr9.
4. **Spearman, A.L.**; Turner, D.W.; Alde, L.; Pengshung, M.; Sletten, E.M.* Designer Fusion Flavylium Polymethine Dyes for Understanding Flavylium Dye Structure-Property Relationships (*Manuscript in preparation*).

CHAPTER ONE

Design Principles for Shortwave Infrared Polymethine Dyes

1.1 Perspective

1.1.1 Introduction

There are a wide number of applications for small-molecule fluorophores: compounds that can absorb and emit light.[1] In the clinical setting, fluorophores can be used to label biologically relevant targets in real-time.[2–4] Aside from its real-time capabilities, fluorescence imaging has utility over other clinical imaging modalities by requiring low amounts of dyes, while also using lower energy irradiation.[4–6] To date, different regions of the electromagnetic spectrum have been employed for optical imaging, with traditional fluorophores falling in either the visible region (VIS: 400–700 nm) or the near-infrared region (NIR: 700–1000 nm) (Figure 1.1).[5] Fluorophores within the visible region have been essential for studying biological processes and pathology within the cellular environment as well as within transparent organisms such as zebrafish.[7] However, extension of these dyes for imaging higher-order organisms presents a handful of challenges.

Fluorescence imaging in mammals requires light that can sufficiently penetrate tissue and excite the target fluorophore. However, visible light has limited tissue penetration (< 3 mm).[8,9] Further, an increase in noise from light scattering and tissue autofluorescence directly worsens the resolution attainable with visible light.[10,11] Fortunately, these limitations are largely mitigated by using lower energy, more red-shifted light.[8,11] As such, developing contrast agents that can absorb and emit red-shifted light will greatly enhance fluorescence imaging applications. Recently, groups have been interested in fluorophores that operate within in the shortwave infrared region (SWIR: 1000–2000 nm).

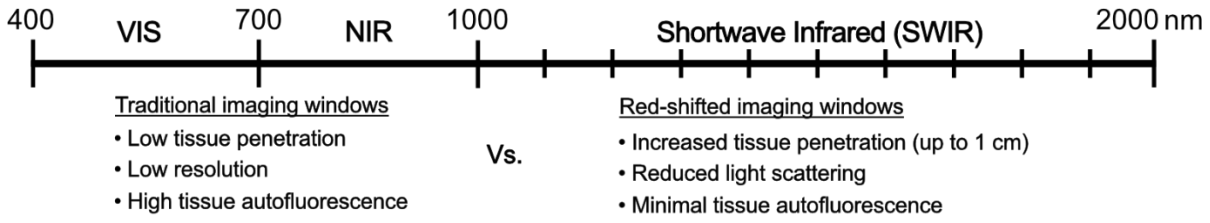

Figure 1.1. Regions of the electromagnetic spectrum relevant for synthetic fluorophores.

Before delving further, it is important to establish the principles and properties important for comparing and designing dyes. Fluorophores are capable of absorbing energy in the form of a photon, promoting electrons in their ground state, S_0 (HOMO) to their excited state, S_1 (LUMO).[12] From the excited state, there are a number of pathways to dissipate the absorbed energy. But ideally, the electron in the excited state will release light back out, known as fluorescence. A typical means of conveying these pathways is via Jablonski diagram (Figure 1.2).[13] The energy level of the LUMO is directly related to the energy the molecule absorbs at, $\lambda_{max,abs}$. The energy of the lowest vibrational mode of the excited state, is the energy of light released via fluorescence, $\lambda_{max,em}$. The difference of emission and absorbance maxima is described as the Stokes shift. Aside from fluorescence, there can be vibrational relaxation, which acts as a non-radiative relaxation pathway. Intersystem crossing (ISC) can also occur, moving over to the triplet excited state (T_1). From the triplet excited state, non-radiative relaxation can also occur, but a phenomenon known as phosphorescence happens when radiative relaxation back to the S_0 takes place.

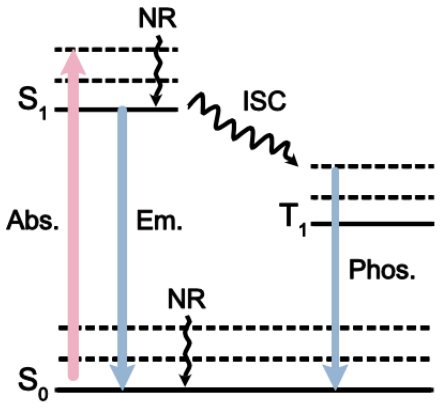

Figure 1.2. A simplified Jablonski diagram outlining various photophysical processes. (Note: Abs. = absorbance, Em. = emission, NR = non-radiative decay, ISC = intersystem crossing, Phos. = phosphorescence).

By comparing radiative rates and non-radiative rates, a molecule's fluorescence quantum efficiency (Φ_F) can be calculated. This is an important metric that describes the output of photons relative to the amount of photons absorbed by a fluorophore. Another photophysical parameter worth considering is molar absorptivity (ε_{max}), which can be determined using the Beer-lambert equation.[14] This parameter describes a molecules' ability to absorb photons at various wavelengths. With these two parameters, another property can be calculated, molecular brightness (m.b.) which is taken as the product of Φ_F and ε_{max}. By measuring these parameters, dyes within the same region of the electromagnetic spectrum can be easily compared for different applications.

As previously mentioned, the SWIR region of the electromagnetic spectrum has been gaining attention, as it can circumvent imaging limitations seen with VIS and NIR excitation. Compounding on the advantages of red-shifted light, the SWIR region generally has improved S/N allowing for imaging at higher-resolutions.[15] Unfortunately, as a dye moves into the lower energy SWIR region, their bandgaps get smaller (Figure 1.3). Smaller bandgaps lead to increased competition with non-radiative pathways, resulting in decreased Φ_Fs. This effect is known as the energy gap law and explains why dyes above 1000 nm have decreased Φ_Fs compared to higher

energy dyes.[16] However, one way to salvage a dye's molecular brightness is to ensure high ε_{max} values. Fortunately, there is a class of fluorophores that are known for having excellent molar absorption coefficients. This class is known as polymethine dyes.

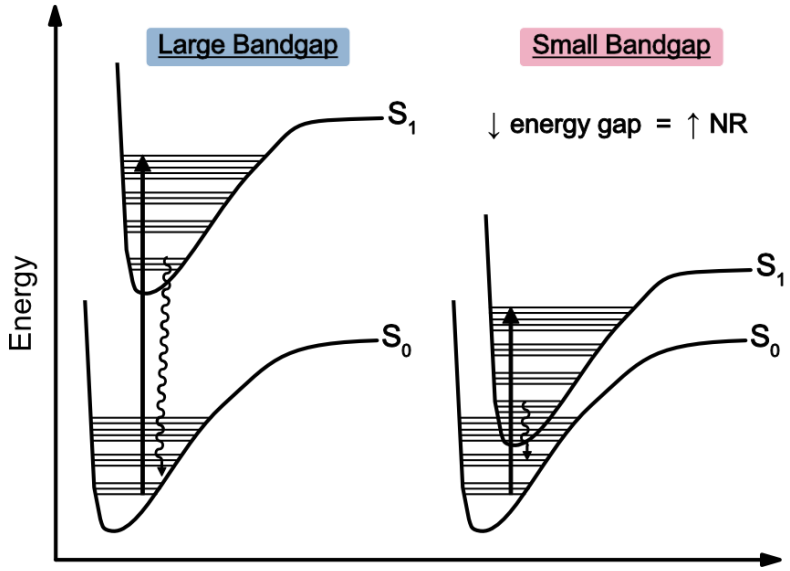

Figure 1.3. Two scenarios demonstrate the energy gap law; decreased bandgap leads to increased non-radiative rates.

1.1.2 Polymethine Dyes

An established class of fluorophores for optical imaging is polymethine dyes. Polymethine dyes are a type of donor-acceptor-donor dyes, composed of two electron rich heterocycles that are linked together by a polymethine chain (Figure 1.4A).[17,18] Typically, the polymethine dye is cationic in nature and stabilized with anionic counterions. However, anionic, zwitterionic, and even neutral polymethine subclasses exist. Polymethine dyes are appealing due to their high molar absorptivity (>10^5 M^{-1} cm^{-1}), narrow stokes shift (~25 nn), and high level of molecular tunability.[17] Another important property of polymethine dyes is their excited-state electronic symmetry (Figure 1.4B). With a completely delocalized exciton, they display typical absorbance and emissive properties – this is known as the ideal polymethine state.[19] This state is also characterized by

having no bond-length alternation (BLA) about the polymethine backbone. However, if the charge becomes localized about a single heterocycle, they exist in the polyene state, indicated by a decrease in molar absorptivity and blue-shifted absorbance.[19] Additionally, if the charge is centered towards the middle of the scaffold a 3rd state known as the bis-dipole form is achieved.[20] This form also has decreased ε_{max} and has λ_{max} blue-shifted to a greater degree than with the polyene state. Aside from structural influences, electronic symmetry can also be dictated by solvent polarity.[21]

At high enough concentrations, these aromatic molecules are prone to aggregation due to π- π stacking, which impacts their photophysical performance.[22,23] Two common forms of dye aggregates are H-aggregates (face to face stacking) and J-aggregates (slip stacking). H-stacking leads to blue-shifted λ_{max} and decreased molecular brightness.[24] While J-aggregates have red-shifted absorbance and even greater ε_{max}.[25] Though separate from the performance of monomeric dyes, these bulk properties should also be considered in fluorophore design as they can become relevant for *in vivo* delivery.

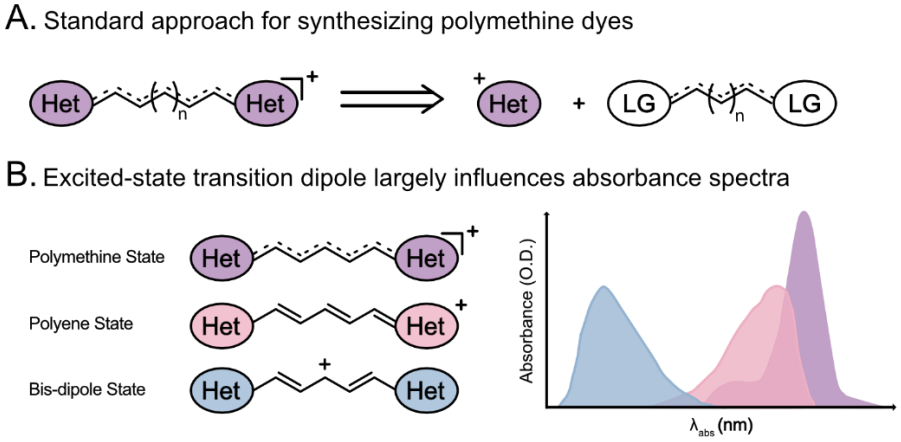

Figure 1.4. A. Polymethine dyes are composed of electron rich heterocycles linked together by methine chains. Het = cationic heterocycle; LG = leaving group **B**. The transition dipole of a polymethine dye's excited state dictates spectral properties.

To date, numerous design principles have been established for polymethine dyes.[17,26] Namely, predictive metrics on how the heterocycle, linker, and even counterion can individually impact photophysical performance. Many strategies for modifying the polymethine chain include direct functionalization as well as rigidification of the chain. However, the most established linker modification is known as the vinylene shift rule (Figure 1.5A).[4,5] Extension of the polymethine chain by two methine units (one vinylene) reliably invokes a red-shift of ~100 nm. The Loiko group experimentally demonstrated this effect using the indoline scaffold, **1.1** (HICI), **1.2 (**HIDCI), and **1.3 (**HITCI).[27,28] One point of caution is that increased chain length can compromise the conformational stability of the polymethine dye. This can disrupt electronic symmetry and begin to favor the polyene state – hampering photophysical performance.[19] Aside from altering the polymethine chain, groups have also explored heterocycle modifications. A heptamethine analogue of **1.3** is known as indocyanine green (**ICG**; also known as IR-125). By comparing the FDA-approved **ICG** to **1.3**, we can see the direct red-shift in λ_{max} achieved through benzannulation (Figure 1.5B). Heterocycles containing heteroatoms beside nitrogen have also been used to develop polymethine dyes. It has been shown that dyes with heavier atoms (such as sulfur, selenium and tellurium) also display red-shifted λ_{max} (Comparing dyes **1.4**–**1.9**; Figure 1.5C).[29,30] However, due to the heavy atom effect, intersystem crossing becomes more predominant, leading to a decrease in quantum yield.[31]

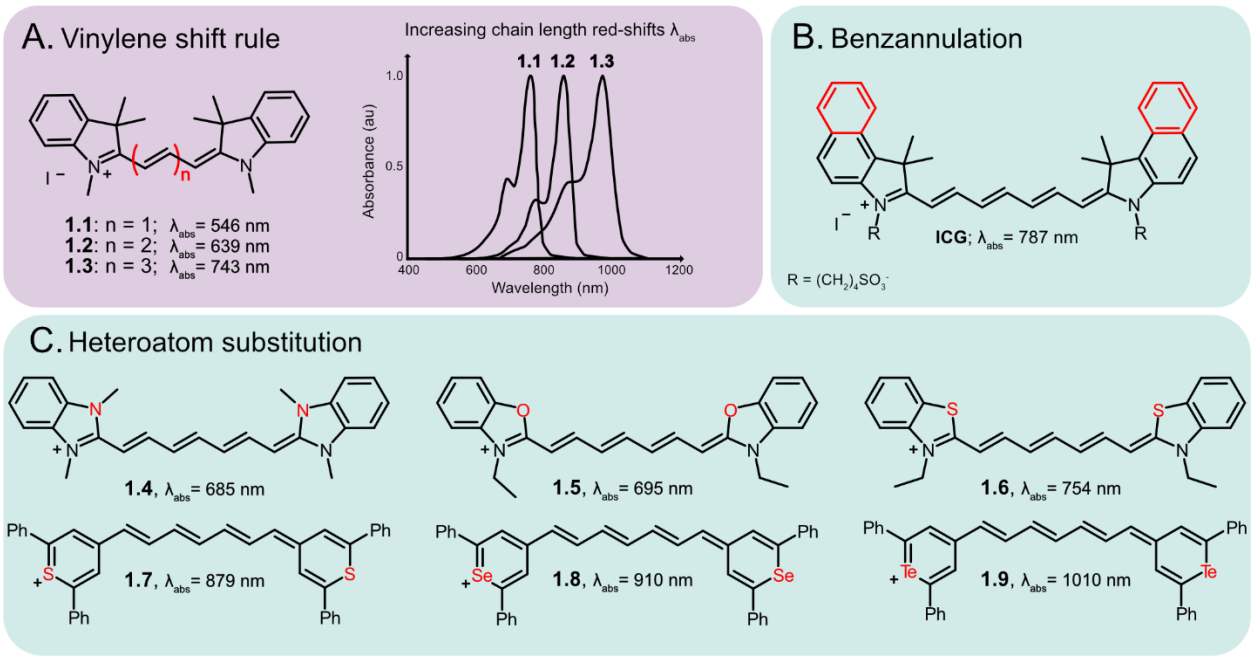

Figure 1.5. **A**. The vinylene shift rule with indoline polymethine dyes. Alongside representative spectra. **B**. Through benzannulation, an additional red-shift can be achieved – this is demonstrated with **ICG**. **C**. By utilizing heavier heteroatoms, dramatic red-shifts in λ_{max} occur.

A notable scaffold among the polymethine community is the flavylium heterocycle. **IR-26** is a commercial standard generally used as a reference dye when calculating relative quantum yields for novel SWIR dyes.[32,33] Due to **IR-26** bearing sulfur as its heteroatom, it has a diminished quantum yield of 0.05%. By substituting sulfur with oxygen, the heavy atom effect is reduced but the resulting dye, **IR-27** is now blue-shifted to 987 nm. In 2017, the Sletten lab theorized that by appending an electron-donating dimetylamino group at the 7-position of **IR-27**, the resulting dye would maintain its good quantum yield while being red-shifted into the SWIR region. Gratifyingly, this dye, deemed **Flav7**, was indeed a bright SWIR fluorophore with a quantum yield of 0.61%.[34,35] These comparisons nicely demonstrate how simple structural modifications can greatly impact the photophysical potential of derivatives. Further, large-scale systematic changes to a scaffold can elucidate novel structure-property relationships – greatly assisting in the design of future fluorophores.

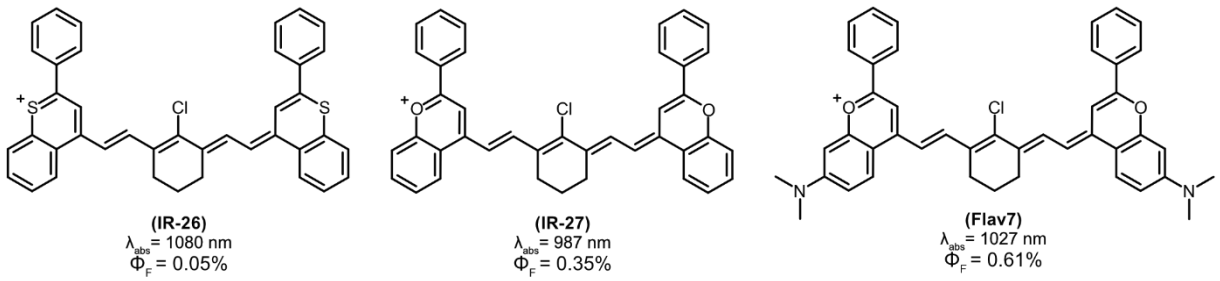

Figure 1.6. Classical examples of flavylium heptamethine dyes, **IR-26**, **IR-27**, and **Flav7**.

1.1.3 Imaging in the SWIR Region

When imaging at SWIR wavelengths, the achievable depth and resolution are significantly influenced by the wavelengths that are captured. As light scattering and tissue-autofluorescence generally fall off > 1200 nm, these water absorption bands largely influence attainable imaging depths as well as resolution (Figure 1.7).[36] The clearest images obtainable fall within the 1350–1450 nm range, where water absorbs stray light. This results in high signal-to-noise ratios and millimeter resolution. Conversely, for optimal depth penetration, recent studies utilizing inorganic particles have shown the benefits of imaging at wavelengths exceeding 1500 nm.[37] The wavelengths used in *in vivo* imaging are determined by a longpass (LP) filter, which permits only lower-energy light to pass through. LP filters can adjust the balance between signal strength and resolution. For SWIR dyes, employing a 1000 nm LP filter captures all emitted photons, maximizing the signal. Generally, using longer-wavelength LP filters leads to higher resolution images since lower-energy light is scattered less by tissue. Thus, imaging with LP filters of 1400 nm or higher is recommended to fully leverage the advantages of SWIR. However, this method necessitates the use of red-shifted, bright, SWIR-emissive fluorophores.

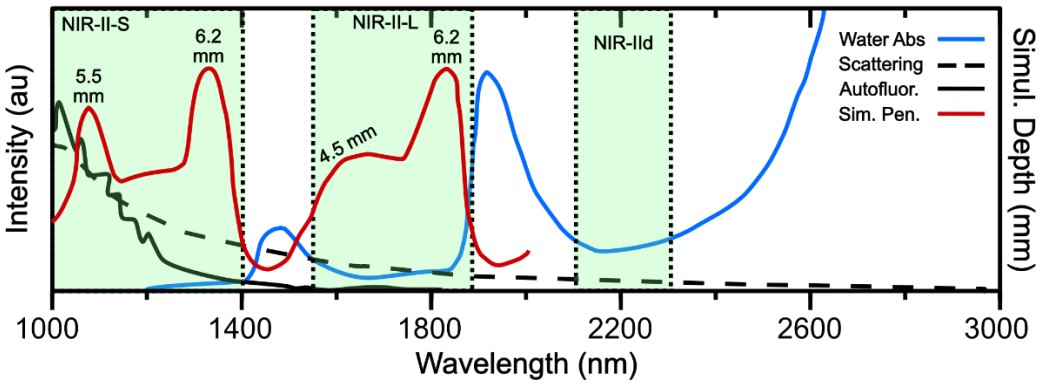

Figure 1.7. Summarized light scattering effects, tissue autofluorescence, and water absorbance in the SWIR region. Coupled together, simulated imaging depths were devised from Ref. 37.

1.1.4 Outlook

As imaging technologies move towards using red-shifted light for *in vivo* imaging, the demand for SWIR fluorophores rises. The polymethine scaffold offers several advantages, including exceptional molar absorptivity. The diverse photophysical capabilities of polymethine fluorophores highlight their potential for advancing future research. Over the past 200 years, ongoing studies of polymethine dyes have led to a comprehensive understanding of their photophysical properties within the visible spectrum. The growing interest in the NIR/SWIR region has created a need for deeper insights into these fluorophores within this red-shifted domain. By clarifying the relationships between structure and photophysical properties, we can design novel fluorophores and optimize their characteristics for specific applications.

1.2 References

(1) Jameson, D. M. *Introduction to Fluorescence*, 1st ed.; CRC Press: Boca Raton, 2014. https://doi.org/10.1201/b16502.

(2) Ishchenko, A. A. Structure and Spectral-Luminescent Properties of Polymethine Dyes *Russ. Chem. Rev*. **1991**, *60*, 865.

(3) Kulinich, A. V; Ishchenko, A. A. Merocyanine Dyes: Synthesis, Structure, Properties and Applications. *Russ. Chem. Rev.* **2009**, *78*, 141–164. https://doi.org/10.1070/rc2009v078n02abeh003900.

(4) König, W. Über Den Begriff Der „Polymethinfarbstoffe" Und Eine Davon Ableitbare Allgemeine Farbstoff-Formel Als Grundlage Einer Neuen Systematik Der Farbenchemie. *J. für Prakt. Chemie* **1926**, *112*, 1–36. https://doi.org/10.1002/prac.19261120101.

(5) Brooker, L. G. S. Absorption and Resonance in Dyes. *Rev. Mod. Phys.* **1942**, *14*, 275–293. https://doi.org/10.1103/RevModPhys.14.275.

(6) Fabian, J.; Nakazumi, H.; Matsuoka, M. Near-Infrared Absorbing Dyes. *Chem. Rev.* **1992**, *92*, 1197–1226. https://doi.org/10.1021/cr00014a003.

(7) Wong, K. C. Y.; Sletten, E. M. Extending Optical Chemical Tools and Technologies to Mice by Shifting to the Shortwave Infrared Region. *Curr. Opin. Chem. Biol.* **2022**, *68*, 102131. https://doi.org/10.1016/j.cbpa.2022.102131.

(8) Thimsen, E.; Sadtler, B.; Berezin, M. Y. Shortwave-Infrared (SWIR) Emitters for Biological Imaging: A Review of Challenges and Opportunities. *Nanophotonics* **2017**, *6*, 1043–1054. https://doi.org/10.1515/nanoph-2017-0039.

(9) Li, C.; Chen, G.; Zhang, Y.; Wu, F.; Wang, Q. Advanced Fluorescence Imaging Technology in the Near-Infrared-II Window for Biomedical Applications. *J. Am. Chem. Soc.* **2020**, *142*, 14789–14804. https://doi.org/10.1021/jacs.0c07022.

(10) Hong, G.; Diao, S.; Antaris, A. L.; Dai, H. Carbon Nanomaterials for Biological Imaging and Nanomedicinal Therapy. *Chem. Rev.* **2015**, *115*, 10816–10906. https://doi.org/10.1021/acs.chemrev.5b00008.

(11) Tu, L.; Xu, Y.; Ouyang, Q.; Li, X.; Sun, Y. Recent Advances on Small-Molecule Fluorophores with Emission beyond 1000 Nm for Better Molecular Imaging in Vivo. *Chinese Chem. Lett.* **2019**, *30*, 1731–1737. https://doi.org/10.1016/j.cclet.2019.05.022.

(12) Lavis, L. D.; Raines, R. T. Bright Ideas for Chemical Biology. *ACS Chem Biol*. **2008**, *3*, 142–155. https://doi.org/10.1021/cb700248m.

(13) Liu, X.; Xu, Z.; Cole, J. M. Molecular Design of UV-Vis Absorption and Emission Properties in Organic Fluorophores: Toward Larger Bathochromic Shifts, Enhanced Molar Extinction Coefficients, and Greater Stokes Shifts. *J. Phys. Chem. C* **2013**, *117*, 16584–16595. https://doi.org/10.1021/jp404170w.

(14) Bondar, M. V; Derevyanko, N. A.; Dyadyusha, G. G.; Zubarovskii, V. M.; Ishchenko, A. A.; Przhonskaya, O. V; Slominskii, Y. L.; Smirnova, A. L.; Tikhonov, E. A.; Tolmachev, A. I. Generation of Light in the Near Infrared Solutions of Asymmetric Polymehine Dyes. *Sov. J. quantum Electron.* **1984**, *14*, 317–322. https://doi.org/10.1070/QE1984v014n03ABEH004888.

(15) Carr, J. A.; Franke, D.; Caram, J. R.; Perkinson, C. F.; Saif, M.; Askoxylakis, V.; Datta, M.; Fukumura, D.; Jain, R. K.; Bawendi, M. G.; Bruns, O. T. Shortwave Infrared Fluorescence Imaging with the Clinically Approved Near-Infrared Dye Indocyanine Green. *Proc. Natl. Acad. Sci. USA* **2018**, *115*, 4465–4470. https://doi.org/10.1073/pnas.1718917115.

(16) Friedman, H. C.; Cosco, E. D.; Atallah, T. L.; Jia, S.; Sletten, E. M.; Caram, J. R. Establishing Design Principles for Emissive Organic SWIR Chromophores from Energy Gap Laws. *Chem* **2021**, *7*, 3359–3376. https://doi.org/10.1016/j.chempr.2021.09.001.

(17) Julia L. Bricks; Alexei D.Kachkovskii; Yurii L.Slominskii; Andrii O.Gerasov; Sergei V.Popov; Bricks, J. L.; Kachkovskii, A. D.; Slominskii, Y. L.; Gerasov, A. O.; Popov, S. V. Molecular Design of near Infrared Polymethine Dyes: A Review. *Dye. Pigment.* **2015**, *121*, 238–255. https://doi.org/10.1016/J.DYEPIG.2015.05.016.

(18) Li, B.; Zhao, M.; Zhang, F. Rational Design of Near-Infrared-II Organic Molecular Dyes for Bioimaging and Biosensing. *ACS Mater. Lett.* **2020**, *2*, 905–917. https://doi.org/10.1021/acsmaterialslett.0c00157.

(19) Bouit, P. A.; Aronica, C.; Toupet, L.; Guennic, B. Le; Andraud, C.; Maury, O. Continuous Symmetry Breaking Induced by Ion Pairing Effect in Heptamethine Cyanine Dyes: Beyond the Cyanine Limit. *J. Am. Chem. Soc.* **2010**, *132*, 4328–4335. https://doi.org/10.1021/ja9100886.

(20) Pascal, S.; Haefele, A.; Monnereau, C.; Charaf-Eddin, A.; Jacquemin, D.; Le Guennic, B.; Andraud, C.; Maury, O. Expanding the Polymethine Paradigm: Evidence for the Contribution of a Bis-Dipolar Electronic Structure. *J. Phys. Chem. A* **2014**, *118*, 4038–4047. https://doi.org/10.1021/jp501358q.

(21) Webster, S.; Padilha, L. A.; Hu, H.; Przhonska, O. V.; Hagan, D. J.; Van Stryland, E. W.;

Bondar, M. V.; Davydenko, I. G.; Slominsky, Y. L.; Kachkovski, A. D. Structure and Linear Spectroscopic Properties of near IR Polymethine Dyes. *J. Lumin.* **2008**, *128*, 1927–1936. https://doi.org/10.1016/j.jlumin.2008.06.002.

(22) Pengshung, M.; Cosco, E. D.; Zhang, Z.; Sletten, E. M. Counterion Pairing Effects on a Flavylium Heptamethine Dye†. *Photochem. Photobiol.* **2022**, *98*, 303–310. https://doi.org/10.1111/php.13531.

(23) Yang, Y.; Sun, C.; Wang, S.; Yan, K.; Zhao, M.; Wu, B.; Zhang, F. Counterion-Paired Bright Heptamethine Fluorophores with NIR-II Excitation and Emission Enable Multiplexed Biomedical Imaging. *Angew. Chem. Int. Ed.* **2022**, *61*, e202117436. https://doi.org/10.1002/anie.202117436.

(24) Luciano, M. P.; Crooke, S. N.; Nourian, S.; Dingle, I.; Nani, R. R.; Kline, G.; Patel, N. L.; Robinson, C. M.; Difilippantonio, S.; Kalen, J. D.; Finn, M. G.; Schnermann, M. J. A Nonaggregating Heptamethine Cyanine for Building Brighter Labeled Biomolecules. *ACS Chem. Biol.* **2019**, *14*, 934–940. https://doi.org/10.1021/acschembio.9b00122.

(25) Würthner, F.; Kaiser, T. E.; Saha-Möller, C. R. J-Aggregates: From Serendipitous Discovery to Supramolecular Engineering of Functional Dye Materials. *Angew. Chem. Int. Ed.* **2011**, *50*, 3376–3410. https://doi.org/10.1002/anie.201002307.

(26) Lei, Z.; Zhang, F. Molecular Engineering of NIR-II Fluorophores for Improved Biomedical Detection. *Angew. Chem. Int. Ed.* **2021**, Jul 19;*60* 16294–16308. https://doi.org/10.1002/anie.202007040.

(27) Mostovnikov, V. A.; Rubinov, A. N.; Al'perovich, M. A.; Avdeeva, V. I.; Levkoev, I. I.; Loiko, M. M. Dependence of the Luminescence and Generation Properties of Solutions of Polymethine Dyes on Their Structure. *J. Appl. Spectrosc.* **1974**, *20*, 31–35. https://doi.org/10.1007/BF00617286.

(28) Tolbert, L. M.; Zhao, X. Beyond the Cyanine Limit: Peierls Distortion and Symmetry Collapse in a Polymethine Dye. *J. Am. Chem. Soc.* **1997**, *119*, 3253–3258. https://doi.org/10.1021/ja9626953.

(29) McGlynn, S. P.; Sltnseri, R.; Christodouleas, N. External Heavy-Atom Spin-Orbital Coupling Effect. I. The Nature of the Interaction. *J. Chem. Phys.* **1962**, *37*, 1818–1824.

https://doi.org/10.1063/1.1733374.

(30) Solov'ev, K. N.; Borisevich, E. A. Intramolecular Heavy-Atom Effect in the Photophysics of Organic Molecules. *Physics-Uspekhi* **2005**, *48*, 231–253. https://doi.org/10.1070/pu2005v048n03abeh001761.

(31) Ormond, A.; Freeman, H.; Alexandra B. Ormond; Harold S. Freeman. Dye Sensitizers for Photodynamic Therapy. *Materials (Basel).* **2013**, *6*, 817–840. https://doi.org/10.3390/ma6030817.

(32) Semonin, O. E.; Johnson, J. C.; Luther, J. M.; Midgett, A. G.; Nozik, A. J.; Beard, M. C. Absolute Photoluminescence Quantum Yields of IR-26 Dye, PbS, and PbSe Quantum Dots. *J. Phys. Chem. Lett.* **2010**, *1*, 2445–2450. https://doi.org/10.1021/jz100830r.

(33) Kranitzky, W.; Kopainsky, B.; Kaiser, W.; Drexhage, K. H.; Reynolds, G. A. A New Infrared Laser Dye of Superior Photostability Tunable to 1.24 Mm with Picosecond Excitation. *Opt. Commun.* **1981**, *36*, 149–152. https://doi.org/10.1016/0030-4018(81)90158-9.

(34) Cosco, E. D.; Caram, J. R.; Bruns, O. T.; Franke, D.; Day, R. A.; Farr, E. P.; Bawendi, M. G.; Sletten, E. M. Flavylium Polymethine Fluorophores for Near- and Shortwave Infrared Imaging. *Angew. Chem. Int. Ed.* **2017**, *56*, 13126–13129. https://doi.org/10.1002/anie.201706974.

(35) Cosco, E. D.; Spearman, A. L.; Ramakrishnan, S.; Lingg, J. G. P.; Saccomano, M.; Pengshung, M.; Arús, B. A.; Wong, K. C. Y.; Glasl, S.; Ntziachristos, V.; Warmer, M.; McLaughlin, R. R.; Bruns, O. T.; Sletten, E. M. Shortwave Infrared Polymethine Fluorophores Matched to Excitation Lasers Enable Non-Invasive, Multicolour in Vivo Imaging in Real Time. *Nat. Chem.* **2020**, *12*, 1123–1130. https://doi.org/10.1038/s41557-020-00554-5.

(36) Carr, J. A.; Aellen, M.; Franke, D.; So, P. T. C.; Bruns, O. T.; Bawendi, M. G. Absorption by Water Increases Fluorescence Image Contrast of Biological Tissue in the Shortwave Infrared. *Proc. Natl. Acad. Sci. USA* **2018**, *115*, 9080–9085. https://doi.org/10.1073/pnas.1803210115.

(37) Chen, Z. H.; Wang, X.; Yang, M.; Ming, J.; Yun, B.; Zhang, L.; Wang, X.; Yu, P.; Xu, J.;

Zhang, H.; Zhang, F. An Extended NIR-II Superior Imaging Window from 1500 to 1900 Nm for High-Resolution In Vivo Multiplexed Imaging Based on Lanthanide Nanocrystals. *Angew. Chem. Int. Ed.* **2023**, *62*, e202311883. https://doi.org/10.1002/anie.202311883.

CHAPTER TWO

Real-time Multiplexed *in vivo* Imaging with Shortwave Infrared Chromenylium Polymethine Dyes

Adapted from: Emily D. Cosco, Anthony L. Spearman, Shyam Ramakrishnan, Jakob G. P. Lingg, Mara Saccomano, Sarah Glasl, Monica Pengshung, Bernardo A. Arús, Kelly C. Y. Wong, Vasilis Ntziachristos, Martin Warmer, Ryan R. McLaughlin, Oliver T. Bruns,* and Ellen M. Sletten* Shortwave infrared polymethine fluorophores matched to excitation lasers enable non-invasive multicolor *in vivo* imaging in real time. *Nat. Chem.* **2020**, *12*, 1123–1130. DOI: 10.1038/s41557-020-00554-5

And: Emily D. Cosco, Bernardo A. Arús, Anthony L. Spearman, Timothy L. Atallah, Irene Lim, Olivia S. Leland, Justin R. Caram, Thomas S. Bischof, Oliver T. Bruns,* and Ellen M. Sletten* Bright Chromenylium Polymethine Dyes Enable Fast, Four-Color *In Vivo* Imaging with Shortwave Infrared Detection. *J. Am. Chem. Soc.* **2021**, *143*, 6836–6846. DOI: 10.1021/jacs.0c11599.

2.1 Abstract

Real-time, high-resolution, multiplexed imaging is quite ubiquitous in cellular imaging. Unfortunately, extension for use in mammals can present challenges. These challenges stem from high light scattering and tissue autofluorescence seen with visible (350–700 nm) and near-infrared (700–1000 nm) light. Herein, we report real-time, *in vivo* multiplexed imaging by developing bright, red-shifted fluorophores for the shortwave infrared (SWIR; 1000-2000 nm) region. Additionally, we improved SWIR imaging technologies to better utilize these contrast agents. With new SWIR-emissive chromenylium polymethine dyes, we elucidated useful structure-property

relationships for the scaffold. Namely, we found that modifying the 7-position of the chromenylium scaffold can modulate λ_{max}, while modifying the 2-position influences Φ_F. In these works, I synthesized a couple of 7-amine substituted Flav7 derivatives with red-shifted λ_{max} and a bright 2-position modified chromenylium dye (which had a 3-fold increase in Φ_F). Additional work towards our new imaging system relied on multiple excitation wavelengths with single-channel collection, allowing for video-rate multicolor imaging. With fluorophores absorbance matched to commercial laser lines, we were able to perform multicolor imaging with great temporal and spatial resolution, up to four colors.

2.2 Introduction

Optical imaging is an indispensable tool for visualizing biological systems.[1,2] Aside from use in cells, fluorescence probes have also been used to study small organisms such as C. elegans, zebrafish, and fruit flies. However, extension to higher order organisms proves difficult for a number of reasons. Traditionally, fluorescence imaging utilizes visible (350–700 nm) and near-infrared (700–1000 nm) light. Visible light is not suitable for imaging mammals due to limited tissue penetration and confounding tissue autofluorescence.[3–5] NIR light can avoid both of these limitations, but high light scattering still hampers resolution. Additionally, limited spectral real estate within the NIR region (a mere 300 nm) limits multiplexing efforts. For these reasons, moving further beyond into the shortwave infrared (1000–2000 nm) region can lead to superior multiplexed imaging in mammals. SWIR light has reduced tissue autofluorescence, low scattering coefficients, and good tissue penetration.[3,6,7] Additionally, water absorption of SWIR light also further improves contrast compared to the NIR region.[8]

Multiplexed imaging in mice has been performed with fluorescent proteins,[9] quantum dots,[10] surface-enhanced Raman scattering nanoparticles,[11] and fluorescently labelled silica

particles.[12] However, these approaches are all limited by low spatial and temporal resolution. To overcome these limitations, certain requirements must be met. For improved multiplexed imaging in mammals (1) detection must lie in a region of the electromagnetic spectrum that gives high spatial resolution; (2) orthogonal excitation and/or emission detection of fluorophores must be established; and (3) emission collection must occur on millisecond timescales. One strategy that employs these requirements involves 'matched-excitation' and single-channel detection within the shortwave infrared region, deemed excitation multiplexed SWIR imaging (Figure 2.1A).

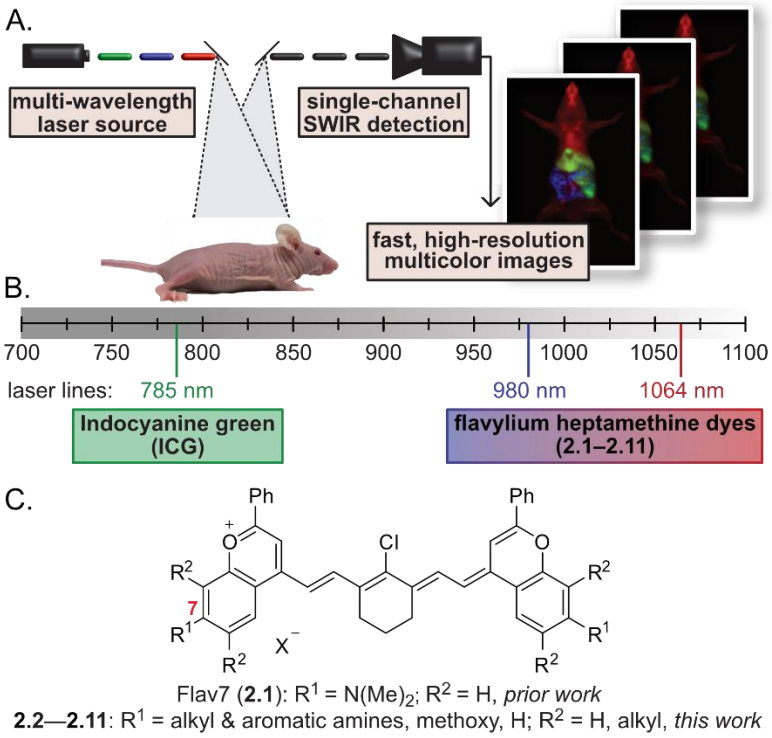

Figure 2.1. Real-time excitation-multiplexed SWIR imaging design. **A**. Multiple laser sources are pulsed and delivered to the biological sample. Single-channel SWIR detection (InGaAs, 1100–1700 nm) acquires frames that are temporally separated by color on the millisecond timescale. Fast frame rates produce real-time multicolor *in vivo* images at up to 50 fps. **B**. Relevant portions of the NIR and SWIR regions of the electromagnetic spectrum, lasers used for excitation and dyes used and/or presented in this study that are excited by the distinct laser lines. **C**. Flavylium polymethine scaffold explored here to match bright SWIR dyes to appropriate lasers. Position 7- on the flavylium heterocycle is indicated in red.

With detection occurring within the SWIR region, the aforementioned imaging advantages of SWIR light can be harnessed. Superior tissue penetration and decreased noise allows for higher resolution and *in vivo* utility compared to NIR wavelengths.[8,13] Furthermore, the increased spectral real estate of the SWIR region increases the number of excitation channels allowed.[14] To date, SWIR *in vivo* imaging has been demonstrated with carbon nanotubes,[15] quantum dots,[16,17] rare-earth nanomaterials,[14] and small molecule fluorophores.[18–20] In these works, it was directly observed that higher spatial resolutions can be attained using SWIR light than with NIR light.

Typically, SWIR multiplexed imaging uses a set excitation wavelength with collection of orthogonal emission windows (hence referred to as emission-multiplexed imaging).[14,21–27] However, due to the spectral difference between the emission channels, discrepancies in contrast and resolution will be observed.[8,28,29] Additionally, imaging speeds can be impeded due to low photon throughput in sectioned regions of the electromagnetic spectrum or by mechanical components, such as filter wheels. Excitation-multiplexed imaging circumvents this with its single channel emission window. This allows for uniform resolution, high photon efficiency, and rapid frame collection.[28,29] To date, this technique has yet to be utilized for imaging animals.[30–32] With preferential excitation, each fluorophore can be optimally excited with photons detected across a wide range of wavelengths. This is useful as it maximizes the signal given by SWIR dyes, contrast agents that have inherently low quantum yields relative to VIS and NIR dyes.[3,33,34]

In order to maximize the potential of excitation-multiplexed imaging, bright fluorophores with λ_{max} at commercial laser lines are required (Figure 2.1B). Polymethine dyes present themselves as a scaffold of choice due to their narrow absorption profiles, high molar absorptivity, and tunability.[35,36] Our group has developed a flavylium heptamethine dye, deemed Flav7 (**2.1**).[37] Flav7 (λ_{max} = 1027 nm) was shown to be a bright fluorophore for SWIR optical imaging and we

envisioned that structural modifications at the 7-position could modulate λ_{max} to access nearby commercial laser lines (Figure 2.1B/C 980 nm and 1064 nm). The resulting panel of flavylium heptamethine derivatives (**2.2**–**2.11**) indeed displayed differences in absorbance, with minimal impact on brightness. Gratifyingly, two fluorophores (**2.3** and **2.10**) proved amenable to excitation at the two target laser lines. Finally, in concert with FDA approved fluorophore indocyanine green (**ICG**; λ_{ex} = 785 nm),[38,39] 3-color excitation-multiplexed SWIR imaging was performed.

2.3 Results and Discussion

2.3.1 Flavylium Polymethine Dye Design and Synthesis

To tune the absorption properties of flavylium polymethine dyes for excitation multiplexing, robust synthetic approaches towards flavylium heterocycles (**2.12a-j**) were necessary. The original report of **Flav7** used a previously published, low-yielding, electronically sensitive and potentially explosive route.[40] We developed an approach relying on a key 7-substituted flavone intermediate (**2.13**) that could be converted to the desired heterocycles by treatment with a methyl nucleophile and dehydration (Scheme 2.1). Using three general routes to flavones, (1) Mentzer pyrone synthesis between β-keto ester (**2.14**) and aminophenol (**2.15**),[41] (2) functionalization of 7-hydroxyflavone (**2.16**) by Buchwald–Hartwig coupling of the corresponding triflate (**2.17**)[42] and (3) acylation of the commercial 7-aminoflavone (**2.18**), we accessed a diverse set of 7-aminoflavylium heterocycles **2.12a–i**. 7-methoxyflavylium (**2.12j**) was accessed via previous literature precedent.[40] Heptamethine dyes **2.1**–**2.11** (Fig. 2.2A) were then obtained through the base-promoted reaction of each flavylium heterocycle with a bis(phenylimine) polymethine linker **2.19** (Table 2.1). Reported isolated yields are lower than conversions due to similar retention times by normal-phase column chromatography between heptamethine dyes and other dye species obtained in small amounts including monomethine, trimethine, and half-dye species. My direct contributions towards this panel of dyes included the synthesis and purification

of triflate precursor **2.17**, amino flavones **2.13e** and **2.13f**, heterocycles **2.12e** and **2.12f**, and finally fluorophores **2.5** and **2.6**.

Scheme 2.1. Retrosynthesis of 7-substituted flavylium heterocycles.

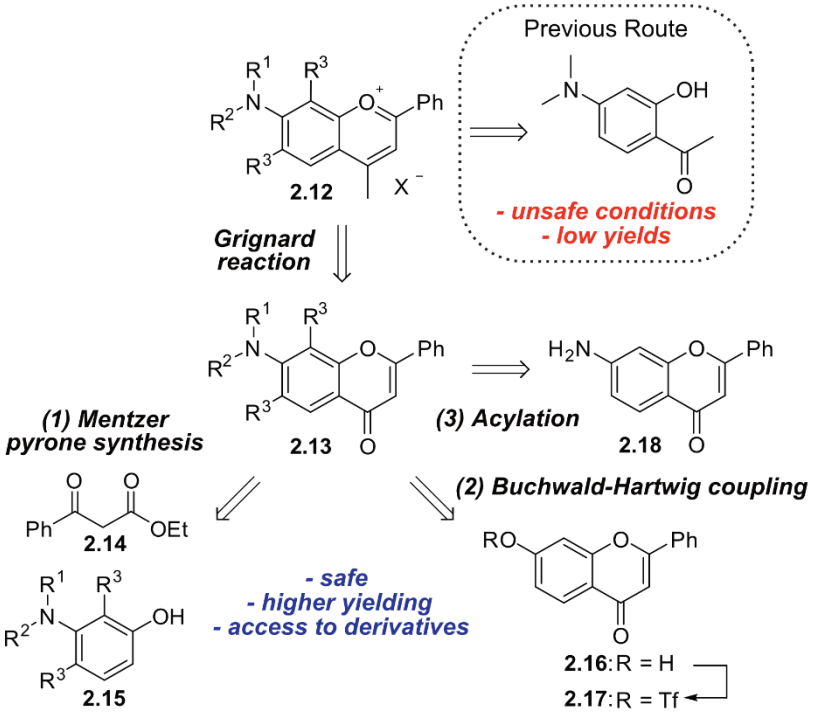

Table 2.1. Forward synthesis of flavylium heptamethine dyes **2.1**–**2.11**.

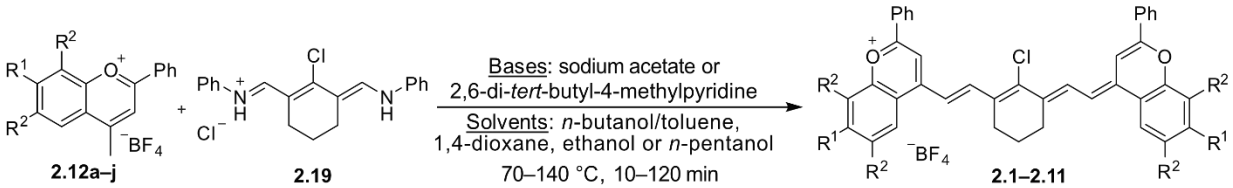

2.12a–j 2.19 2.1–2.11

Flavylium 2.12	*R^1*	*R^2*	*base*[a]	*solvent*	*temp (°C)*	*time (min)*	*yield # (%)*	*dye*
2.12a		H	A	*n*-butanol/toluene	100	15	51	**2.1**
2.12b		H	A	*n*-butanol/toluene	100	10	40	**2.2**
2.12c	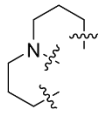		A	ethanol	70	120	37	**2.3**
2.12d		H	A	*n*-butanol/toluene	100	10	37	**2.4**
2.12e		H	B	*n*-pentanol	140	50	8	**2.5**
2.12f		H	B	*n*-butanol/toluene	100	120	26	**2.6**
2.12g		H	B	1,4-dioxane	100	15	11	**2.7**
2.12h	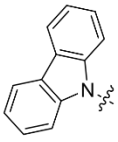	H	B	1,4-dioxane	90	15	13	**2.8**
2.12i	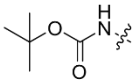	H	B	1,4-dioxane	95	15	33[b]	**2.9**
2.12j[c]		H	B	*n*-butanol/toluene	100	15	33	**2.10**
–		H	B	*n*-butanol/toluene	90	45	5	**2.11**

[a]base: A = sodium acetate; B = 2,6-di-*tert*-butyl-4-methylpyridine
[b]yield over two steps, flavylium **2.12i** not isolated.
[c]counterion is Cl^-

2.3.2 Fluorophore Photophysical Properties

We characterized the photophysical properties of **2.1**–**2.11** in dichloromethane (DCM), finding that the flavylium heptamethine dyes have absorption/emission spanning the NIR to SWIR regions of the electromagnetic spectrum (Figure 2.2A, Table 2.1). Compared to Flav7 (**2.1**), with

$\lambda_{max,abs}$ = 1,027 nm, **2.9** and **2.10** underwent hypsochromic shifts. The 7-methoxy-substituted dye **2.10** is ~43 nm blue-shifted from **Flav7** ($\lambda_{max,abs}$ = 984 nm), similar to the unsubstituted flavylium dye **2.11** (IR-27).[43] Conversely, dyes **2.3** and **2.7** displayed substantial bathochromic shifts compared to **Flav7**. The diphenylamino-substituted **2.7** is ~23 nm red-shifted, while julolidine derivative **2.3** is red-shifted by ~35 nm ($\lambda_{max,abs}$ = 1,061 nm). Linear and cyclic aliphatic amine-substituted dyes **2.2** and **2.4**–**2.6** exhibit minor red-shifts. Plotting absorption/emission wavelengths of nine dyes in the series against Hammett σ_m values[44] resulted in a strong correlation (R^2 = 0.96; Figure 2.2B). This increased understanding of the relationship between structure and absorption/emission wavelengths sets up opportunities for predicting fluorophore structures to match any desired excitation wavelength.

Further characterization of the panel of flavylium polymethine dyes was necessary to determine their maximum brightness (taken as the product of ε_{max} and Φ_F). Absorption coefficients (ε) varied between 110000 and 240000 M^{-1} cm^{-1}, in line with the high-absorption cross-sections characteristic for polymethine fluorophores.[35] The fluorescence quantum yields (Φ_F; relative measurements to dye **IR-26** = 0.05%)[45,46] remain rather constant, in the ~0.4–0.6% range. Notably, we obtained flavylium heptamethine dyes that matched the 980 nm and 1064 nm laser line, MeOFlav7 (**2.10**) and JuloFlav7 (**2.3**), respectively, that maintained high and relatively consistent ε_{max} and Φ_F values (Figure 2.2C).

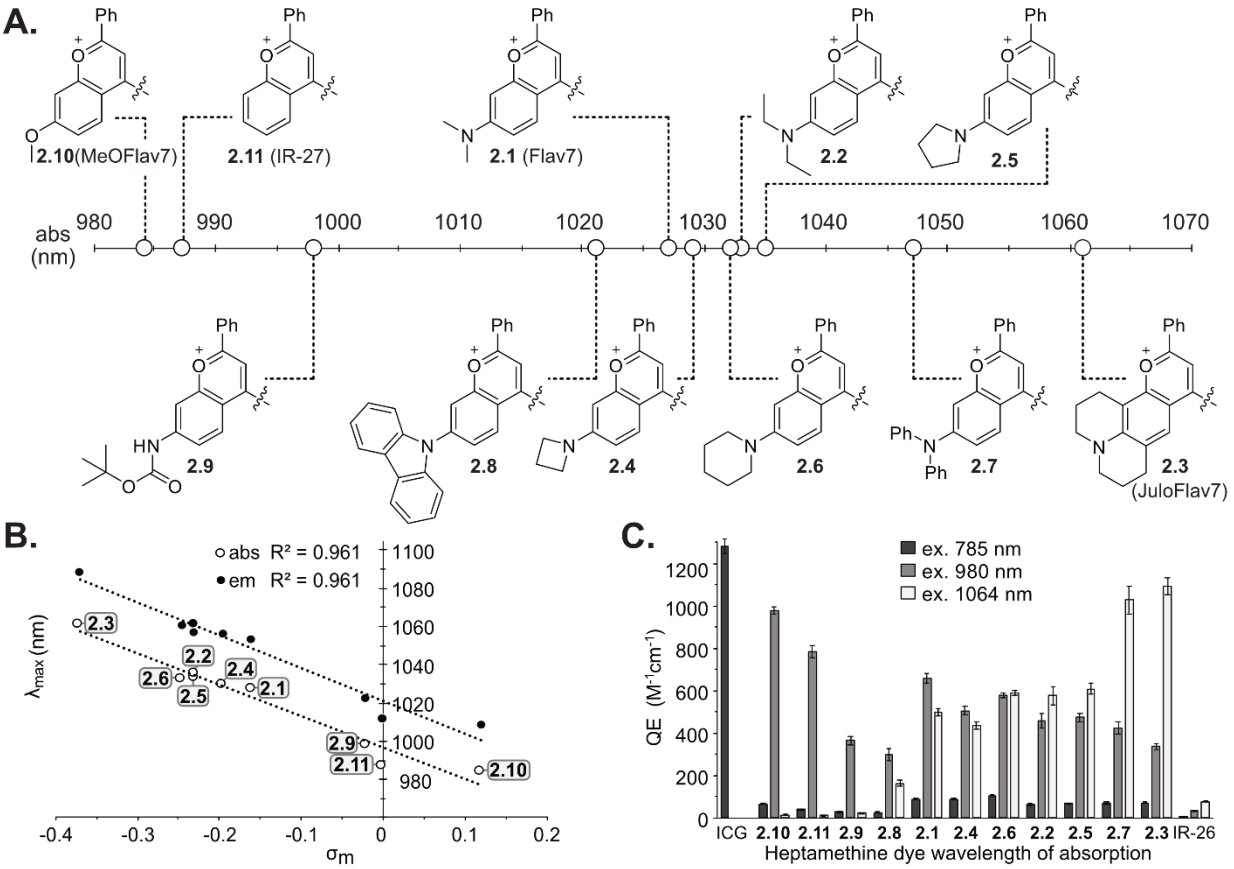

Figure 2.2. Panel of flavylium heptamethine dyes and their photophysical properties. **A**. Heterocycle structures and absorption wavelength maxima visualized graphically on the electromagnetic spectrum. **B**. Hammett plot relating σ_m substituent constants to absorption and emission wavelengths of dyes **2.1**–**2.6** and **2.9**–**2.11**. **C**. Brightness (product of ε_{max} and Φ_F) of the heptamethine derivatives at relevant excitation wavelengths (λ = 785 nm (dark grey), λ = 980 nm (light grey) and λ = 1,064 nm (white)). Error bars represent the propagated error from standard deviations in ε and Φ_F measurements.

Table 2.2. Photophysical properties of flavylium heptamethine dyes (**2.1**–**2.11** and commercial standards).

dye	$\lambda_{max,abs}$ (nm)	ε_{max} ($M^{-1}cm^{-1}$)	$\lambda_{max,em}$ (nm)	Φ_F (%)	Brightness(ε_{max}) ($M^{-1}cm^{-1}$)
2.1 (Flav7)	1027	241,000 ± 1,000	1053	0.61 ± 0.02	1470 ± 50
2.2	1033	190,000 ± 10,000	1057	0.62 ± 0.02	1180 ± 70
2.3 (JuloFlav7)	1061	238,000 ± 7,000	1088	0.46 ± 0.01	1090 ± 40
2.4	1029	207,000 ± 1,000	1056	0.51 ± 0.02	1060 ± 40
2.5	1034	247,000 ± 1,000	1061	0.48 ± 0.02	1190 ± 50
2.6	1032	110,000 ± 10,000	1060	0.54 ± 0.01	590 ± 60
2.7	1047	210,000 ± 10,000	1078	0.58 ± 0.02	1220 ± 70
2.8	1021	140,000 ± 10,000	1048	0.45 ± 0.01	630 ± 40
2.9	998	108,000 ± 4,000	1022	0.42 ± 0.02	450 ± 30
2.10 (MeOFlav7)	984	190,000 ± 1,000	1008	0.52 ± 0.01	990 ± 20
2.11 (IR-27)	987	231,000 ± 6,000	1011	0.35 ± 0.01	810 ± 30
ICG	787[a]	194,000[a] ± 5,000	818[a]	0.66[a,b] ± 0.01	1,280 ± 30[b]
IR-26	1080	171,000 ± 5,000	1114	0.05[c]	86 ± 3

[a]data taken from Rurack, K. & Spieles, M. *Anal. Chem.* **83**, 1232–1242 (2011). (measured in EtOH)
[b]value includes only the % emission between 1000–1300 nm (5%), from Carr, J. A. *et al. Proc. Natl. Acad. Sci. USA* **115**, 4465–4470 (2018).
[c]value from Semonin, O. E. et al. *J. Phys. Chem. Lett.* **1**, 2445–2450 (2010). and treated as a constant for relative Φ_F measurements.

2.3.3 Excitation Multiplexing with Flavylium Dyes

The development of MeOFlav7 (**2.10**) and JuloFlav7 (**2.3**) gave two fluorophores for SWIR excitation multiplexed imaging (at 980 nm and 1064 nm respectively). With the addition of **ICG**, we had three distinct fluorophores that could be individually excited. In preparation for *in vivo* delivery, JuloFlav7 (**2.3**) and MeOFlav7 (**2.10**) were then encapsulated in polyethylene glycol-coated micelles to impart water solubility. Three-color imaging *in vivo* was done by first performing an intraperitoneal (*i.p.*) injection of MeOFlav7 (**2.10**), followed by *i.v.* injections of JuloFlav7 (**2.3**) and finally **ICG** (Figure 2.3A). Representative time points of the three-color video

are displayed in Figure 2.3B. The discussed 3-color *in vivo* imaging was performed by Emily Cosco, Mara Saccomano, Bernardo Arus, and Sarah Glasl. Herein, we have established a new imaging setup as well as molecular tools for high resolution real-time multiplexed imaging *in vivo*. This was achieved through the design of SWIR fluorophores based off a flavylium heptamethine scaffold. Subtle structural modifications allowed for varying $\lambda_{max,\,abs}$ to be obtained which enabled precise excitation with commercially available laser lines. However, brighter fluorophores and lower exposure times could lead to faster, higher-resolution multiplexed imaging. Furthermore, additional sites on the heterocycle could also be explored for new structure-property relationships.

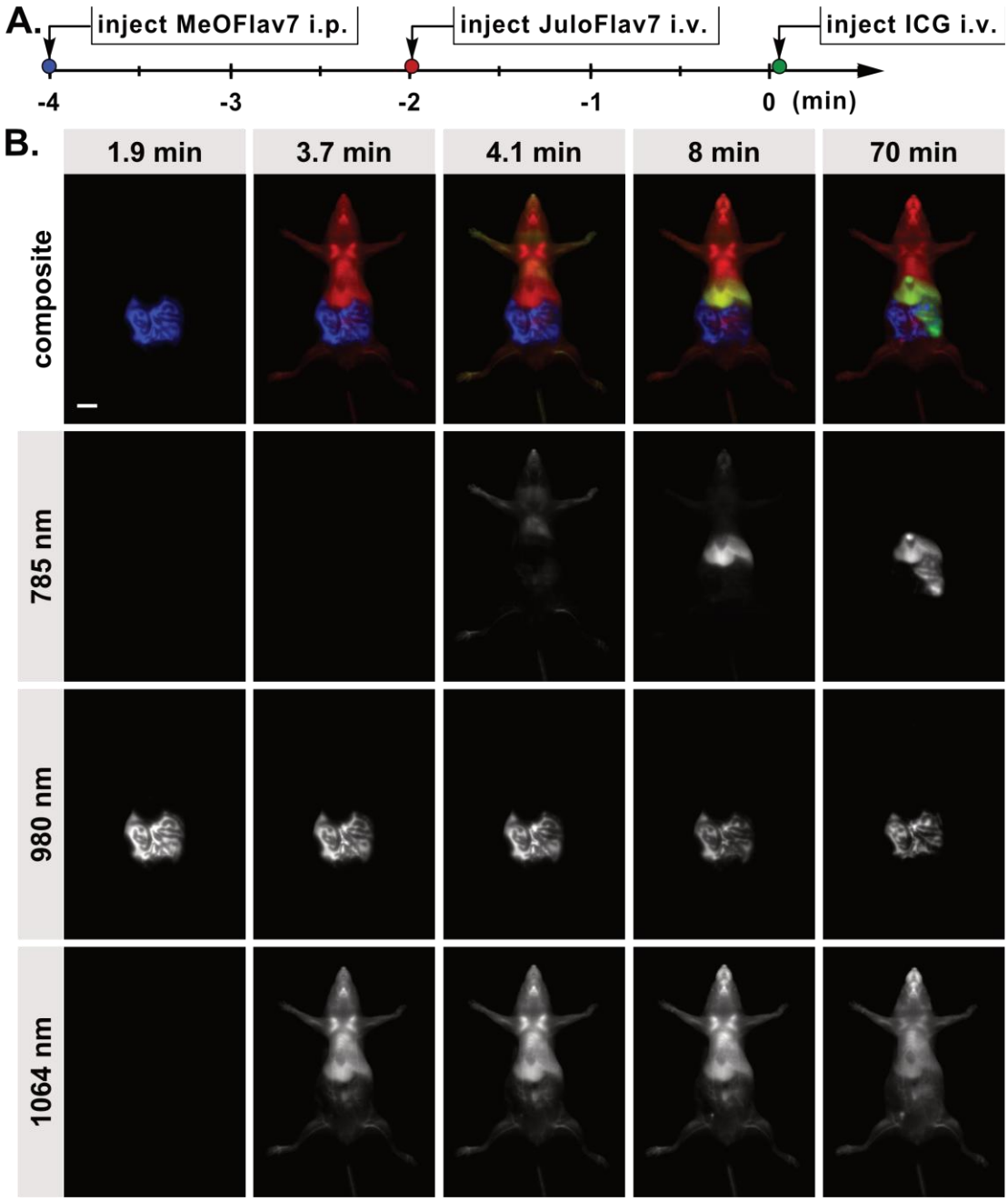

Figure 2.3. Video-rate multiplexed imaging *in vivo*. **A**. Injection timeline for probes **2.10** (*i.p.*, 211 nmol in micelles), **2.3** (*i.v.*, 50 nmol in micelles) and **ICG** (*i.v.*, 6.5 nmol). **B**. Representative multiplexed *in vivo* images. Displayed images averaged over 5 frames. Data are representative of two replicate experiments. Acquisition parameters were excitation for three channels at 785 nm (78 $mWcm^{-1}$), 980 nm (77 $mWcm^{-1}$), and 1,064 nm (79 $mWcm^{-1}$) and 1150–1700 nm collection (10 ms exposure time, 27.8 fps). Scale bar represents 1 cm.

2.3.4 Improving Excitation Multiplexing Capabilities

Our group previously demonstrated non-invasive, real-time, multichannel imaging in living mice in video rate (27 frames per second, fps Figure 2.3). However, this approach was limited to only three colors and produced some challenges in motion artifacts due to the ~10 ms separation between channels. Faster acquisition speeds would allow for enhanced temporal resolution in three color imaging and/or increase the number of orthogonal excitation channels (and thus biological parameters) that can be acquired while maintaining video-rate acquisition.

To produce orthogonal signals from differing, well-separated (~75−100 nm) excitation wavelengths across the NIR and SWIR regions, two classifications of emitters are necessary: (1) fluorophores with SWIR absorption and emission and (2) NIR absorbing dyes which exhibit long wavelength emission tails extending into the SWIR region (Figure 2.4A/B). Imaging NIR dyes in the SWIR requires a higher overall brightness to compensate for the small fraction of the emission signal that is collected (Figure 2.4B). Of note, in our three-color set-up we were unable to utilize the 892 nm laser, as all heptamethine derivatives had too red-shifted λ_{max}.

With existing 7-position flavylium structure−property relationships in hand, we could reliably red- or blue-shift excitation wavelengths but could not enhance emissive properties, offering little insight into further increasing the brightness of the scaffold. However, by modifying the 2-position on the scaffold, we observed differences in emissive behavior. To achieve bright fluorophores for blue-shifted laser lines (namely 892 nm) we explored pentamethine analogues, as reduction of the polymethine chain by 2 methine units should reliably blue-shift ~100 nm. From these modifications, we developed bright fluorophores for imaging at both 892 nm and 968 nm (Figure 2.4C). Finally, in tandem with **2.3** (JuloFlav7) and ICG once more, we achieved non-invasive video-rate *in vivo* imaging with four colors.

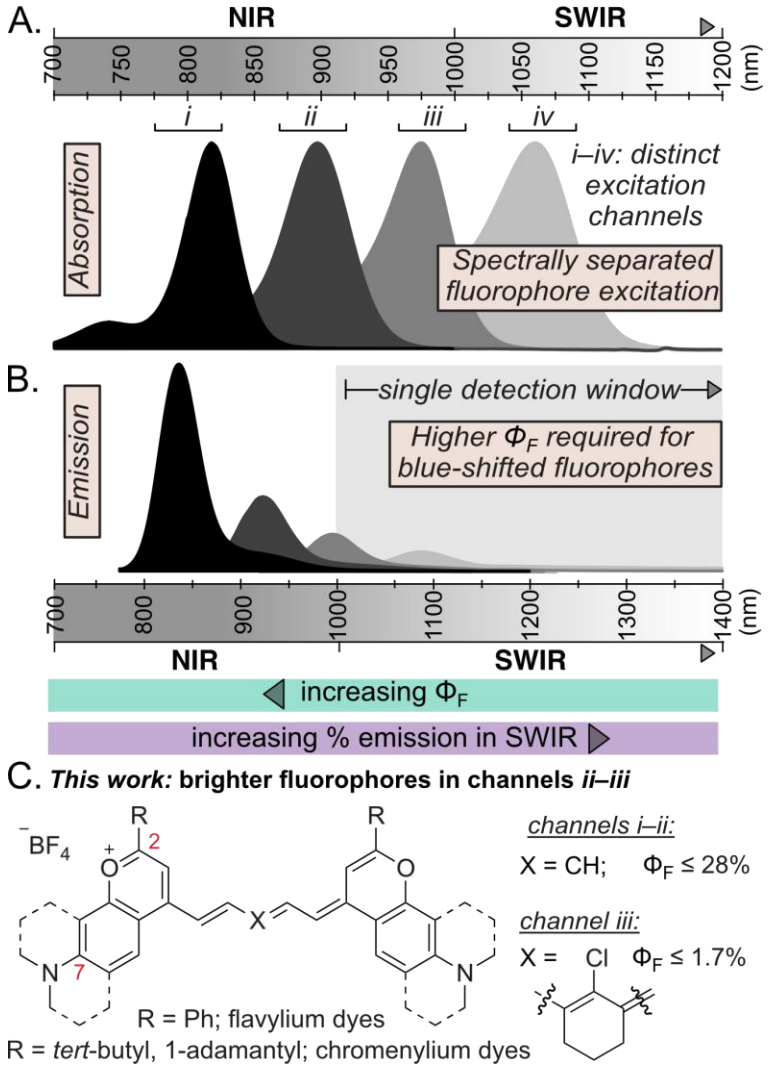

Figure 2.4. Fluorophores in the context of excitation multiplexed SWIR imaging. **A**. Absorption properties of select fluorophores aligned with distinct excitation channels across the NIR and SWIR regions. **B**. Emission properties of select fluorophores across the NIR and SWIR overlaid with a SWIR detection window, defined here as 1000−1700 nm. Intensities are schematized to represent the key imaging concepts defined below. **C**. Pentamethine and heptamethine fluorophores from this work. Positions 2- and 7- on the flavylium and chromenylium heterocycles are indicated in red.

2.3.5 Chromenylium Polymethine Dyes

We hypothesized that rotational and vibrational modes within the phenyl group at the 2-position on flavylium (Figure 2.4C) could be contributing to internal conversion in the resulting polymethine dyes. To investigate this question, we targeted 4-methyl chromenylium heterocycles containing either a *tert*-butyl or a 1-adamanyl group at their 2-positions and applied them to

synthesize pentamethine and heptamethine dyes with absorption between 800 and 1000 nm (Figure 2.5A/B). We found that the chromenylium heterocycles could be synthesized by an analogous route to the prior flavylium variants (Scheme 2.1).[47] From these heterocycles, we synthesized the hepta- and pentamethine chromenylium dyes **2.21**–**2.26** through the classic polymethine condensation reaction with the corresponding conjugated bis(phenylimine) (**2.19** and **2.28**, respectively, Scheme 2.2). In previous work, we found that the introduction of a julolidine-containing flavylium heterocycle provided advantageous red-shifts (**2.3**, JuloFlav7, $\lambda_{max,abs}$ = 1061 nm, Φ_F ~0.46%) compared to Flav7 (**2.1**).[47] Consequently, we were also interested in investigating the pentamethine flavylium dye that would result from this same julolidine-containing heterocycle (**2.21**) and the chromenylium pentamethine and heptamethine fluorophores containing the julolidine functionality (**2.26** and **2.27**, respectively, Figure 2.5A). My direct contributions towards this panel of dyes included the synthesis and purification of chromone **2.13m**, chromenylium **2.12m**, and JuloChrom7 (**2.26**)

Scheme 2.2. Synthesis of chromenylium heptamethine (**A**) and pentamethine (**B**) dyes **2.20**–**2.27**. Refer to the legend (**C**) and Table 2.1 for heterocycle (**2.12**) substitution.

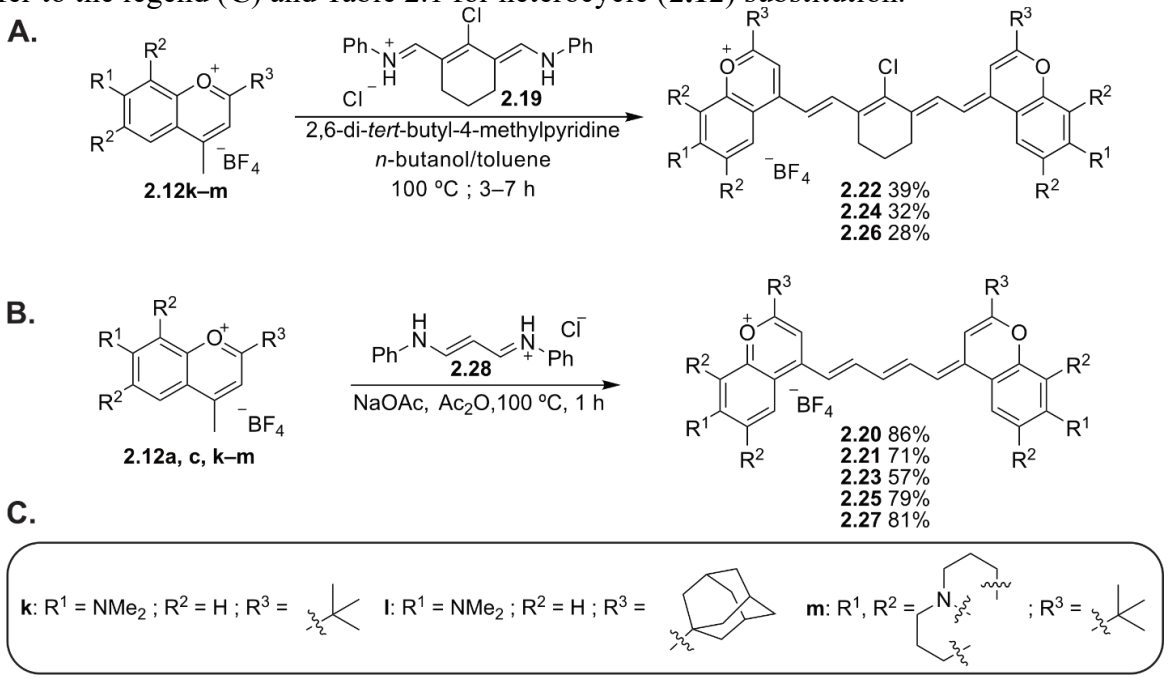

After preparation of the chromenylium dyes **2.22–2.27**, as well as the previously reported flavylium dyes **2.1**, **2.20** (Flav5), and **2.3**, and the new flavylium dye **2.21** (Scheme 2.2, select dyes are named after the heterocycle and the number of methine units in the polymethine chain), we performed a thorough comparative investigation of their photophysical properties (Figure 2.5B-E). The photophysical properties in dichloromethane reveal that the absorption and emission of the chromenylium heptamethine derivatives are blue-shifted by λ ~52 nm (ν ~500 cm^{-1}) and the chromenylium pentamethine dyes by λ ~44 nm (ν ~600 cm^{-1}), from their flavylium counterparts (Figure 2.5B/E). The absorption coefficients remain characteristically high, with the pentamethine dyes having, on average, higher values than the heptamethine dyes, at ~360,000 $M^{-1}cm^{-1}$ and ~250,000 $M^{-1}cm^{-1}$, respectively (Figure 2.5E). Remarkably, the emissive properties were increased substantially, with heptamethine chromenylium dyes Φ_F = 1.6–1.7% (relative measurements to **IR-26** = 0.05%)[45,46] and pentamethine chromenylium dyes Φ_F = 18−28% (absolute quantum yield measurements) (Figure 2.5C/D). Combining the absorptive and emissive properties, **2.22** and **2.24** have the highest brightness of the heptamethines at 4300 $M^{-1}cm^{-1}$, while **2.23** is the brightest pentamethine dye (106,000 $M^{-1}cm^{-1}$).

While overall brightness is an important comparative metric, the more relevant brightness metric for excitation-multiplexed imaging with single channel SWIR detection is the percent of emission that is within the SWIR region. We accounted for this parameter by defining SWIR brightness = ε_{max} x Φ_F x α, where α = emission ≥ 1000 nm/total emission, calculated from the emission spectra. All of the chromenylium heptamethine dyes have a higher SWIR brightness than the flavylium heptamethine dyes, despite their more blue-shifted photophysics (Figure 2.5E). For

the pentamethines, flavylium dye **2.21** and chromenylium dyes **2.23** and **2.27** are the brightest SWIR emitters of the series.

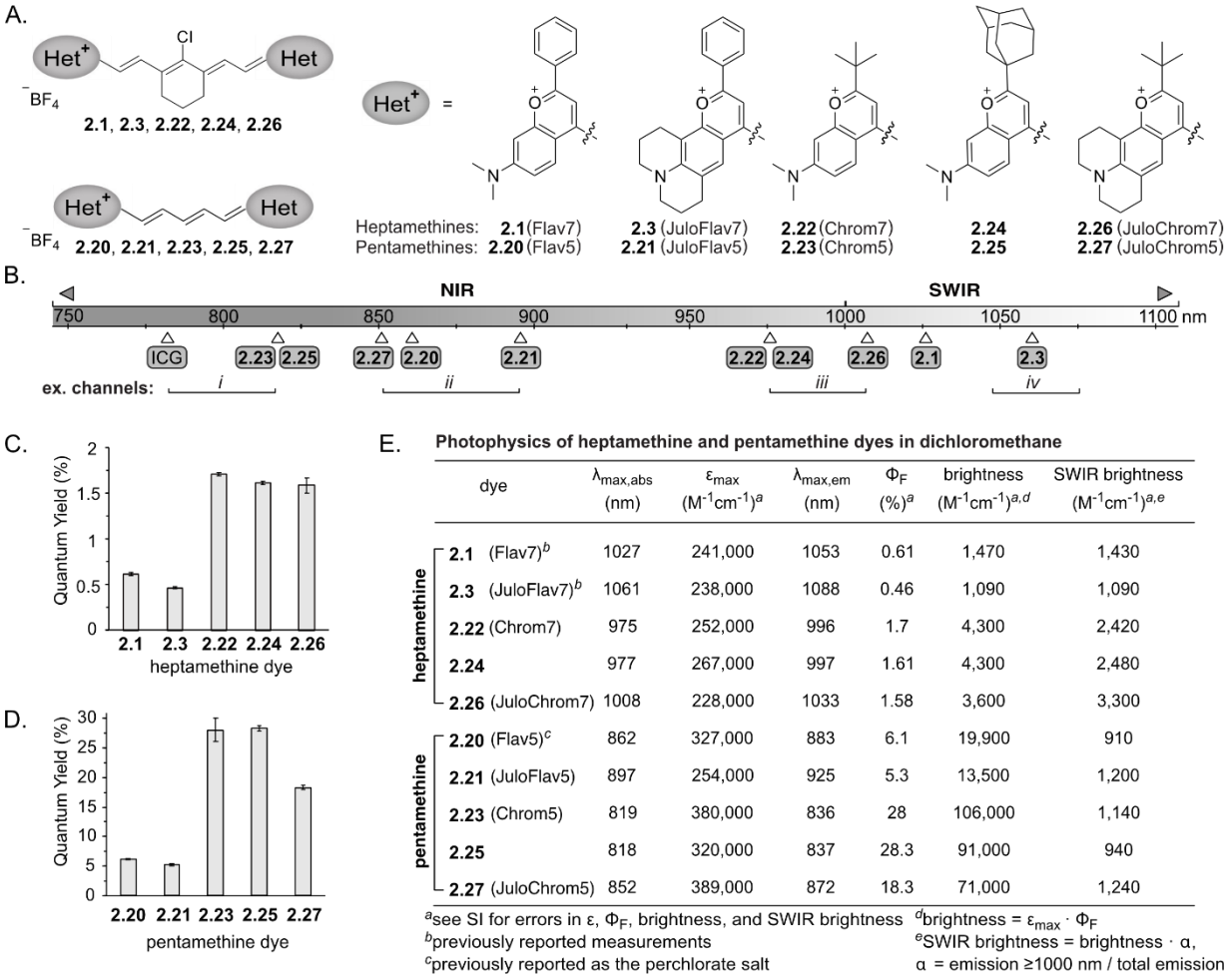

E. **Photophysics of heptamethine and pentamethine dyes in dichloromethane**

	dye	$\lambda_{max,abs}$ (nm)	ε_{max} ($M^{-1}cm^{-1}$)[a]	$\lambda_{max,em}$ (nm)	Φ_F (%)[a]	brightness ($M^{-1}cm^{-1}$)[a,d]	SWIR brightness ($M^{-1}cm^{-1}$)[a,e]
heptamethine	**2.1** (Flav7)[b]	1027	241,000	1053	0.61	1,470	1,430
	2.3 (JuloFlav7)[b]	1061	238,000	1088	0.46	1,090	1,090
	2.22 (Chrom7)	975	252,000	996	1.7	4,300	2,420
	2.24	977	267,000	997	1.61	4,300	2,480
	2.26 (JuloChrom7)	1008	228,000	1033	1.58	3,600	3,300
pentamethine	**2.20** (Flav5)[c]	862	327,000	883	6.1	19,900	910
	2.21 (JuloFlav5)	897	254,000	925	5.3	13,500	1,200
	2.23 (Chrom5)	819	380,000	836	28	106,000	1,140
	2.25	818	320,000	837	28.3	91,000	940
	2.27 (JuloChrom5)	852	389,000	872	18.3	71,000	1,240

[a]see SI for errors in ε, Φ_F, brightness, and SWIR brightness
[b]previously reported measurements
[c]previously reported as the perchlorate salt
[d]brightness = $\varepsilon_{max} \cdot \Phi_F$
[e]SWIR brightness = brightness · α, α = emission ≥1000 nm / total emission

Figure 2.5. Structures and photophysical properties of heptamethine and pentamethine dyes. **A**. Chemical structures of heptamethine and pentamethine dyes explored in this study. **B**. Absorption maxima of **ICG** and dyes **2.1**, **2.3**, and **2.20**–**2.27** displayed graphically on the electromagnetic spectrum and aligned with the distinct excitation channels used for excitation-multiplexed, single-channel SWIR imaging. **C**. Quantum yields of heptamethine dyes. **D**. Quantum yields of pentamethine dyes. For C and D, error bars represent standard deviation. **E**. Table of photophysical properties taken in dichloromethane.

2.3.6 Excitation Multiplexing with Chromenylium Dyes

Once again, to prepare for *in vivo* imaging, we formulated each chromenylium or flavylium dye into water soluble poly(ethylene) glycol-phospholipid micelles. Interestingly, while the

formation of non-emissive aggregates in addition to a monomer species is common for encapsulated long wavelength polymethine dyes, the chromenylium dyes displayed minimal aggregate formation in their absorption spectra. This difference is best visualized by comparing absorbance traces of **2.3** (JuloFlav7) and **2.26** (JuloChrom7) (Figure 2.6A/B).

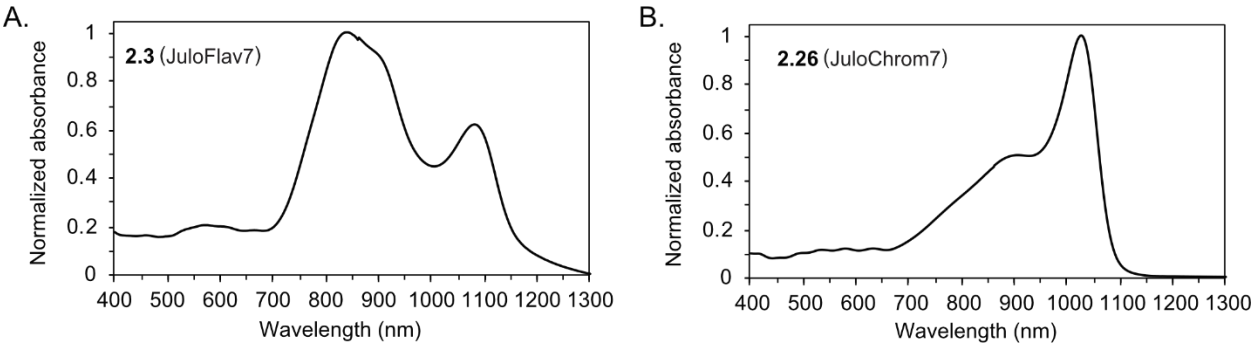

Figure 2.6. Normalized absorbance traces of PEG-phospholipid micelles of chromenylium and flavylium polymethine dyes in PBS buffer at 3–5 μM (path length = 2.0 mm).

With encapsulated flavylium and chromenylium fluorophores, we prepared to improve *in vivo* imaging capabilities. These fluorophores enabled improved single color and 3-color *in vivo* imaging. We were first able to image a whole mouse with Chrom7 (**2.22**) at 300 fps. Then we moved to 3-color excitation multiplexed SWIR imaging. These efforts employed **2.23**, **2.21**, and **2.22** together, preferentially excited by 785, 892, and 968 nm lasers, respectively, with collection using 1000 nm LP filtering. Images with excellent signal were collected with 3.3 ms exposure time (ET) and 100 fps multiplexed frame rate, which is over 3x the speed obtained previously (~27 fps; Figure 2.3).

Finally, the new NIR fluorophores allowed the addition of a fourth channel such that four-color SWIR imaging could be performed for the first time. We chose **ICG**, JuloChrom5 (**2.27**), Chrom7 (**2.22**), and JuloFlav7 (**2.3**) as spectrally distinct fluorophores with preferential excitation at 785, 892, 968, and 1065 nm, respectively, and collection with 1100 nm LP filtering (Figure

2.7A). Again, we optimized injection routes, times, and amounts to ensure a different biodistribution of probes would be present with similar brightness at the time of imaging. First, JuloChrom5 (**2.27**) was injected *i.v.* 27 h prior to serve as a structural reference. Next, **ICG** was injected *i.v.* and allowed to clear for 5 h through the liver into the intestine. JuloFlav7 (**2.3**) was then administered into the *i.p.* space 7 min before imaging, and finally, Chrom7 (**2.22**) was injected *i.v.* to obtain the time-course images of the injection displayed in Figure 2.7B/C. For multiplexed experiments employing 1065 nm laser excitation, longer exposure times were needed due to the smaller, more red-shifted collection window decreasing the percentage of emissive-tails of the dyes collected. Nonetheless, the signal in each channel was sufficient for collection at 30 fps, with a 7.8 ms ET for each channel. Notably, the four-color experiment was able to be performed at similar speeds to previously reported three-color experiments which used 1064 nm laser excitation, providing video-rate temporal resolution of function, visualized in the heart and breathing rates (Figure 2.7D/E). The lower exposure times used herein (7.8 ms vs 10 ms) were possible due to the improved brightness of the chromenylium dyes and the scaled power densities of the excitation wavelengths. The improvements in imaging speed and number of channels open up opportunities to monitor multiple anatomical (such as lymphatic, hepatic, and skeletal) and functional (such as metabolic) parameters simultaneously, on a millisecond time scale. The discussed *in vivo* imaging in this section was performed by Emily Cosco and Bernardo Arus.

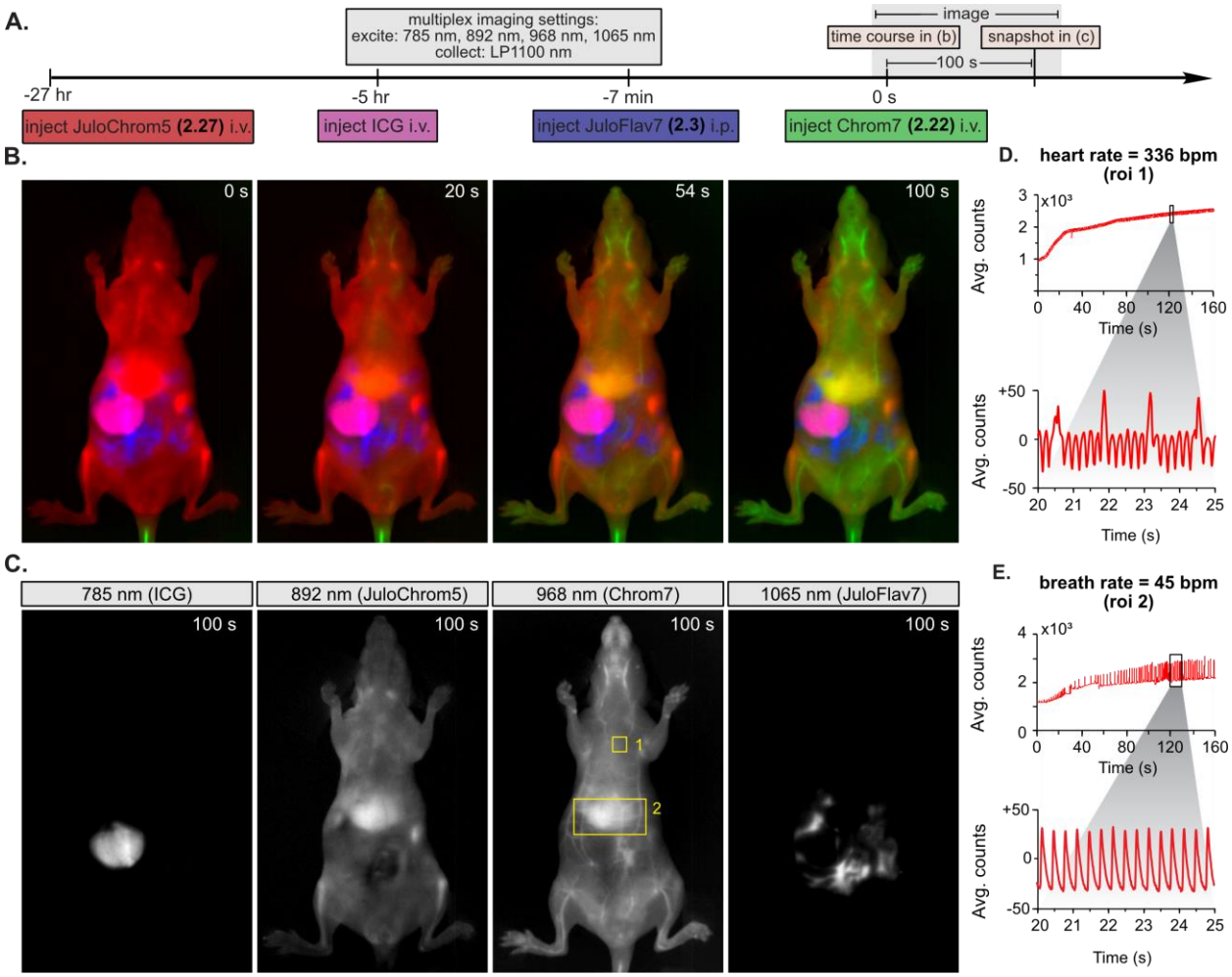

Figure 2.7. Video-rate four-color imaging. **A**. Experimental timeline for experiment in (B/C) (not to scale). **B**/**C**. Composite images (B) and single frames (C) from four-color excitation multiplexed SWIR imaging at 30 fps. Injection amounts are as follows: **ICG** = 200 nmol; JuloChrom5 (**2.27**) = 50 nmol; Chrom7 (**2.22**) = 45 nmol; JuloFlav7 (**2.3**) = 45 nmol. Ex. 785 nm (45 mW cm^{-2}), 892 nm (75 mW cm^{-2}), 968 nm (103 mW cm^{-2}), 1065 nm (156 mW cm^{-2}); collect LP1100 nm, 7.8 ms, 30 fps, single frames are displayed. (**D**/**E**.) Heart rate (D) and breath rate (E) calculated from ROIs specified in (C). Scale bar = 1 cm.

2.4 Conclusions

Non-invasive, multicolor imaging in mammals with high resolution is still a considerable challenge. To overcome this, we developed tunable SWIR polymethine fluorophores, along with a triggered multi-excitation SWIR optical configuration to demonstrate multicolor whole-animal imaging. These studies revealed that structural modifications could alter absorption/emission using physical organic chemistry principles and produced MeOFlav7 (**2.10**), and JuloFlav7 (**2.3**), which

were well matched to laser lines at 980 nm and 1064 nm, respectively. These dyes, along with FDA-approved **ICG**, enabled single-channel imaging at 100 fps and two- or three-color imaging at video-rate speeds (> 27 fps).

To improve further, we then designed and synthesized chromenylium polymethine dyes, which were brighter than their predecessors. The panel of bright dyes enabled single-channel imaging at up to 300 fps, while dyes excitable at orthogonal excitation wavelengths could be used together providing three-channel imaging at up to 100 fps. These experiments represented the fastest single and multichannel SWIR imaging to date.

Combining these dyes with **ICG** and JuloFlav7 (**2.3**), video-rate imaging in mice in four colors was demonstrated for the first time. The contribution puts forth a greater understanding of how to increase the performance and utility of long wavelength probes to visualize complex organisms. These efforts could be improved by improving the brightness of dyes for specific laser lines or perhaps accessing orthogonal laser lines further within the SWIR region. Additional laser lines would also allow for more biologically relevant targets to be visualized together.

2.5 Experimental Procedures

2.5.1 Abbreviations, Materials, and Instrumentation

Abbreviations. DCM = dichloromethane; DMSO = dimethylsulfoxide; ET = exposure time; EtOH = ethanol; EtOAc = ethyl acetate; fps = frames per second; *i.v.* = intravenous; *i.p.* intraperitoneal; LP = longpass; NIR = near-infrared; NMR = nuclear magnetic resonance; PBS = phosphate buffered saline; PEG = polyethylene glycol; ROI = region of interest; SP = shortpass; SWIR = shortwave infrared; THF = tetrahydrofuran; VIS = visible.

Materials. Reagents were purchased from Acros Organics, Alfa Aesar, Fisher Scientific, Sigma-Aldrich, or TCI and used without additional purification. Anhydrous and deoxygenated solvents (toluene, THF, DMF) were dispensed from a Grubb's-type Phoenix Solvent Drying System constructed by the late JC Meyer. Oxygen was removed from solvents by three consecutive freeze–pump–thaw cycles in air-free glassware directly before use. For every reaction, dry Schlenk technique was used.

Instrumentation. Thin layer chromatography was performed using Silica Gel 60 F254 (EMD Millipore) plates. Flash chromatography was executed with technical grade silica gel with 60 Å pores and 40–63 μm mesh particle size (Sorbtech Technologies). Solvent was removed under reduced pressure with a Büchi Rotavapor with a Welch self-cleaning dry vacuum pump and further dried with a Welch DuoSeal pump. Aqueous solvent was removed by lyophilization with a LABCONCO FreeZone Benchtop Freeze Dryer. Bath sonication was performed using a Branson 3800 ultrasonic cleaner or an Elma S15Elmasonic. Nuclear magnetic resonance (^{1}H NMR, ^{13}C NMR) spectra were taken on Bruker Avance 300, AV-500 or AV-600 instruments and processed with MestReNova software. All ^{1}H NMR and ^{13}C NMR peaks are reported in ppm in reference to their respective solvent signals. High resolution mass spectra (electrospray ionization (ESI)) were obtained on a Thermo Scientific Q ExactiveTM Plus Hybrid Quadrupole-OrbitrapTM M with Dionex UltiMate 3000 RSLCnano System. IR spectra were obtained on a Perkin-Elmer UATR Two FT-IR spectrometer and are reported in terms of frequency of absorption (cm^{-1}). Nanomaterial size was analyzed with a Malvern Zetaziser Nano dynamic light scattering in plastic 1 cm cuvettes. Zeta potentials were measured with a Malvern Zetasizer Nano dynamic light scattering with a DTS1070 capillary cell for samples. Absorbance spectra were collected on a JASCO V-770 UV-Visible/NIR spectrophotometer with a 2000 nm/min scan rate after blanking with the appropriate

solvent or on a PerkinElmer LAMBDA 1050+ UV/VIS/NIR Spectrophotometer with a reference sample. Photoluminescence spectra were obtained on a Horiba Instruments PTI QuantaMaster Series fluorometer with InGaAs detector Horiba Edison DSS IGA 020L. Absolute quantum yields were taken in a Horiba KSPHERE-Petite. Quartz cuvettes (1 cm) were used for absorbance and photoluminescence measurements. Absorption coefficients in DCM were calculated with serial dilutions with Hamilton syringes in volumetric glassware. Error was taken as the standard deviation of the triplicate experiments. Relative quantum yields were determined in DCM relative to **IR-26** in DCM.

2.5.2 Animal Imaging Protocols

Animal experiments were conducted in conformity with the institutional guidelines. Non-invasive whole mouse imaging was performed on athymic nude female mice (6-15 weeks old, weight between 20-25 g), purchased from Envigo or Charles River Laboratories. Mice were anesthetized with inhaled isoflurane/oxygen. Tail vein injections were performed with a catheter assembled from a 30-gauge needle connected through plastic tubing to a syringe prefilled with isotonic saline solution. The bevel of the needle was then inserted into the tail vein and secured using tissue adhesive. The plastic tubing was then connected to a syringe (30-gauge needle) prefilled with the probe of interest. All probes were filtered through a 0.22 μm syringe filter prior to i.v. injection.

2.5.3 SWIR Imaging Apparatus

For whole mouse imaging, a custom-built setup was used. Lumics laser units: LU1064DLD350- S70AN03 (35 W) “1065 nm”; LU0980D350-D30AN (35W) “968 nm”, and LU0890D400-U10AF (40W) “892 nm”, LU0785DLU250-S70AN03 (25 W) "785 nm” were used for excitation. Laser modules are specced to ± 10 nm. Laser outputs were coupled in a 4x1 fan-out

fiber-optic bundle (Thorlabs BF46LS01) of 600 μm core diameter for each optical path. The output from the fiber was fixed in an excitation cube (Thorlabs KCB1EC/M), reflected off of a mirror (Thorlabs BBE1- E03), and passed through a positive achromat (Thorlabs AC254-050-B), SP filter (specified for each experiment) and an engineered diffuser (Thorlabs ED1-S20-MD or ED1-S50-MD) to provide uniform illumination over the working area. In a typical experiment, the excitation flux at the object was adjusted to be close to 100 mWcm-2 (power density used is defined separately in each experiment, with an error of ± 3%). The working area was covered by a heating mat coated with blackout fabric (Thorlabs BK5). Emitted light was directed onto an Allied Vision Goldeye G-032 Cool TEC2 camera with a sensor temperature set point of -30 °C or a Goldeye G-033 TECless camera. Emitted light was directed through a custom filter set (defined for each experiment) and a C-mount camera lens (Navitar, SWIR-35). The assembly was partially enclosed to avoid excess light while enabling manipulation of the field of view during operation. Camera and lasers were externally controlled and synchronized by delivering trigger pulses of 5V TTL (5V TransistorTransistor Logic) to the laser drivers and camera using a programmable trigger controller with pulses generated with an Atmel Atmega328 micro-controller unit and programmed using Arduino Nano Rev 3 MCU (A000005) in the Arduino integrated development environment (IDE). Acquired imaging data is then transferred to the PC via either a Gigabit Ethernet (GigE), or CameraLink (CL) interface. For image acquisition with the G-032 camera, the toolbox of MATLAB programming environment was used in combination with a MATLAB script (software used can be found at https://gitlab.com/brunslab/ccda) to preview and collect the required image data in 14-bit depth. For image acquisition with the G-033 camera, FireBird Camera Link Frame Grabber (1xCLD-2PE8 or 1xCLD-2PE4, Active Silicon) along with ActiveCapture (Active Silicon) was used to collect image data in 8-bit or 12-bit depth.

Images were processed using the Fiji distribution of ImageJ and Python. All images were background corrected to correct for non-linearities in the detector and/or excitation. Raw images underwent no further processing. Multiplexed images that underwent unmixing were subjected to either manual or an automated linear unmixing method, specified in the experimental procedures for each figure. All still images are displayed as single frames and converted to 8-bit PNG files for display, unless stated otherwise. Videos were frame averaged to reduce file size, if necessary, before compression with FFmpeg to a .mov file.

2.5.4 Synthetic Procedures

General Synthetic Procedures. Flavones **2.13a–c** were synthesized by subjecting the corresponding 3-aminophenol (150–750 mg scale, 1.0 equiv.) to ethyl benzoylacetate (1.75–2.0 equiv.) and heating at 180 °C for 15–48 h. Compounds were purified by column chromatography with a hexanes/EtOAc solvent gradient (51–55% yield). Flavone **2.17** was synthesized following a known procedure from 7-hydroxyflavone **2.16**. Flavones **2.13d–h** were synthesized by subjecting flavone **2.17** (50–180 mg scale, 1.0 equiv.) to the corresponding secondary amine (1.5–2.8 equiv.), RuPhos Pd G3 (0.1 equiv.), RuPhos (0.1 equiv.) and cesium carbonate (1.5 equiv.), in either toluene (at 100–110 °C; 0.1–0.3 M) or THF (at 50 °C; 0.1–0.3 M) for 5.5–22 h. Compounds were purified by column chromatography with a hexanes/EtOAc solvent gradient (63–83% yield). Flavone **2.13i** was synthesized by subjecting 7-aminoflavone (**2.18**) (180 mg scale, 1.0 equiv.) to di-*tert*-butyl dicarbonate (3.2 equiv.), triethylamine (2.5 equiv.) and dimethylamino pyridine (0.3 equiv.) in THF (0.2 M), and heating to reflux for 48 h. The compound was purified by column chromatography with a hexanes/EtOAc solvent gradient (66% yield).

Flavyliums **2.12a–i** were synthesized by subjecting the corresponding flavone (**2.13a–i**) (20–770 mg scale, 1.0 equiv.) to methyl magnesium bromide (1.5–3.2 equiv.) in THF (0.05–0.1

M) at 0 °C, warming to room temperature and stirring for 12–24 h. The reaction was quenched with aqueous fluoroboric acid, extracted with DCM and aqueous fluoroboric acid, dried and filtered. The compounds were purified by trituration with EtOAc or with diethyl ether and toluene (39–86% yield, **2.12i** not isolated for yield). Flavylium **2.12j** was synthesized following a literature procedure.

Heptamethine dyes **2.1**–**2.11** were synthesized by subjecting the corresponding flavylium (**2.12a**–**j**) (10–150 mg scale, 1.0 equiv.) to *N*-((3-(anilinomethylene)-2-chloro-1-cyclohexen-1-yl)methylene)aniline hydrochloride (**2.19**) (0.40–0.49 equiv.) with either sodium acetate or 2,6-di*tert*-butyl-4-methylpyridine (1.5–5.6 equiv.) in either *n*-butanol/toluene, 1,4-dioxane, ethanol or *n*-pentanol (0.05–0.1 M) at 70–140 °C for 10–120 min. Compounds were purified by a mixture of column chromatography (with a gradient of either DCM/EtOH, DCM/acetone, DCM/MeCN or DCM/toluene/EtOH), trituration (in toluene and THF) and Soxhlet extraction (compound **2.10**, in toluene). Compounds were isolated in 5–51% yield.

These procedures were applied to achieve chromenylium heterocycles **2.12k–m** which were coupled with linkers **2.19** or **2.28** under basic conditions to achieve chromenylium dyes, **2.22**–**2.27** (Scheme 2.2).

Experimental Procedures.

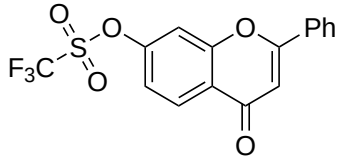

7-(trifluoromethanesulfonate)-2-phenyl-*4H*-chromen-4-one (2.17): In a 150 mL flask, 7-hydroxyflavone (**2.16**) (902 mg, 3.79 mmol, 1.0 equiv.) and pyridine (15.0 mL, 186 mmol, 49

equiv.) were combined and placed in an ice bath. Trifluormethanesulfonic anhydride (1.30 mL, 7.73 mmol, 2.0 equiv.) was added dropwise. After 2 h, the reaction was quenched with sodium bicarbonate, extracted into EtOAc, washed with brine, and evaporated. The crude product was purified via column chromatography in an 8:1 hexanes/EtOAc mixture to yield a white solid (934 mg, 2.52 mmol, 67%. ^{1}H NMR (400 MHz, Chloroform-*d*) δ 8.34 (d, *J* = 8.8 Hz, 1H), 7.96 – 7.86 (m, 2H), 7.63 – 7.50 (m, 4H), 7.34 (dd, *J* = 8.8, 2.3 Hz, 1H), 6.85 (s, 1H). ^{1}H NMR agrees with previous literature.[48]

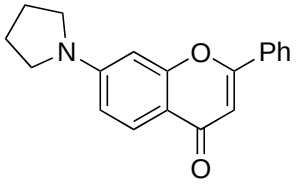

7-(pyrrolidin-1-yl)-2-phenyl-*4H*-chromen-4-one (2.13e): Triflate **2.17** (103 mg, 0.278 mmol, 1.0 equiv.), pyrrolidine (0.042 mL, 0.50 mmol, 1.5 equiv.), RuPhos-Pd-G3 (24.2 mg, 0.0289 mmol, 0.1 equiv.) RuPhos (12.9 mg, 0.0276 mmol, 0.1 equiv.), and cesium carbonate (136 mg, 0.418 mmol, 1.5 equiv.) were dissolved in toluene (2.6 mL) in a 20 mL scintillation vial and heated to 100 °C for 24 h under an N_2 atmosphere. The solution was cooled to rt and evaporated onto silica gel. The crude product was purified via column chromatography, eluting with a 9:1, 7:1 and 5:1 hexanes/EtOAc solvent gradient. This procedure gave an amber solid (59.8 mg, 0.205 mmol, 74%). R_f = 0.5 in 1:1 hexanes/EtOAc. ^{1}H NMR (400 MHz, Chloroform-*d*) δ 8.05 (d, *J* = 8.9 Hz, 1H), 7.95 – 7.90 (m, 2H), 7.55 – 7.48 (m, 3H), 6.87 (s, 1H), 6.68 (dd, *J* = 9.0, 2.3 Hz, 1H), 6.49 (d, *J* = 2.3 Hz, 1H), 3.48 – 3.38 (m, 4H), 2.15 – 2.05 (m, 4H). ^{13}C NMR (126 MHz, Chloroform-*d*) δ 178.0, 162.6, 158.8, 152.1, 132.6, 131.4, 129.2, 127.0, 126.4, 113.4, 111.7, 107.3, 97.1, 48.1, 25.8. HRMS (ESI$^+$) calcd for $C_{19}H_{18}NO_2$ $[M+H]^+$: 292.1332; found: 292.1326. Absorbance (CH_2Cl_2): 233, 275, 307, 364 nm.

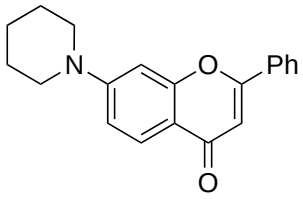

7-(piperidin-1-yl)-2-phenyl-*4H*-chromen-4-one (2.13f): Triflate **2.17** (183 mg, 0.495 mmol, 1.0 equiv.), piperidine (0.072 mL, 0.73 mmol, 1.5 equiv.), RuPhos (21.2 mg, 0.0455 mmol, 0.1 equiv.), RuPhos-Pd-G3 (42.5 mg, 0.0508 mmol, 0.1 equiv.) and cesium carbonate (243 mg, 0.747 mmol, 1.5 equiv.) were dissolved in toluene (4.5 mL) in a 20 mL scintillation vial and heated to 100 °C for 24 h under an N_2 atmosphere. The solution was cooled to rt and evaporated onto silica gel. The crude product was purified via column chromatography, eluting with a 9:1, 7:1 and 5:1 gradient of hexanes/EtOAc to yield an amber solid (106 mg, 348 mmol, 71%). R_f = 0.6 in 1:1 hexanes/EtOAc. ^{1}H NMR (400 MHz, Chloroform-*d*) δ 8.03 (d, *J* = 9.0 Hz, 1H), 7.89 (s, 2H), 7.50 (s, 3H), 7.04 – 6.88 (m, 1H), 6.80 (d, *J* = 2.4 Hz, 1H), 6.70 (s, 1H), 3.41 (s, 4H), 1.69 (s, 6H). ^{13}C NMR (126 MHz, Chloroform-*d*) δ 177.9, 162.6, 158.6, 155.1, 132.4, 131.2, 129.1, 126.7, 126.2, 115.1, 113.5, 107.5, 100.3, 49.1, 25.4, 24.4. HRMS (ESI$^+$) calcd for $C_{20}H_{20}NO_2$ $[M+H]^+$: 306.1489; found: 306.1486. Absorbance (CH_2Cl_2): 275, 308, 356 nm.

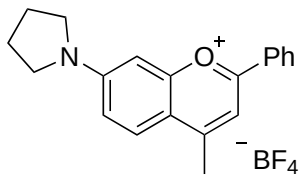

7-(pyrrolidin-1-yl)-4-methyl-2-phenylchromenylium tetrafluoroborate (2.12e): Flavone **2.13e** (62.0 mg, 0.213 mmol, 1.0 equiv.) was dissolved in THF (2.2 mL) in a 15 mL 2-neck round bottom flask and cooled to 0 °C. Methylmagnesium bromide was added dropwise (1.0 M in THF, 0.508 mL, 2.5 equiv.) and the solution was warmed to rt and stirred for 24 h. The reaction was quenched

by dropwise addition of fluoroboric acid (5%, aqueous, ~30 mL) on ice, extracted with dichloromethane after the addition of more 5% HBF_4, dried with Na_2SO_4, filtered, and evaporated. The crude product was triturated with ice cold EtOAc and vacuum filtered to produce a red solid (52.1 mg, 0.138 mmol, 65%). ^{1}H NMR (400 MHz, Acetonitrile-d_3) δ 8.25 – 8.18 (m, 2H), 8.06 (d, J = 9.5 Hz, 1H), 7.76 (d, J = 0.5 Hz, 1H), 7.75 – 7.71 (m, 1H), 7.70 – 7.64 (m, 2H), 7.26 (dd, J = 9.5, 2.3 Hz, 1H), 6.98 (d, J = 2.4 Hz, 1H), 3.69 (t, J = 6.2 Hz, 2H), 3.60 (t, J = 6.1 Hz, 2H), 2.83 (s, 3H), 2.12 – 2.08 (m, 4H). ^{13}C NMR (126 MHz, Acetonitrile-d_3) δ 165.7, 164.3, 159.8, 156.4, 135.0, 130.8, 130.7, 129.7, 128.5, 120.2 119.2, 112.6, 97.2, 50.4, 50.1, 26.0, 25.7, 20.1. HRMS (ESI^+) calcd for $C_{20}H_{20}NO^+$ $[M]^+$: 290.1539; found: 290.1542. Absorbance (CH_2Cl_2): 238, 296, 339, 516 nm. Emission (CH_2Cl_2, ex. 500 nm): 595 nm.

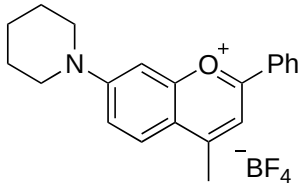

7-(piperidin-1-yl)-4-methyl-2-phenylchromenylium (2.12f): Flavone **2.13f** (90.4 mg, 0.296 mmol, 1.0 equiv.) was dissolved in THF (2.3 mL) in a 15 mL double-neck round bottom flask and cooled to 0 °C. Methylmagnesium bromide was added dropwise on ice (1.0 M in THF, 0.702 mL, 2.5 equiv.). The solution was warmed to rt and left stir under a N_2 atmosphere for 24 h. The reaction was quenched by dropwise addition of fluoroboric acid (5%, aqueous, ~30 mL) on ice, extracted with dichloromethane the addition of more 5% HBF_4, dried with Na_2SO_4, filtered, and evaporated. The crude product was triturated with ice cold EtOAc and vacuum filtered to yield a dark red solid (99.8 mg, 0.255 mmol, 86%). ^{1}H NMR (600 MHz, Acetonitrile-d_3) δ 8.19 – 8.12 (m, 2H), 7.99 (d, J= 9.7 Hz, 1H), 7.73 – 7.66 (m, 2H), 7.66 – 7.59 (m, 2H), 7.44 (dd, J= 9.7, 2.6 Hz, 1H), 7.17 (d, J= 2.6 Hz, 1H), 3.82 – 3.67 (m, 4H), 2.77 (s, 3H), 1.80 – 1.75 (m, 2H), 1.77 – 1.71 (m, 4H). ^{13}C

NMR (126 MHz, Acetonitrile-d_3) δ 164.9, 163.2, 159.4, 157.0, 134.1, 129.8, 129.6, 128.9, 127.5, 118.4, 118.0, 111.9, 96.4, 48.9, 25.8, 23.8, 19.1. HRMS (ESI^+) calcd for $C_{21}H_{22}NO^+$ $[M]^+$: 304.1696; found: 304.1696. Absorbance (CH_2Cl_2): 243, 297, 338, 520 nm. Emission (CH_2Cl_2, ex. 500 nm): 608 nm.

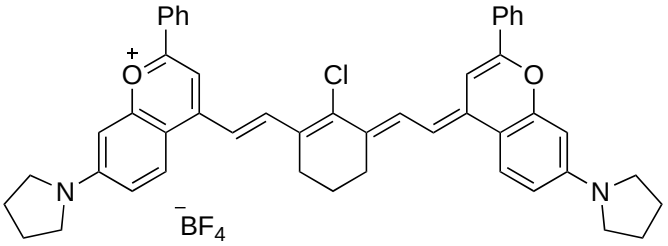

4-((*E*)-2-((*E*)-2-chloro-3-(2-((*E*)-2-phenyl-7-(pyrrolidin-1-yl)-4*H*-chromen-4-ylidene)ethylidene)cyclohex-1-en-1-yl)vinyl)-2-phenyl-7-(pyrrolidin-1-yl)chromenylium tetrafluoroborate (2.5): Flavylium **2.12e** (75.3 mg, 0.199 mmol, 1.0 equiv.) *N*-[(3-(anilinomethylene)-2-chloro-1-cyclohexen-1-yl)methylene]aniline hydrochloride (**2.19**) (29.6 mg, 0.0825 mmol, 0.45 equiv.) and 2,6-di-*tert*-butyl-4-methyl pyridine (137 mg, 0.667 mmol, 3.0 equiv.) were dissolved in *n*-pentanol (1.9 mL) in a 25 mL Schlenk flask, freeze–pump–thawed x3, and heated to 140 °C for 1.5 h. The solution was cooled to rt and evaporated onto silica gel. The crude product was purified via silica gel chromatography, eluting with a 7:3 DCM/toluene solvent mixture plus 0.2 to 10% EtOH, followed by a trituration with ice cold THF. The procedure gave a dark purple solid. (10.3 mg, 0.0128 mmol, 8%). R_f = 0.5 in 9:1 DCM/EtOH. ^{1}H NMR (500 MHz, Methylene Chloride-d_2) δ 8.35 (d, J = 13.8 Hz, 2H), 8.09 – 8.00 (m, 4H), 7.94 (d, J = 9.3 Hz, 2H), 7.64 – 7.55 (m, 6H), 7.48 (s, 2H), 6.99 (d, J = 13.9 Hz, 2H), 6.83 (dd, J = 9.2, 2.5 Hz, 2H), 6.59 (d, J = 2.3 Hz, 2H), 3.56 – 3.46 (m, 8H), 2.84 (t, J = 6.2 Hz, 4H), 2.15 – 2.09 (m, 8H), 2.01 (p, J = 5.6 Hz, 2H). HRMS (ESI^+) calcd for $C_{48}H_{44}ClN_2O_2^+$ $[M]^+$: 715.3086; found: 715.3070. Absorbance (CH_2Cl_2): 525 nm, 924 nm, 1034 nm. Emission (CH_2Cl_2, ex. 885 nm): 1061 nm

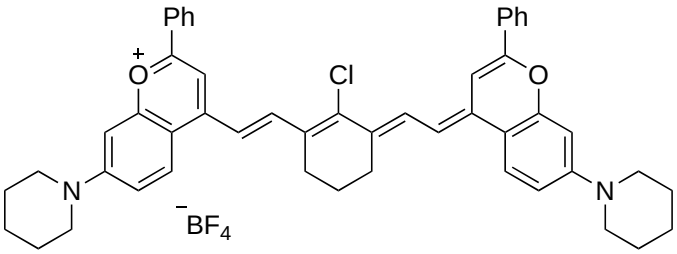

4-((*E*)-2-((*E*)-2-chloro-3-(2-((*E*)-2-phenyl-7-(piperidin-1-yl)-4*H*-chromen-4-ylidene)ethylidene)cyclohex-1-en-1- yl)vinyl)-2-phenyl-7-(piperidin-1-yl)chromenylium tetrafluoroborate (2.6) Flavylium **2.12f** (30.3 mg, 0.0775 mmol, 1.0 equiv.), *N*-[(3-(anilinomethylene)-2-chloro-1-cyclohexen-1-yl)methylene]aniline hydrochloride (**2.19**) (47.5 mg, 0.132 mmol, 0.45 equiv.), and 2,6-di-*tert*-butyl-4-methyl pyridine (15.2 mg, 0.740 mmol, 3.0 equiv.) were dissolved in a mixture of *n*-butanol (0.46 mL) and toluene (0.20 mL) in a 25 mL Schlenk flask, freeze–pump–thawed x3, and heated to 100 °C for 2 h. The solution was cooled to rt and evaporated onto silica gel. The crude product was purified via silica gel chromatography, eluting with a 7:3 DCM/Toluene solvent mixture plus 0.2–10% EtOH, followed by a trituration with ice cold THF. The procedure gave a dark purple solid (17.1 mg, 0.0205 mmol, 26%). R_f = 0.5 in 9:1 DCM/EtOH. ^{1}H NMR (500 MHz, Methylene Chloride-d_2) δ 8.25 (d, *J*= 13.8 Hz, 2H), 7.97 – 7.95 (m, 4H), 7.87 (d, *J*= 9.3 Hz, 2H), 7.61 – 7.53 (m, 6H), 7.38 (s, 2H), 7.04 (dd, *J*= 9.4, 2.6 Hz, 2H), 6.91 (d, *J*= 13.8 Hz, 2H), 6.76 (d, *J*= 2.5 Hz, 2H), 3.50 (m, 8H), 2.82 – 2.78 (m, 4H), 2.00 (p, *J*= 6.2 Hz, 2H), 1.73 (m, 12H). HRMS (ESI$^+$) Calculated for $C_{50}H_{48}ClN_2O_2^+$ $[M]^+$: 743.3399; found: 743.3386. Absorbance (CH_2Cl_2): 523 nm, 922 nm, 1034 nm. Emission (CH_2Cl_2, ex. 885 nm): 1060 nm.

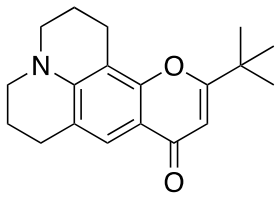

11-(*tert*-butyl)-2,3,6,7-tetrahydro-1*H*,5*H*,9*H*-pyrano[2,3-*f*]pyrido[3,2,1-*ij*]quinolin-9-one (**2.13m**): 8- hydroxyjulolidine (315 mg, 1.66 mmol, 1.00 equiv) and ethyl pivaloylacetate (500 µL, 2.81 mmol, 1.69 equiv.) were added to a 20 mL vial, and heated at 180 ºC for 48 h. The solution was cooled to room temperature, evaporated onto silica, and purified via column chromatography with an 8:1 to 3:1 hexanes/EtOAc gradient to yield an off-white solid (295 mg, 0.992 mmol, 60%). R_f = 0.4 in 1:2 hexanes/EtOAc. ^{1}H NMR (600 MHz, Chloroform-*d*) δ 7.53 (s, 1H), 6.05 (s, 1H), 5.25 (s, 1H), 3.27 – 3.15 (m, 4H), 2.83 (t, *J* = 6.5 Hz, 2H), 2.74 (t, *J* = 6.2 Hz, 2H), 1.96 (p, *J* = 6.3 Hz, 2H), 1.90 (p, *J* = 6.2 Hz, 2H), 1.27 (s, 9H). ^{13}C NMR (126 MHz, Chloroform-*d*) δ 178.4, 173.9, 153.9, 146.9, 122.1, 119.9, 112.2, 105.58, 105.55, 49.9, 49.4, 36.4, 28.1, 27.6, 21.5, 20.7, 20.5. HRMS (ESI$^+$) calcd for $C_{19}H_{24}NO_2^+$ [M+H]$^+$: 298.1802; found: 298.1793. Absorbance (CH_2Cl_2): 272, 300, 355 nm.

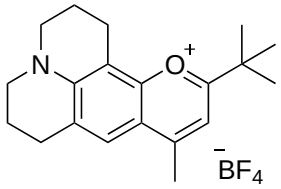

11-(*tert*-butyl)-9-methyl-2,3,6,7-tetrahydro-1*H*,5*H*-pyrano[2,3-*f*]pyrido[3,2,1-*ij*]quinolin-12-ium tetrafluoroborate (**2.12m**): Chromone **2.13m** (256 mg, 0.861 mmol, 1.00 equiv.) was added to a flame dried 50 mL 2-neck flask in a N_2 atmosphere and dissolved in THF (8.8 mL). Methylmagnesium bromide (1.0 M in THF, 2.6 mL, 3.0 equiv.) was added dropwise and the solution was stirred at room temperature for 12 h. The reaction was quenched with fluoroboric acid (50% aqueous, 200 µL). The product was extracted into DCM with the addition of 5% fluoroboric acid, dried with Na_2SO_4, filtered, and evaporated. The product was purified by precipitation upon addition of cold EtOAc, filtration and rinsing with cold EtOAc to obtain a magenta solid (268 mg, 0.669 mmol, 81%). ^{1}H NMR (500 MHz, Acetonitrile-d_3) δ 7.65 (s, 1H),

7.02 (s, 1H), 3.53 (q, J = 5.4 Hz, 4H), 2.95 (t, J = 6.4 Hz, 2H), 2.93 – 2.87 (m, 2H), 2.67 (s, 3H), 2.05 – 1.96 (m, 4H), 1.44 (s, 9H). ^{13}C NMR (126 MHz, Acetonitrile-d_3) δ 178.3, 161.6, 155.2, 153.7, 129.7, 124.7, {peak at 118.6–118.1 beneath CD_3CN solvent peak}, 111.1, 105.6, 51.8, 51.3, 38.5, 28.4, 28.4, 21.0, 20.2, 19.9, 19.7. HRMS (ESI$^+$) calcd for $C_{20}H_{26}NO^+$ [M]$^+$: 296.2009; found: 296.2002. Absorbance (CH_2Cl_2): 300, 351, 488 nm. Emission (CH_2Cl_2, ex. 450 nm): 557 nm.

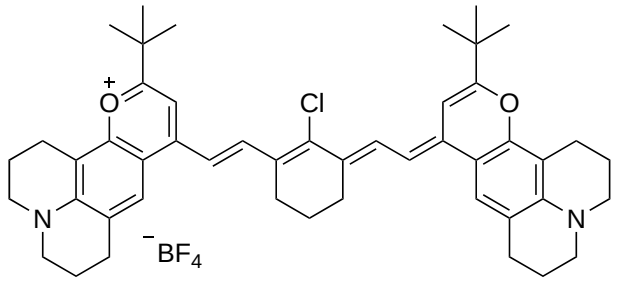

11-(Tert-butyl)-9-((E)-2-((E)-3-((E)-2-(11-(tert-butyl)-2,3,6,7-tetrahydro-1H,5H,9H-pyrano[2,3-f]pyrido[3,2,1-ij]quinolin-9-ylidene)ethylidene)-2-chlorocyclohex-1-en-1-yl)vinyl)-2,3,6,7-tetrahydro-1H,5H-pyrano[2,3-f]pyrido[3,2,1-ij]quinolin-12-ium tetrafluoroborate (**2.26**, JuloChrom7). Chromenylium **2.12m** (52 mg, 0.13 mmol, 1.0 equiv.), *N*-[(3-(anilinomethylene)- 2-chloro-1-cyclohexen-1-yl)methylene]aniline hydrochloride **2.19** (22 mg, 0.062 mmol, 0.48 equiv.), and 2,6-di-*tert*-butyl-4-methyl pyridine (80 mg, 0.4 mmol, 3 equiv.) were dissolved in a mixture of *n*-butanol (820 µL) and toluene (350 µL) in a 25 mL Schlenk flask and heated to 105 °C for 7 hours. The solution was cooled to rt and evaporated onto silica gel. The crude product was purified via silica gel chromatography, eluting with a DCM/toluene/EtOH solvent gradient of 7:3 + 0.2% EtOH, increasing up to 10% EtOH gradually, followed by a trituration with ice cold THF. The procedure gave a dark purple solid (30. mg, 0.036 mmol, 28 %). ^{1}H NMR (500 MHz, Methylene Chloride-d_2) δ 8.15 (d, J = 13.8 Hz, 2H), 7.48 (s, 2H), 6.79 (s, 4H), 3.39 (s, 8H), 2.89 (s, 8H), 2.77 (s, 4H), 2.02 (d, J = 7.2 Hz, 8H), 1.41 (s, 18H), 0.08 (s, 2H). HRMS (ESI$^+$) calcd for $C_{48}H_{56}ClN_2O_2^{++}$ [M]$^+$: 727.4025; found: 727.4003. IR (film): 2925, 2854, 1628,

1234, 1144, 1048, 960, 929, 895 cm^{-1}. Absorbance (CH_2Cl_2): 524, 563, 608, 1008 nm. Emission (CH_2Cl_2): 1033 nm..

2.6 Spectra relevant to Chapter Two

2.6.1 ^{1}H NMR Spectra

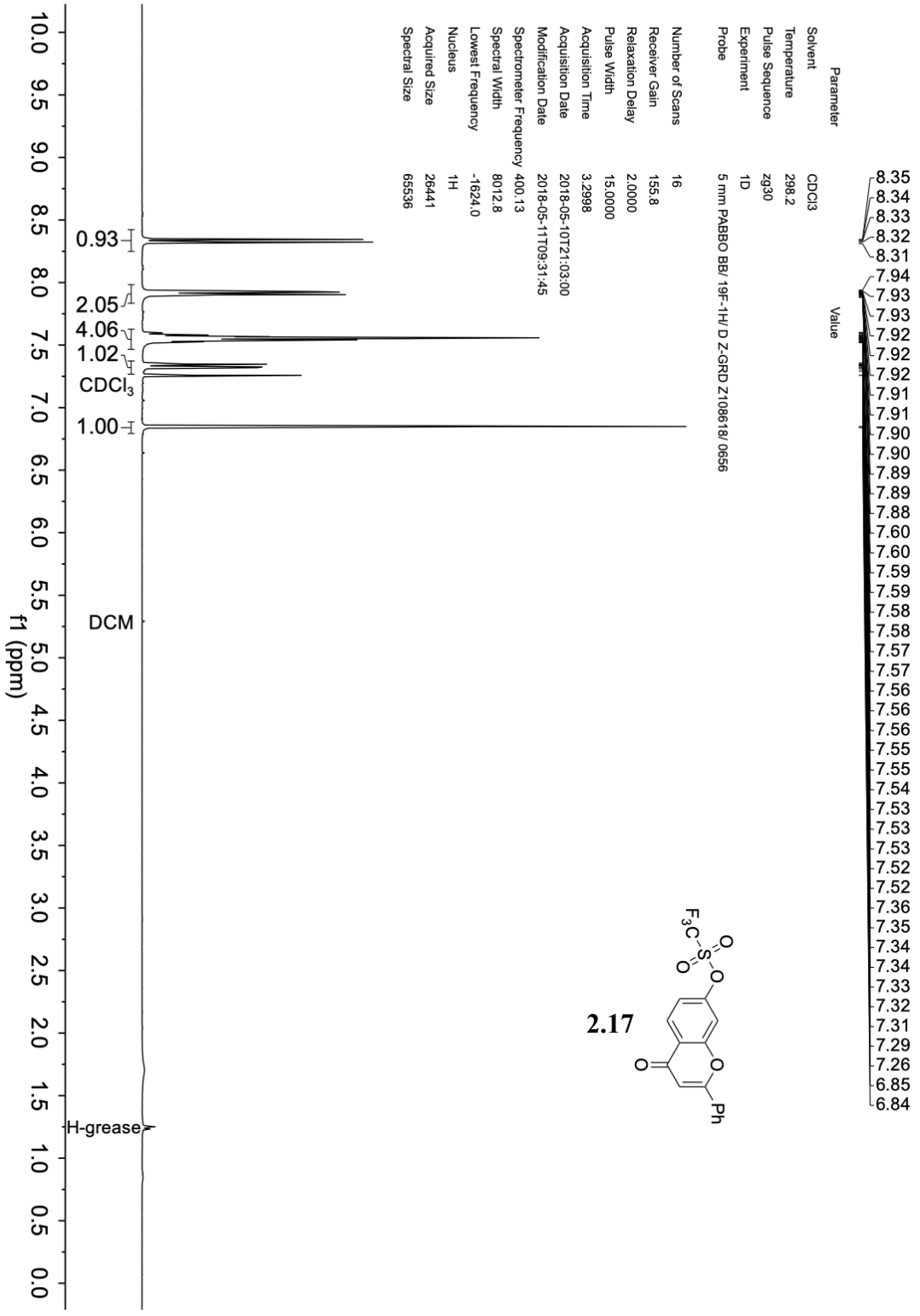

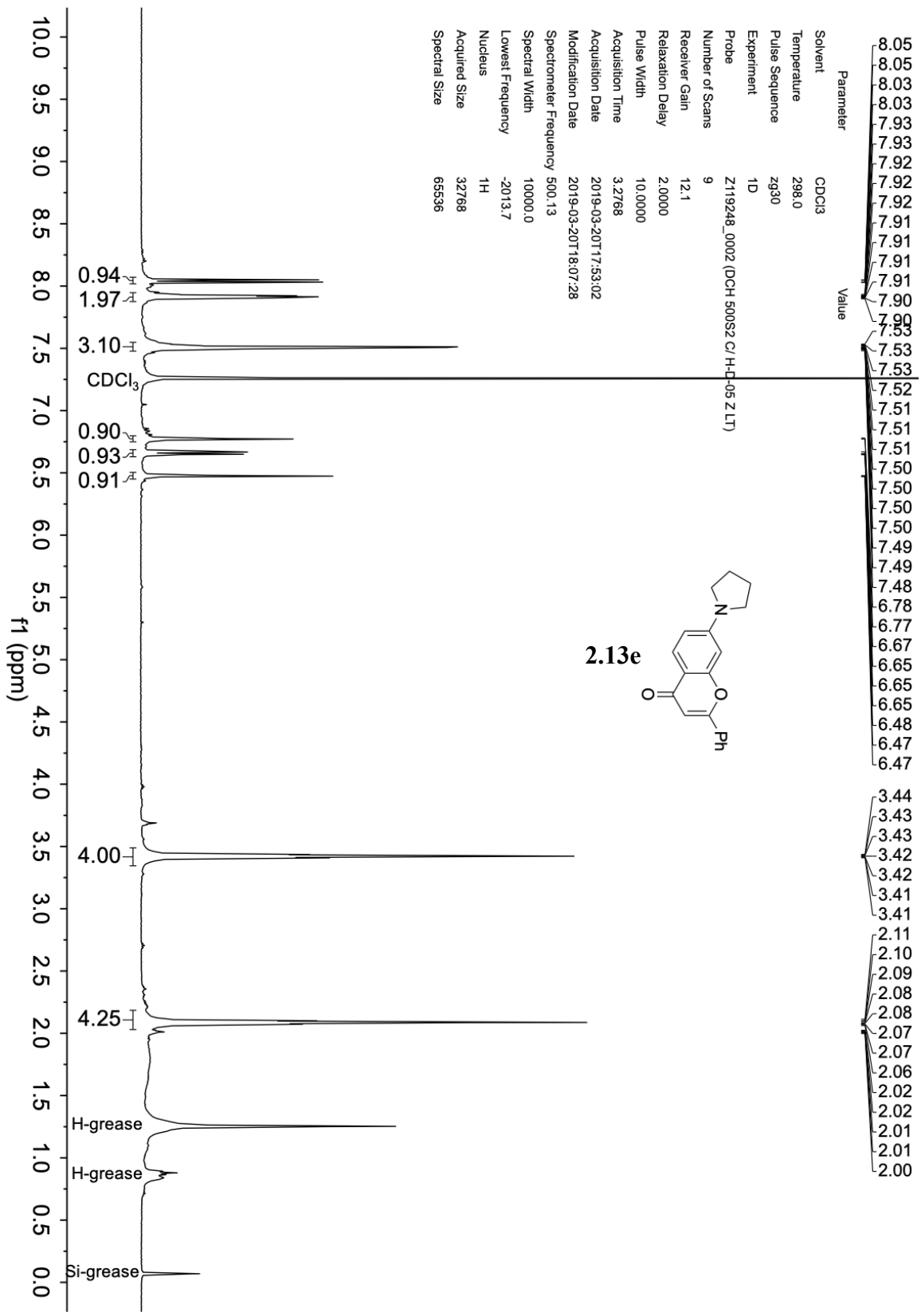
Parameter
Value
Solvent
CDCl3
Temperature
298.0
Pulse Sequence
zg30
Experiment
1D
Probe
Z119248_0002 (DCH 500S2 C/ H-D-05 Z LT)
Number of Scans
9
Receiver Gain
12.1
Relaxation Delay
2.0000
Pulse Width
10.0000
Acquisition Time
3.2768
Acquisition Date
2019-03-20T17:53:02
Modification Date
2019-03-20T18:07:28
Spectrometer Frequency
500.13
Spectral Width
10000.0
Lowest Frequency
-2013.7
Nucleus
1H
Acquired Size
32768
Spectral Size
65536
2.13e
N
O
O
Ph
0.94
1.97
3.10
CDCl3
0.90
0.93
0.91
4.00
4.25
H-grease
H-grease
Si-grease
f1 (ppm)

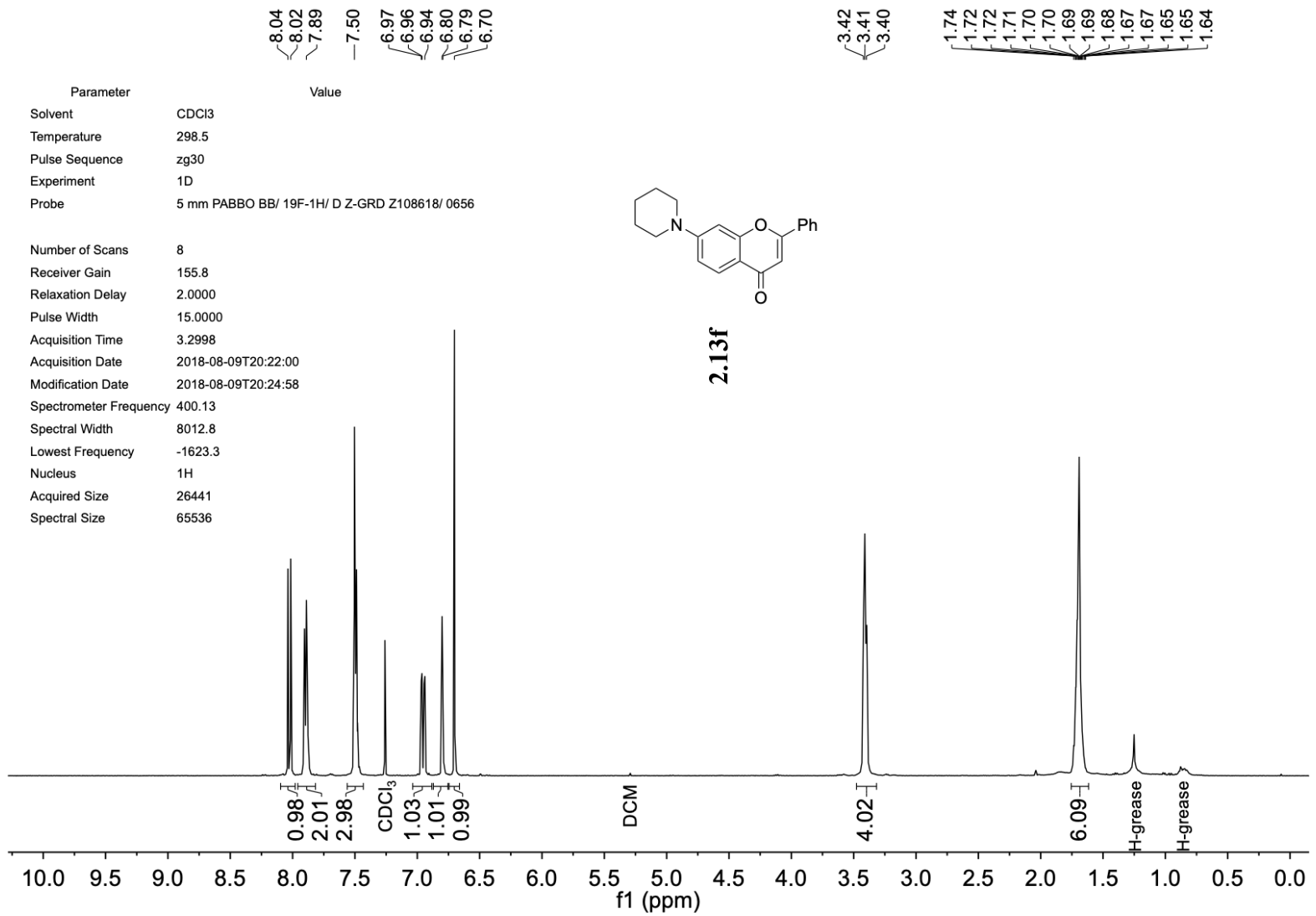
8.04
8.02
7.89
7.50
6.97
6.96
6.94
6.80
6.79
6.70
3.42
3.41
3.40
1.74
1.72
1.72
1.71
1.70
1.70
1.69
1.69
1.68
1.67
1.67
1.65
1.65
1.64
Parameter Value
Solvent CDCl3
Temperature 298.5
Pulse Sequence zg30
Experiment 1D
Probe 5 mm PABBO BB/ 19F-1H/ D Z-GRD Z108618/ 0656
Number of Scans 8
Receiver Gain 155.8
Relaxation Delay 2.0000
Pulse Width 15.0000
Acquisition Time 3.2998
Acquisition Date 2018-08-09T20:22:00
Modification Date 2018-08-09T20:24:58
Spectrometer Frequency 400.13
Spectral Width 8012.8
Lowest Frequency -1623.3
Nucleus 1H
Acquired Size 26441
Spectral Size 65536
N
O
Ph
O
2.13f
0.98
2.01
2.98
CDCl3
1.03
1.01
0.99
DCM
4.02
6.09
H-grease
H-grease
10.0 9.5 9.0 8.5 8.0 7.5 7.0 6.5 6.0 5.5 5.0 4.5 4.0 3.5 3.0 2.5 2.0 1.5 1.0 0.5 0.0
f1 (ppm)

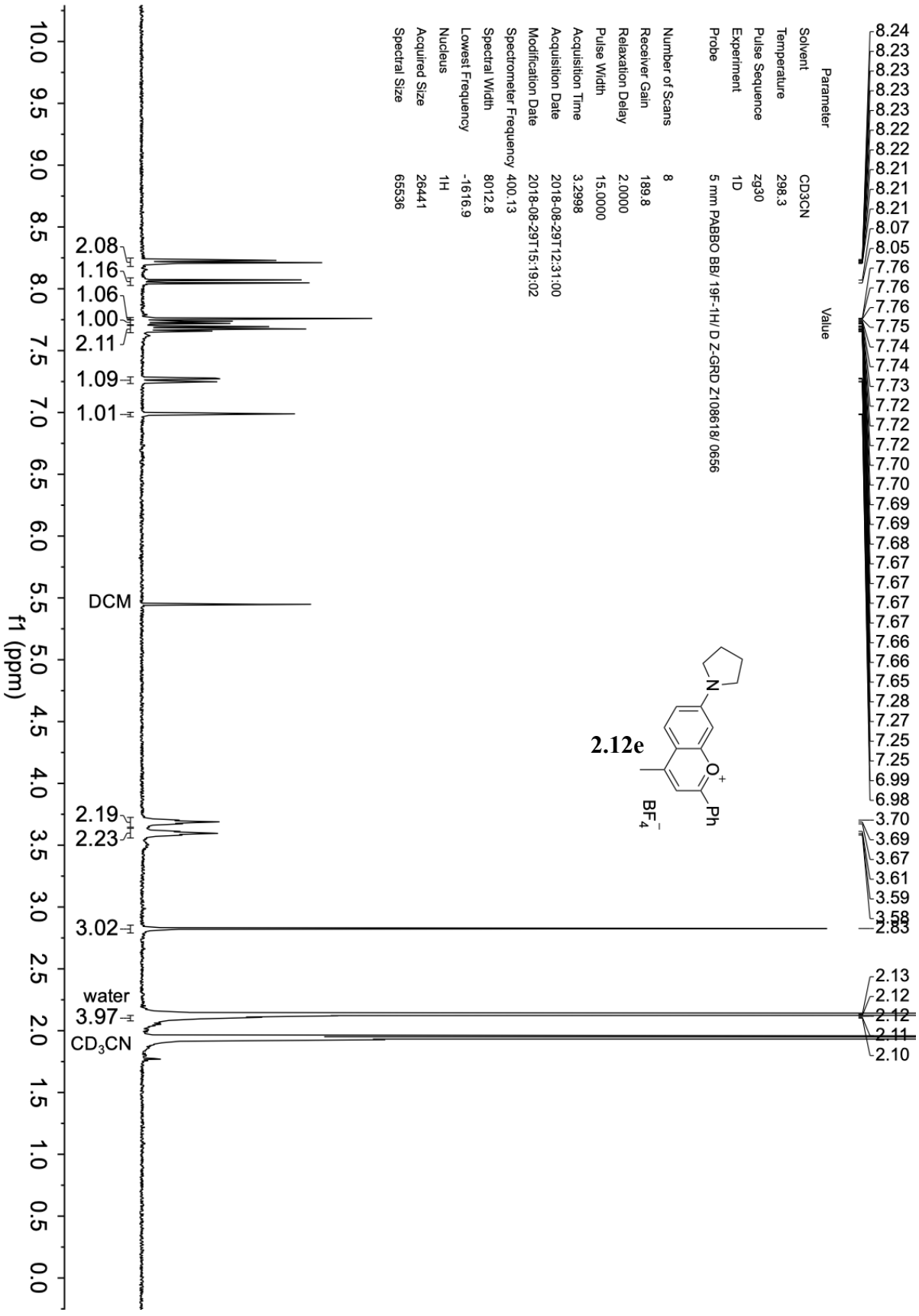
Parameter Value
Solvent CD3CN
Temperature 298.3
Pulse Sequence zg30
Experiment 1D
Probe 5 mm PABBO BB/ 19F-1H/ D Z-GRD Z108618/ 0656
Number of Scans 8
Receiver Gain 189.8
Relaxation Delay 2.0000
Pulse Width 15.0000
Acquisition Time 3.2998
Acquisition Date 2018-08-29T12:31:00
Modification Date 2018-08-29T15:19:02
Spectrometer Frequency 400.13
Spectral Width 8012.8
Lowest Frequency -1616.9
Nucleus 1H
Acquired Size 26441
Spectral Size 65536
2.12e
2.08
1.16
1.06
1.00
2.11
1.09
1.01
DCM
2.19
2.23
3.02
water
3.97
CD3CN
f1 (ppm)

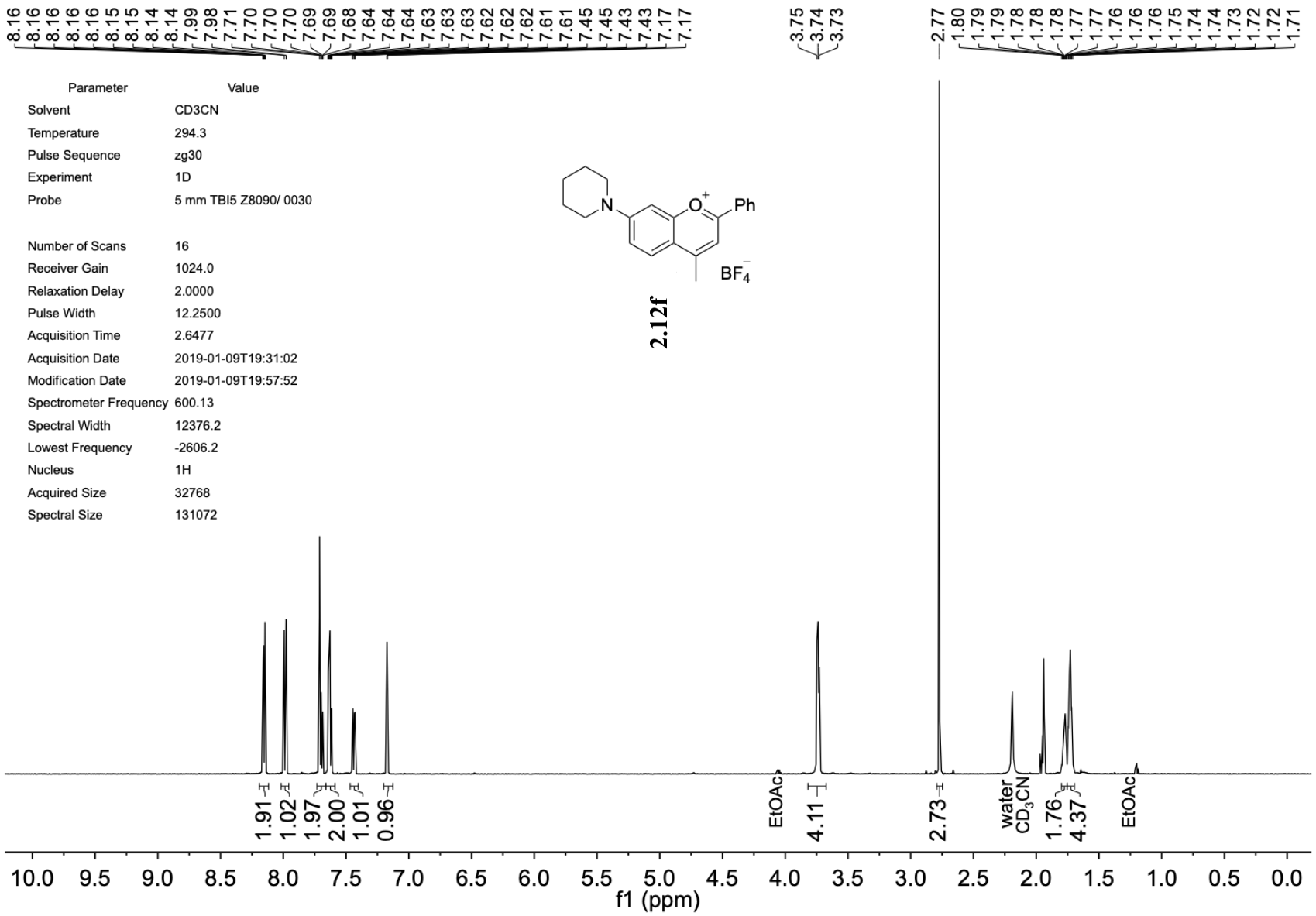
8.16 8.16 8.16 8.16 8.15 8.15 8.14 8.14 7.99 7.98 7.71 7.70 7.70 7.70 7.69 7.69 7.68 7.64 7.64 7.64 7.63 7.63 7.63 7.62 7.62 7.62 7.61 7.61 7.45 7.45 7.43 7.43 7.17 7.17
3.75 3.74 3.73
2.77
1.80 1.79 1.79 1.78 1.78 1.78 1.77 1.77 1.76 1.76 1.76 1.75 1.74 1.74 1.73 1.72 1.72 1.71
Parameter Value
Solvent CD3CN
Temperature 294.3
Pulse Sequence zg30
Experiment 1D
Probe 5 mm TBI5 Z8090/ 0030
Number of Scans 16
Receiver Gain 1024.0
Relaxation Delay 2.0000
Pulse Width 12.2500
Acquisition Time 2.6477
Acquisition Date 2019-01-09T19:31:02
Modification Date 2019-01-09T19:57:52
Spectrometer Frequency 600.13
Spectral Width 12376.2
Lowest Frequency -2606.2
Nucleus 1H
Acquired Size 32768
Spectral Size 131072
N
O+
Ph
BF4−
2.12f
1.91 1.02 1.97 2.00 1.01 0.96
EtOAc
4.11
2.73
water
CD3CN
1.76 4.37
EtOAc
10.0 9.5 9.0 8.5 8.0 7.5 7.0 6.5 6.0 5.5 5.0 4.5 4.0 3.5 3.0 2.5 2.0 1.5 1.0 0.5 0.0
f1 (ppm)

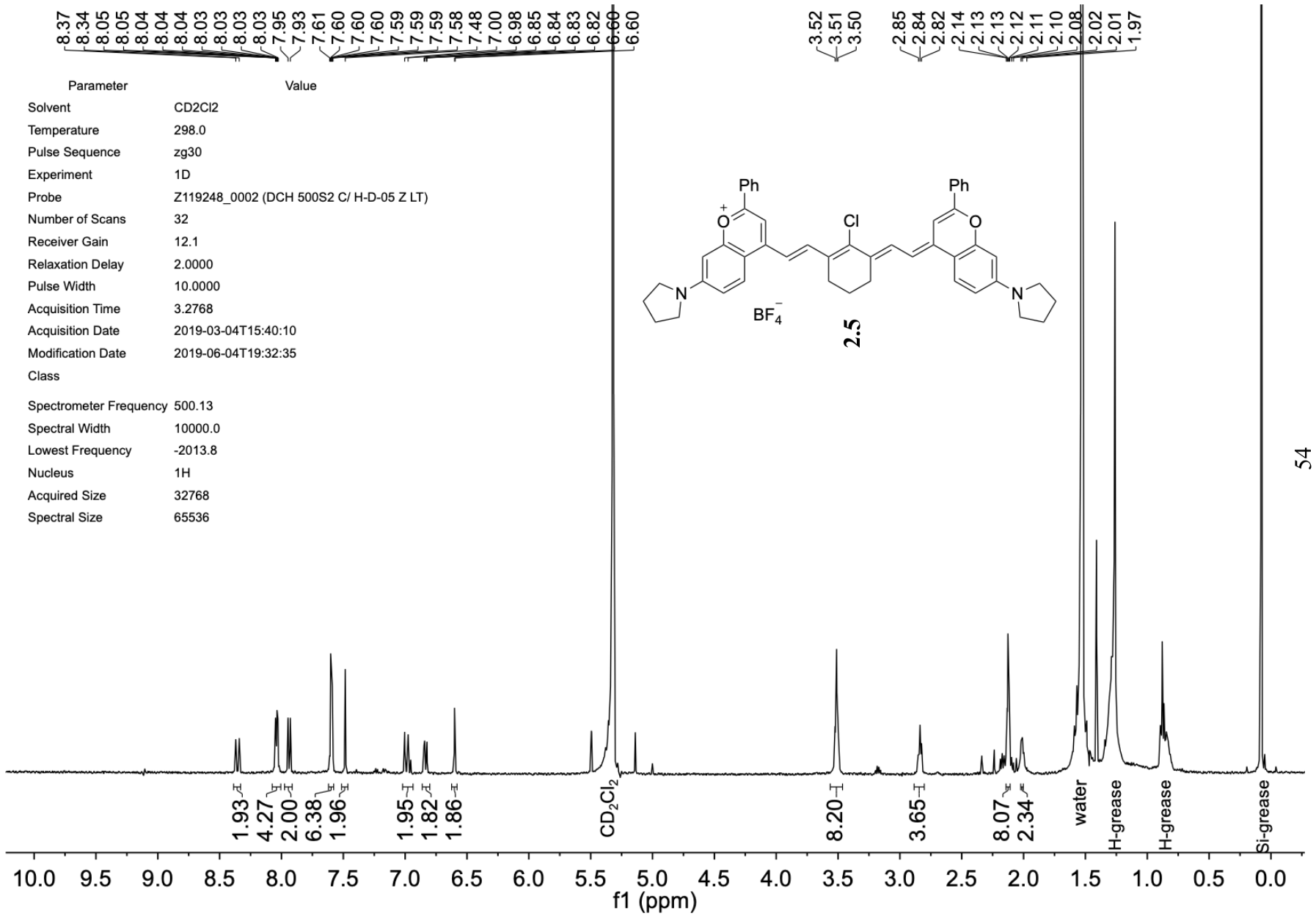
8.37 8.34 8.05 8.05 8.04 8.04 8.04 8.03 8.03 8.03 8.03 7.95 7.93 7.61 7.60 7.60 7.60 7.59 7.59 7.59 7.58 7.48 7.00 6.98 6.85 6.84 6.83 6.82 6.60 6.60
3.52 3.51 3.50 2.85 2.84 2.82 2.14 2.13 2.13 2.12 2.11 2.10 2.08 2.02 2.01 1.97
Parameter Value
Solvent CD2Cl2
Temperature 298.0
Pulse Sequence zg30
Experiment 1D
Probe Z119248_0002 (DCH 500S2 C/ H-D-05 Z LT)
Number of Scans 32
Receiver Gain 12.1
Relaxation Delay 2.0000
Pulse Width 10.0000
Acquisition Time 3.2768
Acquisition Date 2019-03-04T15:40:10
Modification Date 2019-06-04T19:32:35
Class
Spectrometer Frequency 500.13
Spectral Width 10000.0
Lowest Frequency -2013.8
Nucleus 1H
Acquired Size 32768
Spectral Size 65536
Ph
O
Cl
Ph
O
N
N
BF4−
2.5
1.93 4.27 2.00 6.38 1.96 1.95 1.82 1.86 CD2Cl2 8.20 3.65 8.07 2.34 water H-grease H-grease Si-grease
10.0 9.5 9.0 8.5 8.0 7.5 7.0 6.5 6.0 5.5 5.0 4.5 4.0 3.5 3.0 2.5 2.0 1.5 1.0 0.5 0.0
f1 (ppm)

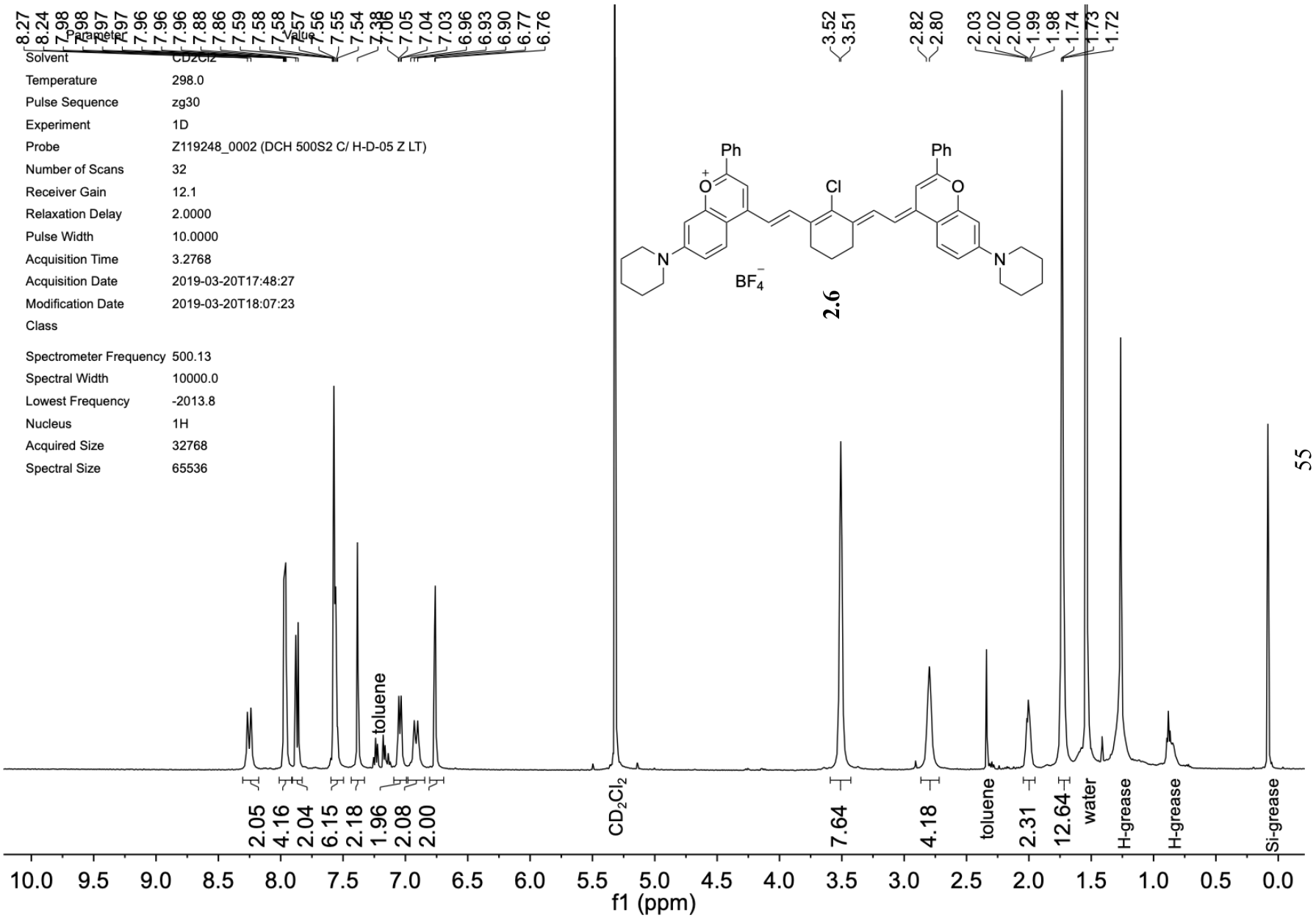
8.27
8.24
7.98
7.98
7.97
7.97
7.96
7.96
7.96
7.88
7.86
7.59
7.58
7.58
7.57
7.56
7.55
7.54
7.38
7.06
7.05
7.04
7.03
6.96
6.93
6.90
6.77
6.76
3.52
3.51
2.82
2.80
2.03
2.02
2.00
1.99
1.98
1.74
1.73
1.72
Parameter
Value
Solvent CD2Cl2
Temperature 298.0
Pulse Sequence zg30
Experiment 1D
Probe Z119248_0002 (DCH 500S2 C/ H-D-05 Z LT)
Number of Scans 32
Receiver Gain 12.1
Relaxation Delay 2.0000
Pulse Width 10.0000
Acquisition Time 3.2768
Acquisition Date 2019-03-20T17:48:27
Modification Date 2019-03-20T18:07:23
Class
Spectrometer Frequency 500.13
Spectral Width 10000.0
Lowest Frequency -2013.8
Nucleus 1H
Acquired Size 32768
Spectral Size 65536
Ph
O
Cl
Ph
O
N
N
BF4−
2.6
toluene
2.05
4.16
2.04
6.15
2.18
1.96
2.08
2.00
CD2Cl2
7.64
4.18
toluene
2.31
12.64
water
H-grease
H-grease
Si-grease
55
10.0 9.5 9.0 8.5 8.0 7.5 7.0 6.5 6.0 5.5 5.0 4.5 4.0 3.5 3.0 2.5 2.0 1.5 1.0 0.5 0.0
f1 (ppm)

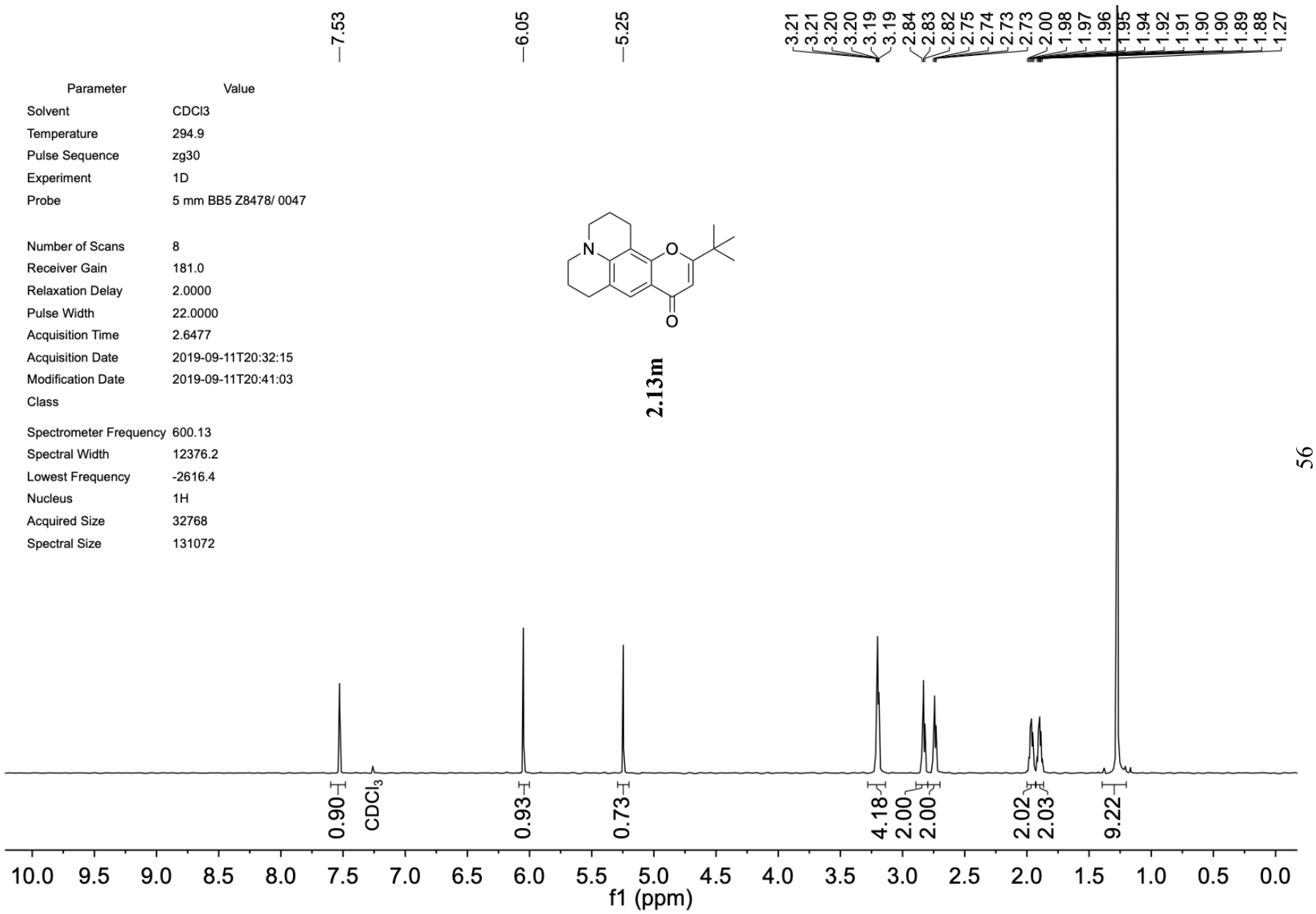
7.53
6.05
5.25
3.21
3.21
3.20
3.20
3.19
3.19
2.84
2.83
2.82
2.75
2.74
2.73
2.73
2.00
1.98
1.97
1.96
1.95
1.94
1.92
1.91
1.90
1.90
1.89
1.88
1.27
Parameter Value
Solvent CDCl3
Temperature 294.9
Pulse Sequence zg30
Experiment 1D
Probe 5 mm BB5 Z8478/ 0047
Number of Scans 8
Receiver Gain 181.0
Relaxation Delay 2.0000
Pulse Width 22.0000
Acquisition Time 2.6477
Acquisition Date 2019-09-11T20:32:15
Modification Date 2019-09-11T20:41:03
Class
Spectrometer Frequency 600.13
Spectral Width 12376.2
Lowest Frequency -2616.4
Nucleus 1H
Acquired Size 32768
Spectral Size 131072
N
O
O
2.13m
0.90
CDCl3
0.93
0.73
4.18
2.00
2.00
2.02
2.03
9.22
10.0 9.5 9.0 8.5 8.0 7.5 7.0 6.5 6.0 5.5 5.0 4.5 4.0 3.5 3.0 2.5 2.0 1.5 1.0 0.5 0.0
f1 (ppm)

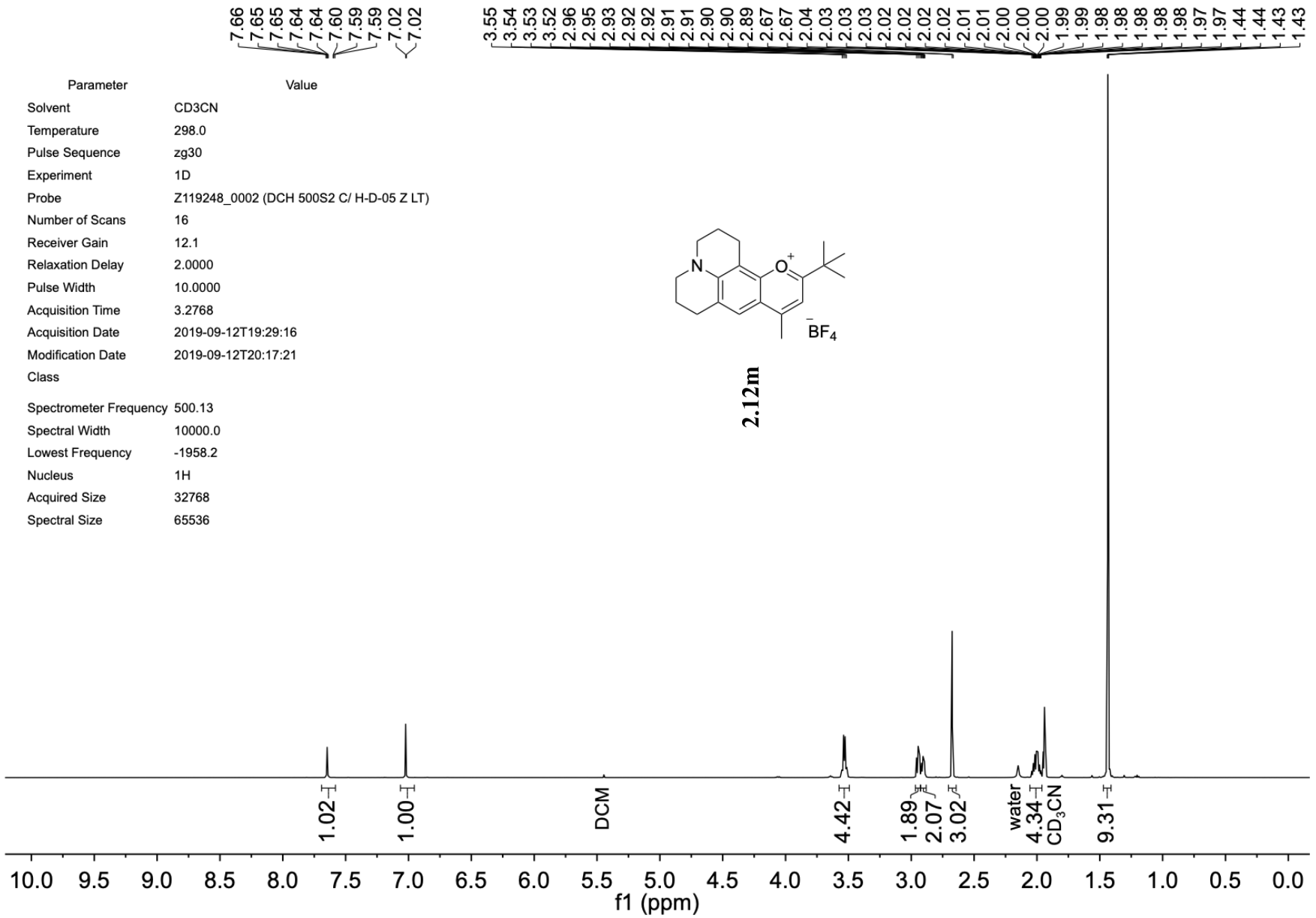
7.66 7.65 7.65 7.64 7.64 7.60 7.59 7.59 7.02 7.02
3.55 3.54 3.53 3.52 2.96 2.95 2.93 2.92 2.92 2.91 2.91 2.90 2.90 2.89 2.67 2.67 2.04 2.03 2.03 2.03 2.02 2.02 2.02 2.02 2.01 2.01 2.00 2.00 2.00 1.99 1.98 1.98 1.98 1.98 1.98 1.97 1.97 1.44 1.44 1.43 1.43
Parameter Value
Solvent CD3CN
Temperature 298.0
Pulse Sequence zg30
Experiment 1D
Probe Z119248_0002 (DCH 500S2 C/ H-D-05 Z LT)
Number of Scans 16
Receiver Gain 12.1
Relaxation Delay 2.0000
Pulse Width 10.0000
Acquisition Time 3.2768
Acquisition Date 2019-09-12T19:29:16
Modification Date 2019-09-12T20:17:21
Class
Spectrometer Frequency 500.13
Spectral Width 10000.0
Lowest Frequency -1958.2
Nucleus 1H
Acquired Size 32768
Spectral Size 65536
N
O+
BF4
2.12m
1.02
1.00
DCM
4.42
1.89
2.07
3.02
water
4.34
CD3CN
9.31
10.0 9.5 9.0 8.5 8.0 7.5 7.0 6.5 6.0 5.5 5.0 4.5 4.0 3.5 3.0 2.5 2.0 1.5 1.0 0.5 0.0
f1 (ppm)

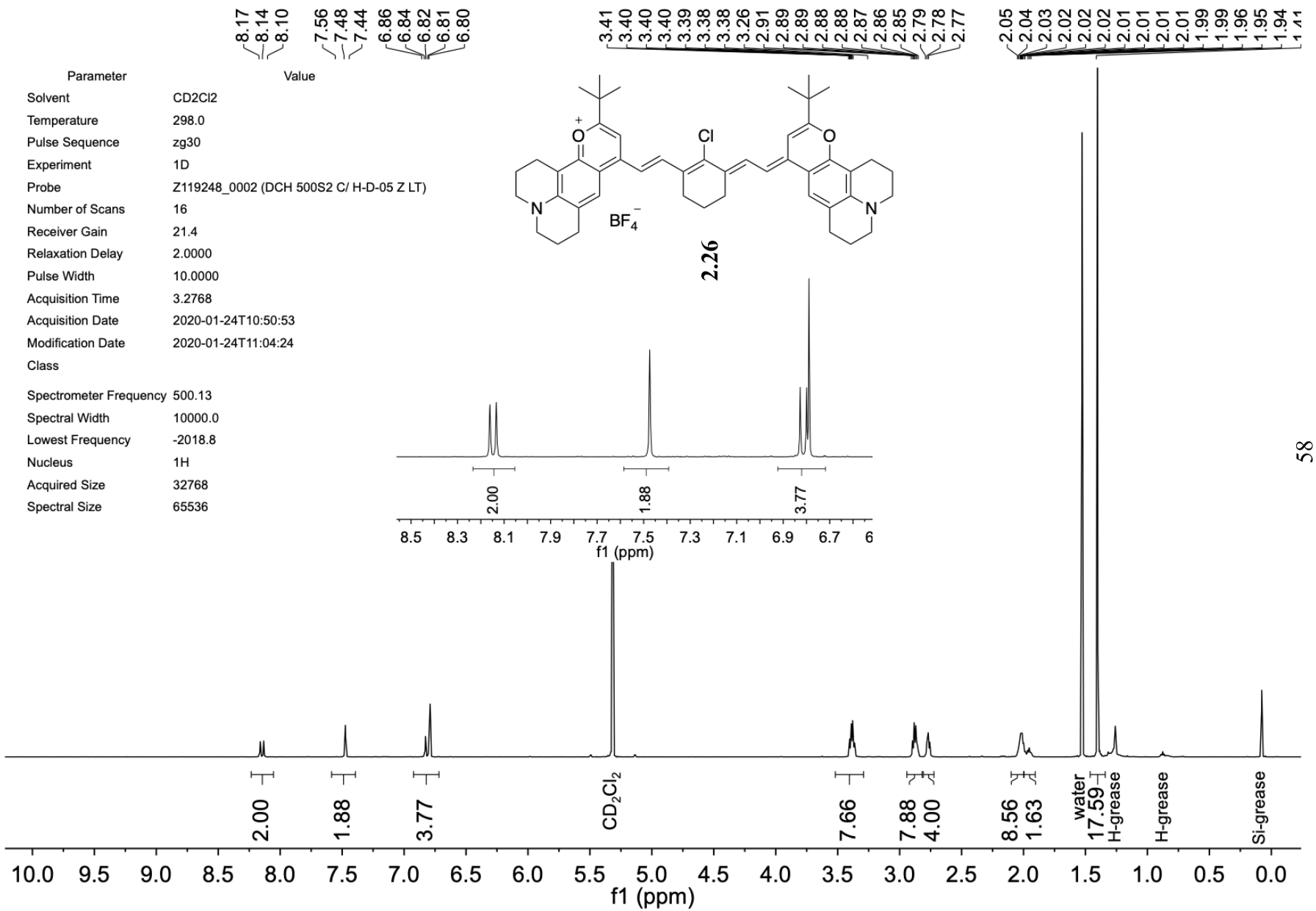
8.17 8.14 8.10 7.56 7.48 7.44 6.86 6.84 6.82 6.81 6.80
3.41 3.40 3.40 3.40 3.39 3.38 3.38 3.26 2.91 2.89 2.89 2.88 2.88 2.87 2.86 2.85 2.79 2.78 2.77
2.05 2.04 2.03 2.02 2.02 2.02 2.01 2.01 2.01 2.01 1.99 1.99 1.96 1.95 1.94
Parameter Value
Solvent CD2Cl2
Temperature 298.0
Pulse Sequence zg30
Experiment 1D
Probe Z119248_0002 (DCH 500S2 C/ H-D-05 Z LT)
Number of Scans 16
Receiver Gain 21.4
Relaxation Delay 2.0000
Pulse Width 10.0000
Acquisition Time 3.2768
Acquisition Date 2020-01-24T10:50:53
Modification Date 2020-01-24T11:04:24
Class
Spectrometer Frequency 500.13
Spectral Width 10000.0
Lowest Frequency -2018.8
Nucleus 1H
Acquired Size 32768
Spectral Size 65536
Cl
O
N
BF4 −
2.26
2.00
1.88
3.77
f1 (ppm)
CD2Cl2
7.66
7.88
4.00
8.56
1.63
water
17.59
H-grease
H-grease
Si-grease
f1 (ppm)

2.6.2 ^{13}C NMR Spectra

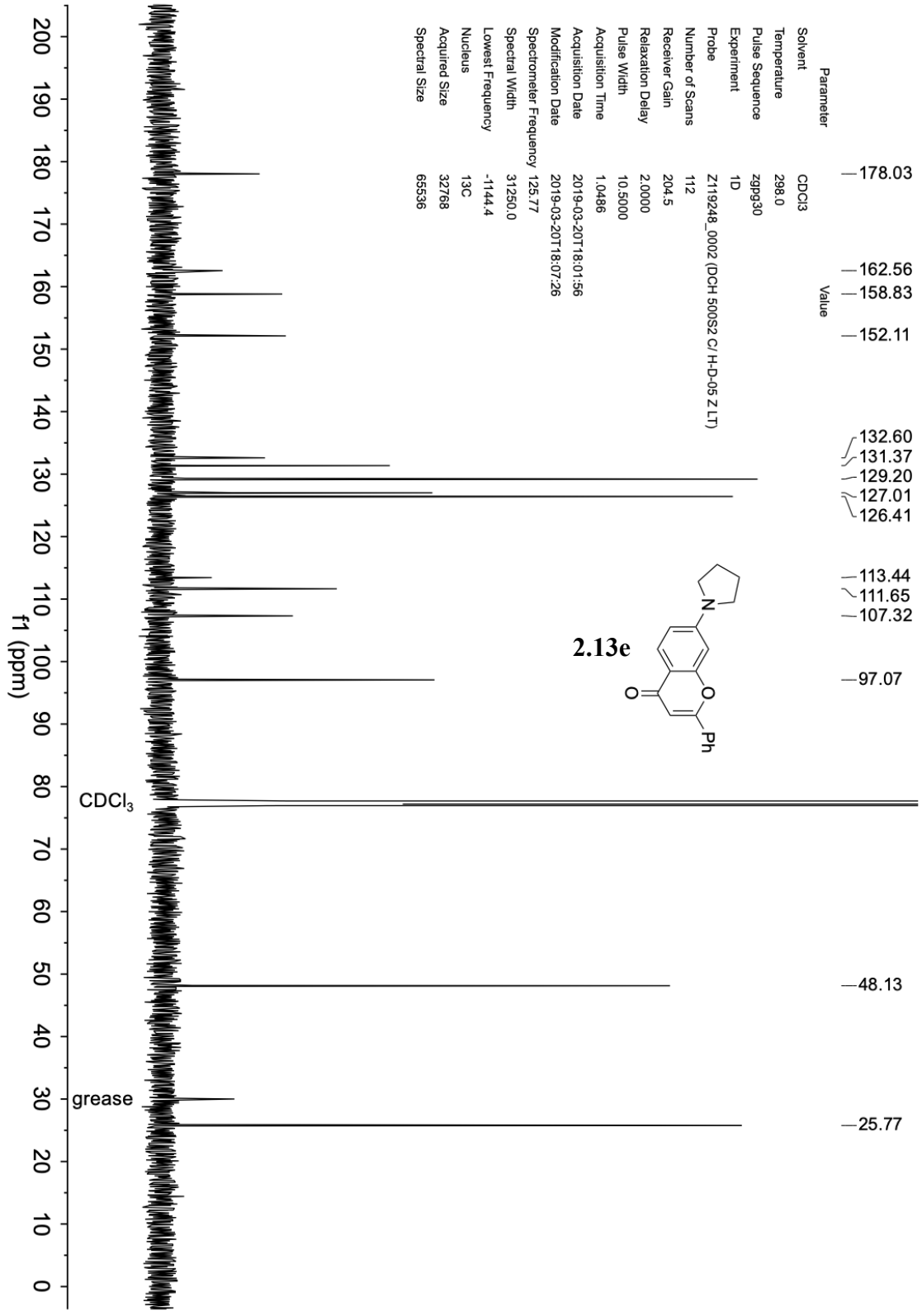

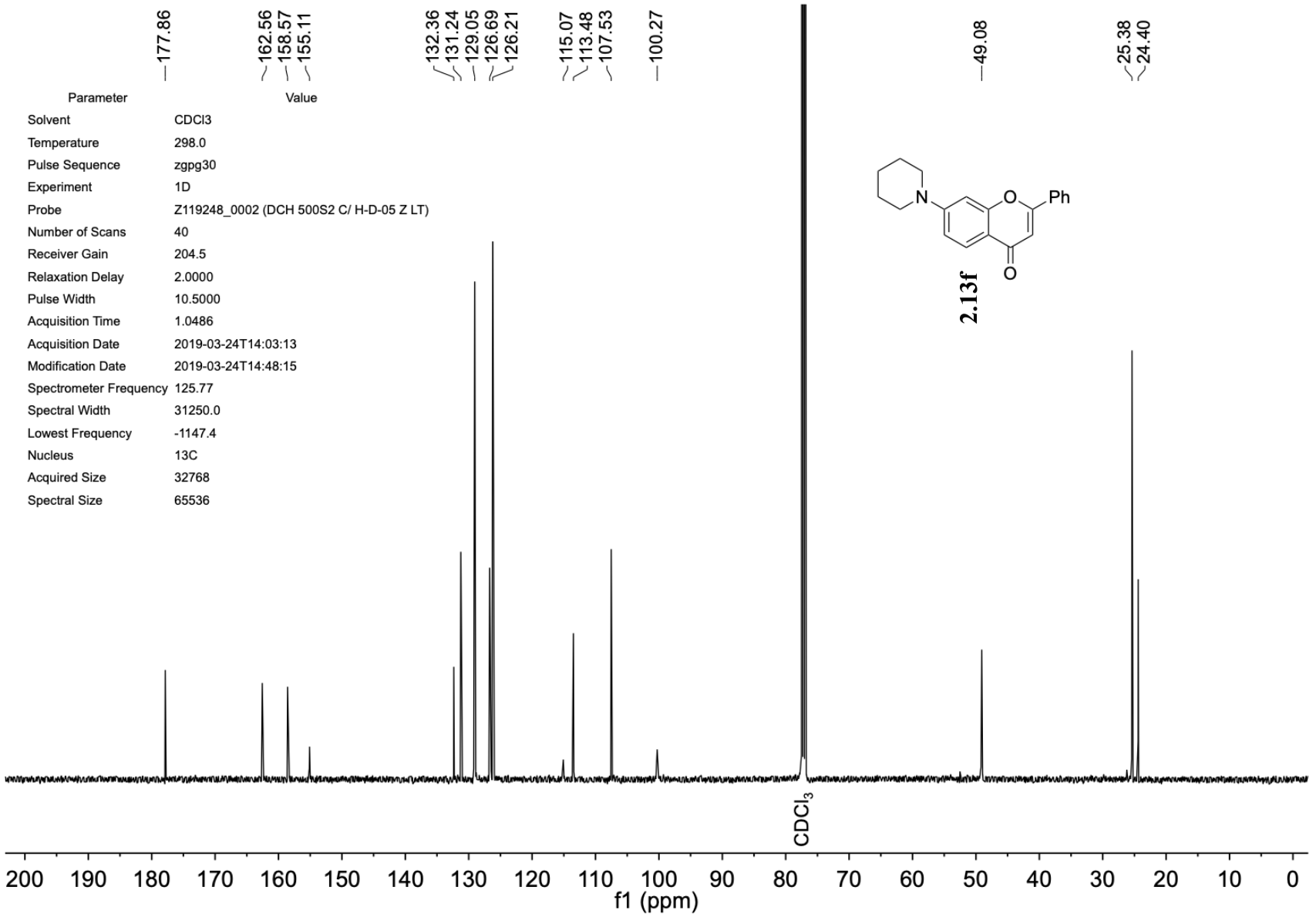
177.86
162.56
158.57
155.11
132.36
131.24
129.05
126.69
126.21
115.07
113.48
107.53
100.27
49.08
25.38
24.40
Parameter Value
Solvent CDCl3
Temperature 298.0
Pulse Sequence zgpg30
Experiment 1D
Probe Z119248_0002 (DCH 500S2 C/ H-D-05 Z LT)
Number of Scans 40
Receiver Gain 204.5
Relaxation Delay 2.0000
Pulse Width 10.5000
Acquisition Time 1.0486
Acquisition Date 2019-03-24T14:03:13
Modification Date 2019-03-24T14:48:15
Spectrometer Frequency 125.77
Spectral Width 31250.0
Lowest Frequency -1147.4
Nucleus 13C
Acquired Size 32768
Spectral Size 65536
N
O
Ph
O
2.13f
CDCl3
200 190 180 170 160 150 140 130 120 110 100 90 80 70 60 50 40 30 20 10 0
f1 (ppm)

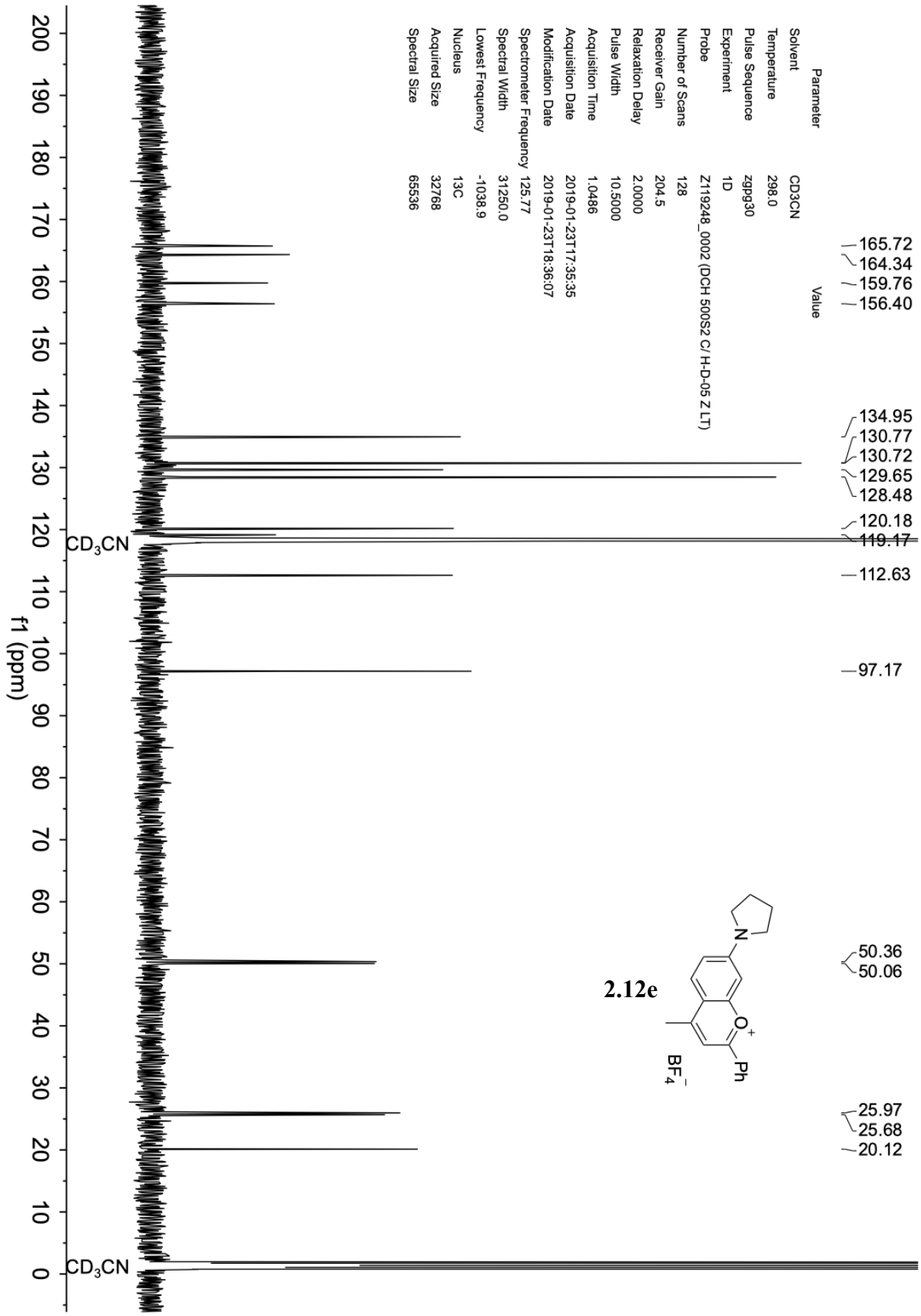
Parameter
Value
Solvent
CD3CN
Temperature
298.0
Pulse Sequence
zgpg30
Experiment
1D
Probe
Z119248_0002 (DCH 500S2 C/ H-D-05 Z LT)
Number of Scans
128
Receiver Gain
204.5
Relaxation Delay
2.0000
Pulse Width
10.5000
Acquisition Time
1.0486
Acquisition Date
2019-01-23T17:35:35
Modification Date
2019-01-23T18:36:07
Spectrometer Frequency
125.77
Spectral Width
31250.0
Lowest Frequency
-1038.9
Nucleus
13C
Acquired Size
32768
Spectral Size
65536
165.72
164.34
159.76
156.40
134.95
130.77
130.72
129.65
128.48
120.18
119.17
112.63
97.17
50.36
50.06
25.97
25.68
20.12
CD3CN
CD3CN
f1 (ppm)
2.12e
N
O+
Ph
BF4−

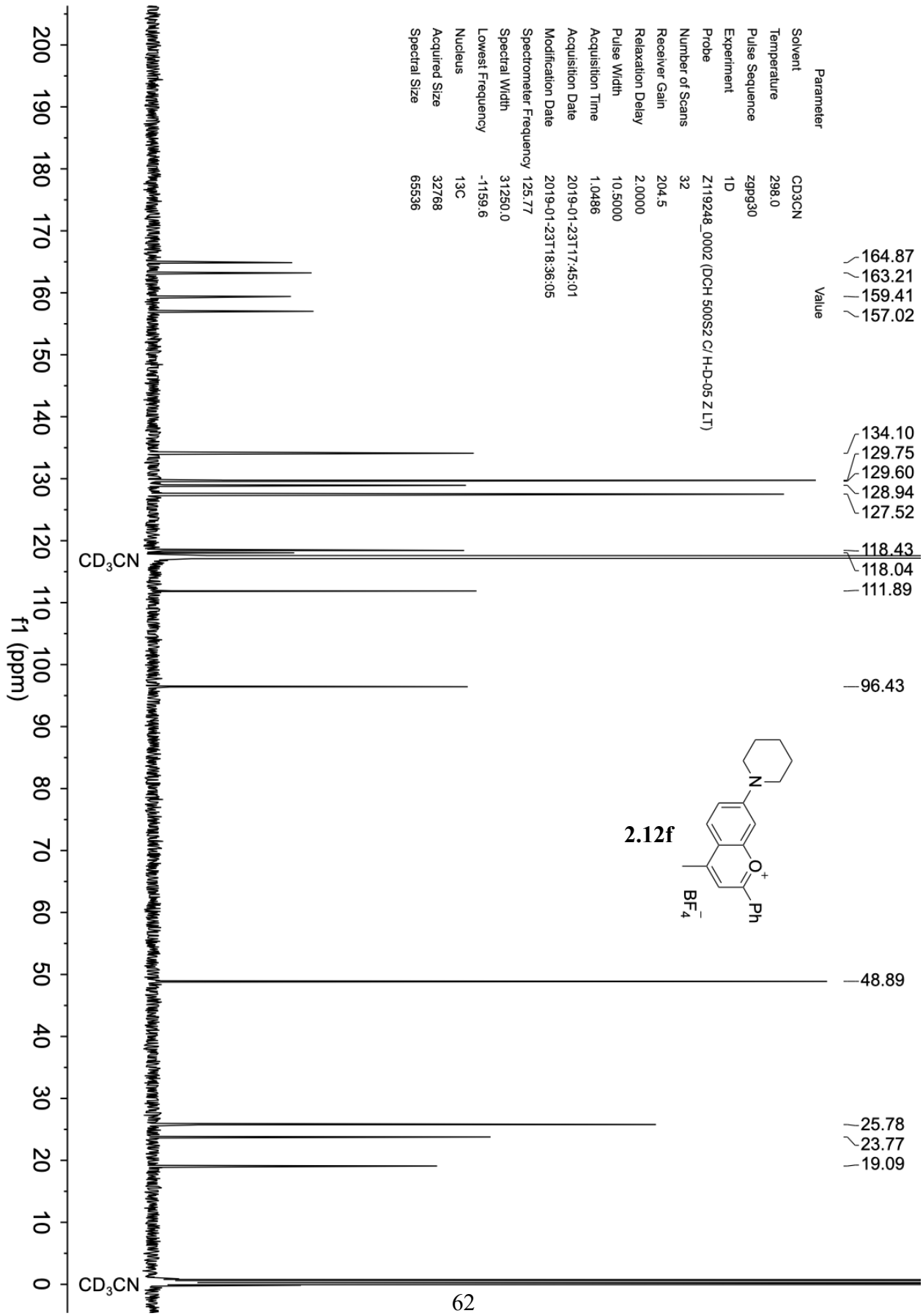
Parameter Value
Solvent CD3CN
Temperature 298.0
Pulse Sequence zgpg30
Experiment 1D
Probe Z119248_0002 (DCH 500S2 C/ H-D-05 Z LT)
Number of Scans 32
Receiver Gain 204.5
Relaxation Delay 2.0000
Pulse Width 10.5000
Acquisition Time 1.0486
Acquisition Date 2019-01-23T17:45:01
Modification Date 2019-01-23T18:36:05
Spectrometer Frequency 125.77
Spectral Width 31250.0
Lowest Frequency -1159.6
Nucleus 13C
Acquired Size 32768
Spectral Size 65536
164.87
163.21
159.41
157.02
134.10
129.75
129.60
128.94
127.52
118.43
118.04
111.89
96.43
48.89
25.78
23.77
19.09
CD3CN
CD3CN
f1 (ppm)
2.12f
N
O+
Ph
BF4−

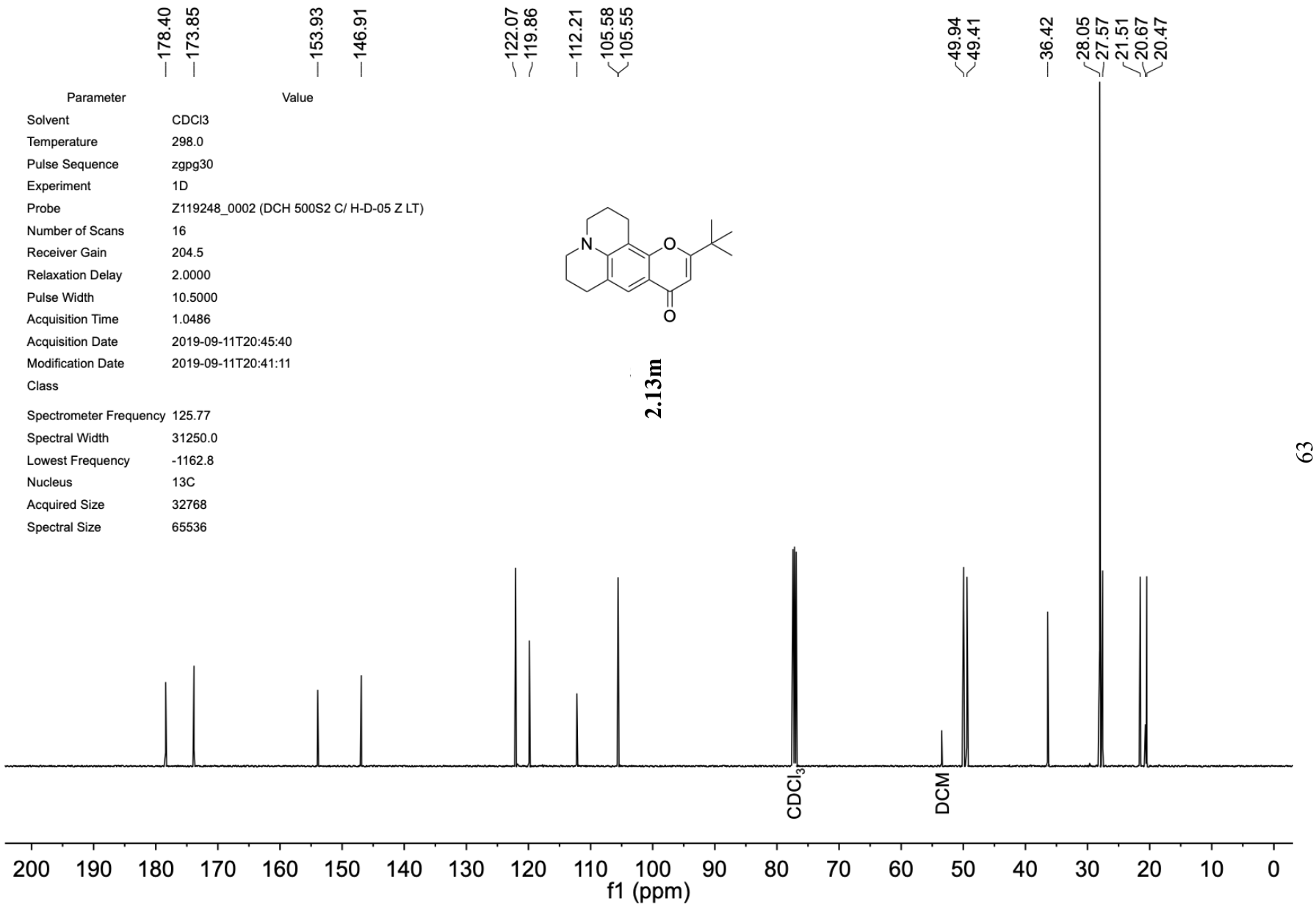
178.40
173.85
153.93
146.91
122.07
119.86
112.21
105.58
105.55
49.94
49.41
36.42
28.05
27.57
21.51
20.67
20.47
Parameter Value
Solvent CDCl3
Temperature 298.0
Pulse Sequence zgpg30
Experiment 1D
Probe Z119248_0002 (DCH 500S2 C/ H-D-05 Z LT)
Number of Scans 16
Receiver Gain 204.5
Relaxation Delay 2.0000
Pulse Width 10.5000
Acquisition Time 1.0486
Acquisition Date 2019-09-11T20:45:40
Modification Date 2019-09-11T20:41:11
Class
Spectrometer Frequency 125.77
Spectral Width 31250.0
Lowest Frequency -1162.8
Nucleus 13C
Acquired Size 32768
Spectral Size 65536
N
O
O
2.13m
CDCl3
DCM
200 190 180 170 160 150 140 130 120 110 100 90 80 70 60 50 40 30 20 10 0
f1 (ppm)

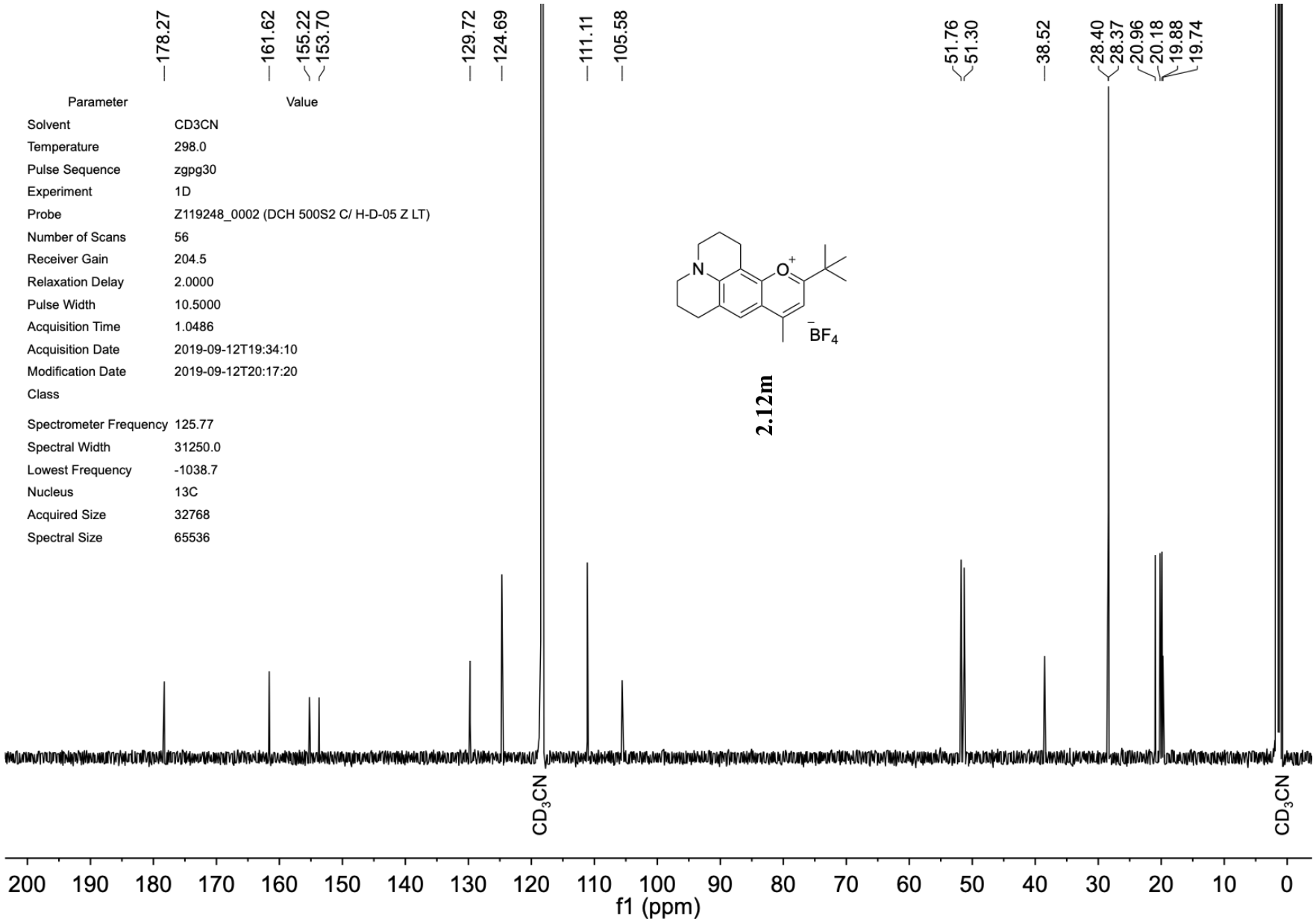
178.27
161.62
155.22
153.70
129.72
124.69
111.11
105.58
51.76
51.30
38.52
28.40
28.37
20.96
20.18
19.88
19.74
Parameter Value
Solvent CD3CN
Temperature 298.0
Pulse Sequence zgpg30
Experiment 1D
Probe Z119248_0002 (DCH 500S2 C/ H-D-05 Z LT)
Number of Scans 56
Receiver Gain 204.5
Relaxation Delay 2.0000
Pulse Width 10.5000
Acquisition Time 1.0486
Acquisition Date 2019-09-12T19:34:10
Modification Date 2019-09-12T20:17:20
Class
Spectrometer Frequency 125.77
Spectral Width 31250.0
Lowest Frequency -1038.7
Nucleus 13C
Acquired Size 32768
Spectral Size 65536
N
O+
BF4
2.12m
CD3CN
CD3CN
200 190 180 170 160 150 140 130 120 110 100 90 80 70 60 50 40 30 20 10 0
f1 (ppm)

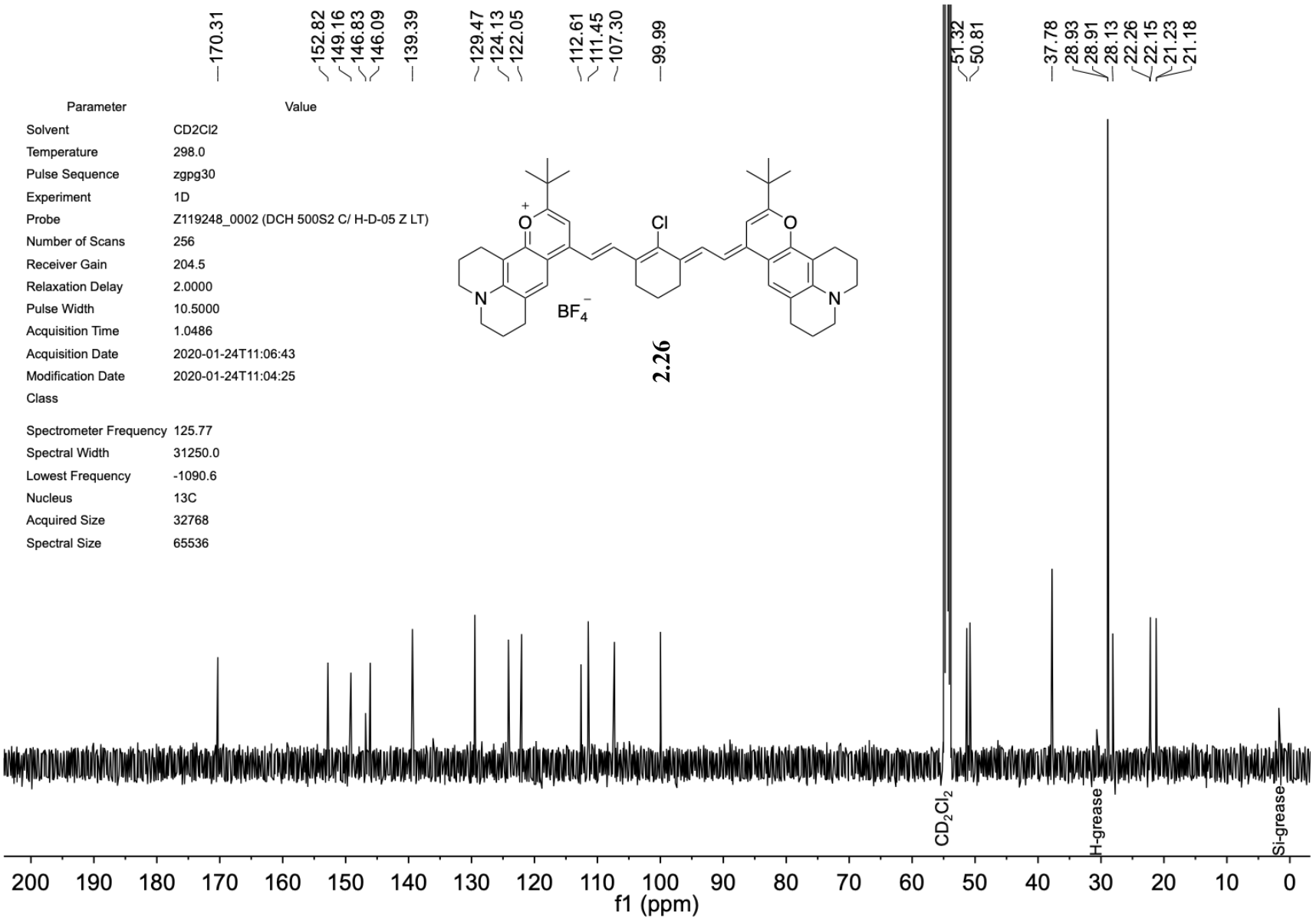
170.31
152.82
149.16
146.83
146.09
139.39
129.47
124.13
122.05
112.61
111.45
107.30
99.99
51.32
50.81
37.78
28.93
28.91
28.13
22.26
22.15
21.23
21.18
Parameter Value
Solvent CD2Cl2
Temperature 298.0
Pulse Sequence zgpg30
Experiment 1D
Probe Z119248_0002 (DCH 500S2 C/ H-D-05 Z LT)
Number of Scans 256
Receiver Gain 204.5
Relaxation Delay 2.0000
Pulse Width 10.5000
Acquisition Time 1.0486
Acquisition Date 2020-01-24T11:06:43
Modification Date 2020-01-24T11:04:25
Class
Spectrometer Frequency 125.77
Spectral Width 31250.0
Lowest Frequency -1090.6
Nucleus 13C
Acquired Size 32768
Spectral Size 65536
Cl
O
N
BF4
2.26
CD2Cl2
H-grease
Si-grease
200 190 180 170 160 150 140 130 120 110 100 90 80 70 60 50 40 30 20 10 0
f1 (ppm)

2.6.3 Absorption and Emission Spectra

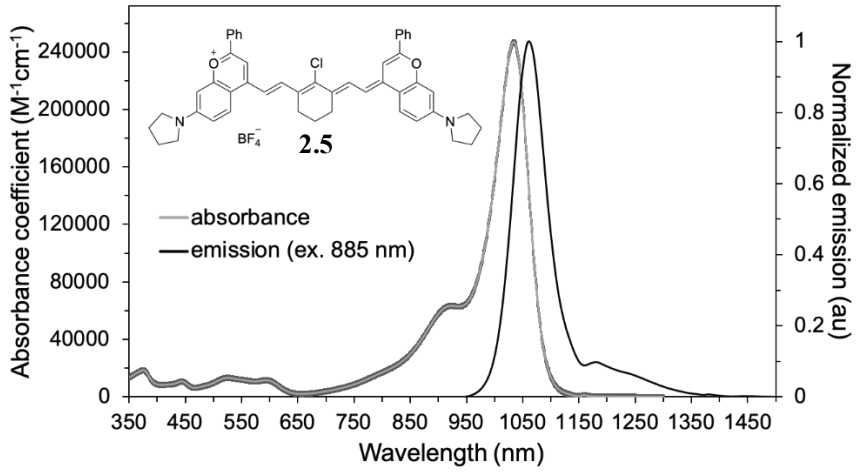

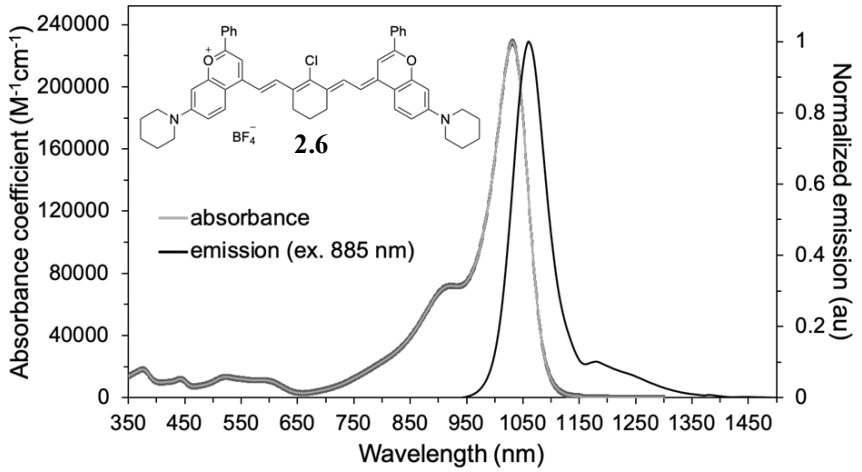

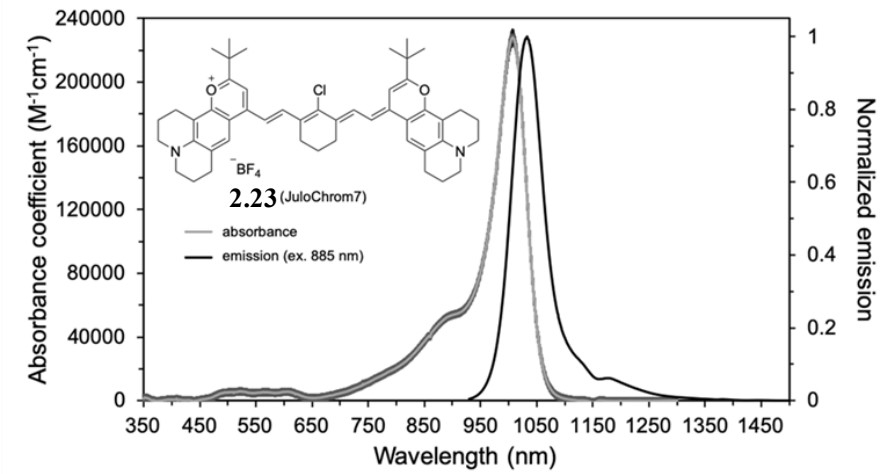

2.7 References

(1) Dean, K. M.; Palmer, A. E. Advances in Fluorescence Labeling Strategies for Dynamic Cellular Imaging. *Nat. Chem. Biol.* **2014**, *10*, 512–523. https://doi.org/10.1038/nchembio.1556.

(2) Wei, L.; Chen, Z.; Shi, L.; Long, R.; Anzalone, A. V.; Zhang, L.; Hu, F.; Yuste, R.; Cornish, V. W.; Min, W. Super-Multiplex Vibrational Imaging. **2017**, *544*, 465–470. https://doi.org/10.1038/nature22051.

(3) Thimsen, E.; Sadtler, B.; Berezin, M. Y. Shortwave-Infrared (SWIR) Emitters for Biological Imaging: A Review of Challenges and Opportunities. *Nanophotonics*. **2017** *6*, 1043–1054. https://doi.org/10.1515/nanoph-2017-0039.

(4) Ding, F.; Zhan, Y.; Lu, X.; Sun, Y. Recent Advances in Near-Infrared II Fluorophores for Multifunctional Biomedical Imaging. *Chem. Sci*. **2018** *9*, 4370–4380. https://doi.org/10.1039/c8sc01153b.

(5) Tu, L.; Xu, Y.; Ouyang, Q.; Li, X.; Sun, Y. Recent Advances on Small-Molecule Fluorophores with Emission beyond 1000 Nm for Better Molecular Imaging in Vivo. *Chinese Chem. Lett.* **2019**, *30*, 1731–1737. https://doi.org/10.1016/j.cclet.2019.05.022.

(6) Lei, Z.; Zhang, F. Molecular Engineering of NIR-II Fluorophores for Improved Biomedical Detection. *Angew. Chem. Int. Ed.* **2021** *6*, 16294–16308. https://doi.org/10.1002/anie.202007040.

(7) Li, C.; Wang, Q. Challenges and Opportunities for Intravital Near-Infrared Fluorescence Imaging Technology in the Second Transparency Window. *ACS Nano* **2018**. https://doi.org/10.1021/acsnano.8b07536.

(8) Carr, J. A.; Aellen, M.; Franke, D.; So, P. T. C.; Bruns, O. T.; Bawendi, M. G. Absorption by Water Increases Fluorescence Image Contrast of Biological Tissue in the Shortwave Infrared. *Proc. Natl. Acad. Sci. USA* . **2018**, *115*, 9080–9085. https://doi.org/10.1073/pnas.1803210115.

(9) Shcherbakova, D. M.; Verkhusha, V. V. Near-Infrared Fluorescent Proteins for Multicolor in Vivo Imaging. *Nat. Methods* **2013**, *10*, 751–754. https://doi.org/10.1038/nmeth.2521.

(10) Kosaka, N.; Ogawa, M.; Sato, N.; Choyke, P. L.; Kobayashi, H. In Vivo Real-Time,

Multicolor, Quantum Dot Lymphatic Imaging. *J. Invest. Dermatol.* **2009**, *129*, 2818–2822. https://doi.org/10.1038/JID.2009.161.

(11) Zavaleta, C. L.; Smith, B. R.; Walton, I.; Doering, W.; Davis, G.; Shojaei, B.; Natan, M. J.; Gambhir, S. S. Multiplexed Imaging of Surface Enhanced Raman Scattering Nanotags in Living Mice Using Noninvasive Raman Spectroscopy. *Proc. Natl. Acad. Sci. USA.* **2009**, *106*, 13511–13516. https://doi.org/10.1073/PNAS.0813327106/SUPPL_FILE/0813327106SI.PDF.

(12) Erogbogbo, F.; Yong, K. T.; Roy, I.; Hu, R.; Law, W. C.; Zhao, W.; Ding, H.; Wu, F.; Kumar, R.; Swihart, M. T.; Prasad, P. N. In Vivo Targeted Cancer Imaging, Sentinel Lymph Node Mapping and Multi-Channel Imaging with Biocompatible Silicon Nanocrystals. *ACS Nano* **2011**, *5*, 413–423. https://doi.org/10.1021/NN1018945/SUPPL_FILE/NN1018945_SI_001.PDF.

(13) Zhang, H.; Salo, D.; Kim, D. M.; Komarov, S.; Tai, Y.-C.; Berezin, M. Y. Penetration Depth of Photons in Biological Tissues from Hyperspectral Imaging in Shortwave Infrared in Transmission and Reflection Geometries. *J. Biomed. Opt.* **2016**, *21*, 126006. https://doi.org/10.1117/1.jbo.21.12.126006.

(14) Naczynski, D. J.; Tan, M. C.; Zevon, M.; Wall, B.; Kohl, J.; Kulesa, A.; Chen, S.; Roth, C. M.; Riman, R. E.; Moghe, P. V. Rare-Earth-Doped Biological Composites as in Vivo Shortwave Infrared Reporters. *Nat. Commun.* **2013**, *4*, 1–10. https://doi.org/10.1038/ncomms3199.

(15) Welsher, K.; Liu, Z.; Sherlock, S. P.; Robinson, J. T.; Chen, Z.; Daranciang, D.; Dai, H. A Route to Brightly Fluorescent Carbon Nanotubes for Near-Infrared Imaging in Mice. *Nat. Nanotechnol.* **2009**, *4* , 773–780. https://doi.org/10.1038/nnano.2009.294.

(16) Hong, G.; Robinson, J. T.; Zhang, Y.; Diao, S.; Antaris, A. L.; Wang, Q.; Dai, H. In Vivo Fluorescence Imaging with Ag2S Quantum Dots in the Second Near-Infrared Region. *Angew. Chem. Int. Ed.* **2012**, *51*, 9818–9821. https://doi.org/10.1002/ANIE.201206059.

(17) Bruns, O. T.; Bischof, T. S.; Harris, D. K.; Franke, D.; Shi, Y.; Riedemann, L.; Bartelt, A.; Jaworski, F. B.; Carr, J. A.; Rowlands, C. J.; Wilson, M. W. B.; Chen, O.; Wei, H.; Hwang, G. W.; Montana, D. M.; Coropceanu, I.; Achorn, O. B.; Kloepper, J.; Heeren, J.;

So, P. T. C.; Fukumura, D.; Jensen, K. F.; Jain, R. K.; Bawendi, M. G. Next-Generation in Vivo Optical Imaging with Short-Wave Infrared Quantum Dots. *Nat. Biomed. Eng.* **2017**, *1*. https://doi.org/10.1038/s41551-017-0056.

(18) Cai, Y.; Wei, Z.; Song, C.; Tang, C.; Han, W.; Dong, X. Optical Nano-Agents in the Second near-Infrared Window for Biomedical Applications. *Chemical Society Reviews*. **2019**, *1*, 22–37. https://doi.org/10.1039/c8cs00494c.

(19) Tao, Z.; Hong, G.; Shinji, C.; Chen, C.; Diao, S.; Antaris, A. L.; Zhang, B.; Zou, Y.; Dai, H. Biological Imaging Using Nanoparticles of Small Organic Molecules with Fluorescence Emission at Wavelengths Longer than 1000 Nm. *Angew. Chem. Int. Ed.* **2013**, *52*, 13002–13006. https://doi.org/10.1002/ANIE.201307346.

(20) Yang, Q.; Ma, Z.; Wang, H.; Zhou, B.; Zhu, S.; Zhong, Y.; Wang, J.; Wan, H.; Antaris, A.; Ma, R.; Zhang, X.; Yang, J.; Zhang, X.; Sun, H.; Liu, W.; Liang, Y.; Dai, H. Rational Design of Molecular Fluorophores for Biological Imaging in the NIR-II Window. *Adv. Mater.* **2017**, *29*, 1605497. https://doi.org/10.1002/ADMA.201605497.

(21) Zhu, S.; Herraiz, S.; Yue, J.; Zhang, M.; Wan, H.; Yang, Q.; Ma, Z.; Wang, Y.; He, J.; Antaris, A. L.; Zhong, Y.; Diao, S.; Feng, Y.; Zhou, Y.; Yu, K.; Hong, G.; Liang, Y.; Hsueh, A. J.; Dai, H. 3D NIR-II Molecular Imaging Distinguishes Targeted Organs with High-Performance NIR-II Bioconjugates. *Adv. Mater.* **2018**, *30*, 1705799. https://doi.org/10.1002/ADMA.201705799.

(22) Wan, H.; Yue, J.; Zhu, S.; Uno, T.; Zhang, X.; Yang, Q.; Yu, K.; Hong, G.; Wang, J.; Li, L.; Ma, Z.; Gao, H.; Zhong, Y.; Su, J.; Antaris, A. L.; Xia, Y.; Luo, J.; Liang, Y.; Dai, H. A Bright Organic NIR-II Nanofluorophore for Three-Dimensional Imaging into Biological Tissues. *Nat. Commun.* **2018**, *9*, 1–9. https://doi.org/10.1038/s41467-018-03505-4.

(23) Wang, F.; Wan, H.; Ma, Z.; Zhong, Y.; Sun, Q.; Tian, Y.; Qu, L.; Du, H.; Zhang, M.; Li, L.; Ma, H.; Luo, J.; Liang, Y.; Li, W. J.; Hong, G.; Liu, L.; Dai, H. Light-Sheet Microscopy in the near-Infrared II Window. *Nat. Methods* **2019**, *16*, 545–552. https://doi.org/10.1038/s41592-019-0398-7.

(24) Zhu, S.; Yang, Q.; Antaris, A. L.; Yue, J.; Ma, Z.; Wang, H.; Huang, W.; Wan, H.; Wang, J.; Diao, S.; Zhang, B.; Li, X.; Zhong, Y.; Yu, K.; Hong, G.; Luo, J.; Liang, Y.; Dai, H.

Molecular Imaging of Biological Systems with a Clickable Dye in the Broad 800- to 1,700-Nm near-Infrared Window. *Proc. Natl. Acad. Sci. USA* **2017**, *114*, 962–967. https://doi.org/10.1073/PNAS.1617990114/SUPPL_FILE/PNAS.1617990114.SAPP.PDF.

(25) Ma, B. L.; Zhai, X.; Du, G.; Zhou, J. Orthogonal Shortwave Infrared Emission Based on Rare Earth Nanoparticles for Interference-Free Logical Codes and Bio-Imaging. *Chem. Sci.* **2019**, *10*, 3281–3288. https://doi.org/10.1039/C8SC05044A.

(26) Wong, K. C. Y.; Sletten, E. M. Extending Optical Chemical Tools and Technologies to Mice by Shifting to the Shortwave Infrared Region. *Curr. Opin. Chem. Biol.* **2022**, *68*, 102131. https://doi.org/10.1016/j.cbpa.2022.102131.

(27) Li, C.; Chen, G.; Zhang, Y.; Wu, F.; Wang, Q. Advanced Fluorescence Imaging Technology in the Near-Infrared-II Window for Biomedical Applications. *J. Am. Chem. Soc.* **2020**, *142*, 14789–14804. https://doi.org/10.1021/jacs.0c07022.

(28) Hong, G.; Diao, S.; Chang, J.; Antaris, A. L.; Chen, C.; Zhang, B.; Zhao, S.; Atochin, D. N.; Huang, P. L.; Andreasson, K. I.; Kuo, C. J.; Dai, H. Through-Skull Fluorescence Imaging of the Brain in a New near-Infrared Window. *Nat. Photonics* **2014**, *8*, 723–730. https://doi.org/10.1038/nphoton.2014.166.

(29) Diao, S.; Blackburn, J. L.; Hong, G.; Antaris, A. L.; Chang, J.; Wu, J. Z.; Zhang, B.; Cheng, K.; Kuo, C. J.; Dai, H. Fluorescence Imaging In Vivo at Wavelengths beyond 1500 Nm. *Angew. Chem. Int. Ed.* **2015**, *54*, 14758–14762. https://doi.org/10.1002/ANIE.201507473.

(30) Lewis, E. K.; Haaland, W. C.; Nguyen, F.; Heller, D. A.; Allen, M. J.; MacGregor, R. R.; Berger, C. S.; Willingham, B.; Burns, L. A.; Scott, G. B. I.; Kittrell, C.; Johnson, B. R.; Curl, R. F.; Metzker, M. L. Color-Blind Fluorescence Detection for Four-Color DNA Sequencing. *Proc. Natl. Acad. Sci. USA* **2005**, *102*, 5346–5351. https://doi.org/10.1073/PNAS.0501606102/ASSET/A628E104-3D03-4C36-B49A-46C9844034AE/ASSETS/GRAPHIC/ZPQ0150579080005.JPEG.

(31) Garbacik, E. T.; Sanz-Paz, M.; Borgman, K. J. E.; Campelo, F.; Garcia-Parajo, M. F. Frequency-Encoded Multicolor Fluorescence Imaging with Single-Photon-Counting Color-Blind Detection. *Biophys. J.* **2018**, *115*, 725–736.

https://doi.org/10.1016/J.BPJ.2018.07.008.

(32) Gómez-García, P. A.; Garbacik, E. T.; Otterstrom, J. J.; Garcia-Parajo, M. F.; Lakadamyali, M. Excitation-Multiplexed Multicolor Superresolution Imaging with Fm-STORM and Fm-DNA-PAINT. *Proc. Natl. Acad. Sci. USA* **2018**, *115*, 12991–12996. https://doi.org/10.1073/PNAS.1804725115/SUPPL_FILE/PNAS.1804725115.SAPP.PDF.

(33) Janeková, H.; Friedman, H. C.; Russo, M.; Zyberaj, M.; Ahmed, T.; Hua, A. S.; Sica, A. V.; Caram, J. R.; Štacko, P. Deuteration of Heptamethine Cyanine Dyes Enhances Their Emission Efficacy. *Chem. Commun.* **2024**, *60*, 1000–1003. https://doi.org/10.1039/D3CC05153F.

(34) Friedman, H. C.; Cosco, E. D.; Atallah, T. L.; Jia, S.; Sletten, E. M.; Caram, J. R. Establishing Design Principles for Emissive Organic SWIR Chromophores from Energy Gap Laws. *Chem* **2021**, *7*, 3359–3376. https://doi.org/10.1016/j.chempr.2021.09.001.

(35) Julia L. Bricks; Alexei D.Kachkovskii; Yurii L.Slominskii; Andrii O.Gerasov; Sergei V.Popov; Bricks, J. L.; Kachkovskii, A. D.; Slominskii, Y. L.; Gerasov, A. O.; Popov, S. V. Molecular Design of near Infrared Polymethine Dyes: A Review. *Dye. Pigment.* **2015**, *121*, 238–255. https://doi.org/10.1016/J.DYEPIG.2015.05.016.

(36) Du, Y.; Liu, X.; Zhu, S. Near-Infrared-II Cyanine/Polymethine Dyes, Current State and Perspective. *Frontiers in Chemistry*. **2021**, *9*, 625. https://doi.org/10.3389/fchem.2021.718709.

(37) Cosco, E. D.; Caram, J. R.; Bruns, O. T.; Franke, D.; Day, R. A.; Farr, E. P.; Bawendi, M. G.; Sletten, E. M. Flavylium Polymethine Fluorophores for Near- and Shortwave Infrared Imaging. *Angew. Chem. Int. Ed.* **2017**, *56*, 13126–13129. https://doi.org/10.1002/anie.201706974.

(38) Marshall, M. V.; Rasmussen, J. C.; Tan, I.-C.; Aldrich, M. B.; Adams, K. E.; Wang, X.; Fife, C. E.; Maus, E. A.; Smith, L. A.; Sevick-Muraca, E. M. Near-Infrared Fluorescence Imaging in Humans with Indocyanine Green: A Review and Update. *Open Surg. Oncol. J.* **2010**, *2*, 12–25. https://doi.org/10.2174/1876504101002010012.

(39) Rurack, K.; Spieles, M. Fluorescence Quantum Yields of a Series of Red and Near-Infrared Dyes Emitting at 600-1000 Nm. *Anal. Chem.* **2011**, *83*, 1232–1242.

https://doi.org/10.1021/AC101329H/SUPPL_FILE/AC101329H_SI_001.PDF.

(40) Chen, J. R.; Wong, J. B.; Kuo, P. Y.; Yang, D. Y. Synthesis and Characterization of Coumarin-Based Spiropyran Photochromic Colorants. *Org. Lett.* **2008**, *10*, 4823–4826. https://doi.org/10.1021/OL8018902/SUPPL_FILE/OL8018902_SI_003.CIF.

(41) Seijas, J. A.; Vázquez-Tato, M. P.; Carballido-Reboredo, R. Solvent-Free Synthesis of Functionalized Flavones under Microwave Irradiation. *J. Org. Chem.* **2005**, *70*, 2855–2858. https://doi.org/10.1021/JO048685Z/SUPPL_FILE/JO048685ZSI20050114_125302.PDF.

(42) Kónya, K.; Pajtás, D.; Kiss-Szikszai, A.; Patonay, T. Buchwald–Hartwig Reactions of Monohaloflavones. *European J. Org. Chem.* **2015**, *2015*, 828–839. https://doi.org/10.1002/EJOC.201403108.

(43) Kopainsky, B.; Qiu, P.; Kaiser, W.; Sens, B.; Drexhage, K. H. Lifetime, Photostability, and Chemical Structure of IR Heptamethine Cyanine Dyes Absorbing beyond 1 ?M. *Appl. Phys. B Photophysics Laser Chem.* **1982**, *29*, 15–18. https://doi.org/10.1007/BF00694363.

(44) Hansch, C.; Leo, A.; Taft, R. W. A Survey of Hammett Substituent Constants and Resonance and Field Parameters. *Chem. Rev.* **1991**, *91*, 165–195. https://doi.org/10.1021/cr00002a004.

(45) Semonin, O. E.; Johnson, J. C.; Luther, J. M.; Midgett, A. G.; Nozik, A. J.; Beard, M. C. Absolute Photoluminescence Quantum Yields of IR-26 Dye, PbS, and PbSe Quantum Dots. *J. Phys. Chem. Lett.* **2010**, *1*, 2445–2450. https://doi.org/10.1021/jz100830r.

(46) Hatami, S.; Würth, C.; Kaiser, M.; Leubner, S.; Gabriel, S.; Bahrig, L.; Lesnyak, V.; Pauli, J.; Gaponik, N.; Eychmüller, A.; Resch-Genger, U. Absolute Photoluminescence Quantum Yields of IR26 and IR-Emissive Cd1−xHgxTe and PbS Quantum Dots – Method- and Material-Inherent Challenges. *Nanoscale* **2014** *7*, 133–143. https://doi.org/10.1039/C4NR04608K.

(47) Cosco, E. D.; Spearman, A. L.; Ramakrishnan, S.; Lingg, J. G. P.; Saccomano, M.; Pengshung, M.; Arús, B. A.; Wong, K. C. Y.; Glasl, S.; Ntziachristos, V.; Warmer, M.; McLaughlin, R. R.; Bruns, O. T.; Sletten, E. M. Shortwave Infrared Polymethine Fluorophores Matched to Excitation Lasers Enable Non-Invasive, Multicolour in Vivo

Imaging in Real Time. *Nat. Chem.* **2020**, *12*, 1123–1130. https://doi.org/10.1038/s41557-020-00554-5.

(48) Kövér, J.; Antus, S. Facile Deoxygenation of Hydroxylated Flavonoids by Palladium Catalysed Reduction of its Triflate Derivatives. *Z. Naturforsch.* **2005**, *60b*, 792–796.

CHAPTER THREE

Exploring the Role of 2-position Chromenylium Modifications in Pursuit of Dye Structure-Property Relationships

Adapted from: Anthony L. Spearman, Daniel W. Turner, Iain Kimpton, Cesar A. Garcia, Steven A. Lopez, Ellen M. Sletten*. Exploring Structure-Property Relationships of Chromenylium-Based Shortwave Infrared Polymethine Dyes. (*Manuscript in preparation*)

3.1 Abstract

Flavylium and chromenylium polymethine dyes have been explored as contrast agents for the shortwave infrared (SWIR; 1000–2000 nm) region. Previously, our group has augmented the 2-, 5-, 6-, 7-, and 8- positions on the core flavylium heterocycle, developing insight for modulating flavylium photophysical properties in the process. The 2-position on the scaffold was the only site where molecular brightness was observed to dramatically increase. This observation sparked a systematic investigation of how the various molecular properties of 2-position substituents caused this effect. Herein, we report a panel of electronically and sterically varied 2-position chromenylium derivatives and their photophysical performance. We found that certain *p*-substituents can improve Φ_F and for the first time, we observed 2-position substituents invoking red-shifts in λ_{max} up to 32 nm.

3.2 Introduction

Over the past decade, the shortwave infrared (SWIR/NIR-II, 1000-2000 nm) region has consistently shown dominance over traditional near-infrared (NIR, 700-1000 nm) windows for high-resolution optical imaging.[1–6] This superiority arose from a combination of reduced light

scattering, minimal endogenous SWIR emitters, and attenuation of background via water absorption in the SWIR.[3,7–9] The SWIR region has proven itself with notable applications in image-guided surgery in humans, and non-invasive through-skull imaging and real-time multiplexed imaging in mouse models.[10–13] A popular fluorophore class for SWIR imaging is polymethine dyes, composed of two heterocycles linked by a polymethine chain. Key features of polymethine dyes are narrow absorption profiles and excellent molar absorptivity (ε_{max}, ~10^5 M^{-1} cm^{-1}).[14–16] However, due to energy gap law effects, the fluorescence quantum yield (Φ_F) of SWIR dyes plummet as their bandgaps decrease/absorbance is red-shifted.[3,17] As such, the elucidation of strategies for designing bright, red-shifted SWIR emitting fluorophores is a chief priority.

Our lab has explored structure-property relationships for flavylium-based heptamethine dyes (Flav7 scaffold; Figure 3.1A).[18] In previous works, we came to understand the role of the 6- and 7-positions by establishing Hammett linear free energy relationships between substituent electronics (σ_p/σ_m) and absorbance ($\lambda_{max,abs}$) (Figure 3.1B).[12] As all 7-modified dyes were similarly bright, this strategy helped us develop fluorophores nicely matched for excitation by commercial laser lines. Placing amine substituents at the 6-position led to dyes redder than their 7-position counterparts, but with significantly decreased Φ_F's.[19] From these studies, we gained a strong handle on red-shifting strategies but were still interested in learning how to improve Φ_F.

In follow-up work, we synthesized Flav7 derivatives with 2-position modifications (**Chrom7**), by replacing the phenyl ring with bulky aliphatic groups.[11] For clarities sake, flavylium heterocycles require a 2-phenyl group, whereas the chromenyliums do not. In comparison to **Flav7**, this modification led to blue-shifted absorbance (1027 to 975 nm) but to our delight, a staggering 3-fold increase in Φ_F (0.61 to 1.70%). We then became interested in understanding how such a modification resulted in brighter polymethine dyes.

To this end, Caram and coworkers developed a parameter, ξ, which deconvolutes band gap effects to better compare quantum yields between two dyes.[17] In short, a reference dye is fitted to the same band gap as a comparison dye, where ξ represents the improvement/worsening of the comparison dye's Φ_F. A positive ξ is interpreted as an improvement in Φ_F and vice versa. And in practice, this can help show how specific structural differences in these dyes can improve or worsen brightness. The design of Flav7 was inspired by commercial fluorophores **IR-26** and **IR-27**.[18] Despite structural similarities, we initially found **Flav7** with a Φ_F greater by one order of magnitude. In collaboration with the Caram group, we then calculated ξ values for this set of dyes, using **IR-26** as the reference dye. We found Flav7 to have high ξ values relative to commercial standards, suggesting the 7-dimethylamino group as a moiety to improve Φ_F for this scaffold.[17] A similar analysis with **Chrom7**, showed the chromenylium scaffold gave even greater ξ values than **Flav7**. Altogether, these findings motivated an investigation of how 2-position substitution impacted chromenylium dye brightness.

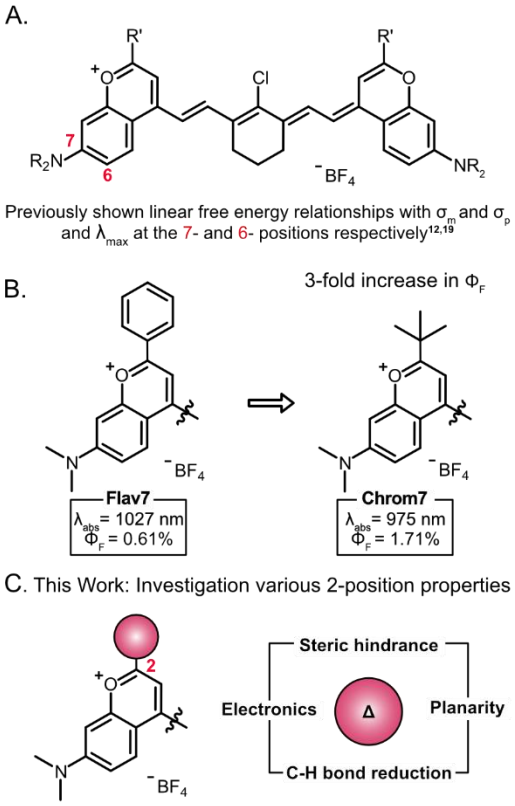

Figure 3.1. A. The chromenylium heptamethine scaffold and different sites of functionalization. **B.** Initial 2-position modifications led to the phenomenally bright Chrom7 dye. **C.** This work investigates how 2-position groups impact photophysical performance towards new design trends.

Herein, we designed a panel of 2-position Chrom7 derivatives to better understand the photophysical contributions of this site on the heterocycle. Inspired by our previous structure-property studies at the 6 and 7-position,[12,19] we selected a diverse panel of 2-position substituents and compared different molecular parameters against their photophysical properties. We took electronic effects, steric hindrance, π-conjugation and C-H bond reduction into consideration. Lastly, we decoupled energy-gap law effects to find which modifications maximized molecular brightness overall. From these studies, we generally found that red-shifting can be invoked by appending electron withdrawing groups at the 2-position (*meta*- directed) or 4”-position (*para* directed). To improve Φ_F, *p*-methoxy incorporation at the 4”-position can be selected without major impact on λ_{max} but *p*-amine incorporation also improved Φ_F while also red-shifting. We

believe these elucidated design principles will greatly guide the design of future chromenylium-based polymethine dyes as well as encourage similar analyses for other SWIR fluorophore scaffolds.

3.3 Results and Discussion

3.3.1 Design Rationale

Perplexed by how the Chrom7 modification, replacing the phenyl ring at the 2-position with a *tert*-butyl group, led to increased Φ_F (Figure 3.1B/3.2A), we considered molecular differences between a phenyl ring and bulky aliphatic groups (**3.1**–**3.3**). We suspected **Chrom7** could be brighter by 2-position electronic effects, decreased molecular motion due to stereoelectronic effects or structural rigidity, or perhaps from sp^2 C-H bond reduction. To test these theories, we designed a new panel of Flav7 derivatives with structurally diverse substituents at the 2-position of the flavylium scaffold (**3.4**–**3.15**; Figure 3.1C/3.2B)

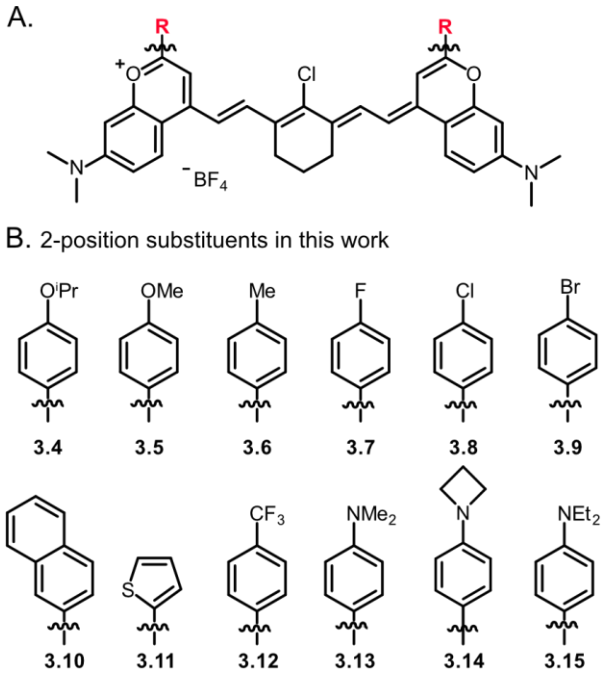

Figure 3.2. **A.** Chromenylium structure explored in this work. **B.** Panel of 2-position substituents selected to probe molecular effects on photophysical performance.

3.3.2 Synthesis of 2-position Derivatives

A modular synthesis allowed access to all target dyes **3.4**–**3.15** (**Scheme 3.1**). First, 7-dimethylamino phenol (**3.16**) was reacted with a functionalized β-ketoester (**3.17a–l**) in a Mentzer pyrone reaction to afford compounds, **3.18a–l**. We also explored similar prep in the microwave for quicker conversion.[20] β-ketoesters **3.17a–l** were either commercially available or synthesized according to literature precedent.[21–26] Additionally, Buchwald-Hartwig amination with **3.18f** and azetidine hydrochloride provided **3.18k**.[27,28] Treatment of compounds **3.18a–l** with methyl Grignard and dehydration gave heterocycles **3.19a–f**. Subsequent condensation with heptamethine linker **3.20**, afforded target dyes, **3.4–3.15**. Despite excellent conversion, the low reported yields were due to difficulties in isolation. Dyes were purified by column chromatography, however trituration of the crude dye with cold ether, THF, and ethyl acetate greatly assisted with purification.

Scheme 3.1. Modular synthesis of 2-position Chrom7 derivatives (3.4–3.15).

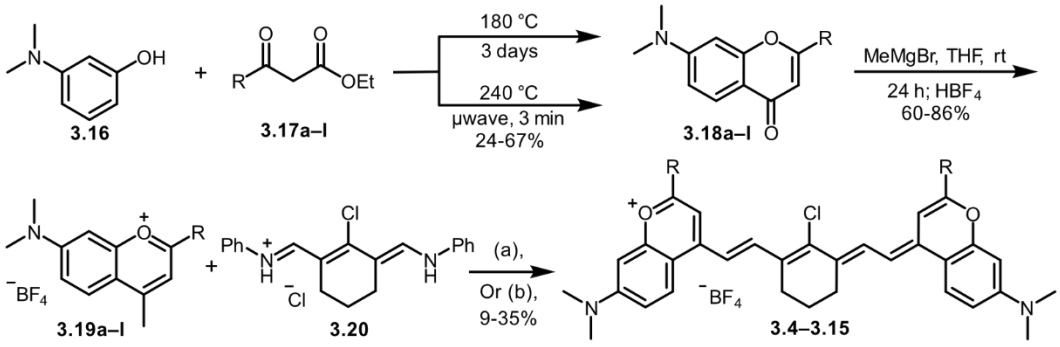

Note: (a) NaOAc, *n*-butanol/toluene, 100 °C. (b) NaOAc, acetic anhydride, 110 °C. See SI for synthetic procedures.

3.3.3 Photophysical Properties of 2-position Derivatives

After synthesizing derivatives **3.4**–**3.15**, a thorough photophysical investigation was performed (**Table 1**). Initially, we measured the $\lambda_{max,abs/em}$, Φ_F, and ε_{max} of each dye. Compared to **3.1** (**Chrom7**), all substituents displayed red-shifted $\lambda_{max,abs}$, with the reddest dyes being the *p*-

amine dyes **3.13**–**3.15** (~1055 nm). These dyes had an average Stokes shift (the difference of $\lambda_{max,em}$ and $\lambda_{max,abs}$) of around 23 nm, and as such, their $\lambda_{max,em}$ followed a similar trend. For imaging applications, an important dye property is molecular brightness (m.b.). This can be calculated as the product of ε_{max} and Φ_F. The panel of dyes had a wide range of Φ_F (Using **IR-26** for relative Φ_F measurements),[29,30] spanning between 0.3 (**3.12**; *p*-CF_3) and 0.74% (**3.5**; *p*-OMe). Unfortunately, no derivative displayed Φ_F values on par with the previously reported dyes **3.1** and **3.2** (Φ_F ~1.7%), instead they generally performed similarly to **3.3**, Flav7 (Φ_F = 0.61%). There seemed to be no major impact on ε_{max}, as all dyes displayed typical values for heptamethine dyes (~10^5 $M^{-1}cm^{-1}$). Therefore, as is the case with most polymethine dyes, here we found that the molecular brightness (given by the product of ε_{max} and Φ_F) of these dyes was largely determined by Φ_F. In this panel, while dyes **3.5**–**3.7** had similar λ_{max} to **3.3** (Flav7), they all displayed higher brightness values with an upwards of 1700 $M^{-1}cm^{-1}$. Lastly, we calculated the energy-gap improvement factor ξ for each dye.[17] Again, this parameter represents the improvement or worsening of the target dye Φ_F compared to a set reference dye. And with this parameter, we can better compare the Φ_F of dyes at different bandgaps. A few dyes were identified to have positive ξ values: **3.5** (*p*-OMe), **3.4** (*p*-^{i}PrO), and the *p*-amines (**3.13**, **3.14**, and **3.15**). We were pleased to see positive ξ values for the *p*-OMe derivative, as other groups have developed bright flavylium dyes bearing *para* -methoxy groups.[31,32] However, it was noteworthy that despite significantly red-shifting $\lambda_{max,abs}$, *p*-amine incorporation returned positive ξ values.

Table 3.1. Photophysical parameters of dyes 3.1–3.15, taken in dichloromethane (DCM)

Dye (2-Pos)	$\lambda_{max,abs}$ (nm)	$\lambda_{max,em}$ (nm)	ε_{max} ($M^{-1}cm^{-1}$)	Φ_F (%)	M.B. ($M^{-1}cm^{-1}$)	ξ (wrt Flav7)
3.1 tBu (Chrom7)	975	996	252000 ± 5000	1.7 ± 0.02	4300 ± 100	0.19
3.2 Adamantyl	977	997	267000 ± 8000	1.61 ± 0.02	4300 ± 100	0.16
3.3 Phenyl (Flav7)	1027	1053	241000 ± 1000	0.61 ± 0.02	1500 ± 100	0
3.4 *p*-O^{i}Pr Ph	1025	1048	191000 ± 5000	0.71 ± 0.03	1300 ± 70	0.11

3.5 *p*-OMe Ph	1027	1047	222000 ± 9000	0.74 ± 0.07	1600 ± 200	0.16
3.6 *p*-Me Ph	1027	1049	259000 ± 4000	0.64 ± 0.03	1700 ± 80	0.02
3.7 *p*-F Ph	1028	1050	257000 ± 6000	0.66 ± 0.04	1700 ± 100	0.07
3.8 *p*-Cl Ph	1036	1059	199000 ± 6000	0.49 ± 0.03	980 ± 70	-0.1
3.9 *p*-Br Ph	1038	1063	230000 ± 3000	0.46 ± 0.03	1100 ± 70	-0.12
3.10 Naphthalene	1042	1068	120000 ± 4000	0.46 ± 0.06	570 ± 70	-0.06
3.11 Thiophene	1043	1066	220000 ± 7000	0.39 ± 0.03	900 ± 50	-0.21
3.12 *p*-CF_3 Ph	1044	1070	211000 ± 5000	0.30 ± 0.04	630 ± 90	-0.37
3.13 *p*-NMe_2 Ph	1051	1073	180000 ±10000	0.48 ± 0.03	860 ± 70	0.08
3.14 *p*-Azet Ph	1054	1074	120000 ± 10000	0.49 ± 0.09	580 ± 100	0.11
3.15 *p*-NEt_2 Ph	1059	1081	210000 ± 1000	0.43 ± 0.01	920 ± 20	0.08

3.3.4 Investigating the Effects of Sterics

First, we considered the effects of steric hindrance on photophysical performance. Steric effects could decrease vibrational/rotational motion within the fluorophore, which are avenues for non-radiative decay. In the past, we successfully established linear free-energy relationships with substituent electronics and were eager to extend this analysis to steric hindrance. To probe these substituent effects, we correlated photophysical parameters with Taft parameters (σ^*),[33] values that consider substituent steric effects. Armed with Taft values for eight 2-position substituents (**3.1**, **3.3**, **3.5**, **3.6**, **3.7**, **3.8**, **3.12**, **3.13**), we attempted to establish Taft correlations. Unfortunately, poor correlations were observed between Taft parameters and all tested photophysical parameters (Figure 3.3A; R^2 between 0.1 and 0.3) Another metric for describing steric hindrance is using Charton parameters, however, only 3 dyes could be compared in this fashion. With limited insight provided from this analysis, we considered other factors.

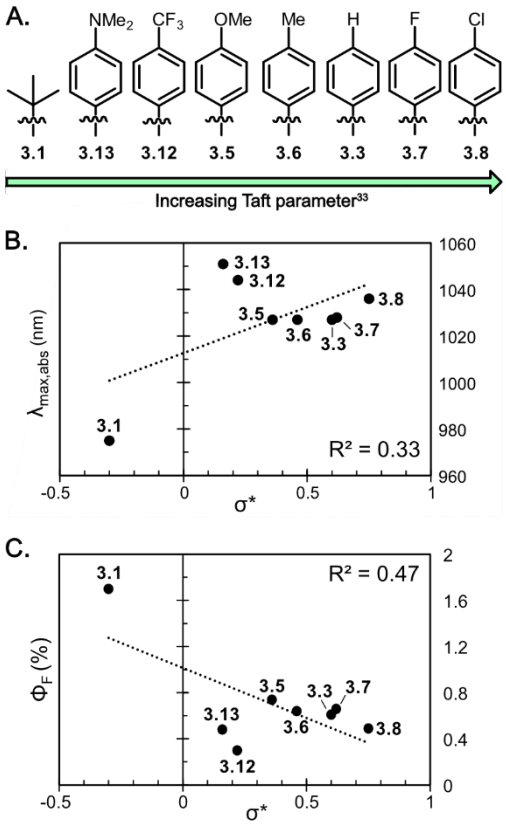

Figure 3.3. A. Dye set arranged by reported Taft values B. Taft vs. λ_{max}. C. Taft vs. Φ_F.

3.3.5 Investigating the Effects of C-H Bond Reduction

Another hypothesis from the Chrom7 modification was that removal of C_{sp2}-H bonds weakened non-radiative pathways. The Caram and Stacko Groups have recently looked at the effects of deuteration on several dyes, including a couple flavylium heptamethine dyes.[17,34,35] In preliminary work, Caram found that partial deuteration of the linker potentially deactivated non-radiative pathways.[17] The Stacko Group then followed up by developing Flav7 derivatives with deuterated amines (7-position) which improved Φ_F (1.56 to 2.39%).[34] Interested in seeing if C-H bond removal was responsible for Chrom7s brightness, our group designed a Flav7 derivative with fully deuterated phenyl rings at the 2-position.[35] By comparing these reported Flav7 derivatives that had deuterated polymethine chains ("**1D**"), deuterated 2-position phenyl rings (**"Flav7d10"**),

and deuterated 7-position amines ("**1DD"**) against the non-deuterated controls (**Flav7**) we can determine the overall effects of deuterium on Φ_F (**Figure 3B**). Generally, the deuterated dyes had higher quantum yields overall, supporting C-H bond reduction as a strategy to improve quantum yield. However, based on the work done by Caram and Stacko, the removal of sp^3 C-H bonds seems more impactful than sp^2 C-H bonds. When comparing **Flav7** vs **Flav7d10** we saw a meager increase in Φ_F (0.61 to 0.67%). Another approach to validate this theory would be through pentafluorophenyl incorporation at the 2-position. Regardless, this analysis encouraged the exploration of other parameters.

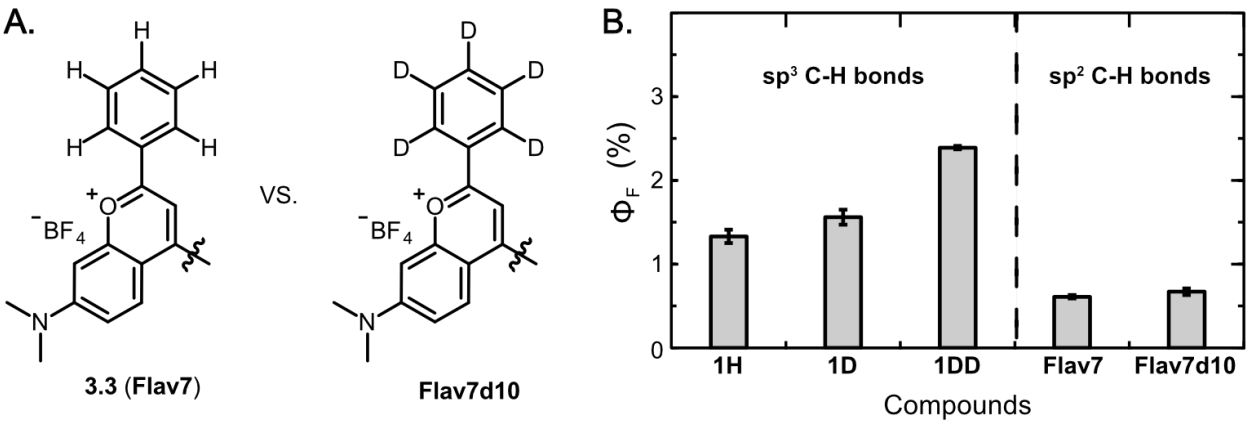

Figure 3.4. Understanding the effects of C-H bond (sp^3 and sp^2 alike) reduction on Φ_F.

3.3.6 Investigating the Effects of Planarity

In recent work, Zhu and coworkers saw interesting results when performing computational analyses on their flavylium derivatives.[36] They observed that 2-position substituents with low torsional angles had red-shifted $\lambda_{max,abs}$, owed to greater π-conjugation, whereas dyes with higher angles were blue-shifted. To perform a similar analysis with our dyes, we chose dyes (**3.5** and **3.11**–**3.14**) and calculated their ground-state geometries (Figure 3.5). Dyes were selected to give a decent spread of substituent electronics, **3.11** was chosen to compare to literature precedent, and **3.14** was chosen as the effects of ring constraint against **3.13** (NMe_2 vs. azetidine) could be seen.

By determining the angles of their 2-position substituents against the core heterocycle, referred to as β (°), we could learn how different 2-position modifications affected conjugation.

Flav7 was calculated to have a β angle of 22°, meaning the phenyl ring was by default a bit out of plane. **3.12** (*p*-CF_3) and **3.5** (*p*-4"OMe) had similar angles of 22° and 18° respectively. A difference was seen with the more electron-donating *p*-amine substituted dyes (**3.13** and **3.14**). Notably, both dyes **3.13** and **3.14** had angles around 8°, demonstrating these dyes approached a greater level of conjugation. Interestingly enough we found that the constrained azetidine (**3.14**) had similar planarity to the free amine (**3.13**). As these dyes had similar Φ_F and now supported with calculated geometries, we reasoned that twisted intermolecular charge transfer (TICT), a common quenching effect from the rotation of amines, is not a major contributor to non-radiative pathways for these *p*-amine substituents in organic solvent.[31] Lastly, and in congruence with the Zhu groups findings, our 2-position thiophene derivative (**3.11**) was calculated to be completely in conjugation (0°) – further validating the observed red-shifted λ_{max} of this dye (~ 16 nm).[36] While reduced β angles tended to correlate with red-shifted λ_{max} there was still one more factor to consider, substituent electronics.

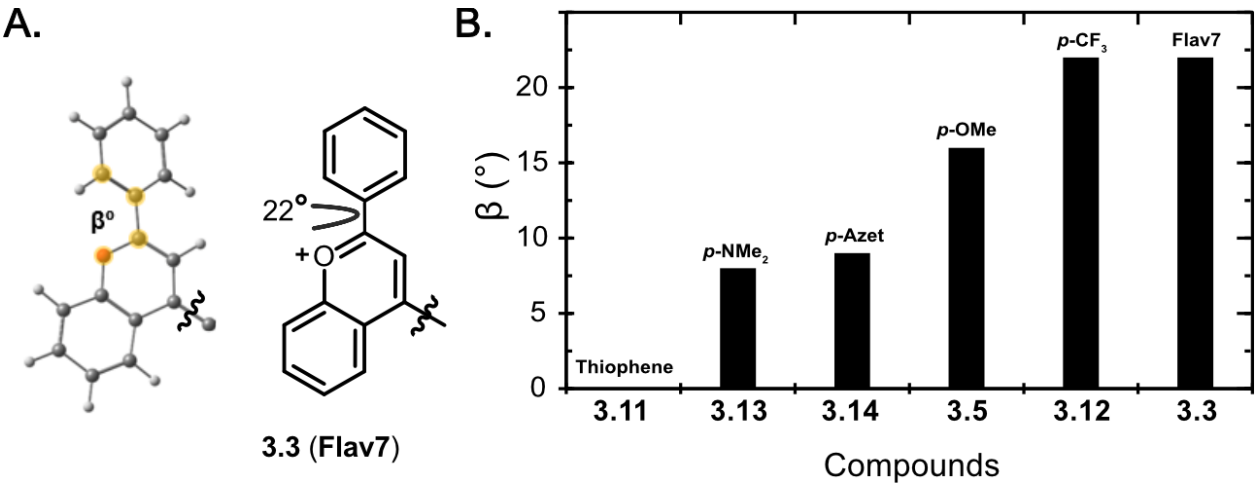

Figure 3.5. **A**. Global minimum geometry of **3.3** (**Flav7**) and calculated β° at the 2-position. **B**. Plotted β° for selected Flav7 derivatives.

3.3.7 Investigating Electronic Effects

With preliminary insight on how stereoelectronic effects on planarity and sp^2 C-H bond removal both impact λ_{max} and Φ_F we at last turned to probing electronic effects. With dyes **3.4**–**3.15** in hand, we were eager to conduct Hammett studies[37] against measured photophysical parameters to elucidate design trends, a strategy that has been fruitful for our past derivatives. Since these dyes had similar Stokes shifts and ε_{max}, we homed in on $\lambda_{max,abs}$ and Φ_F as key photophysical parameters in these studies (Figure 3.6). First, we performed a direct 2-position analysis by correlating the aforementioned photophysical parameters against Hammett values of the 2-position substituents. A lack of Hammett parameters for some substituents precluded a full 2-position analysis, but by including previously reported dyes (**3.1** and **3.2**), we were still able to compare 6 substituents (Figure 3.6A). We found strong correlations with *meta*-position Hammet values (σ_m). First, we saw a positive correlation between λ_{max} and σ_m (Figure 3.6B). The more the 2-position group pulled electron density from the flavylium core, the more red-shifted the λ_{max} became. Next, we saw a negative correlation between Φ_F and σ_m, potentially due to energy gap effects (Figure 3.6C).

As a majority of derivatives had *para*-substituted phenyl groups, or functionality at the 4" position, we were interested in conducting a similar investigation using *para*-position Hammett values (σ_p). This grouping compared 7- substituents and we had similar results to the 2-position analysis (Figure 3.6D). Again, increased electron-withdrawing character invoked red-shifted λ_{max} but this time outliers were present. The electron-donating amines (**3.13**, **3.15**) demonstrated a significant red-shift, rivaling the *p*-CF_3 dye, **3.12**. For quantum yield we saw a negative correlation between σ_p and Φ_F but again the amines clustered against this trend (Figure 3.6E). Based on computation and informed by reduced β angles, we can rationalize the amines acting as outliers as

they feel stronger effects of conjugation than other *p*-substituted derivatives. Overall, it was gratifying to find good correlations with Hammett parameters and Φ_F/λ_{max}.

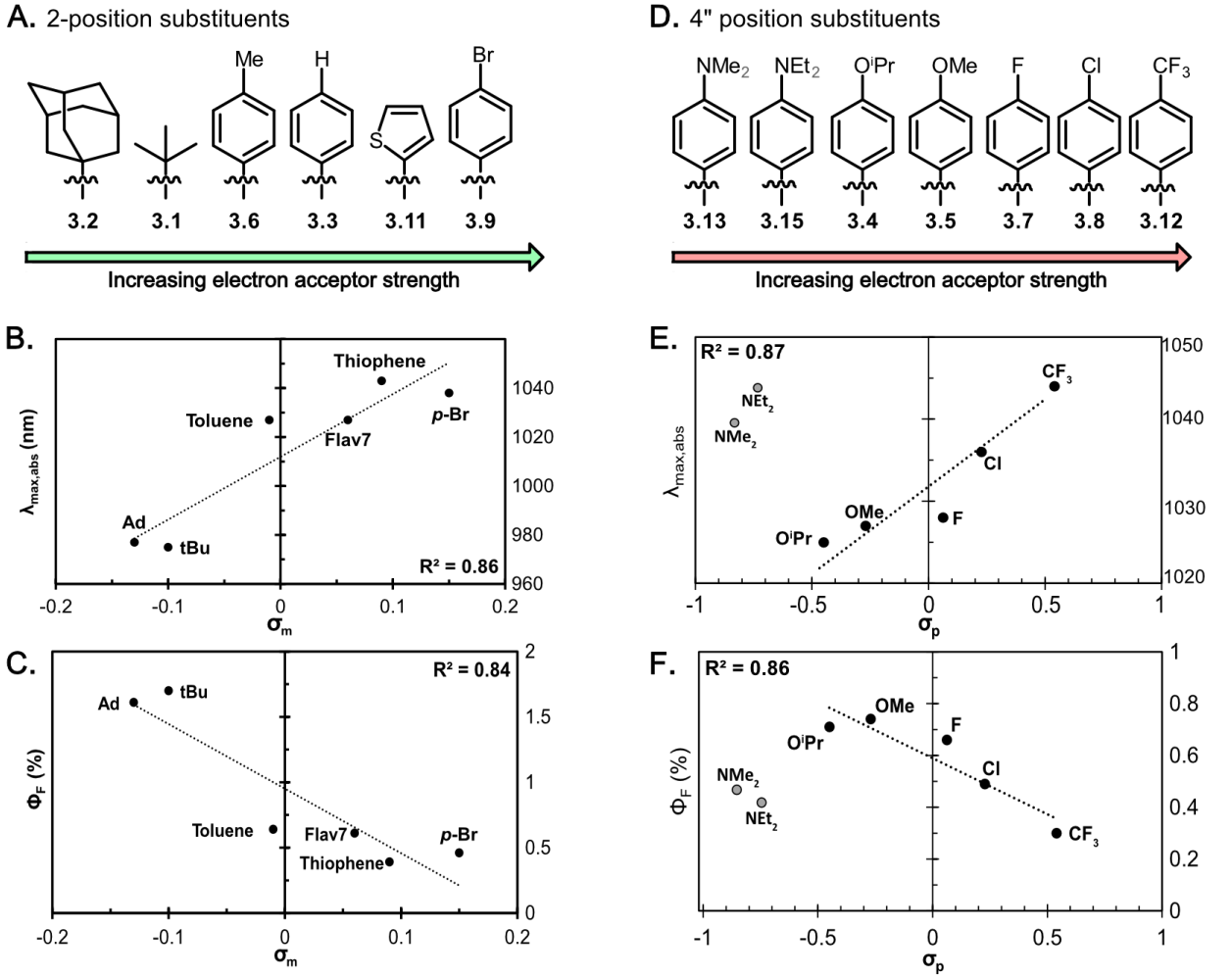

Figure 3.6. Hammett studies for dyes **3.1**–**3.15**. 2-position (**A**) and 4" (**D**) derivatives organized by reported Hammet values. Hammet correlations between $\lambda_{max,abs}$ and either σ_m (**B**) or σ_p (**E**). Hammett correlations between and either σ_m (**C**) or σ_p (**F**). *p*-amines (**3.13** and **3.15** in gray) not used in R^2 calculations. (see discussion).

To conclude our Hammet studies, we then compared computed ξ values of our 2-position derivatives using **3.3** (Flav7) as the reference dye. With a new parameter, we sought to correlate ξ with electronics, sterics, or conjugation parameters. Interestingly, we saw strong correlations with σ_m and ξ at the 2-position, as well as σ_p and ξ at the 4" position (Figure 3.7A/B). While these

studies provide useful information for red-shifting, we also gained insight on which substituents improve quantum yield.

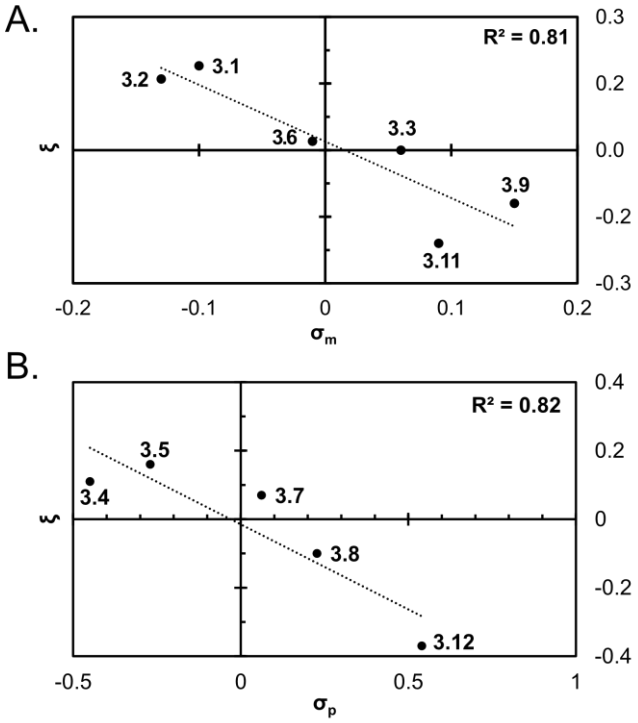

Figure 3.7. Hammett correlation between energy gap improvement factor ξ and σ_m (**A**) or σ_p (**B**).

3.4 Conclusions

Previous work led to interest in the 2-position of the flavylium scaffold, where we had observed Φ_F to dramatically increase (up to 3-fold). This observation sparked a systematic investigation of how the various molecular properties of 2-position substituents influence photophysical performance. In this study, we synthesized a panel of electronically and sterically varied 2-position chromenylium derivatives and characterized their photophysical properties. The effects of steric bulk were largely inconclusive but exploring other effects was more fruitful. Analyzing Flav7 derivatives synthesized by the Caram and Stacko group showed that C-H bond reduction of the 2-position phenyl ring could slightly improve Φ_F but nothing to the likes seen with

3.1 and **3.2**. When we turned to computation, we found that substituents with increased β angles generally had red-shifted λ_{max}, consistent with literature precedent. Finally, we found that certain 2-position modifications and certain *p*-substituents could improve Φ_F and for the first time we observed 2-position substituents invoking red-shifts in $\lambda_{max,abs}$, up to 32 nm.

3.5 Experimental Procedures

3.5.1 Abbreviations, Materials, and Instrumentation

Abbreviations. DCM = dichloromethane; DMSO =dimethylsulfoxide; EtOH = ethanol; EtOAc = ethyl acetate; MeOH = methanol; TFA = trifluoroacetic acid; DMF = dimethylformamide; THF = tetrahydrofuran; MeCN = acetonitrile; Ac_2O = acetic anhydride; PBS = phosphate buffered saline; HBF_4 = fluoroboric acid; $NaClO_4$ = sodium perchlorate; MeMgBr = methyl magnesium bromide; $POCl_3$ = phosphoryl chloride; *t*Bu = *tert*-butyl; Ph = phenyl; NaOAc = sodium acetate; OMe = methoxy; CF_3 = trifluoromethyl; ^{i}PrO = isopropyl ether; Azet = azetidine; m.b. = molecular brightness; TICT = twisted intermolecular charge transfer; rt = room temperature; h = hour; min = minutes; NMR = nuclear magnetic resonance; HRMS = high resolution mass spectrometry; DLS = dynamic light scattering; NIR = near-infrared; SWIR = shortwave infrared;

Materials. Reagents were purchased from Acros Organics, Alfa Aesar, Fisher Scientific, Sigma-Aldrich, or TCI and used without additional purification. Anhydrous and deoxygenated solvents (toluene, THF, DMF) were dispensed from a Grubb's-type Phoenix Solvent Drying System constructed by the late JC Meyer. Oxygen was removed from solvents by three consecutive

freeze–pump–thaw cycles in air-free glassware directly before use. For every reaction, dry Schlenk technique was used.

Instrumentation. Thin layer chromatography was performed using Silica Gel 60 F254 (EMD Millipore) plates. Flash chromatography was executed with technical grade silica gel with 60 Å pores and 40–63 μm mesh particle size (Sorbtech Technologies). Solvent was removed with a Büchi Rotovapor and further dried with a Welch DuoSeal pump. Masses for analytical measurements were taken on a Sartorius MSE6.6S-000-DM S13 Cubis Micro Balance. Bath sonication was performed using a Branson 3800 ultrasonic cleaner. Nuclear magnetic resonance (^{1}H NMR) spectra were taken on Bruker AV-400, or AV-500 instruments and processed with MestReNova or TopSpin software. All ^{1}H NMR peaks are reported in ppm in reference to their respective solvent signals (CD_3CN $\delta H=1.94$; MeOD $\delta H=3.31$, $\delta C=49.00$; CD_2Cl_2 $\delta H=5.32$, $\delta C=53.84$; $(CD_3)_2SO$ $\delta H=2.50$).

3.5.2 Computational Data

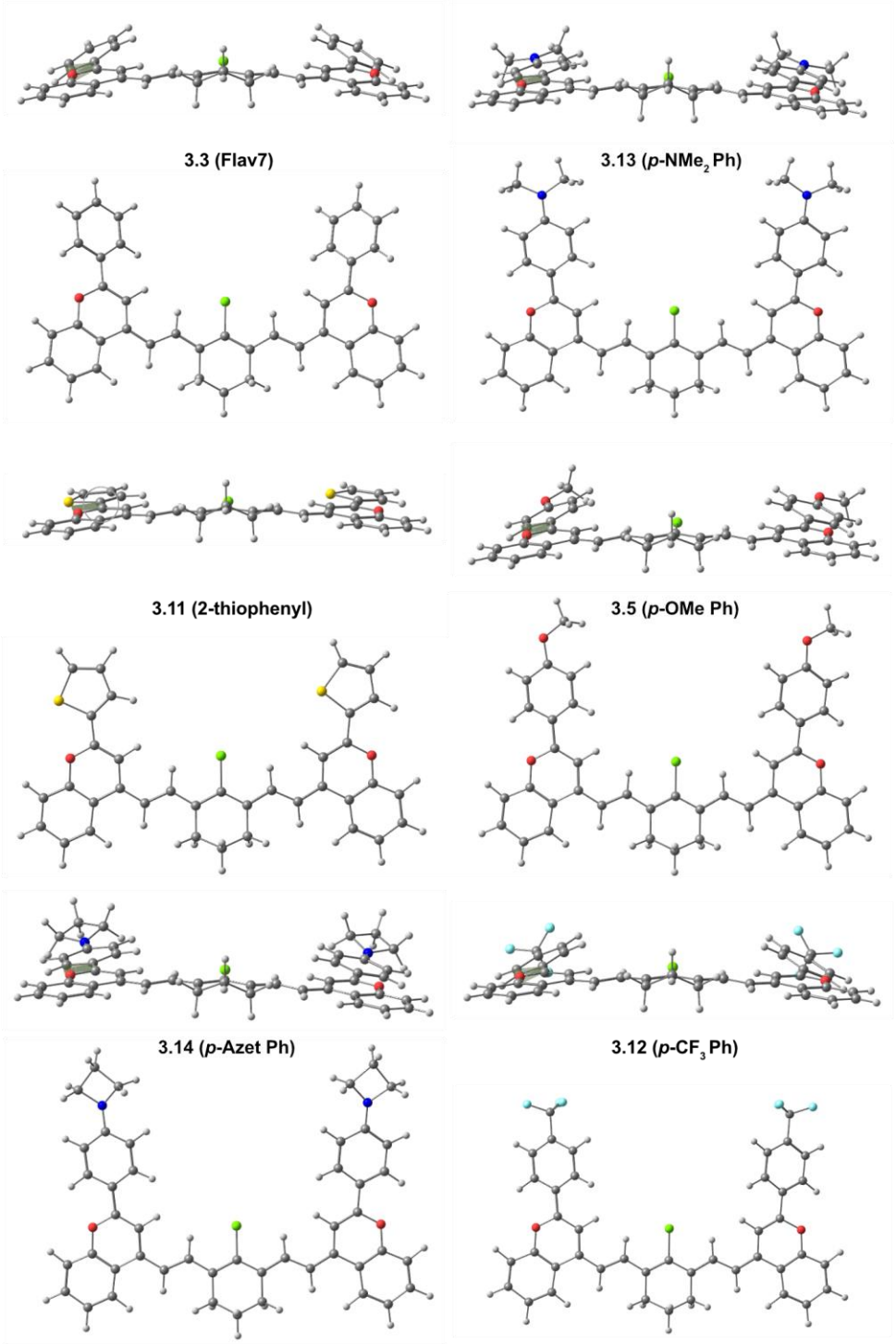

Global minimum geometries for dyes **3.3**, **3.5**, **3.11**, **3.12**, **3.13**, **3.14** optimized at pbe0/6-31G(d,p) level of theory with Solvent = DCM, IEFPCM). Computation performed by Iain Kimpton.

3.5.3 Synthetic Procedures

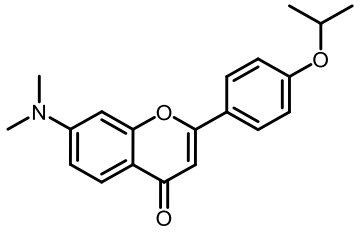

7-(dimethylamino)-2-(4-isopropoxyphenyl)-4*H*-chromen-4-one (3.18a): Ethyl 3-(4-isopropoxyphenyl)-3-oxopropanoate **3.17a** (515 mg, 2.06 mmol, 2 equiv.), and 3-(dimethylamino)phenol (141 mg, 1.03 mmol, 1 equiv.) were placed in a microwave tube and heated in a microwave at 300 W, at 240 °C for 3 minutes. The solution was cooled to rt and evaporated onto silica gel. The crude product was purified via column chromatography, eluting with a 20:1 Hexanes/EtOAc gradient to yield a yellow solid (141 mg, 0.17 mmol, 42% yield). R_f = 0.2 in 1:1 Hexanes/EtOAc. ^{1}H NMR (500 MHz, Chloroform-*d*) δ 8.03 (d, *J* = 9.0 Hz, 1H), 7.83 (d, *J* = 9.0 Hz, 2H), 6.97 (d, *J* = 8.9 Hz, 2H), 6.77 (d, *J* = 9.0 Hz, 1H), 6.63 (s, 1H), 6.58 (d, *J* = 2.4 Hz, 1H), 4.64 (p, *J* = 6.0 Hz, 1H), 3.11 (s, 6H), 1.38 (d, *J* = 6.0 Hz, 6H). HRMS (ESI$^+$) calcd for $C_{20}H_{21}NO_3^+$ $[M+H]^+$: 324.1600; found 324.1610 Absorbance (CH_2Cl_2): 355 nm.

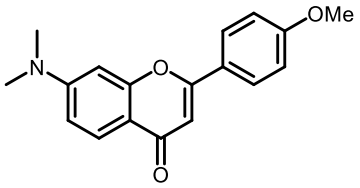

7-(dimethylamino)-2-(4-methoxyphenyl)-4*H*-chromen-4-one (3.18b): Ethyl 3-(4-methoxyphenyl)-3-oxopropanoate **3.17b** (160 mg, 0.72 mmol, 2 equiv.), and 3-(dimethylamino)phenol (49 mg, 0.36 mmol, 1.0 equiv.) were placed in a microwave tube and

heated in a microwave at 300 W, at 240 °C for 3 minutes. The solution was cooled to rt and evaporated onto silica gel. The crude product was purified via column chromatography, eluting with a 20:1 hexanes/EtOAc gradient to yield a yellow solid (25 mg, 0.084 mmol, 24% yield). R_f = 0.2 in 1:1 Hexanes/EtOAc. ^{1}H NMR (400 MHz, Chloroform-*d*) δ 8.03 (d, *J* = 9.0 Hz, 1H), 7.86 (d, *J* = 8.9 Hz, 2H), 7.00 (d, *J* = 8.9 Hz, 2H), 6.77 (dd, *J* = 9.0, 2.5 Hz, 1H), 6.65 (s, 1H), 6.58 (d, *J* = 2.4 Hz, 1H), 3.88 (s, 3H). HRMS (ESI$^+$) calcd for $C_{18}H_{17}NO_3^+$ [M+H]$^+$: 296.1287; found 296.1295 Absorbance (CH_2Cl_2): 360 nm.

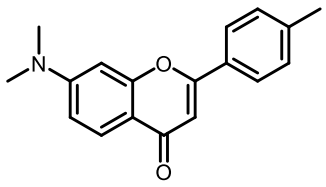

7-(dimethylamino)-2-(*p*-tolyl)-4*H*-chromen-4-one (3.18c): Ethyl 3-oxo-3-(*p*-tolyl)propanoate **3.17c** (150 mg, 0.73 mmol, 1.0 equiv.), and 3-(dimethylamino)phenol (98 mg, 0.73 mmol, 1.0 equiv.) were placed in a microwave tube and heated in a microwave at 300 W, at 240 °C for 3 minutes. The solution was cooled to rt and evaporated onto silica gel. The crude product was purified via column chromatography, eluting with a 20:1 hexanes/EtOAc gradient to yield a yellow solid (87 mg, 0.31 mmol, 43% yield). R_f = 0.3 in 1:1 Hexanes/EtOAc. ^{1}H NMR (400 MHz, Chloroform-*d*) δ 8.04 (d, *J* = 9.0 Hz, 1H), 7.80 (d, *J* = 8.3 Hz, 2H), 7.30 (d, *J* = 8.0 Hz, 2H), 7.26 (s, 1H), 6.77 (dd, *J* = 9.0, 2.5 Hz, 1H), 6.67 (s, 1H), 6.59 (d, *J* = 2.4 Hz, 1H), 3.11 (s, 6H), 2.43 (s, 3H). HRMS (ESI$^+$) calcd for $C_{18}H_{17}NO_2^+$ [M+H]$^+$: 280.1338; found 280.1347 Absorbance (CH_2Cl_2): 359 nm.

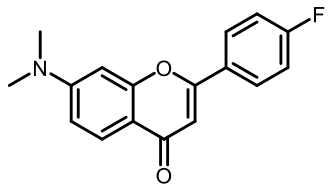

7-(dimethylamino)-2-(4-fluorophenyl)-4*H*-chromen-4-one (3.18d): Ethyl 3-(4-fluorophenyl)-3-oxopropanoate **3.17d** (140 mg, 0.66 mmol, 1.8 equiv.), and 3-(dimethylamino)phenol (50 mg, 0.36 mmol, 1.0 equiv.) were placed in a microwave tube and heated in a microwave at 300 W, at 240 °C for 3 minutes. The solution was cooled to rt and evaporated onto silica gel. The crude product was purified via column chromatography, eluting with a 20:1 hexanes/EtOAc gradient to yield a yellow solid (56 mg, 0.196 mmol, 54% yield). R_f = 0.3 in 1:1 Hexanes/EtOAc. ^{1}H NMR (500 MHz, Chloroform-*d*) δ 8.03 (d, *J* = 9.0 Hz, 1H), 7.92 – 7.87 (m, 2H), 7.18 (dd, *J* = 9.0, 8.3 Hz, 2H), 6.77 (d, *J* = 9.0 Hz, 1H), 6.63 (s, 1H), 6.58 (d, *J* = 2.4 Hz, 1H), 3.11 (s, 6H). HRMS (ESI$^+$) calcd for $C_{17}H_{14}FNO_2^+$ $[M+H]^+$: 284.1087; found 282.1290 Absorbance (CH_2Cl_2): 361 nm.

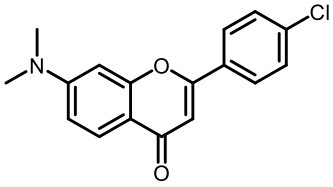

2-(4-chlorophenyl)-7-(dimethylamino)-4*H*-chromen-4-one (3.18e): Ethyl 3-(4-chlorophenyl)-3-oxopropanoate **3.17e** (290 mg, 1.3 mmol, 1.8 equiv.), and 3-(dimethylamino)phenol (99 mg, 0.73 mmol, 1.0 equiv.) were placed in a microwave tube and heated in a microwave at 300 W, at 240 °C for 3 minutes. The solution was cooled to rt and evaporated onto silica gel. The crude product was purified via column chromatography, eluting with a 20:1 hexanes/EtOAc gradient to yield a yellow solid (89 mg, 0.29 mmol, 40% yield). R_f = 0.3 in 1:1 Hexanes/EtOAc. ^{1}H NMR

(500 MHz, Chloroform-*d*) δ 8.03 (d, *J* = 9.0 Hz, 1H), 7.83 (d, *J* = 8.8 Hz, 2H), 7.47 (d, *J* = 8.8 Hz, 2H), 6.78 (dd, *J* = 9.0, 2.5 Hz, 1H), 6.66 (s, 1H), 6.58 (d, *J* = 2.4 Hz, 1H), 3.11 (s, 6H). Absorbance (CH_2Cl_2): 365 nm.

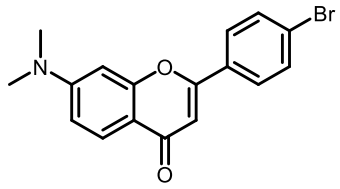

2-(4-bromophenyl)-7-(dimethylamino)-4*H*-chromen-4-one (3.18f): Ethyl 3-(4-bromophenyl)-3-oxopropanoate **3.17f** (180 mg, 0.66 mmol, 1.8 equiv.), and 3-(dimethylamino)phenol (52 mg, 0.36 mmol, 1.0 equiv.) were placed in a microwave tube and heated in a microwave at 300 W, at 240 °C for 3 minutes. The solution was cooled to rt and evaporated onto silica gel. The crude product was purified via column chromatography, eluting with a 20:1 hexanes/EtOAc gradient to yield a yellow solid (59 mg, 0.17 mmol, 47% yield). R_f = 0.3 in 1:1 Hexanes/EtOAc. ^{1}H NMR (500 MHz, Chloroform-*d*) δ 8.03 (d, *J* = 9.0 Hz, 1H), 7.76 (d, *J* = 8.7 Hz, 2H), 7.63 (d, *J* = 8.8 Hz, 2H), 6.78 (dd, *J* = 9.0, 2.4 Hz, 1H), 6.67 (s, 1H), 6.57 (s, 1H), 3.11 (s, 6H). HRMS (ESI^+) calcd for $C_{17}H_{14}BrNO_2^+$ $[M+H]^+$: 344.0286; found 344.0273. Absorbance (CH_2Cl_2): 364 nm.

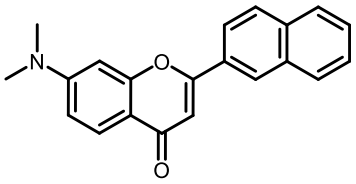

7-(dimethylamino)-2-(naphthalen-2-yl)-4*H*-chromen-4-one (3.18g): Ethyl 3-(naphthalen-2-yl)-3-oxopropanoate **3.17g** (240 mg, 0.99 mmol, 2 equiv.), and 3-(dimethylamino)phenol (68 mg,

0.49 mmol, 1.0 equiv.) were placed in a microwave tube and heated in a microwave at 300 W, at 240 °C for 3 minutes. The solution was cooled to rt and evaporated onto silica gel. The crude product was purified via column chromatography, eluting with a 20:1 hexanes/EtOAc gradient to yield a yellow solid (70 mg, 0.220 mmol, 45% yield). ^{1}H NMR (400 MHz, Chloroform-*d*) δ 8.47 (s, 1H), 8.06 (s, 1H), 8.00 – 7.86 (m, 4H), 7.61 – 7.54 (m, 2H), 6.84 (s, 1H), 6.80 (dd, *J* = 9.0, 2.4 Hz, 1H), 6.68 (d, *J* = 2.4 Hz, 1H), 3.14 (s, 6H).

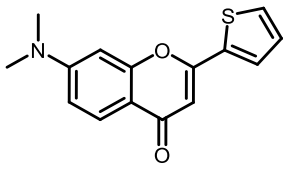

7-(dimethylamino)-2-(thiophen-2-yl)-4*H*-chromen-4-one (3.18h): Ethyl 3-oxo-3-(thiophen-2-yl)propanoate **3.17h** (108 mg, 1.6 mmol, 2 equiv.), and 3-(dimethylamino)phenol (50 mg, 0.77 mmol, 1.0 equiv.) were placed in a microwave tube and heated in a microwave at 300 W, at 240 °C for 3 minutes. The solution was cooled to rt and evaporated onto silica gel. The crude product was purified via column chromatography, eluting with a 20:1 hexanes/EtOAc gradient to yield a yellow solid (62 mg, 0.23 mmol, 63% yield). R_f = 0.3 in 1:1 Hexanes/EtOAc. ^{1}H NMR (400 MHz, Chloroform-*d*) δ 8.00 (s, 1H), 7.66 (s, 1H), 7.51 (s, 1H), 7.16 (s, 1H), 6.76 (s, 1H), 6.58 (s, 2H), 3.10 (s, 6H). HRMS (ESI$^+$) calcd for $C_{15}H_{13}NO_2S^+$ $[M+H]^+$: 272.0745; found 272.0745 Absorbance (CH_2Cl_2): 367 nm.

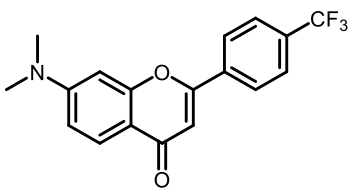

7-(dimethylamino)-2-(4-(trifluoromethyl)phenyl)-4*H*-chromen-4-one (3.18i): Ethyl 3-oxo-3-(4-(trifluoromethyl)phenyl)propanoate **3.17i** (160 mg, 0.63 mmol, 1.8 equiv.), and 3-(dimethylamino)phenol (49 mg, 0.36 mmol, 1.0 equiv.) were placed in a microwave tube and heated in a microwave at 300 W, at 240 °C for 3 minutes. The solution was cooled to rt and evaporated onto silica gel. The crude product was purified via column chromatography, eluting with a 20:1 hexanes/EtOAc gradient to yield a yellow solid (55 mg, 0.17 mmol, 46 % yield). R_f = 0.4 in 1:1 Hexanes/EtOAc. ^{1}H NMR (500 MHz, Chloroform-*d*) δ 8.08 (d, *J* = 9.0 Hz, 1H), 8.05 (d, *J* = 8.8 Hz, 2H), 7.77 (d, *J* = 8.3 Hz, 2H), 6.99 (s, 1H), 6.86 (dd, *J* = 9.0, 2.4 Hz, 1H), 6.67 (d, *J* = 2.4 Hz, 1H), 3.16 (s, 6H). Absorbance (CH_2Cl_2): 372 nm.

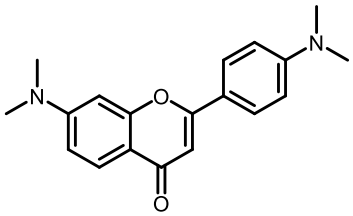

7-(dimethylamino)-2-(4-(dimethylamino)phenyl)-4*H*-chromen-4-one (3.18j): Ethyl 3-(4-(dimethylamino)phenyl)-3-oxopropanoate **3.17j** (89 mg, 0.38 mmol, 1.5 equiv.), and 3-(dimethylamino)phenol (35 mg, 0.25 mmol, 1.0 equiv.) were placed in a microwave tube and heated in a microwave at 300 W, at 240 °C for 3 minutes. The solution was cooled to rt and evaporated onto silica gel. The crude product was purified via column chromatography, eluting with a 20:1 Hexanes/EtOAc gradient to yield a yellow solid (27 mg, 0.087 mmol, 35% yield). R_f = 0.4 in 1:1 Hexanes/EtOAc. ^{1}H NMR (400 MHz, Chloroform-*d*) δ 8.03 (d, *J* = 8.9 Hz, 1H), 7.80 (d, *J* = 9.0 Hz, 2H), 6.75 (d, *J* = 9.0 Hz, 3H), 6.59 (d, *J* = 3.8 Hz, 2H), 3.10 (s, 6H), 3.06 (s, 6H). Absorbance (CH_2Cl_2): 358 nm.

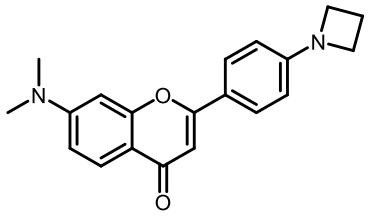

2-(4-(azetidin-1-yl)phenyl)-7-(dimethylamino)-4*H*-chromen-4-one (3.18k): **3.18f** (300 mg, 0.87 mmol, 1.0 equiv.), azetidine (0.29 mL, 4.4 mmol, 5 equiv.), RuPhos-Pd-G3 (74 mg, 0.086 mmol, 0.1 equiv.) RuPhos (41 mg, 0.088 mmol, 0.1 equiv.), and cesium carbonate (1.4 g, 4.2 mmol, 4.8 equiv.) were dissolved in dioxane (7 mL) in a 20 mL scintillation vial and heated to 100 °C for 24 h under an N_2 atmosphere. The solution was cooled to rt and evaporated onto silica gel. The crude product was purified via column chromatography, eluting with a 6:1, 4:1, 2:1, 1:1 hexanes/EtOAc solvent gradient. The product was then rinsed with hexanes. This procedure gave a yellow solid (190 mg, 0.59 mmol, 68%). ^{1}H NMR (400 MHz, Chloroform-*d*) δ 8.03 (d, *J* = 9.0 Hz, 1H), 7.77 (d, *J* = 8.9 Hz, 2H), 6.76 (dd, *J* = 9.0, 2.5 Hz, 1H), 6.58 (d, *J* = 2.7 Hz, 2H), 6.46 (d, *J* = 8.9 Hz, 2H), 3.99 (t, *J* = 7.3 Hz, 4H), 3.10 (s, 6H), 2.43 (p, *J* = 7.4 Hz, 2H). HRMS (ESI^+) calcd for $C_{20}H_{20}N_2O_2^+$ $[M+H]^+$: 321.1603; found 321.1608. Absorbance (CH_2Cl_2): 377 nm.

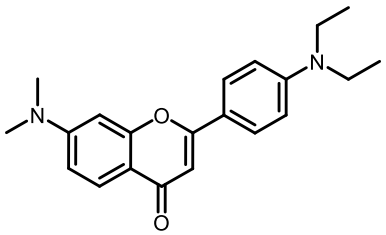

2-(4-(diethylamino)phenyl)-7-(dimethylamino)-4*H*-chromen-4-one (3.18l): Ethyl 3-(4-(diethylamino)phenyl)-3-oxopropanoate **3.17l** (150 mg, 0.58 mmol, 2 equiv.), and 3-

(dimethylamino)phenol (40 mg, 0.29 mmol, 1.0 equiv.) were placed in a microwave tube and heated in a microwave at 300 W, at 240 °C for 3 minutes. The solution was cooled to rt and evaporated onto silica gel. The crude product was purified via column chromatography, eluting with a 20:1 hexanes/EtOAc gradient to yield a yellow solid (48 mg, 0.14 mmol, 49% yield). R_f = 0.2 in 1:1 Hexanes/EtOAc. ^{1}H NMR (500 MHz, Chloroform-*d*) δ 8.03 (d, *J* = 9.0 Hz, 1H), 7.77 (d, *J* = 9.1 Hz, 2H), 6.74 (dd, *J* = 9.0, 2.4 Hz, 1H), 6.71 (d, *J* = 9.1 Hz, 2H), 6.58 (d, *J* = 2.4 Hz, 1H), 6.56 (s, 1H), 3.43 (q, *J* = 7.1 Hz, 4H), 3.10 (s, 6H), 1.21 (t, *J* = 7.1 Hz, 7H). HRMS (ESI^+) calcd for $C_{21}H_{24}N_2O_2^+$ $[M+H]^+$: 337.1916 found 337.1921. Absorbance (CH_2Cl_2): 389 nm.

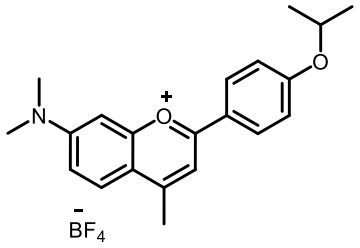

7-(dimethylamino)-2-(4-isopropoxyphenyl)-4-methylchromenylium tetrafluoroborate (3.19a). Flavone **3.18a** (170 mg, 0.51 mmol, 1.0 equiv.) was dissolved in THF (3.3 mL) in a double-neck round bottom flask and cooled to 0 °C. Methylmagnesium bromide was added dropwise (1.5 mL, 1.0 M in THF, 3 equiv.) and the solution was warmed to rt and stirred for 24 h. The reaction was quenched by dropwise addition of 5% HBF_4 on ice, extracted with dichloromethane, dried with Na_2SO_4, filtered, and evaporated. The crude product was triturated with ice cold ethyl acetate and vacuum filtered to produce a purple solid (140 mg, 0.34 mmol, 67% yield).R_f = 0.4 in 9:1 DCM/EtOH. ^{1}H NMR (500 MHz, Acetonitrile-d_3) δ 8.10 (d, *J* = 9.1 Hz, 2H), 7.92 (d, *J* = 9.5 Hz, 1H), 7.59 (s, 1H), 7.22 (dd, *J* = 9.5, 2.6 Hz, 1H), 7.09 (d, *J* = 9.1 Hz, 2H), 6.96 (d, *J* = 2.6 Hz, 1H), 4.78 (p, *J* = 6.1 Hz, 1H), 3.22 (s, 6H), 2.73 (s, 3H), 1.36 (d, *J* = 6.1 Hz, 6H).

HRMS (ESI$^+$) Calculated for $C_{21}H_{24}NO_2^+$ [M]$^+$: 322.1802; found: 332.1819. Absorbance (CH_2Cl_2): 530 nm.

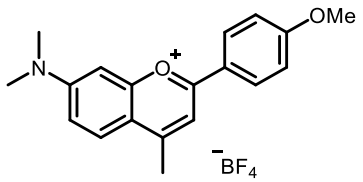

7-(dimethylamino)-2-(4-methoxyphenyl)-4-methylchromenylium tetrafluoroborate (3.19b): Flavone **3.18b** (25 mg, 0.084 mmol, 1.0 equiv.) was dissolved in THF (0.82 mL) in a double-neck round bottom flask and cooled to 0 °C. Methylmagnesium bromide was added dropwise (0.21 mL, 1.0 M in THF, 2.5 equiv.) and the solution was warmed to rt and stirred for 24 h. The reaction was quenched by dropwise addition of 5% HBF_4 on ice, extracted with dichloromethane, dried with Na_2SO_4, filtered, and evaporated. The crude product was triturated with ice cold ethyl acetate and vacuum filtered to produce a purple solid (21 mg, 0.055 mmol, 65% yield). R_f = 0.3 in 9:1 DCM/EtOH. ^{1}H NMR (500 MHz, Acetonitrile-d_3) δ 8.22 (d, J = 9.0 Hz, 2H), 8.02 (d, J = 9.6 Hz, 1H), 7.70 (s, 1H), 7.32 (dd, J = 9.6, 2.5 Hz, 1H), 7.19 (d, J = 9.0 Hz, 2H), 7.08 (d, J = 2.6 Hz, 1H), 3.93 (s, 3H), 3.28 (s, 6H), 2.79 (s, 3H). HRMS (ESI$^+$) Calculated for $C_{19}H_{20}NO_2^+$ [M]$^+$: 294.1489; found: 294.1488. Absorbance (CH_2Cl_2): 526 nm.

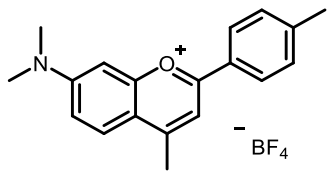

7-(dimethylamino)-4-methyl-2-(*p*-tolyl)chromenylium tetrafluoroborate (3.19c): Flavone **3.18c** (87 mg, 0.33 mmol, 1.0 equiv.) was dissolved in THF (3.1 mL) in a double-neck round

bottom flask and cooled to 0 °C. Methylmagnesium bromide was added dropwise (0.78 mL, 1.0 M in THF, 2.5 equiv.) and the solution was warmed to rt and stirred for 24 h. The reaction was quenched by dropwise addition of 5% HBF_4 on ice, extracted with dichloromethane, dried with Na_2SO_4, filtered, and evaporated. The crude product was triturated with ice cold ethyl acetate and vacuum filtered to produce a purple solid (77 mg, 0.21 mmol, 67% yield). R_f = 0.4 in 9:1 DCM/EtOH. ^{1}H NMR (400 MHz, Acetonitrile-d_3) δ 8.15 – 8.09 (m, 2H), 8.04 (d, J = 9.6 Hz, 1H), 7.75 (s, 1H), 7.48 (d, J = 8.0 Hz, 2H), 7.35 (dd, J = 9.6, 2.6 Hz, 1H), 7.09 (d, J = 2.5 Hz, 1H), 3.29 (s, 6H), 2.81 (s, 3H), 2.46 (s, 3H). HRMS (ESI$^+$) Calculated for $C_{19}H_{20}NO^+$ [M]$^+$: 278.1539; found: 278.1553. Absorbance (CH_2Cl_2): 512 nm.

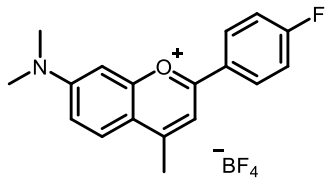

7-(dimethylamino)-2-(4-fluorophenyl)-4-methylchromenylium tetrafluoroborate (3.19d): Flavone **3.18d** (80 mg, 0.28 mmol, 1.0 equiv.) was dissolved in THF (2.8 mL) in a double-neck round bottom flask and cooled to 0 °C. Methylmagnesium bromide was added dropwise (0.71 mL, 1.0 M in THF, 2.5 equiv.) and the solution was warmed to rt and stirred for 24 h. The reaction was quenched by dropwise addition of 5% HBF_4 on ice, extracted with dichloromethane, dried with Na_2SO_4, filtered, and evaporated. The crude product was triturated with ice cold ethyl acetate and vacuum filtered to produce a purple solid (82 mg, 0.22 mmol, 77% yield). R_f = 0.3 in 9:1 DCM/EtOH. ^{1}H NMR (500 MHz, Acetonitrile-d_3) δ 8.28 (dd, J = 9.1, 5.2 Hz, 2H), 8.07 (d, J = 9.6 Hz, 1H), 7.75 (s, 1H), 7.43 (dd, J = 9.1, 8.6 Hz, 2H), 7.39 (dd, J = 9.7, 2.5 Hz, 1H), 7.11 (d, J =

2.6 Hz, 1H), 3.32 (s, 6H), 2.83 (s, 3H). HRMS (ESI$^+$) Calculated for $C_{18}H_{17}FNO^+$ [M]$^+$: 282.1289; found: 282.1290. Absorbance (CH_2Cl_2): 515 nm.

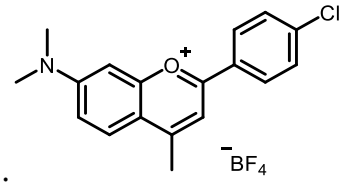

2-(4-chlorophenyl)-7-(dimethylamino)-4-methylchromenylium tetrafluoroborate (3.19e): Flavone **3.18e** (95 mg, 0.32 mmol, 1.0 equiv.) was dissolved in THF (3.1 mL) in a double-neck round bottom flask and cooled to 0 °C. Methylmagnesium bromide was added dropwise (0.79 mL, 1.0 M in THF, 2.5 equiv.) and the solution was warmed to rt and stirred for 24 h. The reaction was quenched by dropwise addition of 5% HBF_4 on ice, extracted with dichloromethane, dried with Na_2SO_4, filtered, and evaporated. The crude product was triturated with ice cold ethyl acetate and vacuum filtered to produce a purple solid (94 mg, 0.24 mmol, 78% yield). R_f = 0.4 in 9:1 DCM/EtOH. ^{1}H NMR (500 MHz, Acetonitrile-d_3) δ 8.19 (d, J = 8.7 Hz, 2H), 8.07 (d, J = 9.6 Hz, 1H), 7.77 (s, 1H), 7.69 (d, J = 8.7 Hz, 2H), 7.40 (dd, J = 9.7, 2.6 Hz, 1H), 7.11 (d, J = 2.6 Hz, 1H), 3.32 (s, 6H), 2.83 (s, 3H). HRMS (ESI$^+$) Calculated for $C_{18}H_{17}ClNO_2^+$ [M]$^+$: 298.0993; found: 298.0998. Absorbance (CH_2Cl_2): 538 nm.

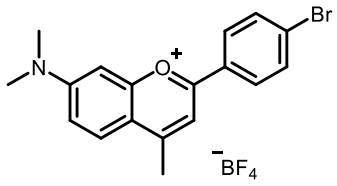

2-(4-bromophenyl)-7-(dimethylamino)-4-methylchromenylium tetrafluoroborate (3.19f): Flavone **3.18f** (117 mg, 0.340 mmol, 1.0 equiv.) was dissolved in THF (3.3 mL) in a double-neck

round bottom flask and cooled to 0 °C. Methylmagnesium bromide was added dropwise (0.85 mL, 1.0 M in THF, 2.5 equiv.) and the solution was warmed to rt and stirred for 24 h. The reaction was quenched by dropwise addition of 5% HBF_4 on ice, extracted with dichloromethane, dried with Na_2SO_4, filtered, and evaporated. The crude product was triturated with ice cold ethyl acetate and vacuum filtered to produce a purple solid (110 mg, 0.26 mmol, 75% yield). R_f = 0.4 in 9:1 DCM/EtOH. ^{1}H NMR (500 MHz, Acetonitrile-d_3) δ 8.11 (d, *J* = 8.8 Hz, 2H), 8.07 (d, *J* = 9.7 Hz, 1H), 7.86 (d, *J* = 8.8 Hz, 2H), 7.77 (d, *J* = 0.5 Hz, 1H), 7.40 (dd, *J* = 9.6, 2.6 Hz, 1H), 7.11 (d, *J* = 2.5 Hz, 1H), 3.32 (s, 6H), 2.83 (s, 3H). ^{13}C NMR (126 MHz, Acetonitrile-d_3) δ 163.93, 163.82, 158.91, 158.20, 132.98, 129.07, 128.95, 128.66, 128.53, 118.37, 118.24, 112.08, 95.95, 40.53, 19.18. HRMS (ESI^+) Calculated for $C_{18}H_{17}BrNO^+$ $[M+2]^+$: 344.0468; found: 344.0487. Absorbance (CH_2Cl_2): 522 nm.

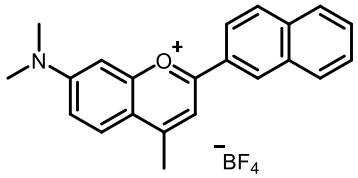

7-(dimethylamino)-4-methyl-2-(naphthalen-2-yl)chromenylium tetrafluoroborate (**3.19g**): Flavone **3.18g** (204 mg, 0.67 mmol, 1.0 equiv.) was dissolved in THF (4.2 mL) in a double-neck round bottom flask and cooled to 0 °C. Methylmagnesium bromide was added dropwise (1.9 mL, 1.0 M in THF, 3 equiv.) and the solution was warmed to rt and stirred for 24 h. The reaction was quenched by dropwise addition of 5% HBF_4 on ice, extracted with dichloromethane, dried with Na_2SO_4, filtered, and evaporated. The crude product was triturated with ice cold ethyl acetate and vacuum filtered to produce a purple solid (98 mg, 0.24 mmol, 38% yield). R_f = 0.3 in 9:1 DCM/EtOH. ^{1}H NMR (400 MHz, Acetonitrile-d_3) δ 8.82 (s, 1H), 8.19 – 8.12 (m, 1H), 8.08 (s,

2H), 7.99 (d, J = 6.9 Hz, 2H), 7.86 (s, 1H), 7.68 (dd, J = 10.8, 7.7 Hz, 3H), 7.33 (d, J = 2.8 Hz, 1H), 7.09 (s, 1H), 3.30 (s, 6H), 2.82 (s, 3H). HRMS (ESI^+) Calculated for $C_{22}H_{20}NO^+$ $[M]^+$: 314.1539; found: 314.1577. Absorbance (CH_2Cl_2): 523 nm.

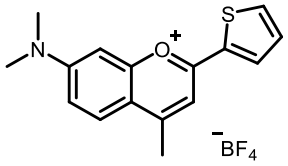

7-(dimethylamino)-4-methyl-2-(thiophen-2-yl)chromenyliumtetrafluoroborate (**3.19h**): Flavone **3.18h** (70 mg, 0.26 mmol, 1.0 equiv.) was dissolved in THF (1.5 mL) in a double-neck round bottom flask and cooled to 0 °C. Methylmagnesium bromide was added dropwise (0.77 mL, 1.0 M in THF, 3 equiv.) and the solution was warmed to rt and stirred for 24 h. The reaction was quenched by dropwise addition of 5% HBF_4 on ice, extracted with dichloromethane, dried with Na_2SO_4, filtered, and evaporated. The crude product was triturated with ice cold ethyl acetate and vacuum filtered to produce a purple solid (59 mg, 0.17 mmol, 64% yield). R_f = 0.2 in 9:1 DCM/EtOH. ^1H NMR (400 MHz, Acetonitrile-d_3) δ 8.14 (d, J = 1.2 Hz, 1H), 8.03 (d, J = 1.1 Hz, 1H), 8.02 (s, 1H), 7.62 (s, 1H), 7.38 (s, 1H), 7.32 (s, 1H), 7.02 (s, 1H), 3.28 (s, 6H), 2.77 (s, 3H). HRMS (ESI^+) Calculated for $C_{16}H_{16}NOS^+$ $[M]^+$: 270.0947; found: 270.0956. Absorbance (CH_2Cl_2): 536 nm.

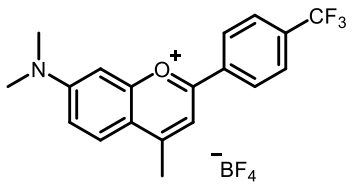

7-(dimethylamino)-4-methyl-2-(4-(trifluoromethyl)phenyl)chromenylium tetrafluoroborate (3.19i): Flavone **3.18i** (203 mg, 0.61 mmol, 1.0 equiv.) was dissolved in THF (5.9 mL) in a double-neck round bottom flask and cooled to 0 °C. Methylmagnesium bromide was added dropwise (1.5 mL, 1.0 M in THF, 2.5 equiv.) and the solution was warmed to rt and stirred for 24 h. The reaction was quenched by dropwise addition of 5% HBF_4 on ice, extracted with dichloromethane, dried with Na_2SO_4, filtered, and evaporated. The crude product was triturated with ice cold ethyl acetate and vacuum filtered to produce a purple solid (180 mg, 0.43 mmol, 70 % yield). R_f = 0.6 in 9:1 DCM/EtOH. ^{1}H NMR (500 MHz, Acetonitrile-d_3) δ 8.35 (d, *J* = 8.3 Hz, 2H), 8.09 (d, *J* = 9.7 Hz, 1H), 7.97 (d, *J* = 8.4 Hz, 2H), 7.83 (s, 1H), 7.42 (d, *J* = 7.1 Hz, 1H), 7.12 (d, *J* = 2.4 Hz, 1H), 3.33 (s, 6H), 2.84 (s, 4H). HRMS (ESI$^+$) Calculated for $C_{19}H_{17}F_3NO^+$ $[M]^+$: 332.1257; found: 332.1262. Absorbance (CH_2Cl_2): 518 nm.

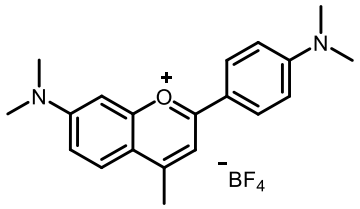

7-(dimethylamino)-2-(4-(dimethylamino)phenyl)-4-methylchromenylium tetrafluoroborate (3.19j): Flavone **3.18j** (21 mg, 0.068 mmol, 1.0 equiv.) was dissolved in THF (0.63 mL) in a double-neck round bottom flask and cooled to 0 °C. Methylmagnesium bromide was added dropwise (0.17 mL, 1.0 M in THF, 2.5 equiv.) and the solution was warmed to rt and stirred for 24 h. The reaction was quenched by dropwise addition of 5% HBF_4 on ice, extracted with dichloromethane, dried with Na_2SO_4, filtered, and evaporated. The crude product was triturated with ice cold ethyl acetate and vacuum filtered to produce a purple solid (16 mg, 0.041 mmol, 60%

yield). R_f = 0.5 in 9:1 DCM/EtOH. ^{1}H NMR (400 MHz, Acetonitrile-d_3) δ 8.11 (d, J = 9.4 Hz, 2H), 7.90 (d, J = 9.4 Hz, 1H), 7.56 (s, 1H), 7.17 (dd, J = 9.4, 2.6 Hz, 1H), 7.00 (d, J = 2.6 Hz, 1H), 6.90 (d, J = 9.4 Hz, 2H), 3.22 (s, 6H), 3.16 (s, 7H), 2.70 (s, 3H). HRMS (ESI$^+$) Calculated for $C_{20}H_{23}N_2O^+$ [M]$^+$: 307.1805; found: 307.1803. Absorbance (CH_2Cl_2): 586 nm.

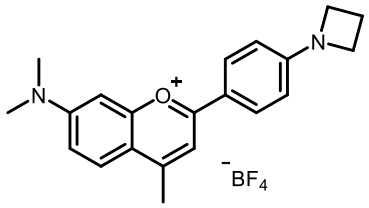

2-(4-(azetidin-1-yl)phenyl)-7-(dimethylamino)-4-methylchromenylium tetrafluoroborate (**3.19k**): Flavone **3.18k** (100 mg, 0.310 mmol, 1.0 equiv.) was dissolved in THF (1.8 mL) in a double-neck round bottom flask and cooled to 0 °C. Methylmagnesium bromide was added dropwise (0.94 mL, 1.0 M in THF, 3 equiv.) and the solution was warmed to rt and stirred for 24 h. The reaction was quenched by dropwise addition of 5% HBF_4 on ice, extracted with dichloromethane, dried with Na_2SO_4, filtered, and evaporated. The crude product was triturated with ice cold ethyl acetate and vacuum filtered to produce a purple solid (86 mg, 0.21 mmol, 68% yield). R_f = 0.3 in 9:1 DCM/EtOH. ^{1}H NMR (400 MHz, Acetonitrile-d_3) δ 8.06 (d, J = 9.1 Hz, 2H), 7.87 (d, J = 9.4 Hz, 1H), 7.51 (s, 1H), 7.14 (dd, J = 9.4, 2.6 Hz, 1H), 6.96 (d, J = 2.6 Hz, 1H), 6.51 (d, J = 9.1 Hz, 2H), 4.18 – 4.08 (m, 4H), 3.20 (s, 6H), 2.68 (s, 3H), 2.45 (p, J = 7.6 Hz, 3H). HRMS (ESI$^+$) Calculated for $C_{21}H_{23}N_2O^+$ [M]$^+$: 319.1805; found: 319.1608. Absorbance (CH_2Cl_2): 587 nm.

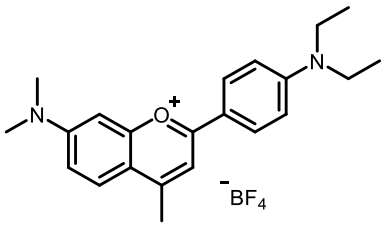

2-(4-(diethylamino)phenyl)-7-(dimethylamino)-4-methylchromenylium tetrafluoroborate (**3.19l**): Flavone **3.18i** (210 mg, 0.62 mmol, 1.0 equiv.) was dissolved in THF (3.7 mL) in a double-neck round bottom flask and cooled to 0 °C. Methylmagnesium bromide was added dropwise (3.7 mL, 1.0 M in THF, 3 equiv.) and the solution was warmed to rt and stirred for 24 h. The reaction was quenched by dropwise addition of 5% HBF_4 on ice, extracted with dichloromethane, dried with Na_2SO_4, filtered, and evaporated. The crude product was triturated with ice cold ethyl acetate and vacuum filtered to produce a purple solid (210 mg, 0.49 mmol, 79% yield). R_f = 0.3 in 9:1 DCM/EtOH. ^{1}H NMR (400 MHz, Acetonitrile-d_3) δ 8.07 (d, J = 9.4 Hz, 2H), 7.87 (d, J = 9.4 Hz, 1H), 7.52 (s, 1H), 7.14 (dd, J = 9.4, 2.6 Hz, 1H), 6.97 (d, J = 2.5 Hz, 1H), 6.88 (d, J = 9.4 Hz, 2H), 3.55 (t, J = 7.1 Hz, 4H), 3.20 (s, 6H), 2.68 (s, 3H), 1.21 (t, J = 7.1 Hz, 6H). HRMS (ESI$^+$) Calculated for $C_{22}H_{27}N_2O_2^+$ [M]$^+$: 335.2118; found: 335.2118. Absorbance (CH_2Cl_2): 591 nm.

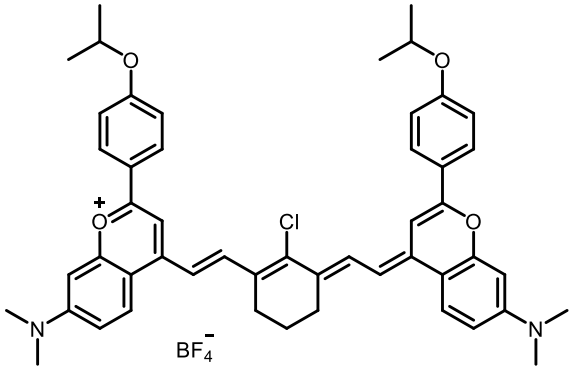

4-((*E*)-2-((*E*)-2-chloro-3-(2-((*E*)-7-(dimethylamino)-2-(4-isopropoxyphenyl)-4*H*-chromen-4-ylidene)ethylidene)cyclohex-1-en-1-yl)vinyl)-7-(dimethylamino)-2-(4-

isopropoxyphenyl)chromenylium tetrafluoroborate (**3.4**). Flavylium **3.19a** (30 mg, 0.073 mmol, 1.0 equiv.), linker **3.20** (11 mg, 0.035 mmol, 0.48 equiv.), and sodium acetate (18 mg, 0.22 mmol, 3 equiv.) were dissolved in a mixture of *n*-butanol (460 μL) and toluene (190 μL) in a Schlenk flask and heated to 100 °C for 30 minutes. The solution was cooled to rt and evaporated onto silica gel. The crude product was purified via silica gel chromatography, eluting with a DCM/EtOH solvent gradient, increasing up to 5% EtOH gradually, followed by a trituration with THF and toluene. The procedure gave a dark purple solid (4 mg, 0.005 mmol, 6% yield). ^{1}H NMR (500 MHz, DMSO-d_6) δ 8.18 (dd, *J* = 24.0, 11.7 Hz, 4H), 8.13 (d, *J* = 8.9 Hz, 4H), 7.60 (s, 2H), 7.11 (d, *J* = 8.9 Hz, 4H), 7.06 (d, *J* = 13.8 Hz, 2H), 6.98 (dd, *J* = 9.4, 2.6 Hz, 2H), 6.86 (d, *J* = 2.6 Hz, 2H), 4.79 (p, *J* = 6.0 Hz, 2H), 3.14 (s, 13H), 2.82 (s, 4H), 1.87 (s, 2H), 1.31 (d, *J* = 6.1 Hz, 13H). Absorbance (CH_2Cl_2): 1025 nm. Emission (CH_2Cl_2): 1048 nm.

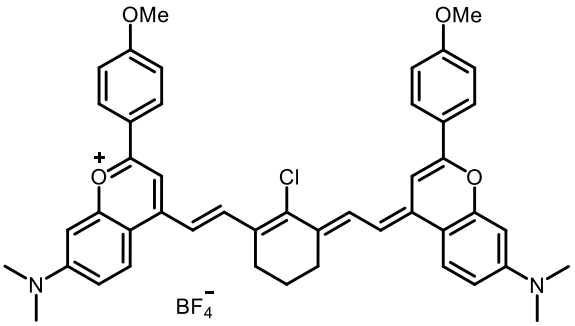

4-((*E*)-2-((*E*)-2-chloro-3-(2-((*E*)-7-(dimethylamino)-2-(4-methoxyphenyl)-4*H*-chromen-4-ylidene)ethylidene)cyclohex-1-en-1-yl)vinyl)-7-(dimethylamino)-2-(4-methoxyphenyl)chromenylium tetrafluoroborate (3.5). Flavylium **3.19b** (18 mg, 0.047 mmol, 1.0 equiv.), linker **3.20** (8 mg, 0.002 mmol, 0.48 equiv.), and sodium acetate (12 mg, 0.14 mmol, 3.0 equiv.) were dissolved in a mixture of *n*-butanol (0.3 mL) and toluene (0.1 mL) in a Schlenk flask and heated to 105 °C for 20 minutes. The solution was cooled to rt and evaporated onto silica gel. The crude product was purified via silica gel chromatography, eluting with a DCM/Toluene

(7:3) + 0.2% EtOH, increasing up to 10% EtOH gradually. The procedure gave a dark purple solid (8 mg, 0.01 mmol, 21% yield). ^{1}H NMR (500 MHz, DMSO-d_6) δ 8.12 (d, J = 13.6 Hz, 1H), 7.99 (d, J = 8.8 Hz, 3H), 7.41 (s, 1H), 7.05 (d, J = 8.8 Hz, 2H), 6.98 – 6.80 (m, 2H), 6.69 (s, 1H), 3.87 (s, 3H), 3.11 (s, 6H), 2.77 (s, 2H), 1.87 (s, 1H). Absorbance (CH_2Cl_2): 1027 nm. Emission (CH_2Cl_2): 1047 nm.

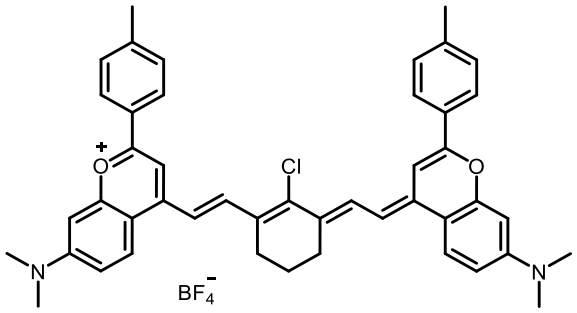

4-((*E*)-2-((*E*)-2-chloro-3-(2-((*E*)-7-(dimethylamino)-2-(*p*-tolyl)-4*H*-chromen-4-ylidene)ethylidene)cyclohex-1-en-1-yl)vinyl)-7-(dimethylamino)-2-(*p*-tolyl)chromenylium tetrafluoroborate (3.6). Flavylium **3.19c** (12 mg, 0.03 mmol, 1.0 equiv.), linker **3.20** (5.5 mg, 0.01 mmol, 0.48 equiv.), and sodium acetate (7.5 mg, 0.09 mmol, 3 equiv.) were dissolved in a mixture of *n*-butanol (190 μL) and toluene (80 μL) in a Schlenk flask and heated to 100 °C for 15 minutes. The solution was cooled to rt and evaporated onto silica gel. The crude product was purified via silica gel chromatography, eluting with a DCM/Toluene (7:3) + 0.2% EtOH, increasing up to 10% EtOH gradually, followed by a trituration with THF and toluene. The procedure gave a dark purple solid (3 mg, 0.004 mmol, 12% yield). ^{1}H NMR (500 MHz, DMSO-d_6) δ 8.15 (d, J = 13.7 Hz, 2H), 8.07 (d, J = 9.5 Hz, 2H), 7.98 (d, J = 8.3 Hz, 4H), 7.53 (s, 2H), 7.34 (d, J = 8.1 Hz, 4H), 6.99 (d, J = 13.8 Hz, 2H), 6.93 (dd, J = 9.3, 2.6 Hz, 2H), 6.76 (d, J = 2.6

Hz, 2H), 3.12 (s, 13H), 2.78 (t, *J* = 6.3 Hz, 4H), 2.39 (s, 6H), 1.86 (t, *J* = 6.2 Hz, 2H). Absorbance (CH_2Cl_2): 1027 nm. Emission (CH_2Cl_2): 1049 nm.

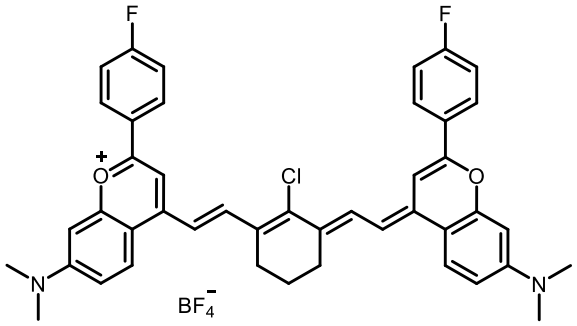

4-((*E*)-2-((*E*)-2-chloro-3-(2-((*E*)-7-(dimethylamino)-2-(4-fluorophenyl)-4*H*-chromen-4-ylidene)ethylidene)cyclohex-1-en-1-yl)vinyl)-7-(dimethylamino)-2-(4-fluorophenyl)chromenylium tetrafluoroborate (3.7). Flavylium **3.19d** (22 mg, 0.06 mmol, 1.0 equiv.), linker **3.20** (11 mg, 0.02 mmol, 0.48 equiv.), and sodium acetate (15 mg, 0.17 mmol, 3 equiv.) were dissolved in a mixture of *n*-butanol (350 µL) and toluene (150 µL) in a Schlenk flask and heated to 100 °C for 10 minutes. The solution was cooled to rt and evaporated onto silica gel. The crude product was purified via silica gel chromatography, eluting with a DCM/Toluene (7:3) + 0.2% EtOH, increasing up to 10% EtOH gradually, followed by a trituration with THF. The procedure gave a dark purple solid (16 mg, 0.02 mmol, 35% yield). ^{1}H NMR (500 MHz, Acetonitrile-d_3) δ 8.04 (d, *J* = 13.8 Hz, 2H), 7.81 (dd, *J* = 8.3, 5.4 Hz, 4H), 7.60 (d, *J* = 9.2 Hz, 2H), 7.16 (t, *J* = 8.7 Hz, 4H), 7.10 (s, 2H), 6.70 – 6.59 (m, 4H), 6.36 (d, *J* = 2.5 Hz, 2H), 3.02 (s, 12H), 2.70 (s, 4H), 2.11 – 2.10 (m, 2H). Absorbance (CH_2Cl_2): 1028 nm. Emission (CH_2Cl_2): 1050 nm.

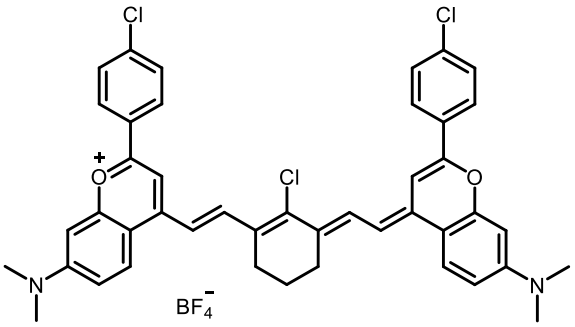

4-((*E*)-2-((*E*)-2-chloro-3-(2-((*E*)-2-(4-chlorophenyl)-7-(dimethylamino)-4*H*-chromen-4-ylidene)ethylidene)cyclohex-1-en-1-yl)vinyl)-2-(4-chlorophenyl)-7-(dimethylamino)chromenylium tetrafluoroborate (3.8). Flavylium **3.19e** (20 mg, 0.05 mmol, 1.0 equiv.), linker **3.20** (8.7 mg, 0.021 mmol, 0.48 equiv.), and sodium acetate (12 mg, 0.16 mmol, 3 equiv.) were dissolved in a mixture of *n*-butanol (320 μL) and toluene (134 μL) in a Schlenk flask and heated to 100 °C for 20 minutes. The solution was cooled to rt and evaporated onto silica gel. The crude product was purified via silica gel chromatography, eluting with a DCM/Toluene (7:3) + 0.2% EtOH, increasing up to 10% EtOH gradually, followed by a trituration with ice cold THF and Toluene. Followed by an additional column, as previously described. The procedure gave a dark purple solid (12 mg, 0.014 mmol, 28% yield). ^{1}H NMR (500 MHz, Acetonitrile-d_3) δ 7.96 (d, J = 13.8 Hz, 2H), 7.64 (d, J = 8.2 Hz, 5H), 7.50 (d, J = 9.2 Hz, 2H), 7.40 – 7.31 (m, 5H), 7.03 (s, 2H), 6.62 – 6.52 (m, 4H), 6.27 (d, J = 2.5 Hz, 2H), 2.99 (s, 13H), 2.66 (s, 4H), 2.11 – 2.10 (m, 2H). Absorbance (CH_2Cl_2): 1036 nm. Emission (CH_2Cl_2): 1059 nm.

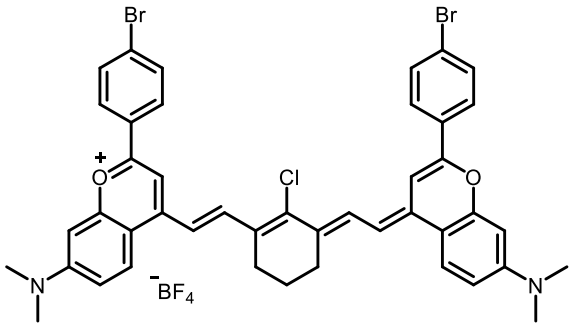

2-(4-bromophenyl)-4-((*E*)-2-((*E*)-3-(2-((*E*)-2-(4-bromophenyl)-7-(dimethylamino)-4*H*-chromen-4-ylidene)ethylidene)-2-chlorocyclohex-1-en-1-yl)vinyl)-7-(dimethylamino)chromenylium tetrafluoroborate (**3.9**). Flavylium **3.19f** (35 mg, 0.082 mmol, 1.0 equiv.), linker **3.20** (13 mg, 0.040 mmol, 0.48 equiv.), and sodium acetate (20 mg, 0.24 mmol, 3 equiv.) were dissolved in acetic anhydride (720 μL) in a Schlenk flask and heated to 100 °C for 35 minutes. The solution was cooled to rt and evaporated onto silica gel. The crude product was purified via silica gel chromatography, eluting with a DCM/Toluene (7:3) + 0.2% EtOH, increasing up to 10% EtOH gradually, followed by a trituration with THF. The procedure gave a dark purple solid (4 mg, 0.004 mmol, 5% yield). ^{1}H NMR (500 MHz, Acetonitrile-d_3) δ 7.90 (d, J = 13.8 Hz, 2H), 7.50 (s, 8H), 7.42 (d, J = 9.2 Hz, 2H), 6.95 (s, 2H), 6.51 (m, 4H), 6.19 (s, 2H), 2.96 (s, 12H), 2.62 (m, 4H), 2.25 (m, 1H). Absorbance (CH_2Cl_2): 1038 nm. Emission (CH_2Cl_2): 1063 nm.

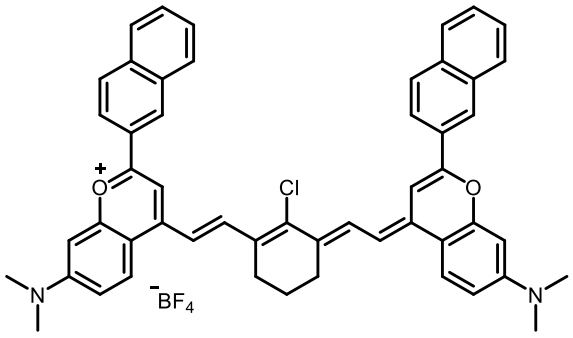

4-((*E*)-2-((*E*)-2-chloro-3-(2-((*E*)-7-(dimethylamino)-2-(naphthalen-2-yl)-4*H*-chromen-4-ylidene)ethylidene)cyclohex-1-en-1-yl)vinyl)-7-(dimethylamino)-2-(naphthalen-2-yl)chromenylium tetrafluoroborate (**3.10**). Flavylium **3.19g** (8 mg, 0.02 mmol, 1.0 equiv.), linker **3.20** (3 mg, 0.01 mmol, 0.48 equiv.), and sodium acetate (5 mg, 0.06 mmol, 3 equiv.) were dissolved in acetic anhydride (180 μL) in a Schlenk flask and heated to 110 °C for 10 minutes. The

solution was cooled to rt and evaporated onto silica gel. The crude product was purified via silica gel chromatography, eluting with a DCM/Toluene (7:3) + 0.2% EtOH, increasing up to 10% EtOH gradually, followed by a trituration with ice cold THF. The procedure gave a dark purple solid (4 mg, 0.005 mmol, 24% yield). ^{1}H NMR (500 MHz, DMSO-d_6) δ 8.74 (s, 2H), 8.29 (d, J = 13.6 Hz, 2H), 8.25 – 8.15 (m, 4H), 8.10 – 8.03 (m, 4H), 8.00 – 7.93 (m, 2H), 7.81 (s, 2H), 7.66 – 7.59 (m, 4H), 7.22 (d, J = 7.5 Hz, 2H), 7.18 – 7.07 (m, 4H), 6.99 (dd, J = 9.3, 2.6 Hz, 2H), 6.91 (s, 2H), 3.17 (s, 12H), 2.86 (s, 4H), 1.91 (t, J = 6.2 Hz, 2H). Absorbance (CH_2Cl_2): 1042 nm. Emission (CH_2Cl_2): 1068 nm.

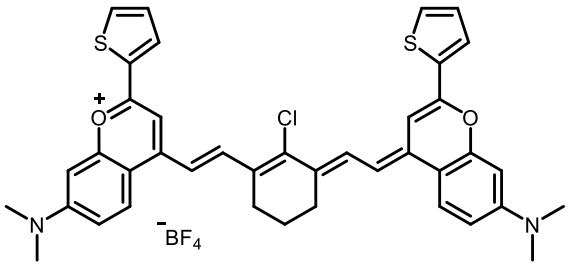

4-((*E*)-2-((*E*)-2-chloro-3-(2-((*E*)-7-(dimethylamino)-2-(thiophen-2-yl)-4*H*-chromen-4-ylidene)ethylidene)cyclohex-1-en-1-yl)vinyl)-7-(dimethylamino)-2-(thiophen-2-yl)chromenylium tetrafluoroborate (**3.11**). Flavylium **3.19h** (30 mg, 0.08 mmol, 1.0 equiv.), linker **3.20** (13 mg, 0.041 mmol, 0.48 equiv.), and sodium acetate (21 mg, 0.025 mmol, 3 equiv.) were dissolved in acetic anhydride (750 μL) in a Schlenk flask and heated to 110 °C for 20 minutes. The solution was cooled to rt and evaporated onto silica gel. The crude product was purified via silica gel chromatography, eluting with a DCM/Toluene (7:3) + 0.2% EtOH, increasing up to 10% EtOH gradually, followed by a trituration with ice cold THF. The procedure gave a dark purple solid (19 mg, 0.025 mmol, 30% yield). ^{1}H NMR (500 MHz, DMSO-d_6) δ 8.16 (s, 2H), 8.12 (s, 4H), 7.96 (s, 2H), 7.53 (s, 2H), 7.31 (s, 2H), 7.03 (s, 2H), 6.96 (s, 2H), 6.68 (s, 2H), 3.13 (s, 12H),

2.85 – 2.77 (m, 4H), 1.87 (t, *J* = 6.8 Hz, 2H). Absorbance (CH_2Cl_2): 1043 nm. Emission (CH_2Cl_2): 1066 nm.

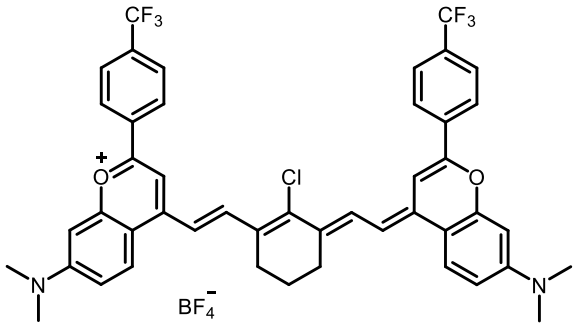

4-((*E*)-2-((*E*)-2-chloro-3-(2-((*E*)-7-(dimethylamino)-2-(4-(trifluoromethyl)phenyl)-4*H*-chromen-4-ylidene)ethylidene)cyclohex-1-en-1-yl)vinyl)-7-(dimethylamino)-2-(4-(trifluoromethyl)phenyl)chromenylium tetrafluoroborate (**3.12**). Flavylium **3.19i** (31 mg, 0.074 mmol, 1.0 equiv.), linker **3.20** (13 mg, 0.035 mmol, 0.48 equiv.), and sodium acetate (18 mg, 0.22 mmol, 3 equiv.) were dissolved in a mixture of *n*-butanol (0.47 mL) and toluene (0.2 mL) in a Schlenk flask and heated to 105 °C for 30 minutes. The solution was cooled to rt and evaporated onto silica gel. The crude product was purified via silica gel chromatography, eluting with a DCM/Toluene (7:3) + 0.2% EtOH, increasing up to 10% EtOH gradually, followed by a trituration with THF. The procedure gave a dark purple solid (6 mg, 0.01 mmol, 9% yield). ^{1}H NMR (500 MHz, Acetonitrile-d_3) δ 8.03 (d, *J* = 13.8 Hz, 2H), 7.89 (d, *J* = 8.1 Hz, 4H), 7.68 (d, *J* = 8.2 Hz, 4H), 7.55 (d, *J* = 9.3 Hz, 2H), 7.20 (s, 2H), 6.68 (d, *J* = 13.9 Hz, 2H), 6.57 (dd, *J* = 9.2, 2.6 Hz, 2H), 6.35 (d, *J* = 2.6 Hz, 2H), 3.01 (s, 13H), 2.72 (t, *J* = 6.3 Hz, 4H), 2.12 – 2.11 (m, 2H). Absorbance (CH_2Cl_2): 1044 nm. Emission (CH_2Cl_2): 1070 nm.

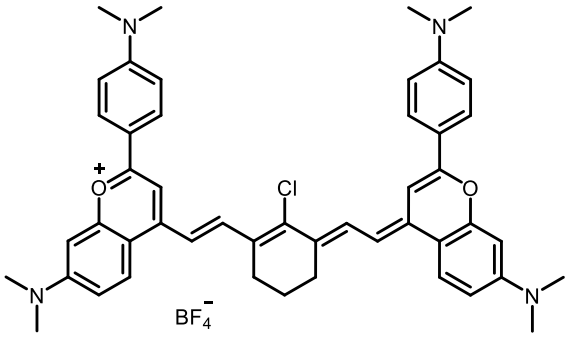

4-((*E*)-2-((*E*)-2-chloro-3-(2-((*E*)-7-(dimethylamino)-2-(4-(dimethylamino)phenyl)-4*H*-chromen-4-ylidene)ethylidene)cyclohex-1-en-1-yl)vinyl)-7-(dimethylamino)-2-(4 (dimethylamino)phenyl)chromenylium tetrafluoroborate (**3.13**). Flavylium **3.19j** (10 mg, 0.03 mmol, 1.0 equiv.), linker **3.20** (4 mg, 0.01 mmol, 0.48 equiv.), and sodium acetate (6 mg, 0.08 mmol, 3 equiv.) were dissolved in a mixture of *n*-butanol (200 μL) and toluene (90 μL) in a Schlenk flask and heated to 100 °C for 35 minutes. The solution was cooled to rt and evaporated onto silica gel. The crude product was purified via silica gel chromatography, eluting with a DCM/Toluene (7:3) + 0.2% EtOH, increasing up to 10% EtOH gradually, followed by a trituration with ice cold THF. The procedure gave a dark purple solid (5 mg, 0.006 mmol, 20% yield). ^{1}H NMR (500 MHz, DMSO-d_6) δ 8.06 (d, J = 13.6 Hz, 2H), 7.94 (d, J = 9.3 Hz, 2H), 7.87 (d, J = 8.7 Hz, 4H), 7.30 (s, 2H), 6.84 (s, 2H), 6.83 – 6.80 (m, 2H), 6.75 (d, J = 9.0 Hz, 4H), 6.66 (d, J = 2.5 Hz, 2H), 3.08 (s, 12H), 3.04 (s, 12H), 2.73 (t, J = 6.3 Hz, 4H), 1.84 (t, J = 6.2 Hz, 2H). Absorbance (CH_2Cl_2): 1051 nm. Emission (CH_2Cl_2): 1073 nm.

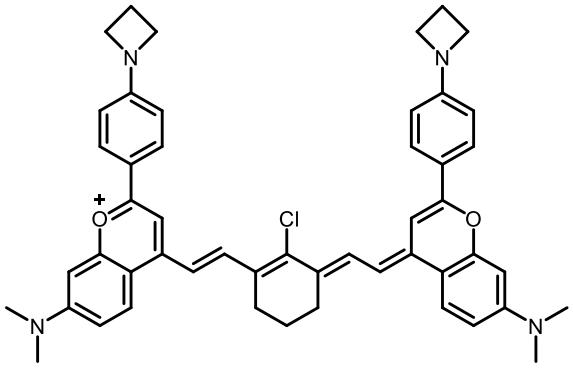

2-(4-(azetidin-1-yl)phenyl)-4-((*E*)-2-((*E*)-3-(2-((*E*)-2-(4-(azetidin-1-yl)phenyl)-7-(dimethylamino)-4*H*-chromen-4-ylidene)ethylidene)-2-chlorocyclohex-1-en-1-yl)vinyl)-7-(dimethylamino)chromenylium tetrafluoroborate (**3.14**). Flavylium **3.19k** (10 mg, 0.03 mmol, 1.0 equiv.), linker **3.20** (4 mg, 0.01 mmol, 0.48 equiv.), and sodium acetate (6 mg, 0.08 mmol, 3 equiv.) were dissolved in acetic anhydride (220 μL) in a Schlenk flask and heated to 100 °C for 20 minutes. The solution was cooled to rt and evaporated onto silica gel. The crude product was purified via silica gel chromatography, eluting with a DCM/Toluene (7:3) + 0.2% EtOH, increasing up to 10% EtOH gradually, followed by a trituration with THF. The procedure gave a dark purple solid (5 mg, 0.006 mmol, 24% yield). ^{1}H NMR (500 MHz, DMSO-d_6) δ 8.12 (d, J = 13.7 Hz, 2H), 8.08 (d, J = 9.5 Hz, 2H), 8.00 (d, J = 8.9 Hz, 4H), 7.46 (s, 2H), 6.97 (d, J = 13.9 Hz, 2H), 6.93 (dd, J = 9.4, 2.6 Hz, 2H), 6.82 (d, J = 2.6 Hz, 2H), 6.50 (d, J = 8.9 Hz, 4H), 4.00 (t, J = 7.4 Hz, 8H), 3.12 (s, 12H), 2.79 (s, 4H), 2.40 – 2.36 (m, 3H), 2.35 (s, 3H). Absorbance (CH_2Cl_2): 1054 nm. Emission (CH_2Cl_2): 1074 nm.

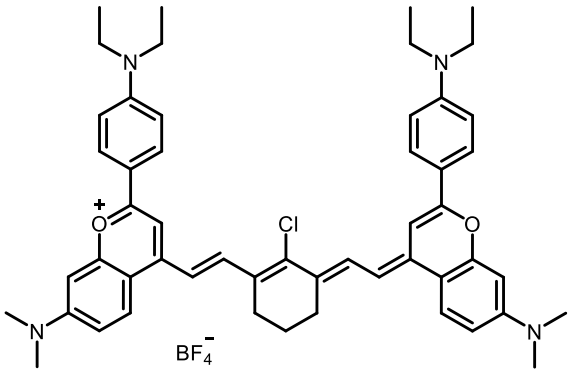

4-((*E*)-2-((*E*)-2-chloro-3-(2-((*E*)-2-(4-(diethylamino)phenyl)-7-(dimethylamino)-4*H*-chromen-4-ylidene)ethylidene)cyclohex-1-en-1-yl)vinyl)-2-(4-(diethylamino)phenyl)-7-(dimethylamino)chromenylium tetrafluoroborate (**3.15**). Flavylium **3.19l** (101 mg, 0.240 mmol, 1.0 equiv.), linker **3.20** (37 mg, 0.11 mmol, 0.48 equiv.), and sodium acetate (59 mg, 0.72 mmol, 3 equiv.) were dissolved in a mixture of *n*-butanol (1.5 mL) and toluene (640 μL) in a Schlenk flask and heated to 100 °C for 35 minutes. The solution was cooled to rt and evaporated onto silica gel. The crude product was purified via silica gel chromatography, eluting with a DCM/Toluene (7:3) + 0.2% EtOH, increasing up to 10% EtOH gradually, followed by a trituration with ice cold THF. The procedure gave a dark purple solid (17 mg, 0.019 mmol, 8% yield). ^{1}H NMR (500 MHz, DMSO-d_6) δ 8.02 (d, J = 13.6 Hz, 2H), 7.89 (d, J = 9.5 Hz, 2H), 7.83 (d, J = 9.2 Hz, 4H), 7.23 (s, 2H), 6.79 – 6.76 (m, 2H), 6.73 (d, J = 9.3 Hz, 4H), 6.60 (d, J = 2.5 Hz, 2H), 3.44 (q, J = 7.1 Hz, 8H), 3.06 (s, 12H), 2.70 (t, J = 6.3 Hz, 4H), 1.14 (t, J = 7.0 Hz, 13H). Absorbance (CH_2Cl_2): 1059 nm. Emission (CH_2Cl_2): 1081 nm.

3.6 Spectra Relevant to Chapter Three

3.6.1 ^{1}H NMR Spectra

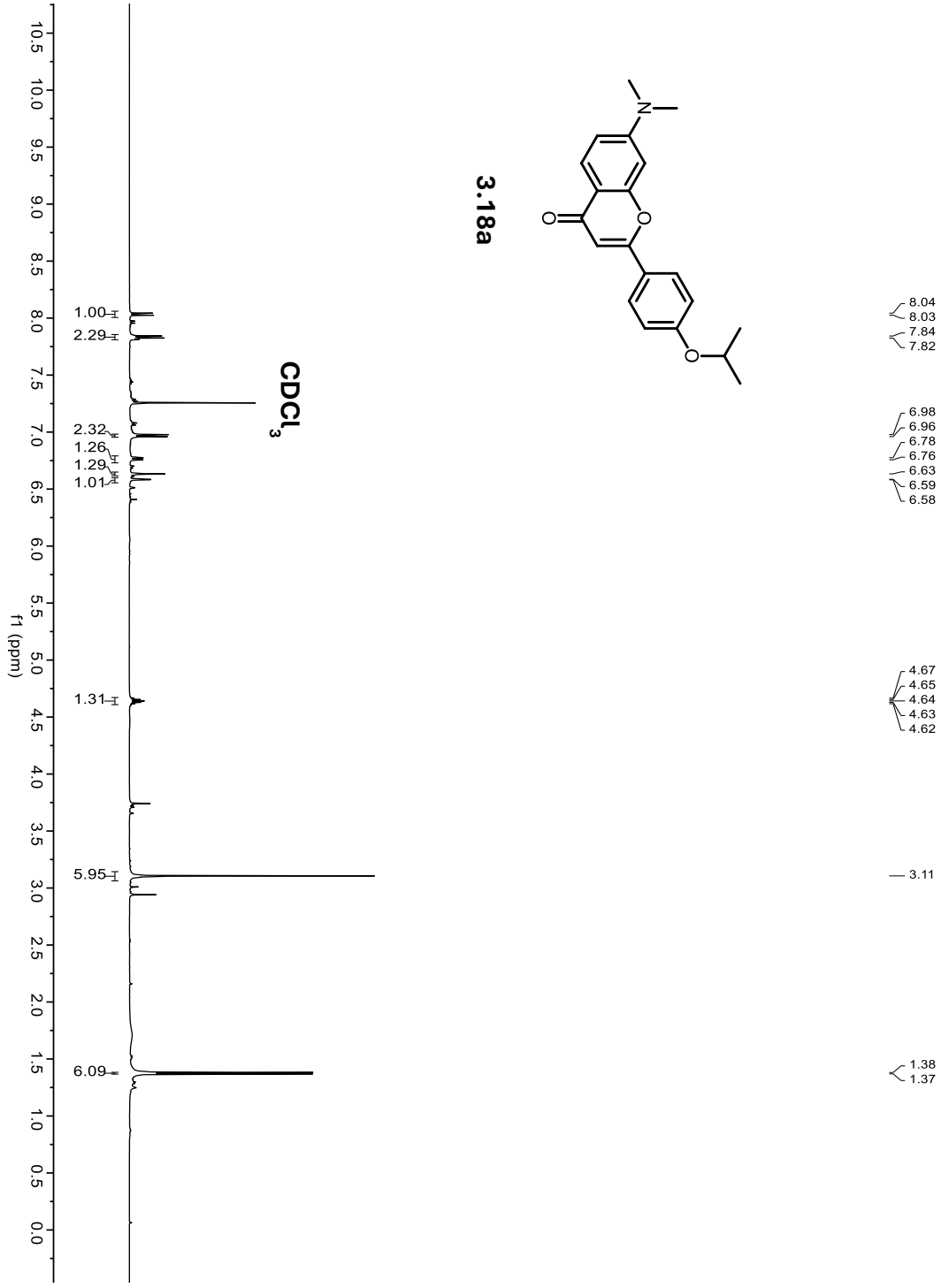

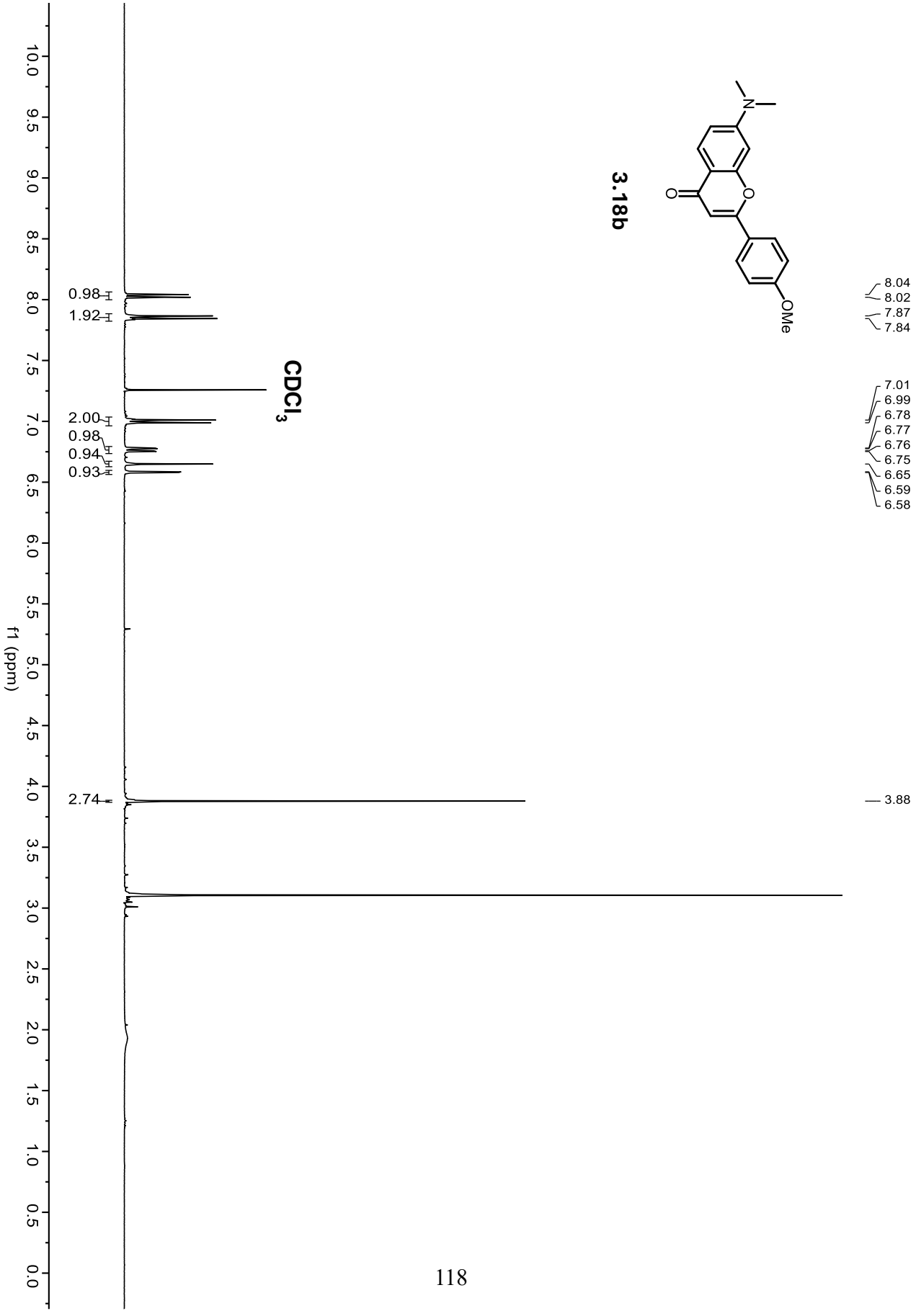
3.18b
CDCl3
8.04
8.02
7.87
7.84
7.01
6.99
6.78
6.77
6.76
6.75
6.65
6.59
6.58
3.88
0.98
1.92
2.00
0.98
0.94
0.93
2.74
OMe
f1 (ppm)

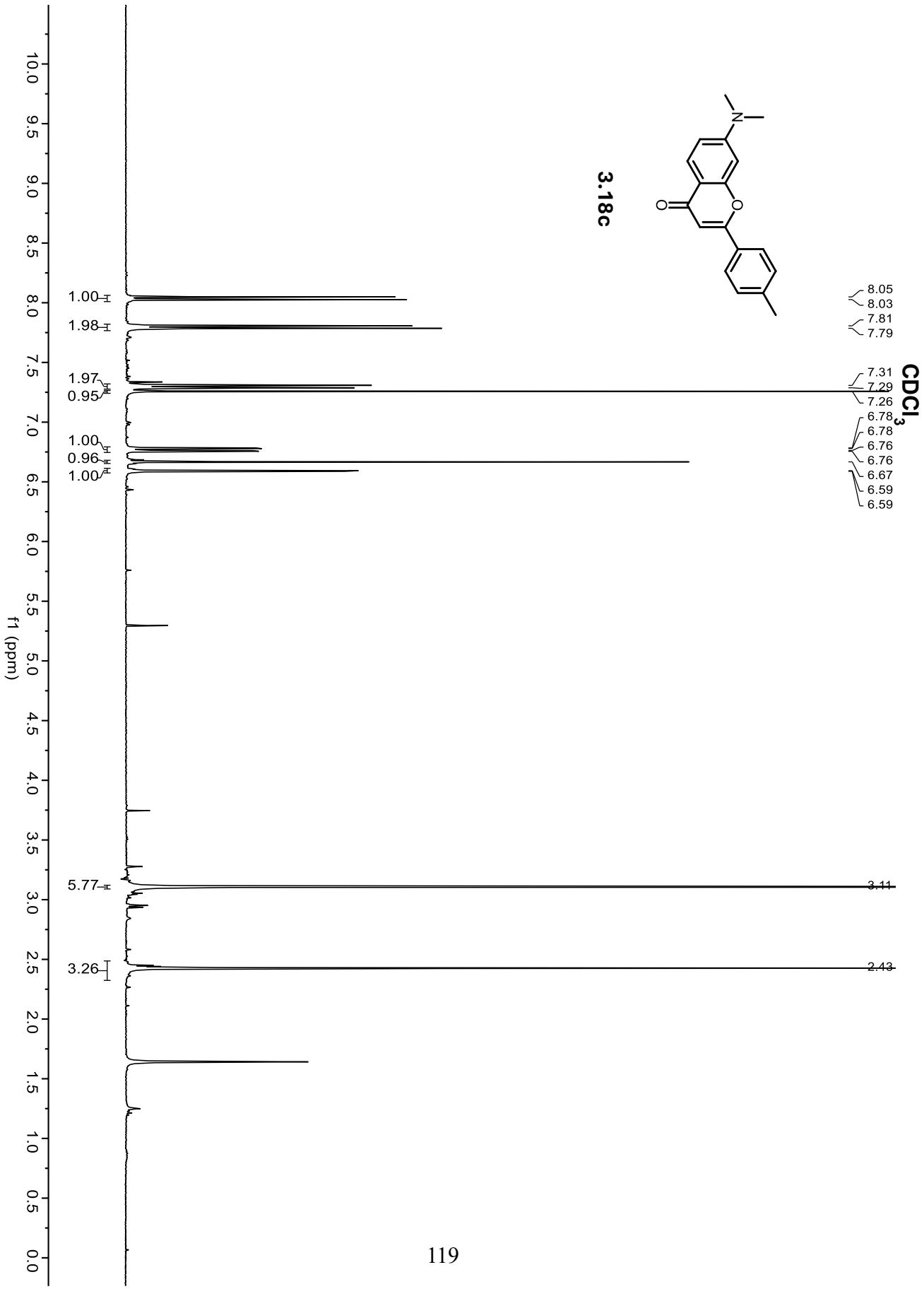
3.18c
CDCl3
8.05
8.03
7.81
7.79
7.31
7.29
7.26
6.78
6.78
6.76
6.76
6.67
6.59
6.59
1.00
1.98
1.97
0.95
1.00
0.96
1.00
5.77
3.26
3.11
2.43
f1 (ppm)

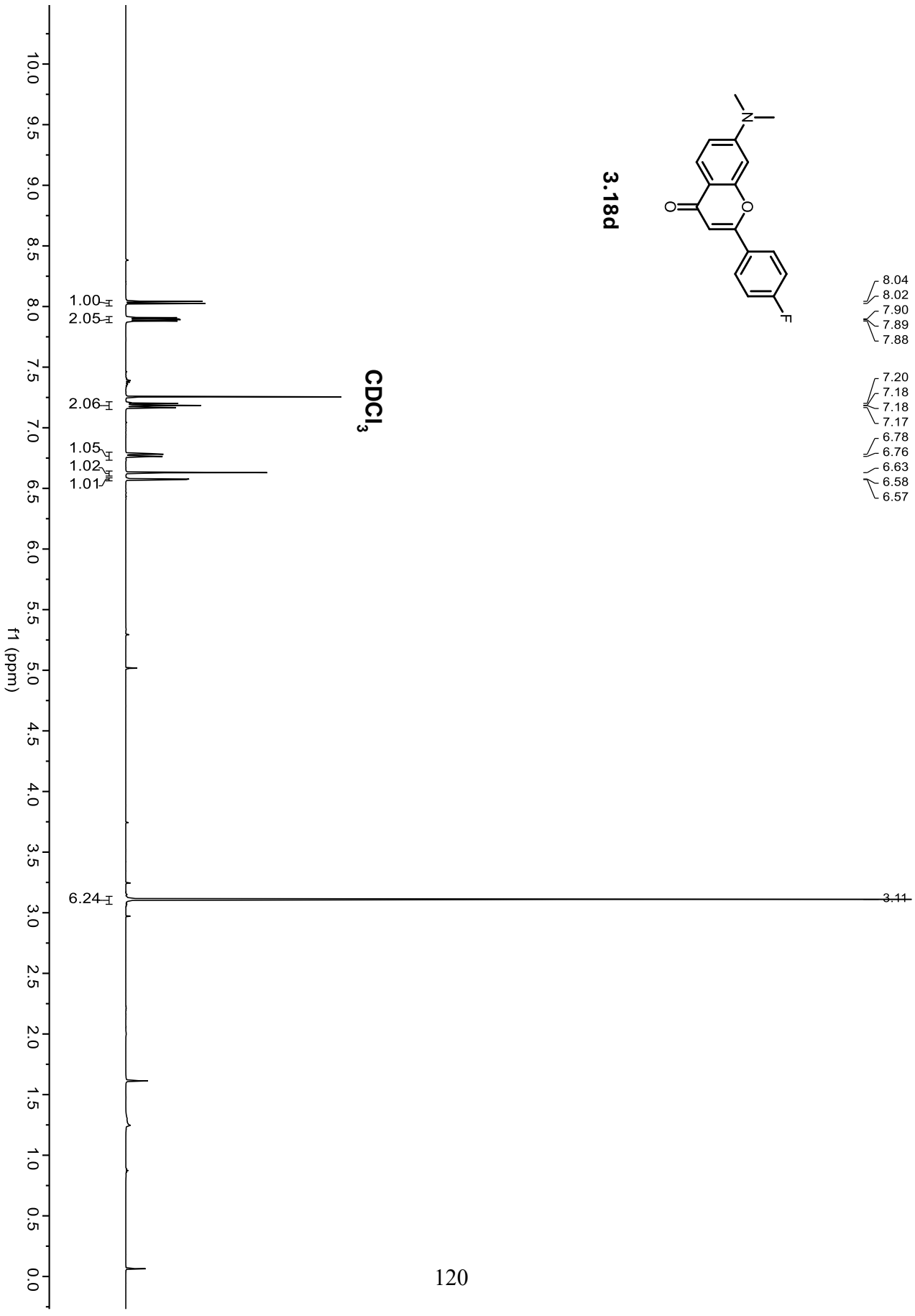
3.18d
CDCl3
8.04
8.02
7.90
7.89
7.88
7.20
7.18
7.18
7.17
6.78
6.76
6.63
6.58
6.57
1.00
2.05
2.06
1.05
1.02
1.01
6.24
3.11
f1 (ppm)

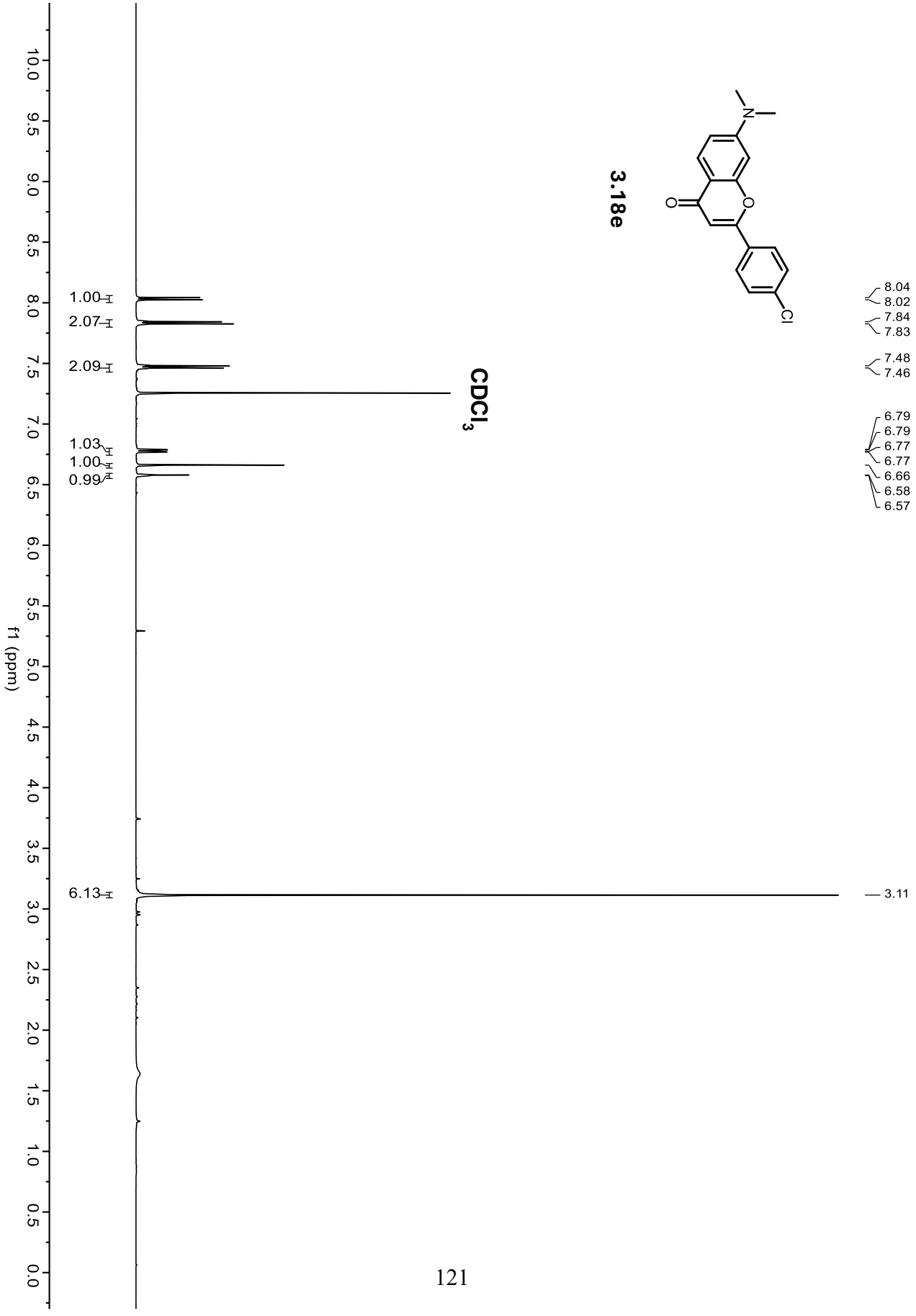
3.18e
CDCl3
N
O
O
Cl
8.04
8.02
7.84
7.83
7.48
7.46
6.79
6.79
6.77
6.77
6.66
6.58
6.57
3.11
1.00
2.07
2.09
1.03
1.00
0.99
6.13
f1 (ppm)

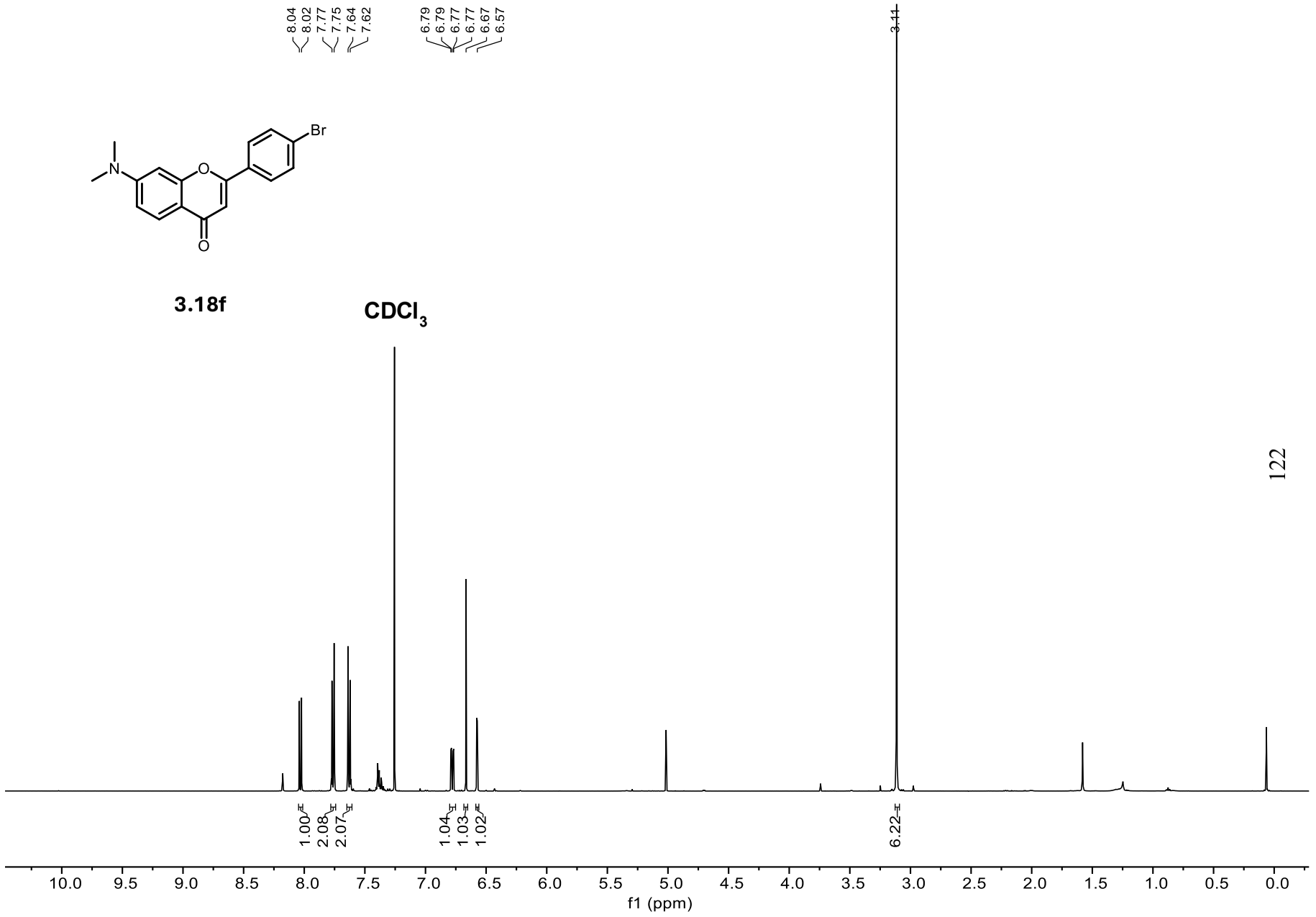
8.04
8.02
7.77
7.75
7.64
7.62
6.79
6.79
6.77
6.77
6.67
6.57
3.11
Br
N
O
O
3.18f
CDCl3
1.00
2.08
2.07
1.04
1.03
1.02
6.22
10.0
9.5
9.0
8.5
8.0
7.5
7.0
6.5
6.0
5.5
5.0
4.5
4.0
3.5
3.0
2.5
2.0
1.5
1.0
0.5
0.0
f1 (ppm)

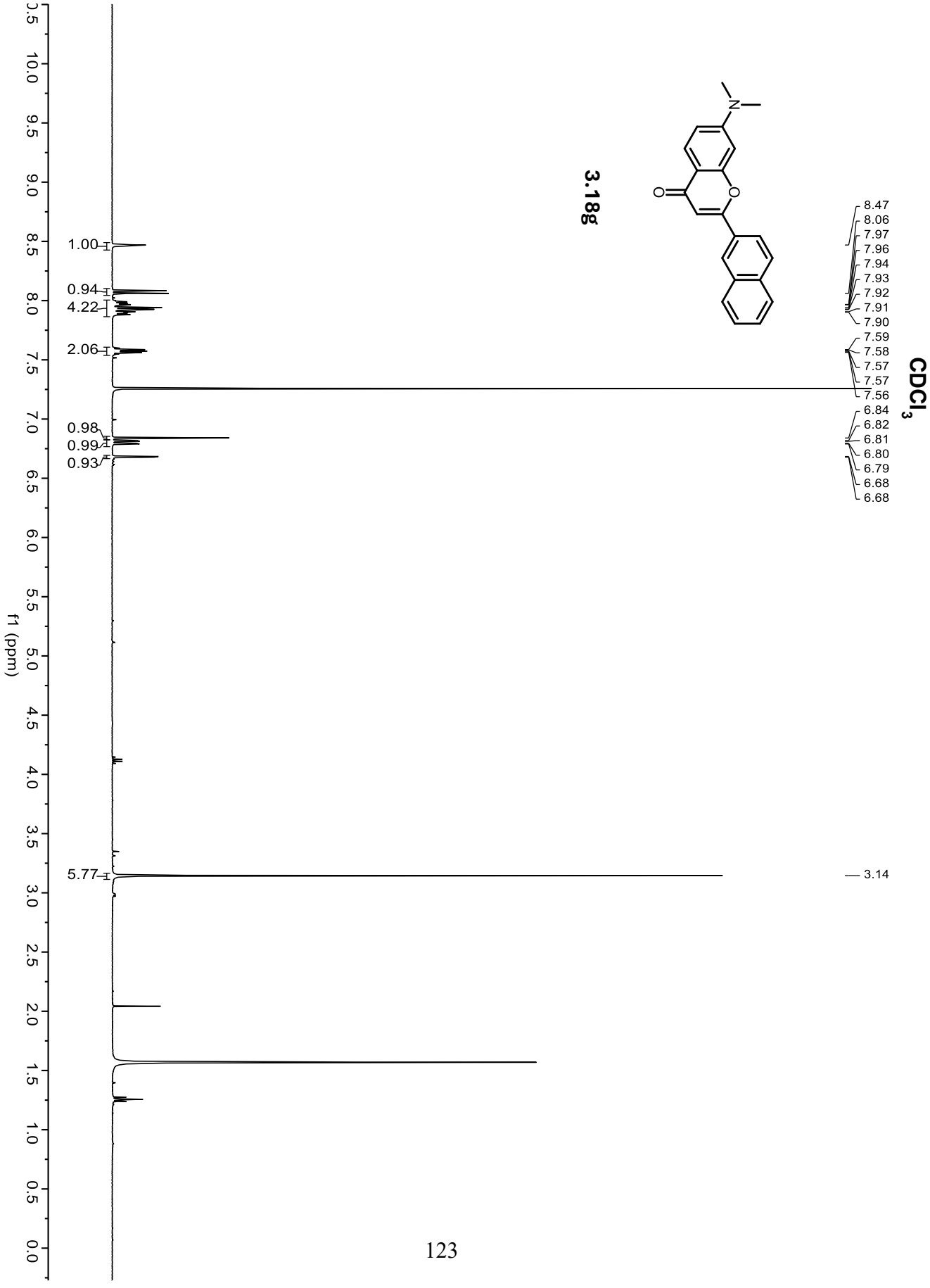
3.18g
CDCl3
8.47
8.06
7.97
7.96
7.94
7.93
7.92
7.91
7.90
7.59
7.58
7.57
7.57
7.56
6.84
6.82
6.81
6.80
6.79
6.68
6.68
1.00
0.94
4.22
2.06
0.98
0.99
0.93
5.77
3.14
f1 (ppm)

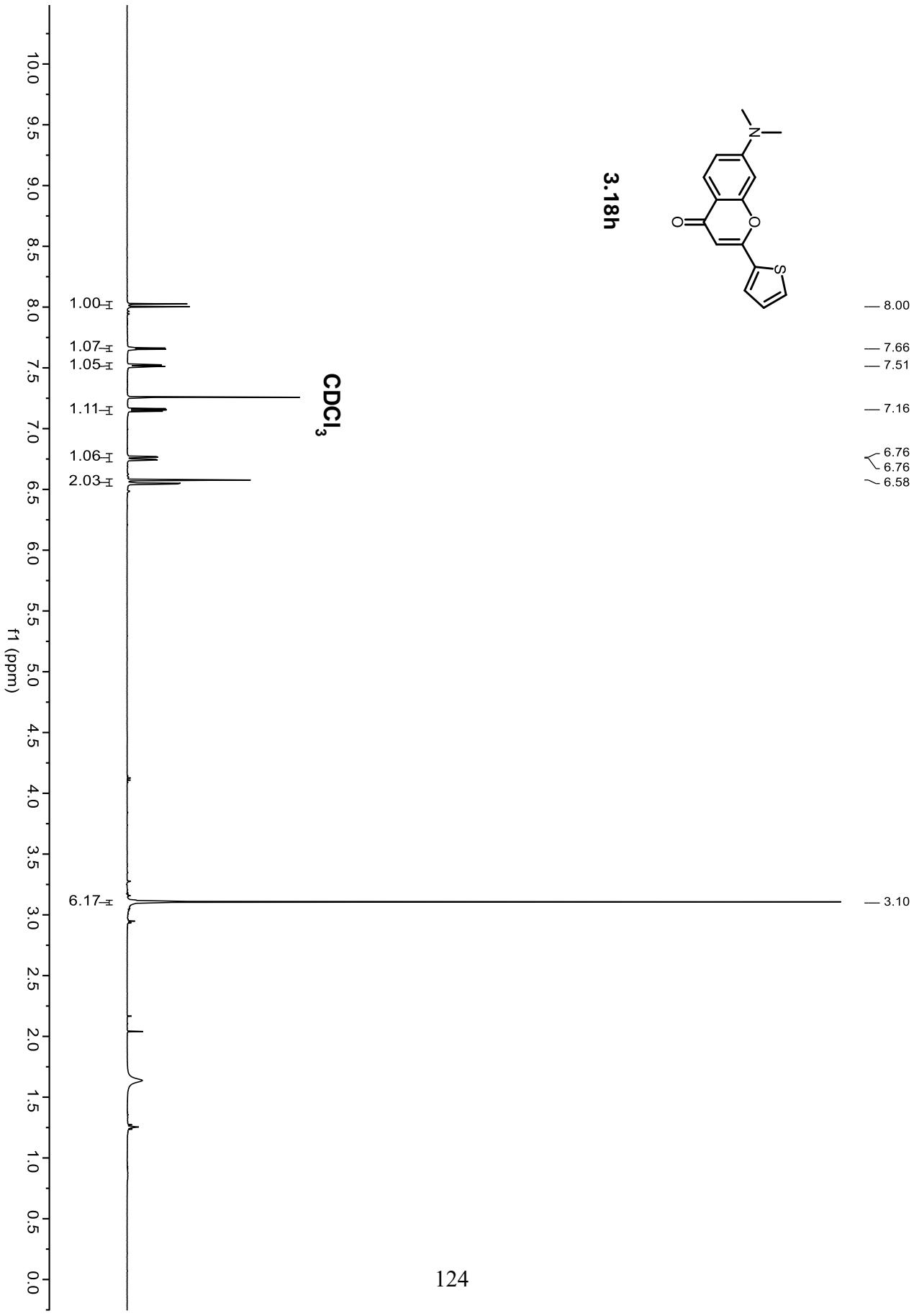
3.18h
CDCl3
1.00
1.07
1.05
1.11
1.06
2.03
6.17
8.00
7.66
7.51
7.16
6.76
6.76
6.58
3.10
f1 (ppm)

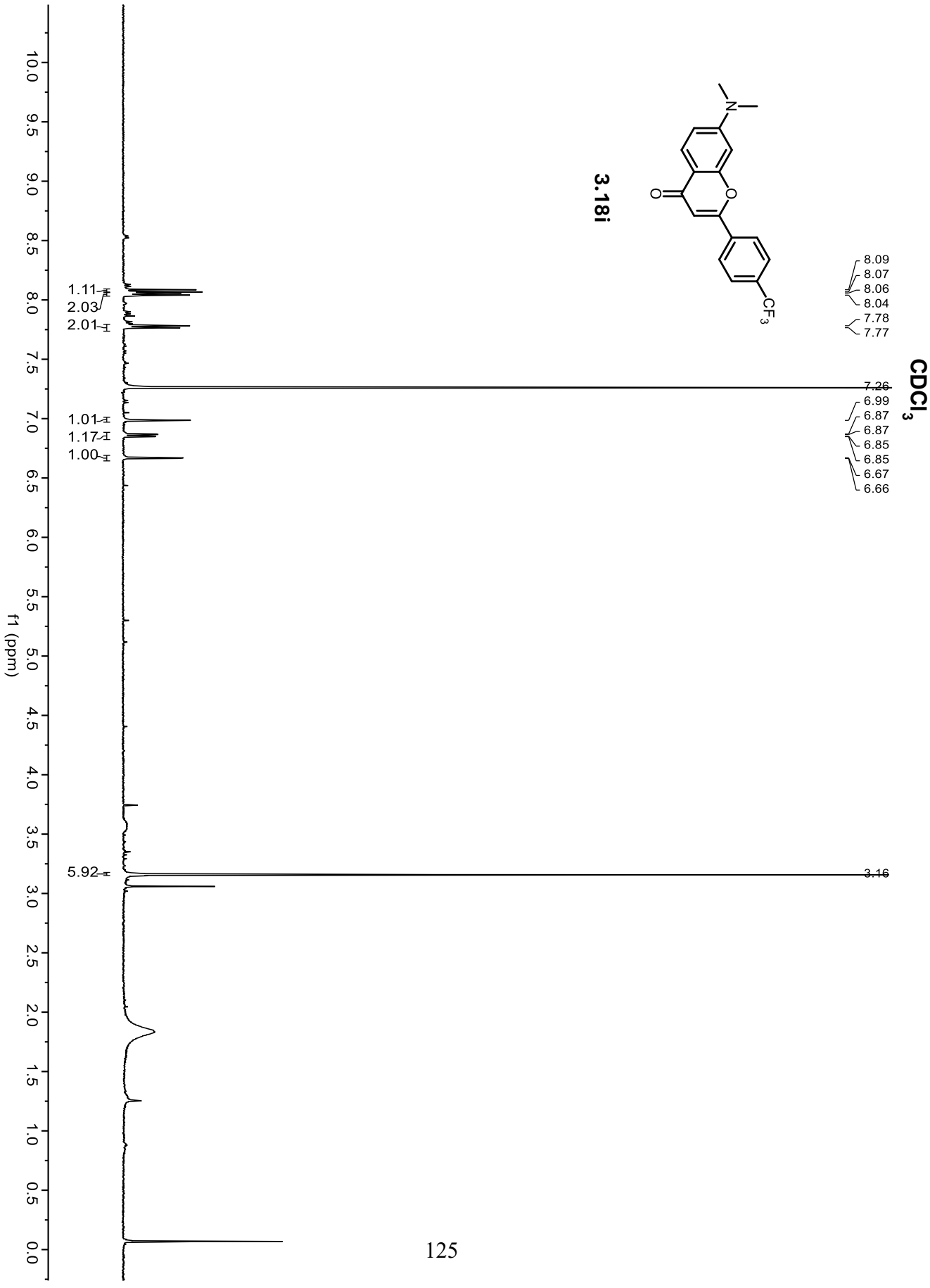
3.18i
CDCl3
8.09
8.07
8.06
8.04
7.78
7.77
7.26
6.99
6.87
6.87
6.85
6.85
6.67
6.66
3.16
1.11
2.03
2.01
1.01
1.17
1.00
5.92
f1 (ppm)

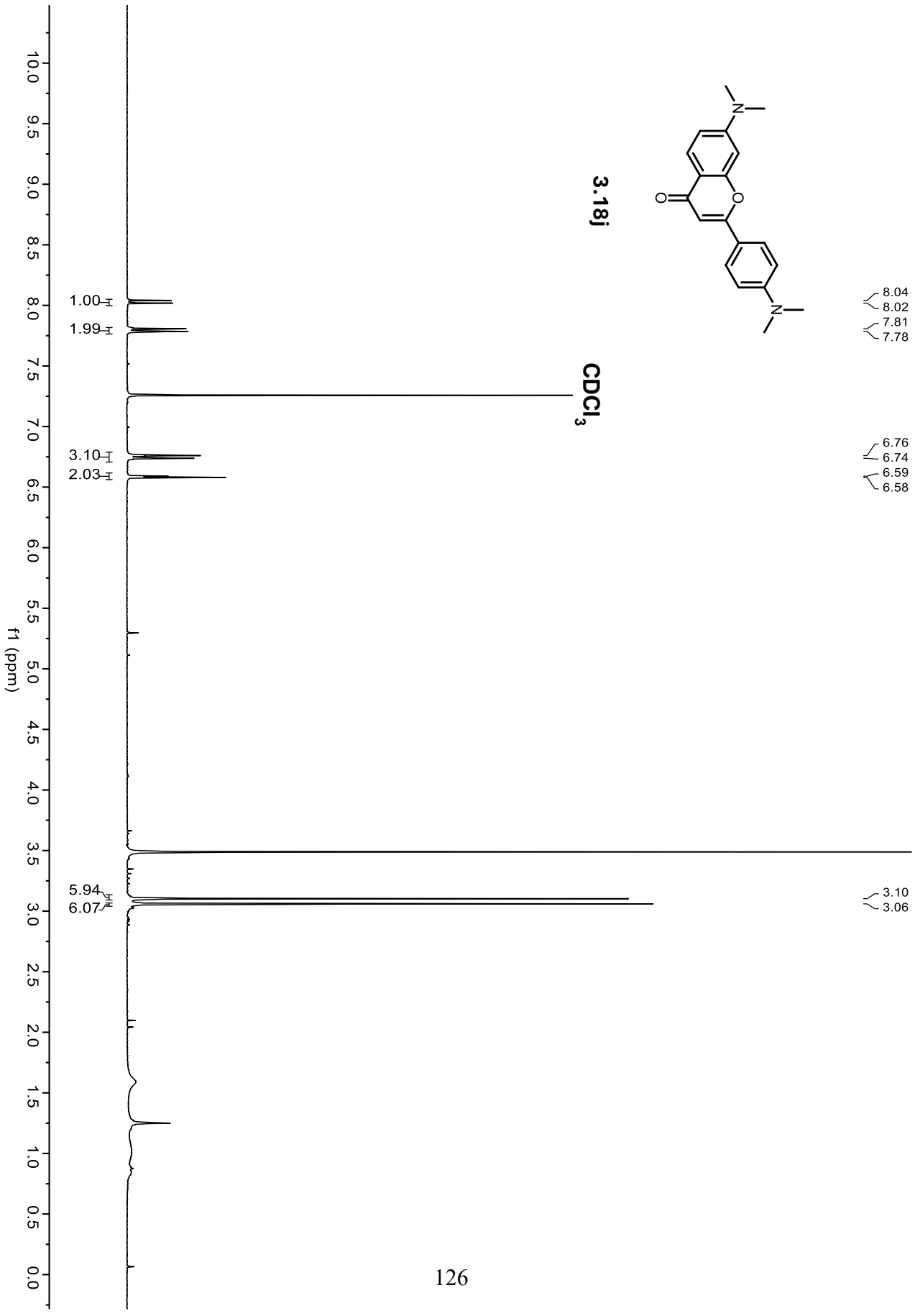
3.18j
CDCl3
8.04
8.02
7.81
7.78
6.76
6.74
6.59
6.58
3.10
3.06
1.00
1.99
3.10
2.03
5.94
6.07
f1 (ppm)

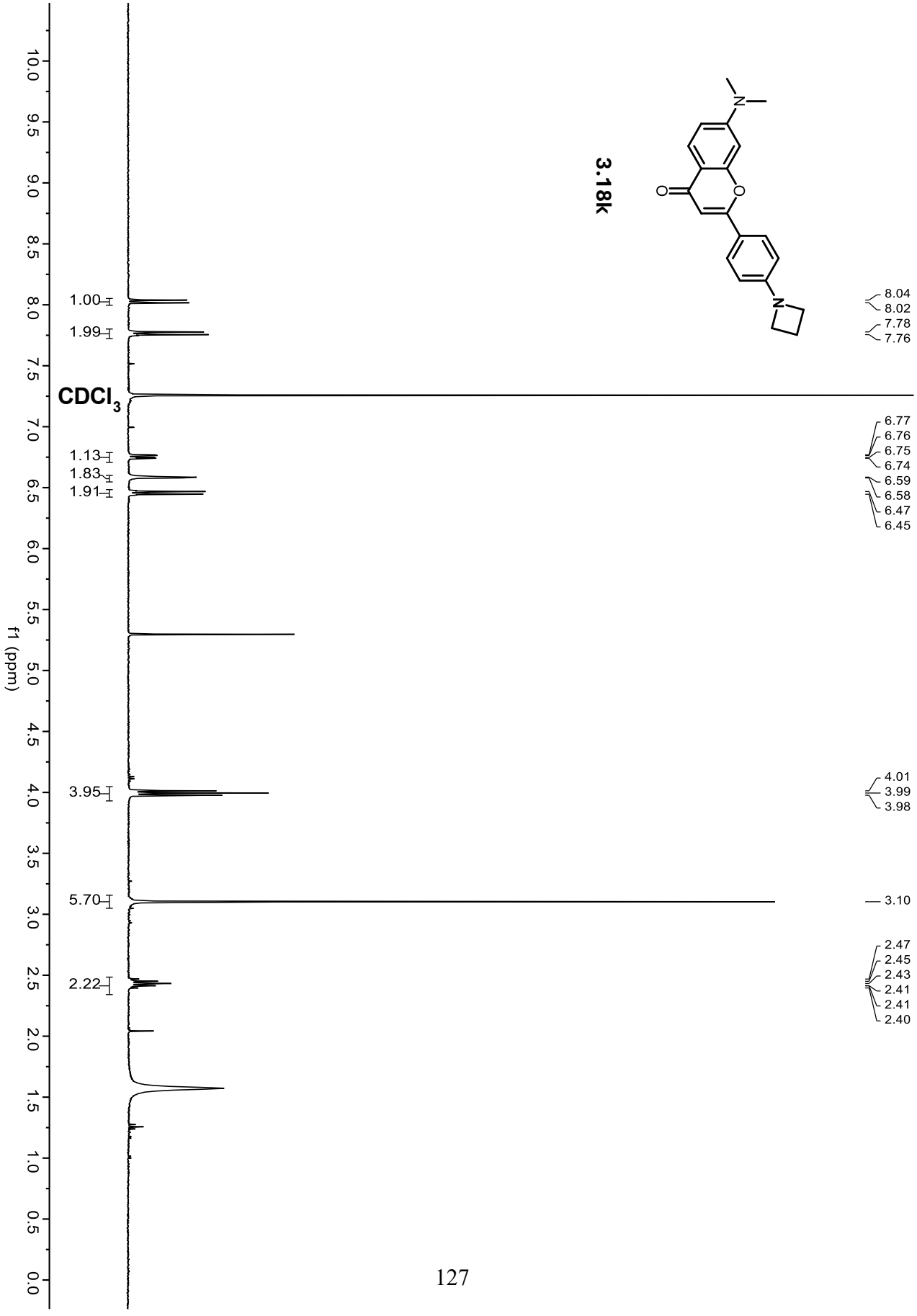
3.18k
CDCl3
f1 (ppm)
10.0
9.5
9.0
8.5
8.0
7.5
7.0
6.5
6.0
5.5
5.0
4.5
4.0
3.5
3.0
2.5
2.0
1.5
1.0
0.5
0.0
1.00
1.99
1.13
1.83
1.91
3.95
5.70
2.22
8.04
8.02
7.78
7.76
6.77
6.76
6.75
6.74
6.59
6.58
6.47
6.45
4.01
3.99
3.98
3.10
2.47
2.45
2.43
2.41
2.41
2.40

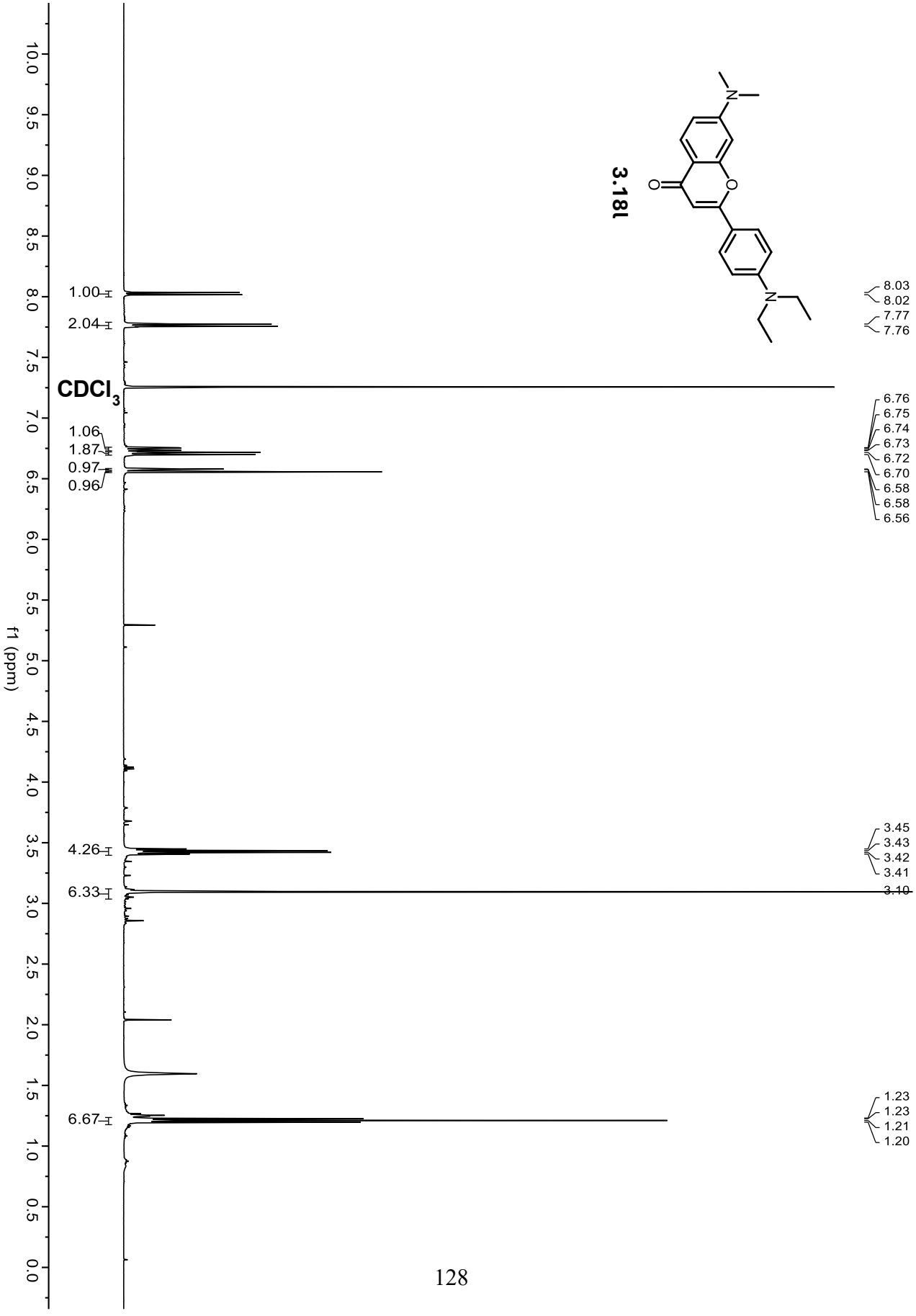
3.18l
CDCl3
1.00
2.04
1.06
1.87
0.97
0.96
4.26
6.33
6.67
8.03
8.02
7.77
7.76
6.76
6.75
6.74
6.73
6.72
6.70
6.58
6.58
6.56
3.45
3.43
3.42
3.41
3.10
1.23
1.23
1.21
1.20
f1 (ppm)

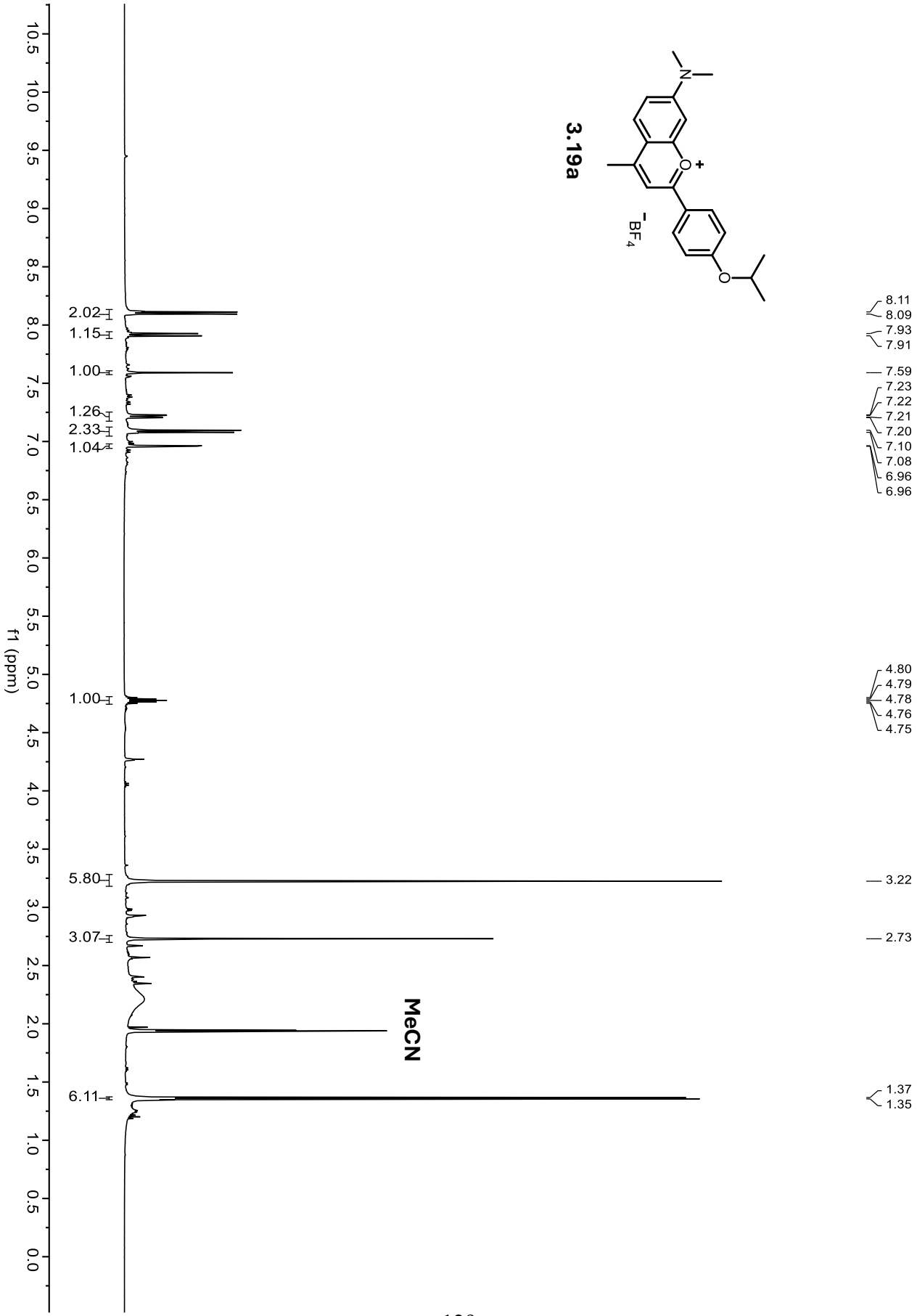
3.19a
MeCN
f1 (ppm)
2.02
1.15
1.00
1.26
2.33
1.04
1.00
5.80
3.07
6.11
8.11
8.09
7.93
7.91
7.59
7.23
7.22
7.21
7.20
7.10
7.08
6.96
6.96
4.80
4.79
4.78
4.76
4.75
3.22
2.73
1.37
1.35

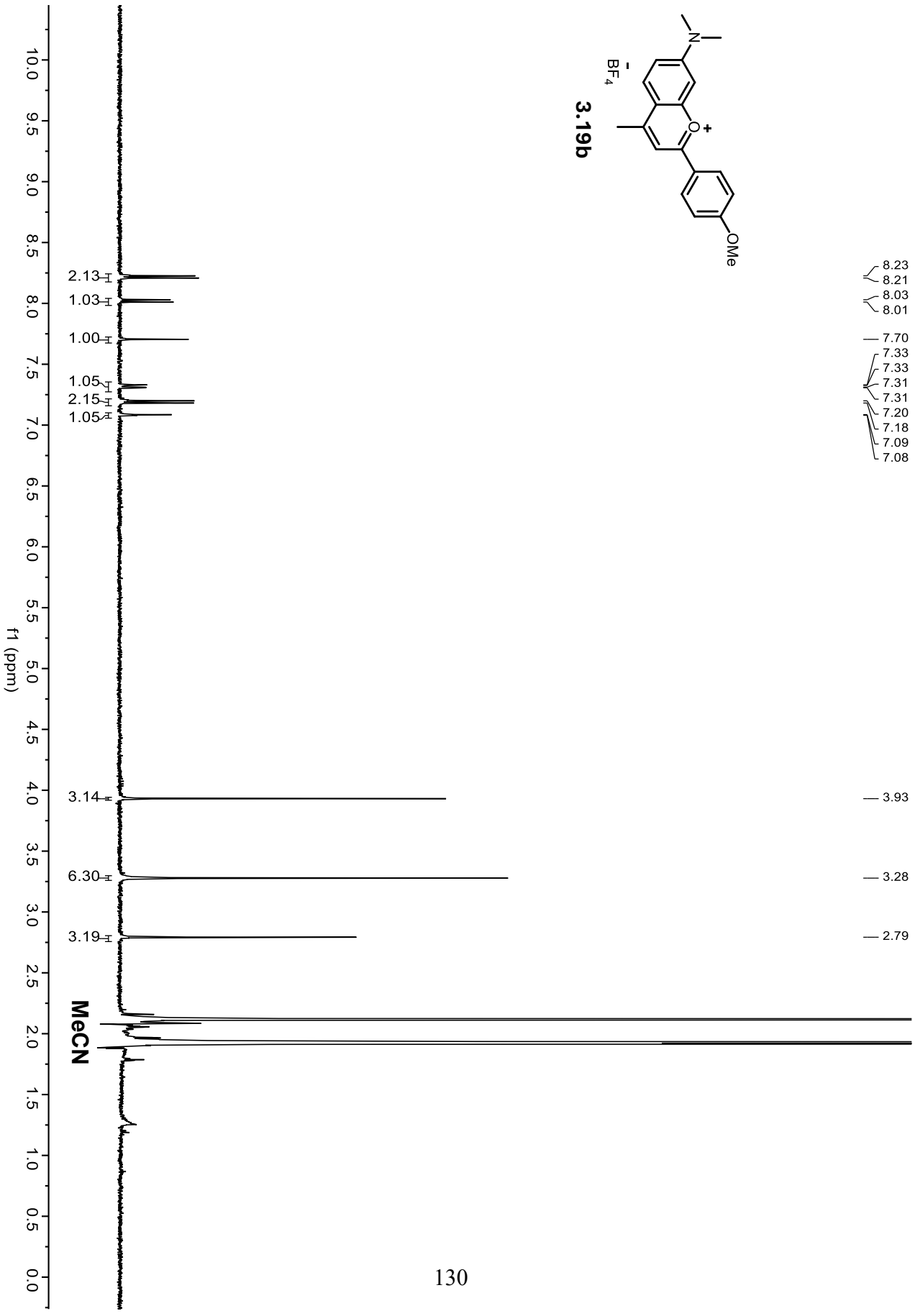
3.19b
BF4
OMe
f1 (ppm)
10.0
9.5
9.0
8.5
8.0
7.5
7.0
6.5
6.0
5.5
5.0
4.5
4.0
3.5
3.0
2.5
2.0
1.5
1.0
0.5
0.0
2.13
1.03
1.00
1.05
2.15
1.05
3.14
6.30
3.19
MeCN
8.23
8.21
8.03
8.01
7.70
7.33
7.33
7.31
7.31
7.20
7.18
7.09
7.08
3.93
3.28
2.79

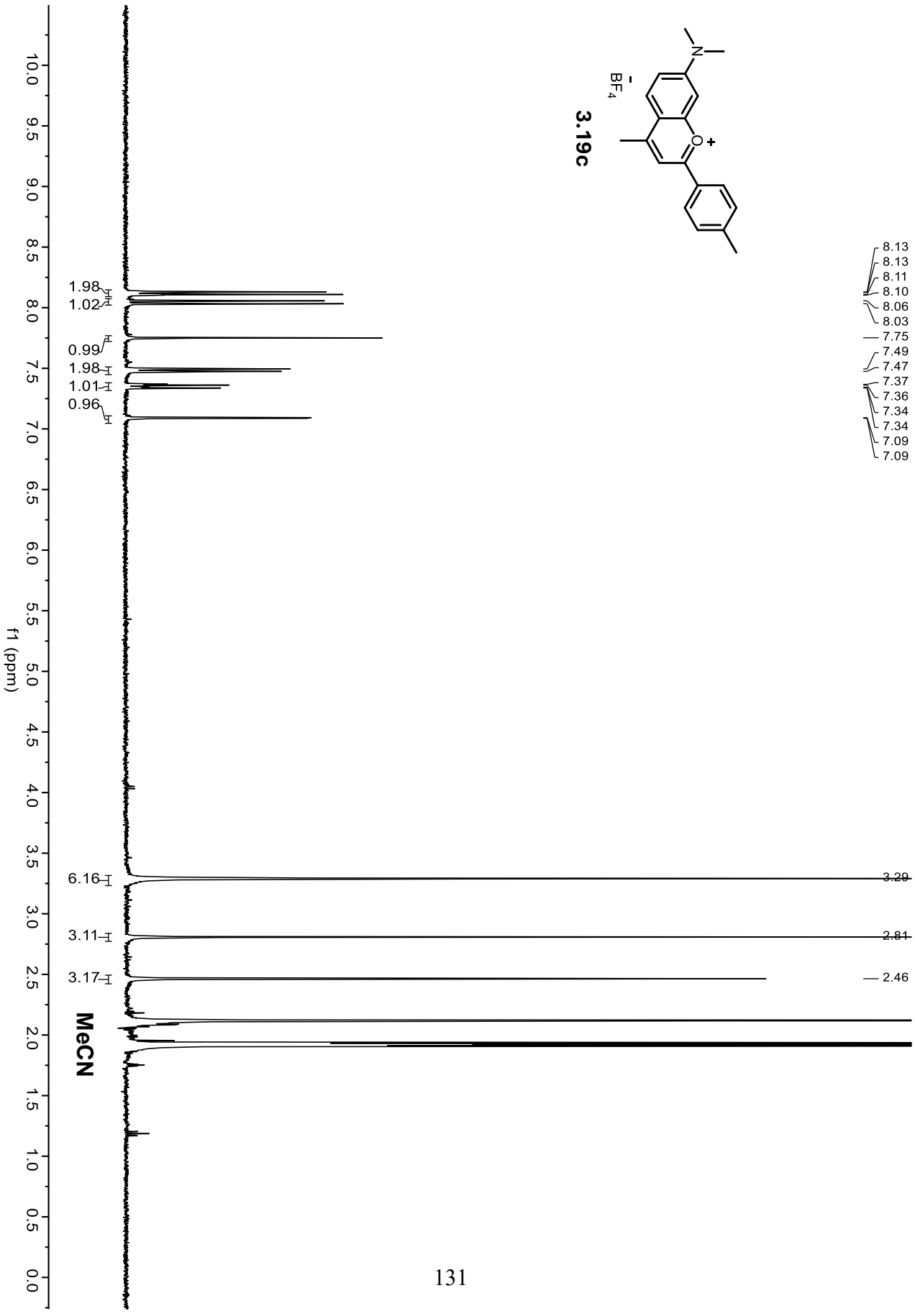
3.19c
BF4
N
O
+
8.13
8.13
8.11
8.10
8.06
8.03
7.75
7.49
7.47
7.37
7.36
7.34
7.34
7.09
7.09
1.98
1.02
0.99
1.98
1.01
0.96
6.16
3.11
3.17
3.29
2.81
2.46
MeCN
f1 (ppm)

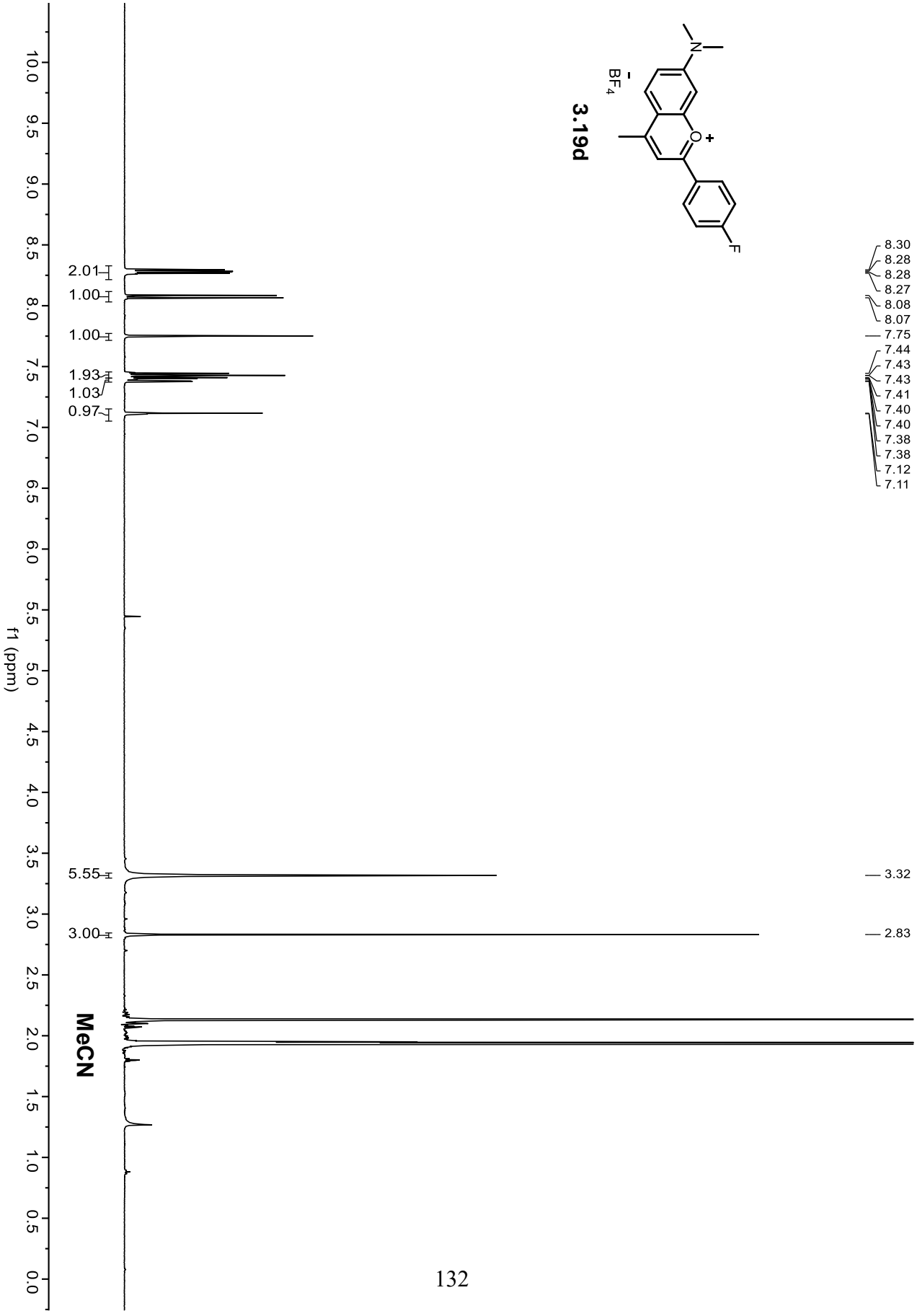
3.19d
BF4
-
+
O
N
F
8.30
8.28
8.28
8.27
8.08
8.07
7.75
7.44
7.43
7.43
7.41
7.40
7.40
7.38
7.38
7.12
7.11
3.32
2.83
2.01
1.00
1.00
1.93
1.03
0.97
5.55
3.00
MeCN
f1 (ppm)
10.0
9.5
9.0
8.5
8.0
7.5
7.0
6.5
6.0
5.5
5.0
4.5
4.0
3.5
3.0
2.5
2.0
1.5
1.0
0.5
0.0

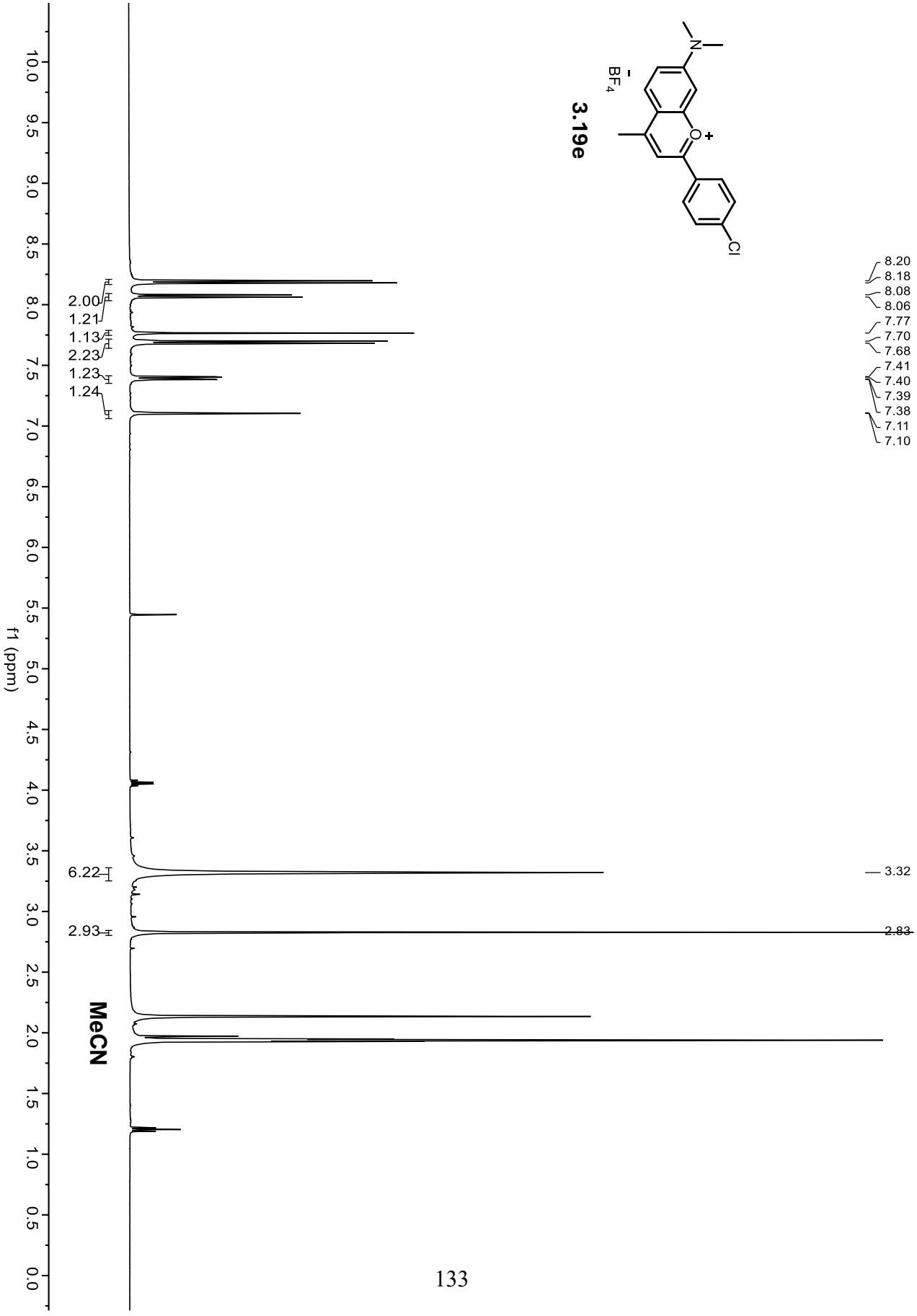
3.19e
BF4
Cl
8.20
8.18
8.08
8.06
7.77
7.70
7.68
7.41
7.40
7.39
7.38
7.11
7.10
2.00
1.21
1.13
2.23
1.23
1.24
6.22
2.93
3.32
2.83
MeCN
f1 (ppm)

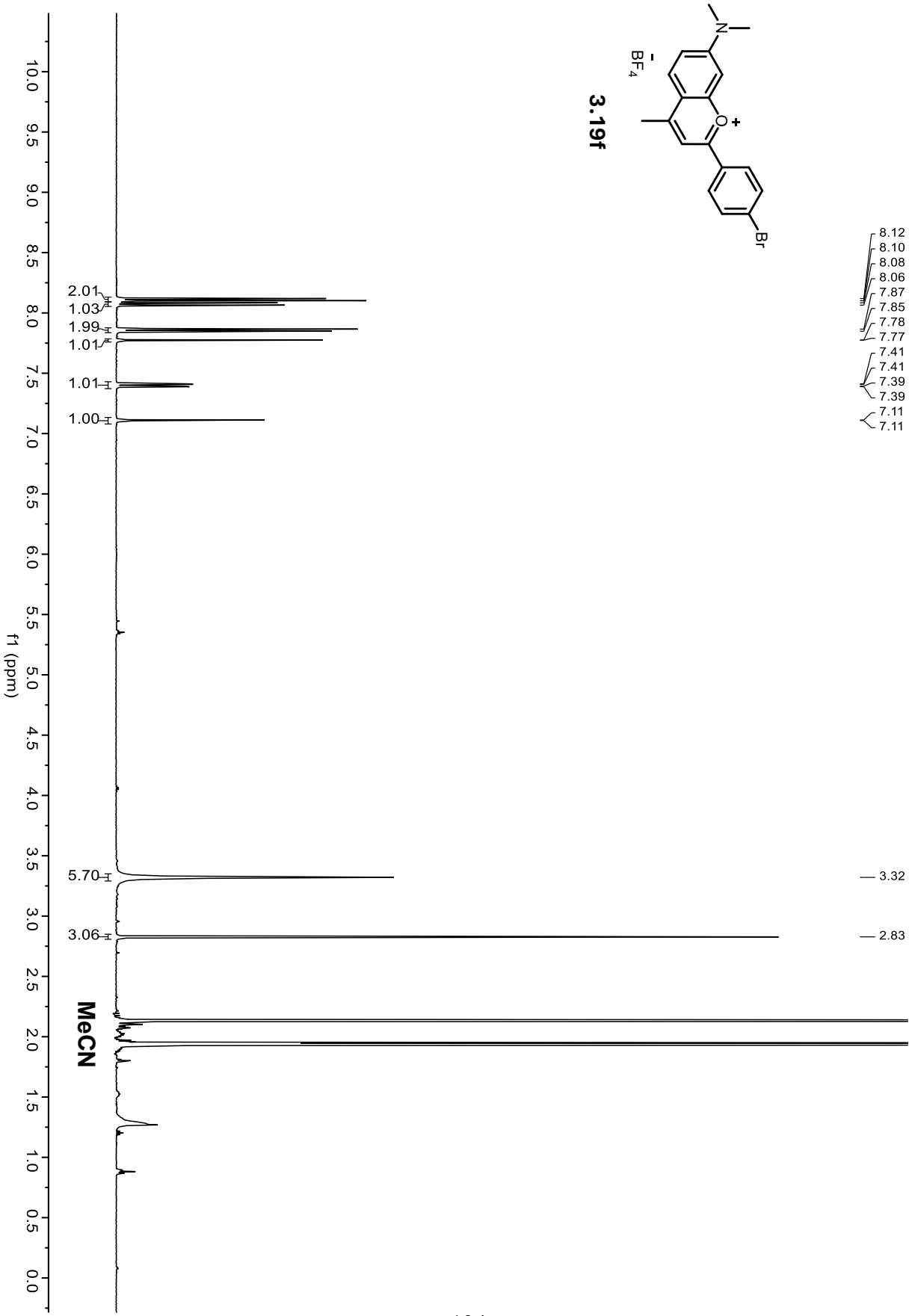
3.19f
BF4
Br
8.12
8.10
8.08
8.06
7.87
7.85
7.78
7.77
7.41
7.41
7.39
7.39
7.11
7.11
2.01
1.03
1.99
1.01
1.01
1.00
5.70
3.06
3.32
2.83
MeCN
f1 (ppm)

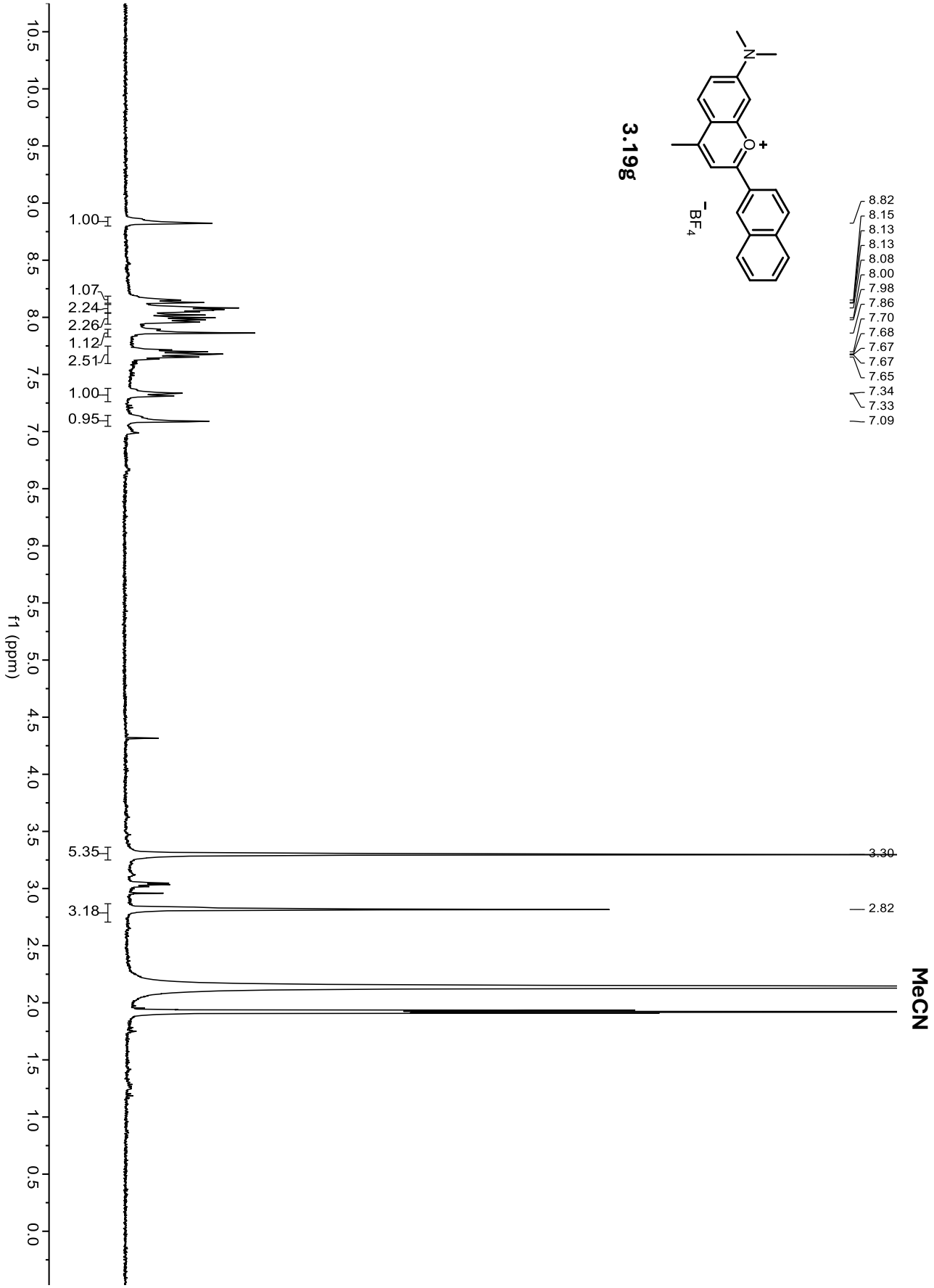
3.19g
MeCN
f1 (ppm)
1.00
1.07
2.24
2.26
1.12
2.51
1.00
0.95
5.35
3.18
8.82
8.15
8.13
8.13
8.08
8.00
7.98
7.86
7.70
7.68
7.67
7.67
7.65
7.34
7.33
7.09
3.30
2.82

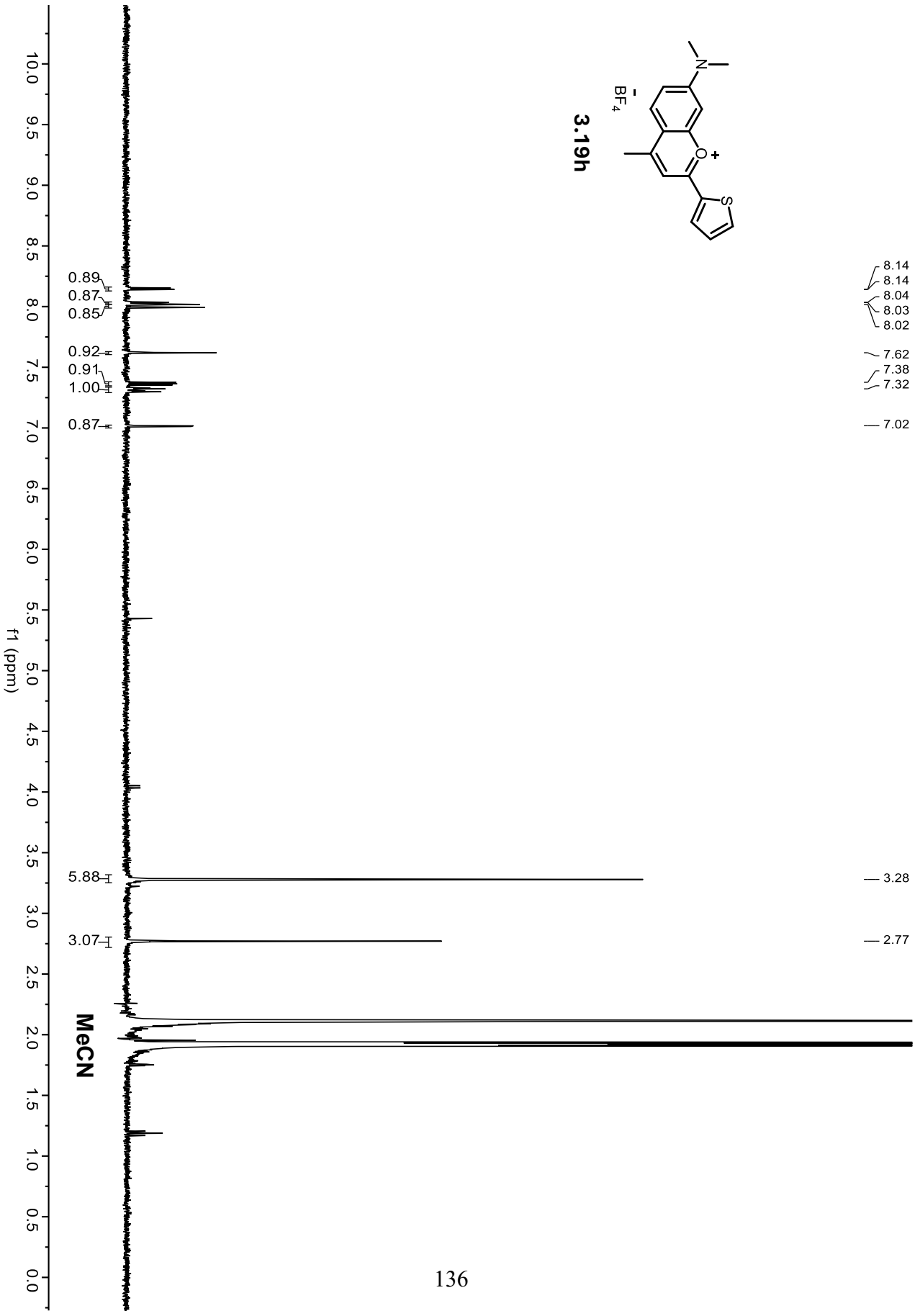
3.19h
BF4
MeCN
f1 (ppm)
0.89
0.87
0.85
0.92
0.91
1.00
0.87
5.88
3.07
8.14
8.14
8.04
8.03
8.02
7.62
7.38
7.32
7.02
3.28
2.77

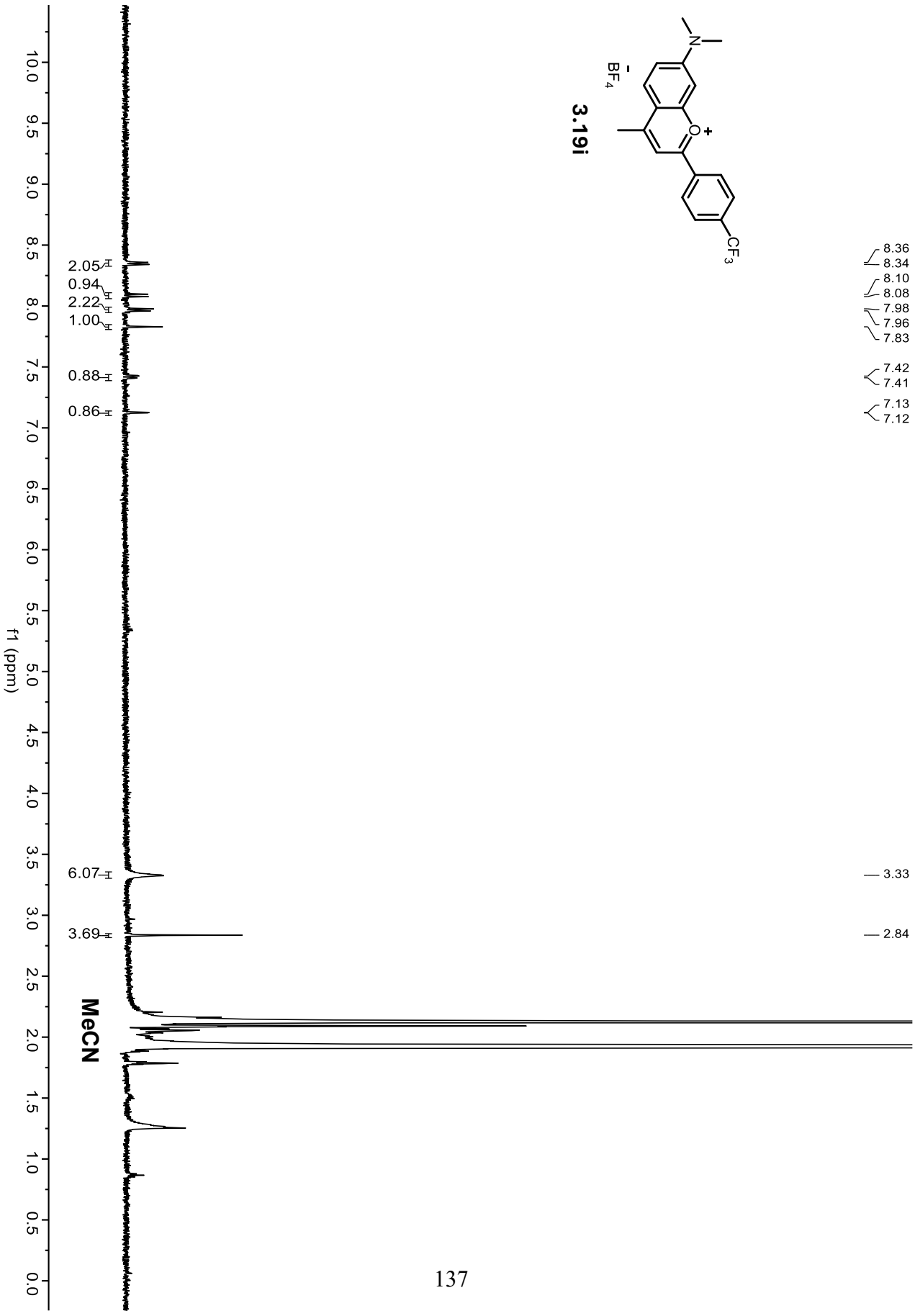
3.19i
BF4
CF3
8.36
8.34
8.10
8.08
7.98
7.96
7.83
7.42
7.41
7.13
7.12
3.33
2.84
2.05
0.94
2.22
1.00
0.88
0.86
6.07
3.69
MeCN
f1 (ppm)

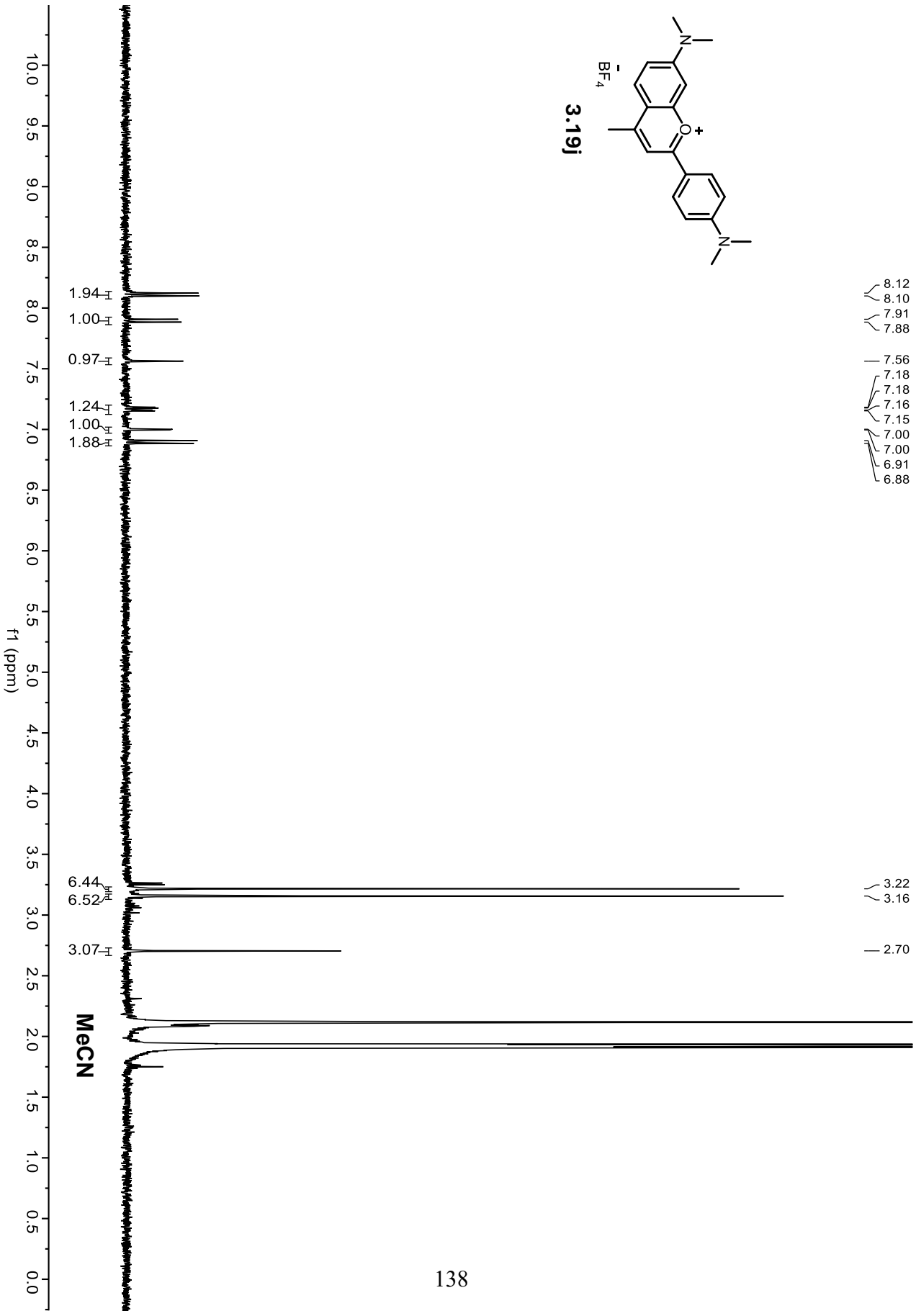
3.19j
BF4
-
O
+
N
N
1.94
1.00
0.97
1.24
1.00
1.88
6.44
6.52
3.07
MeCN
8.12
8.10
7.91
7.88
7.56
7.18
7.18
7.16
7.15
7.00
7.00
6.91
6.88
3.22
3.16
2.70
f1 (ppm)

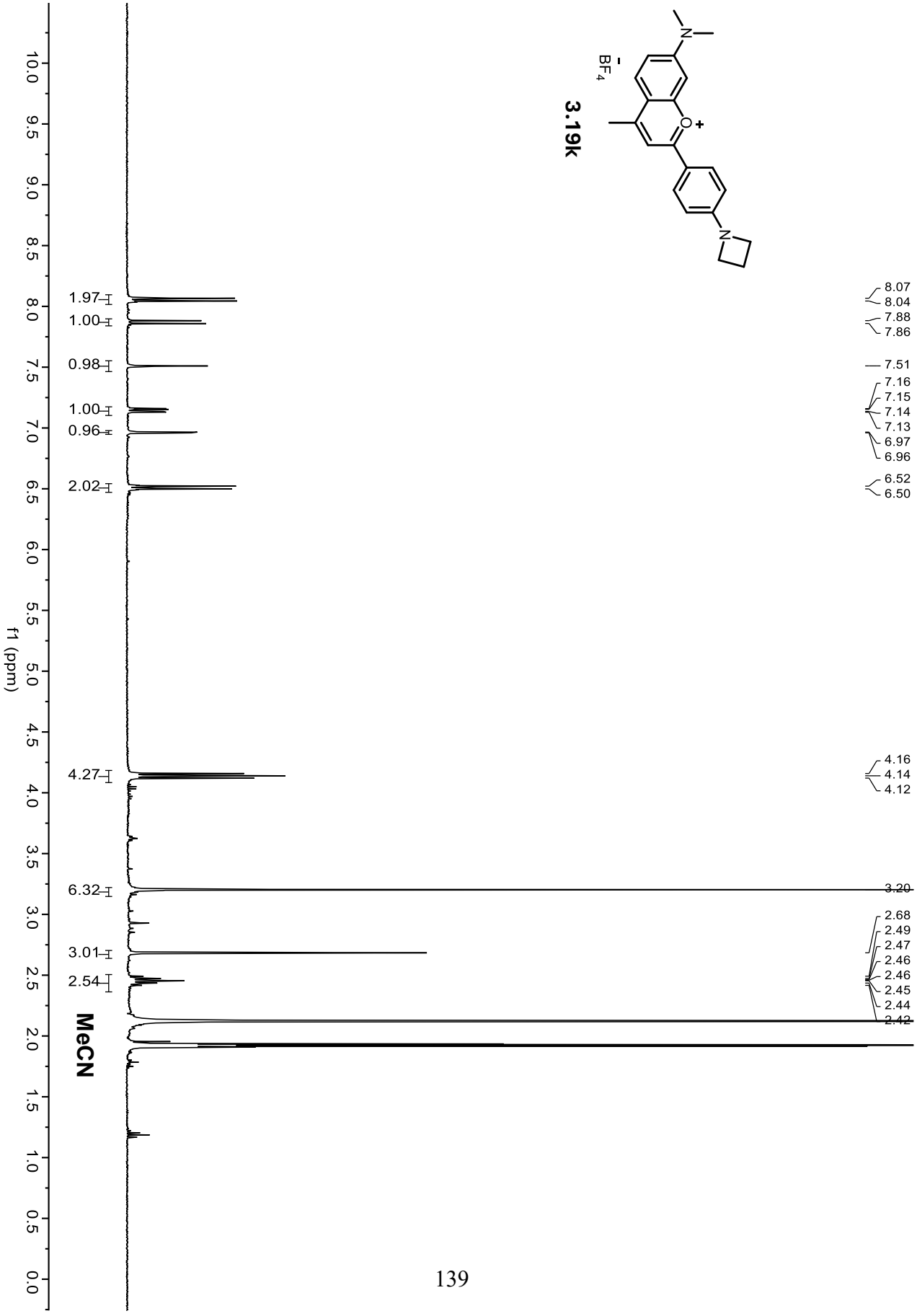
3.19k
BF4
N
O
N
8.07
8.04
7.88
7.86
7.51
7.16
7.15
7.14
7.13
6.97
6.96
6.52
6.50
4.16
4.14
4.12
3.20
2.68
2.49
2.47
2.46
2.46
2.45
2.44
2.42
1.97
1.00
0.98
1.00
0.96
2.02
4.27
6.32
3.01
2.54
MeCN
f1 (ppm)
10.0
9.5
9.0
8.5
8.0
7.5
7.0
6.5
6.0
5.5
5.0
4.5
4.0
3.5
3.0
2.5
2.0
1.5
1.0
0.5
0.0

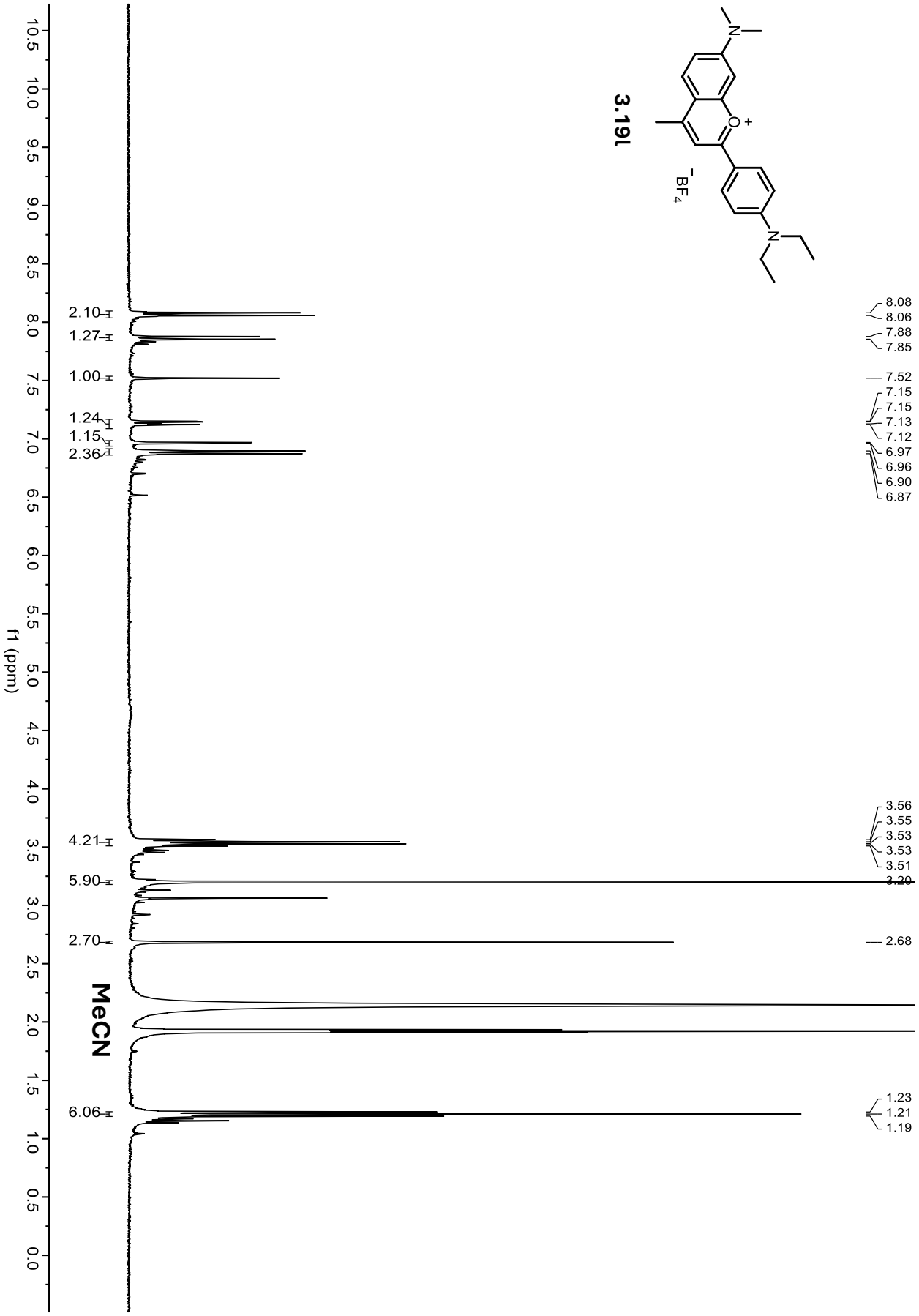
3.19l
MeCN
f1 (ppm)
2.10
1.27
1.00
1.24
1.15
2.36
4.21
5.90
2.70
6.06
8.08
8.06
7.88
7.85
7.52
7.15
7.15
7.13
7.12
6.97
6.96
6.90
6.87
3.56
3.55
3.53
3.53
3.51
3.20
2.68
1.23
1.21
1.19

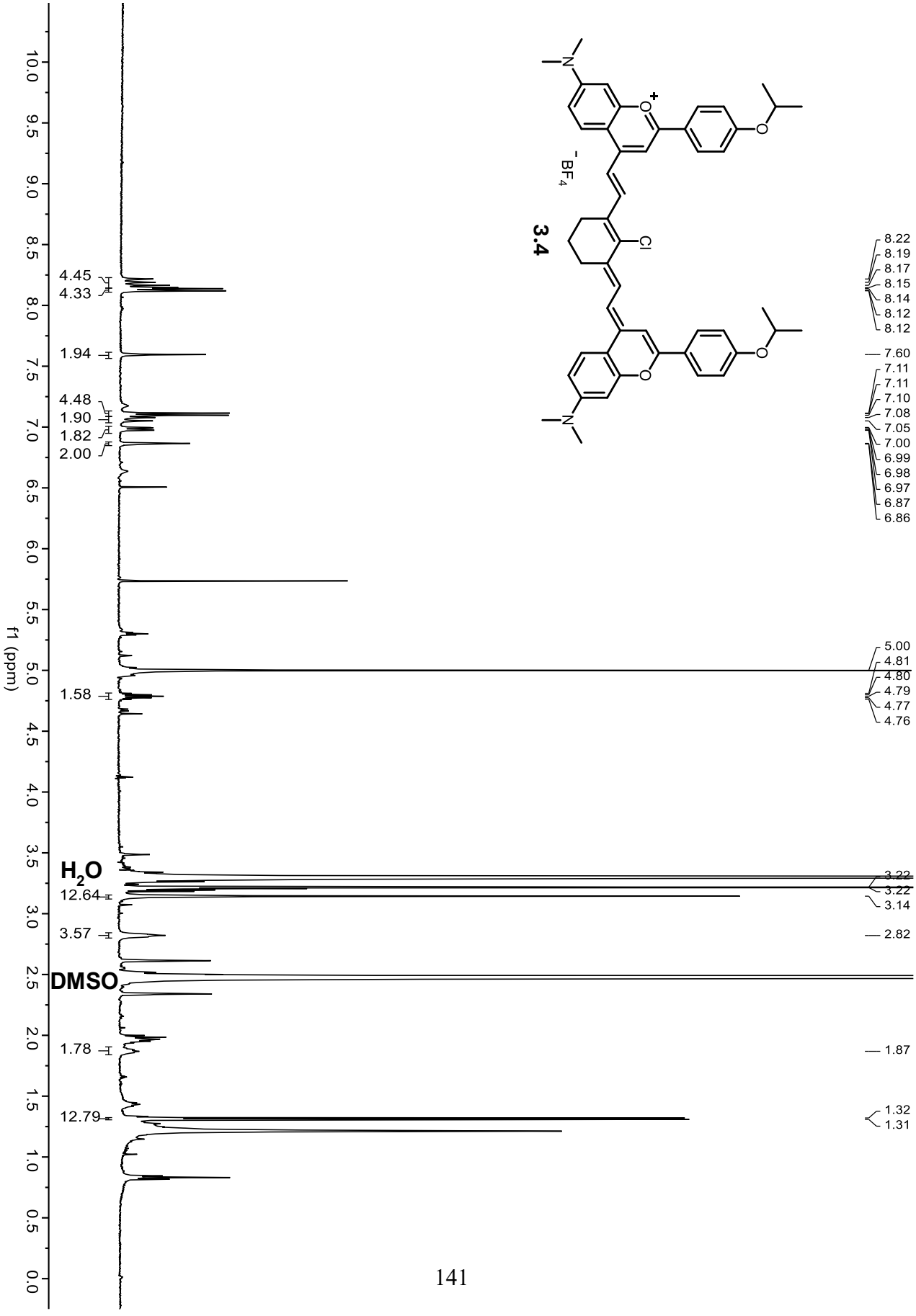
3.4
$^{-}BF_4$
Cl
f1 (ppm)
10.0
9.5
9.0
8.5
8.0
7.5
7.0
6.5
6.0
5.5
5.0
4.5
4.0
3.5
3.0
2.5
2.0
1.5
1.0
0.5
0.0
4.45
4.33
1.94
4.48
1.90
1.82
2.00
1.58
H_2O
12.64
3.57
DMSO
1.78
12.79
8.22
8.19
8.17
8.15
8.14
8.12
8.12
7.60
7.11
7.11
7.10
7.08
7.05
7.00
6.99
6.98
6.97
6.87
6.86
5.00
4.81
4.80
4.79
4.77
4.76
3.22
3.22
3.14
2.82
1.87
1.32
1.31

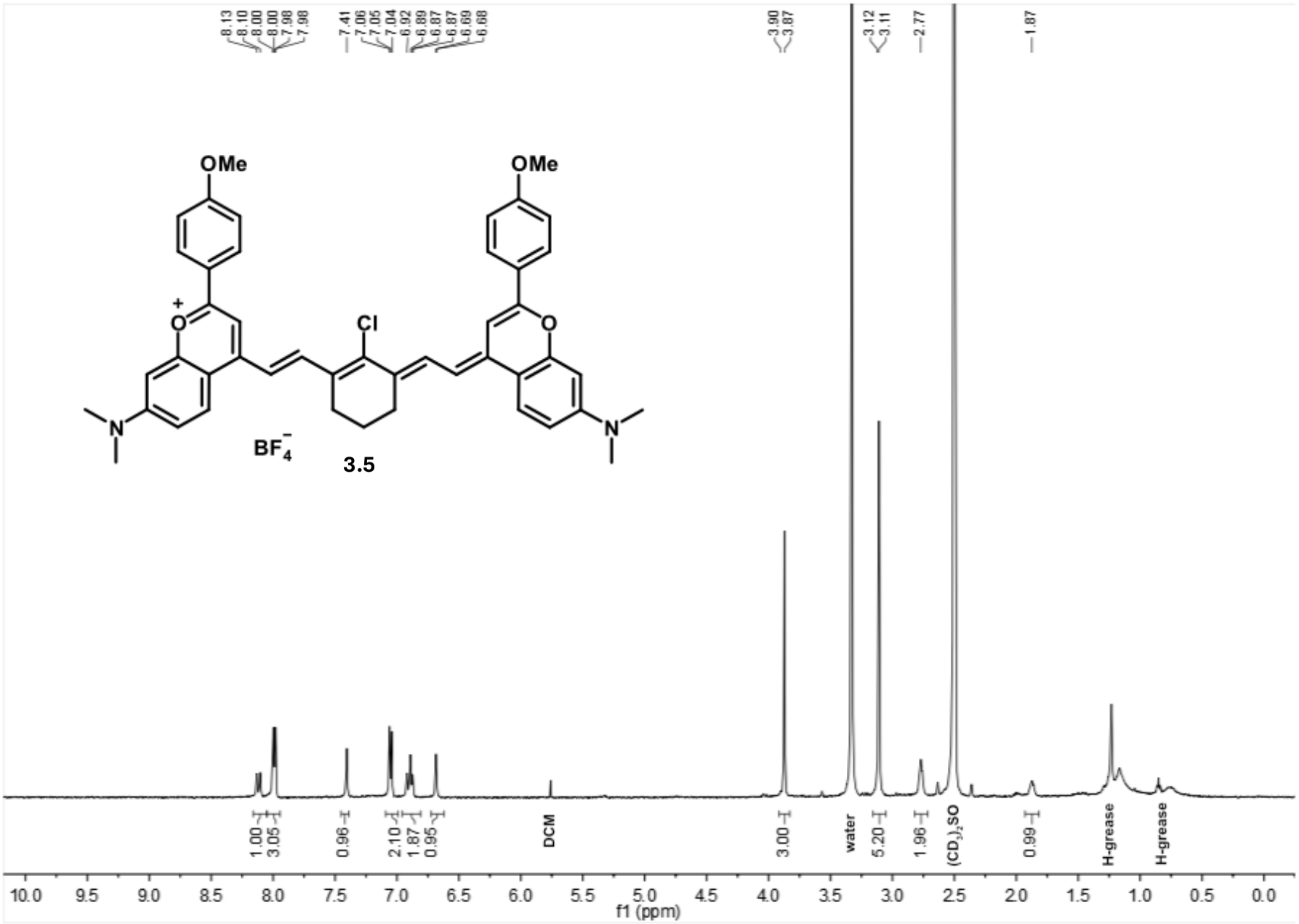
8.13
8.10
8.00
8.00
7.98
7.98
7.41
7.06
7.05
7.04
6.92
6.89
6.87
6.87
6.69
6.68
3.90
3.87
3.12
3.11
2.77
1.87
OMe
OMe
O
Cl
O
N
N
BF4−
3.5
1.00
3.05
0.96
2.10
1.87
0.95
DCM
3.00
water
5.20
1.96
(CD3)2SO
0.99
H-grease
H-grease
10.0
9.5
9.0
8.5
8.0
7.5
7.0
6.5
6.0
5.5
5.0
4.5
4.0
3.5
3.0
2.5
2.0
1.5
1.0
0.5
0.0
f1 (ppm)

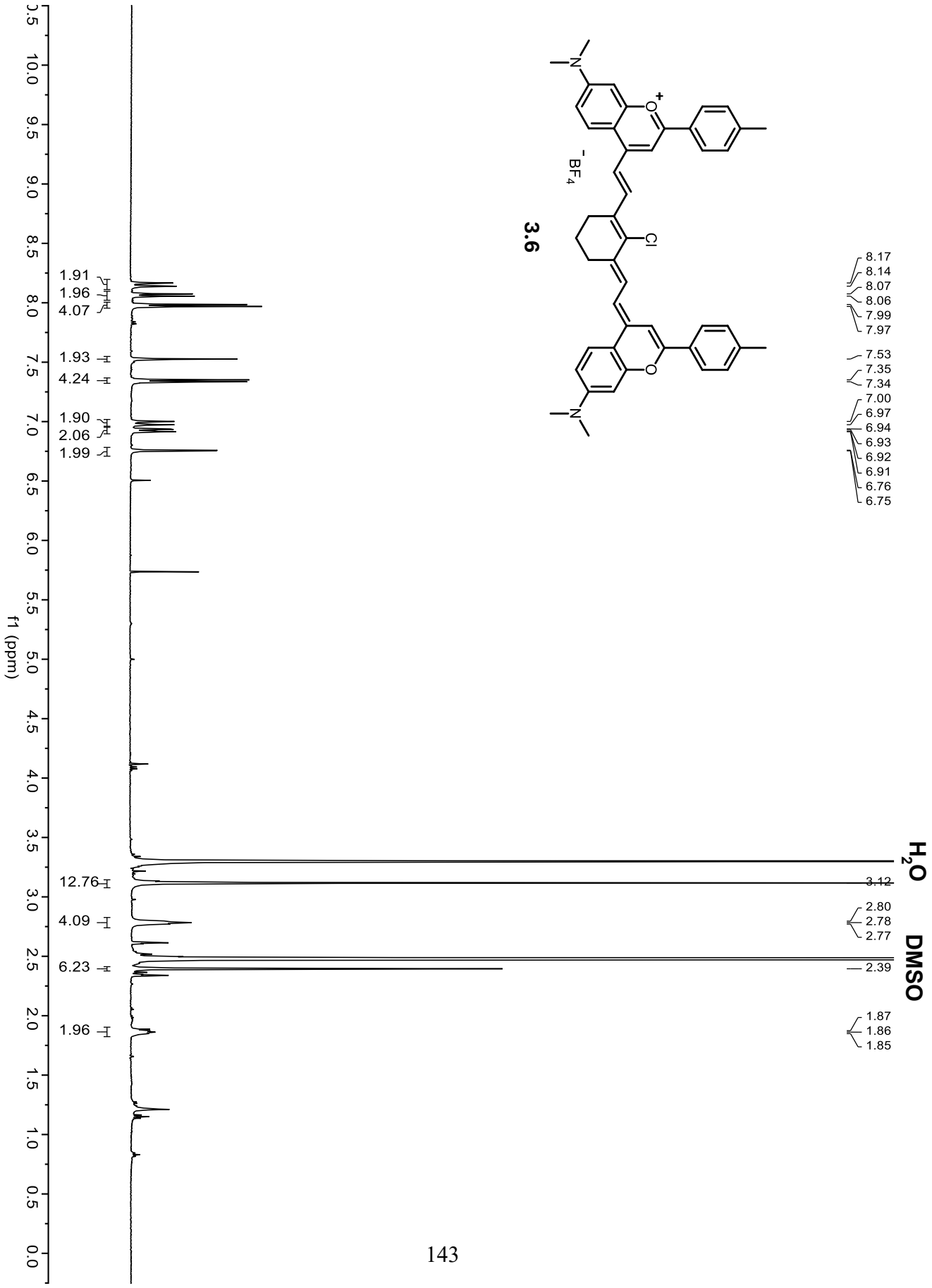
3.6
$^{-}BF_4$
Cl
O
N
8.17
8.14
8.07
8.06
7.99
7.97
7.53
7.35
7.34
7.00
6.97
6.94
6.93
6.92
6.91
6.76
6.75
H_2O
3.12
DMSO
2.80
2.78
2.77
2.39
1.87
1.86
1.85
1.91
1.96
4.07
1.93
4.24
1.90
2.06
1.99
12.76
4.09
6.23
1.96
f1 (ppm)

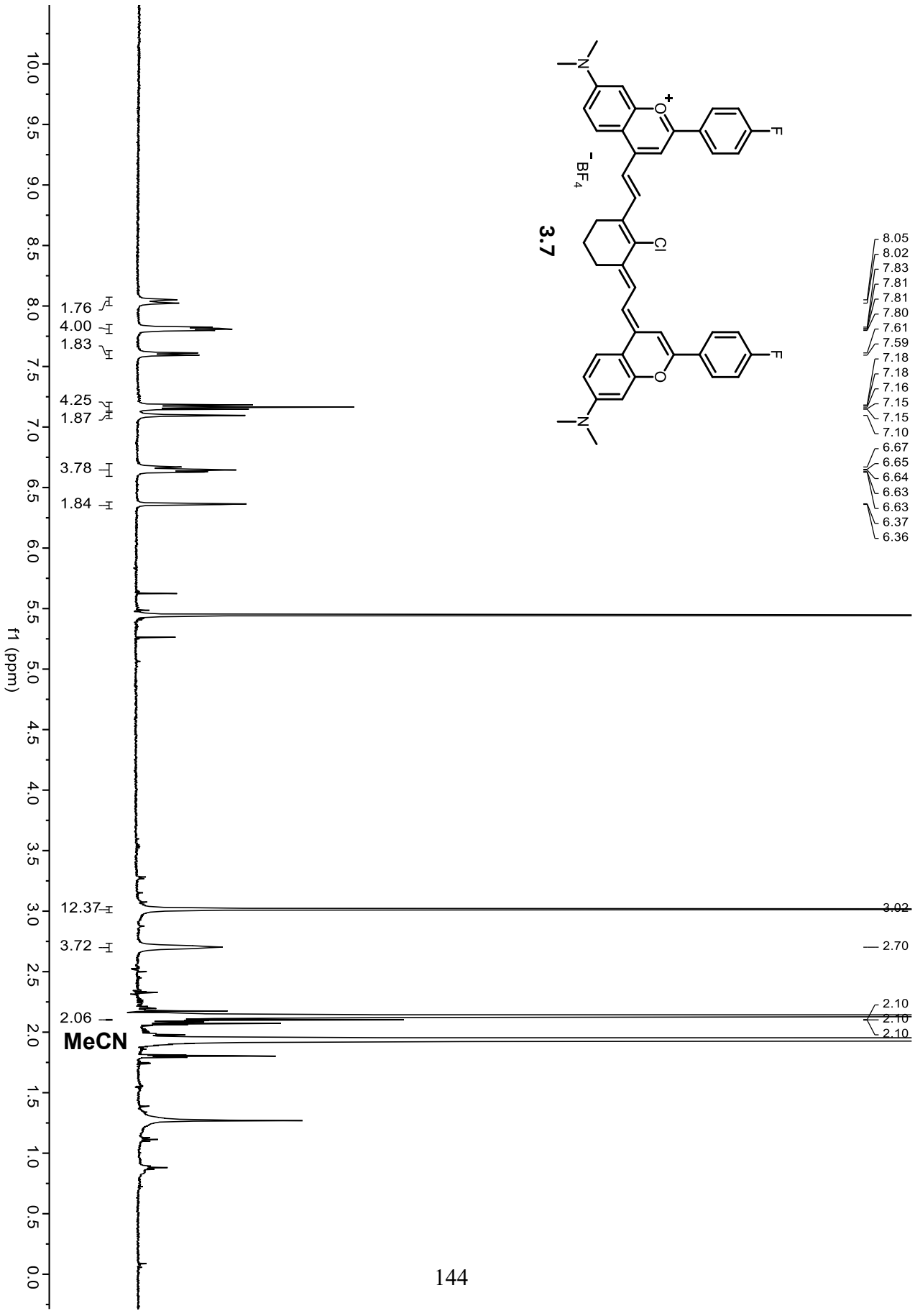
3.7
MeCN
f1 (ppm)
1.76
4.00
1.83
4.25
1.87
3.78
1.84
12.37
3.72
2.06
3.02
2.70
2.10
2.10
2.10
8.05
8.02
7.83
7.81
7.81
7.80
7.61
7.59
7.18
7.18
7.16
7.15
7.15
7.10
6.67
6.65
6.64
6.63
6.63
6.37
6.36

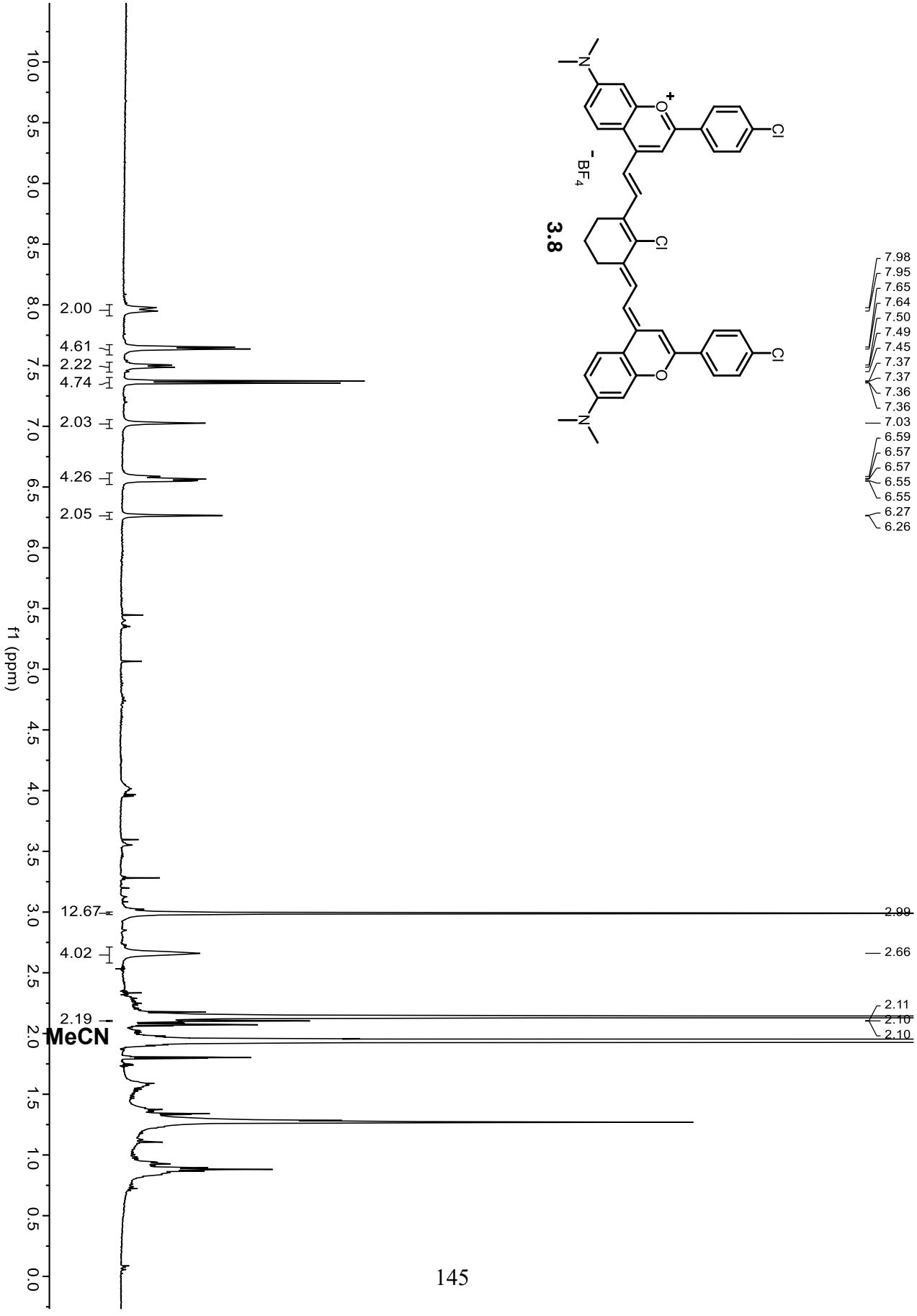
3.8
MeCN
f1 (ppm)

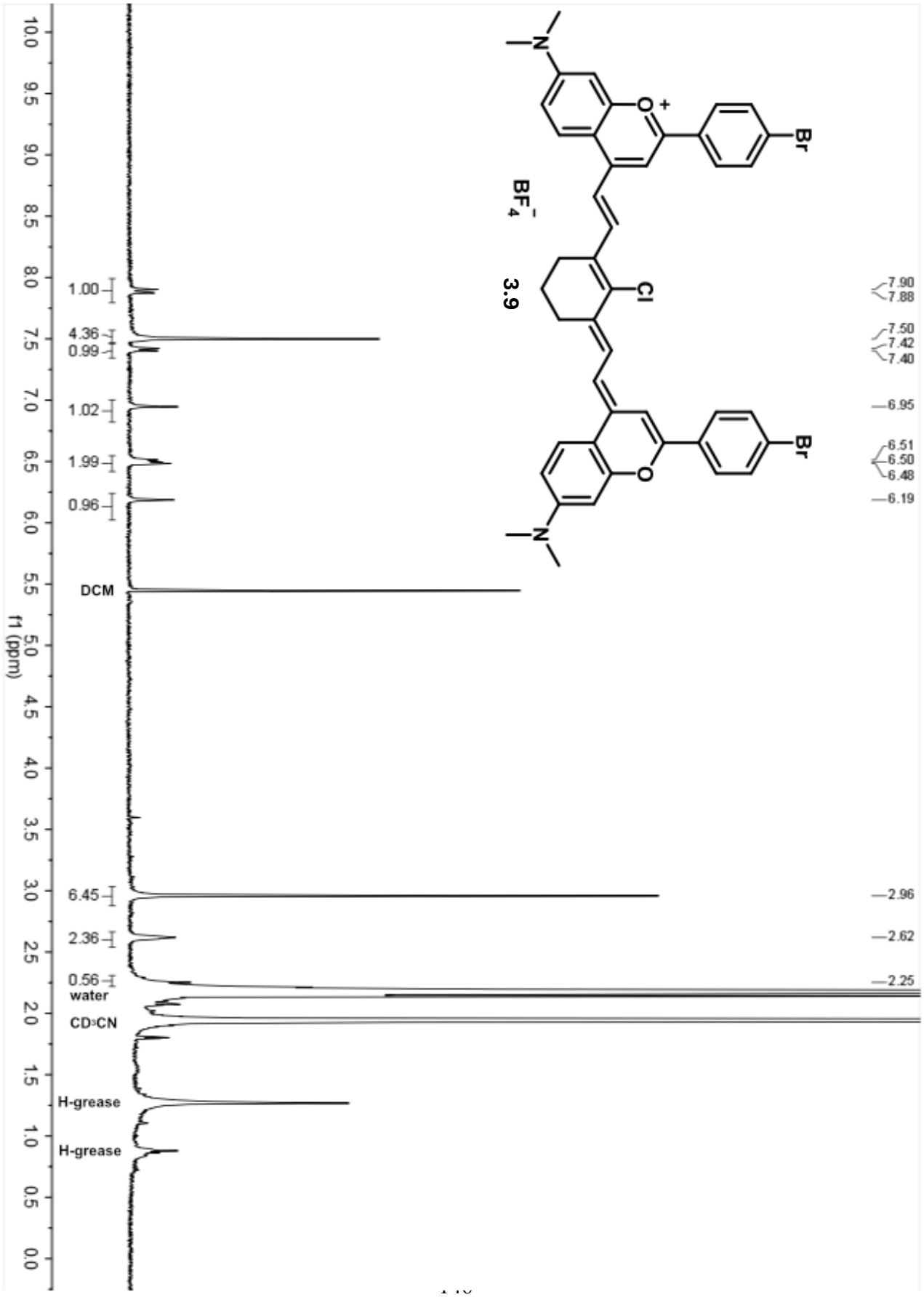
3.9
BF4−
Br
Cl
Br
7.90
7.88
7.50
7.42
7.40
6.95
6.51
6.50
6.48
6.19
2.96
2.62
2.25
1.00
4.36
0.99
1.02
1.99
0.96
DCM
6.45
2.36
0.56
water
CD3CN
H-grease
H-grease
f1 (ppm)

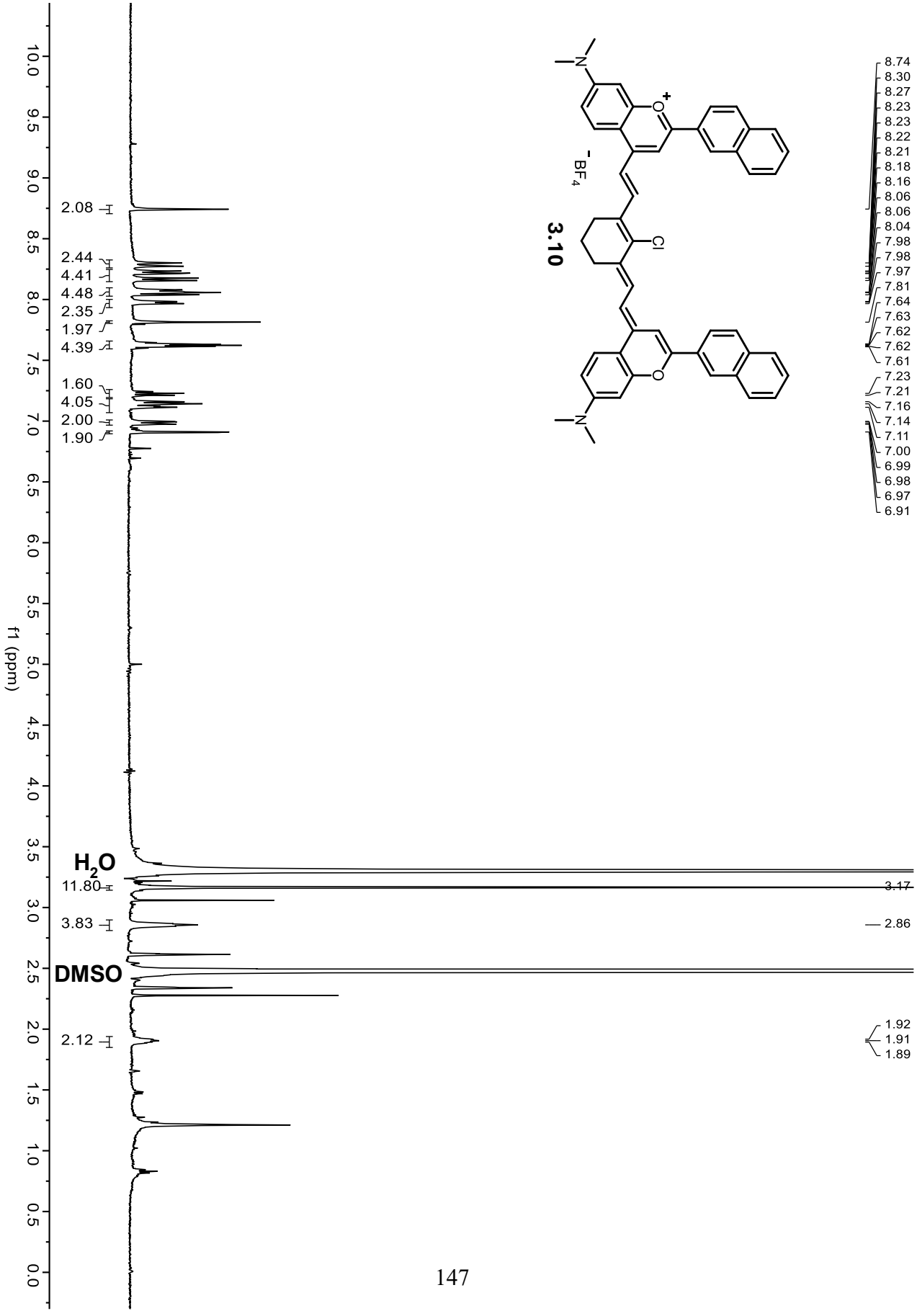
3.10
8.74
8.30
8.27
8.23
8.23
8.22
8.21
8.18
8.16
8.06
8.06
8.04
7.98
7.98
7.97
7.81
7.64
7.63
7.62
7.62
7.61
7.23
7.21
7.16
7.14
7.11
7.00
6.99
6.98
6.97
6.91
2.08
2.44
4.41
4.48
2.35
1.97
4.39
1.60
4.05
2.00
1.90
H2O
11.80
3.83
DMSO
2.12
3.17
2.86
1.92
1.91
1.89
f1 (ppm)

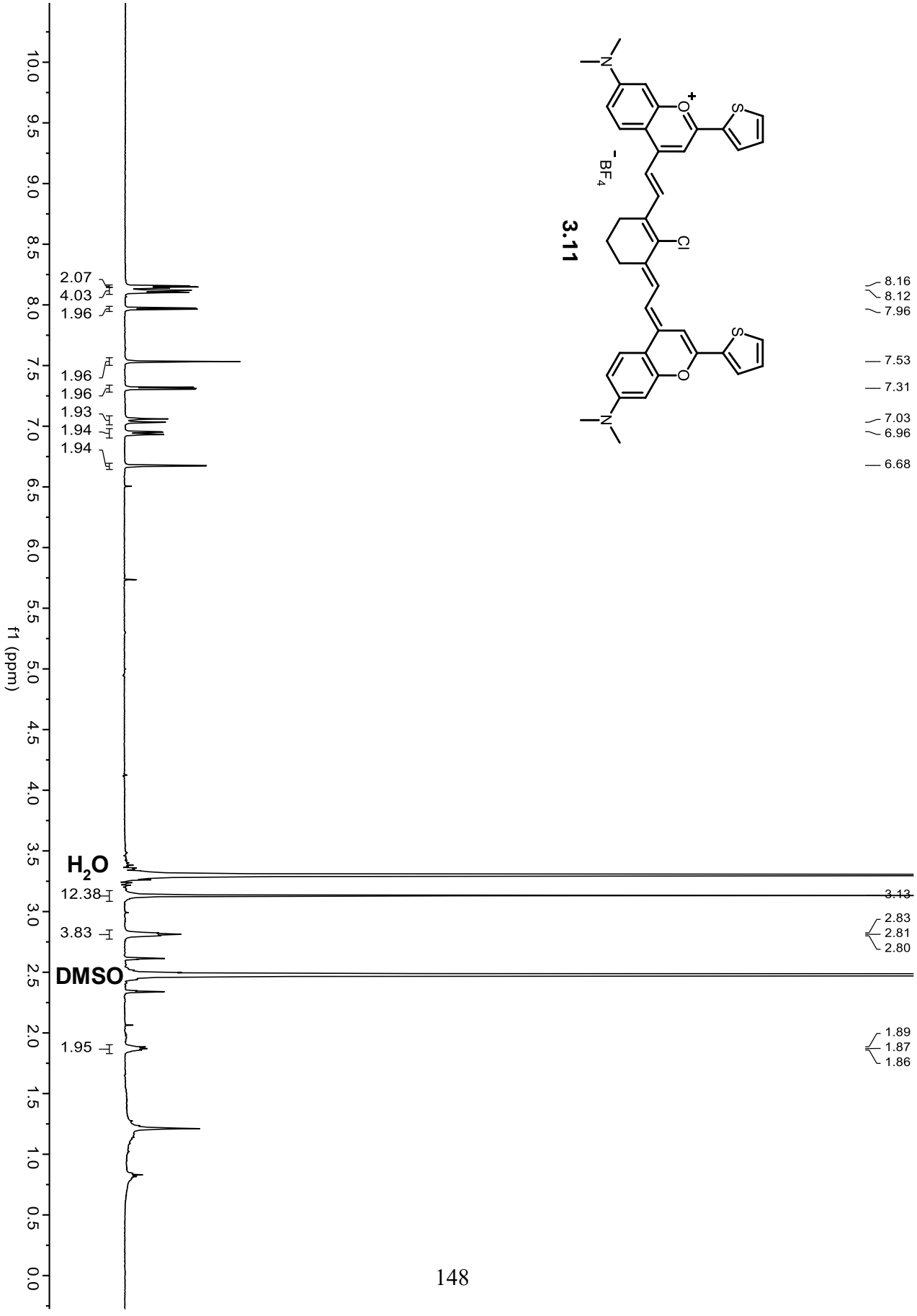
3.11
Cl
S
O
N
BF4
2.07
4.03
1.96
1.96
1.96
1.93
1.94
1.94
8.16
8.12
7.96
7.53
7.31
7.03
6.96
6.68
H2O
12.38
3.83
DMSO
1.95
3.13
2.83
2.81
2.80
1.89
1.87
1.86
f1 (ppm)

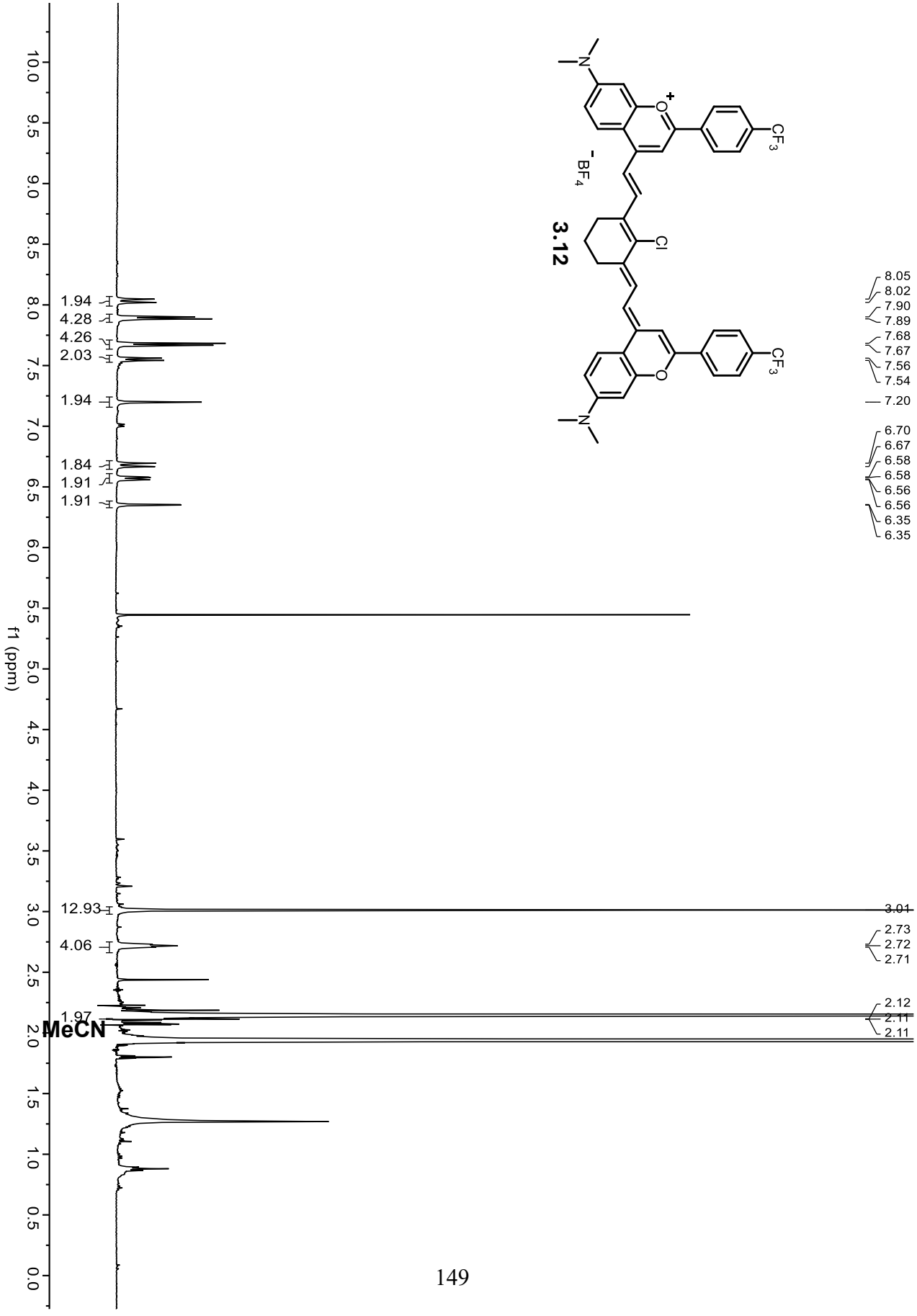
3.12
MeCN
f1 (ppm)

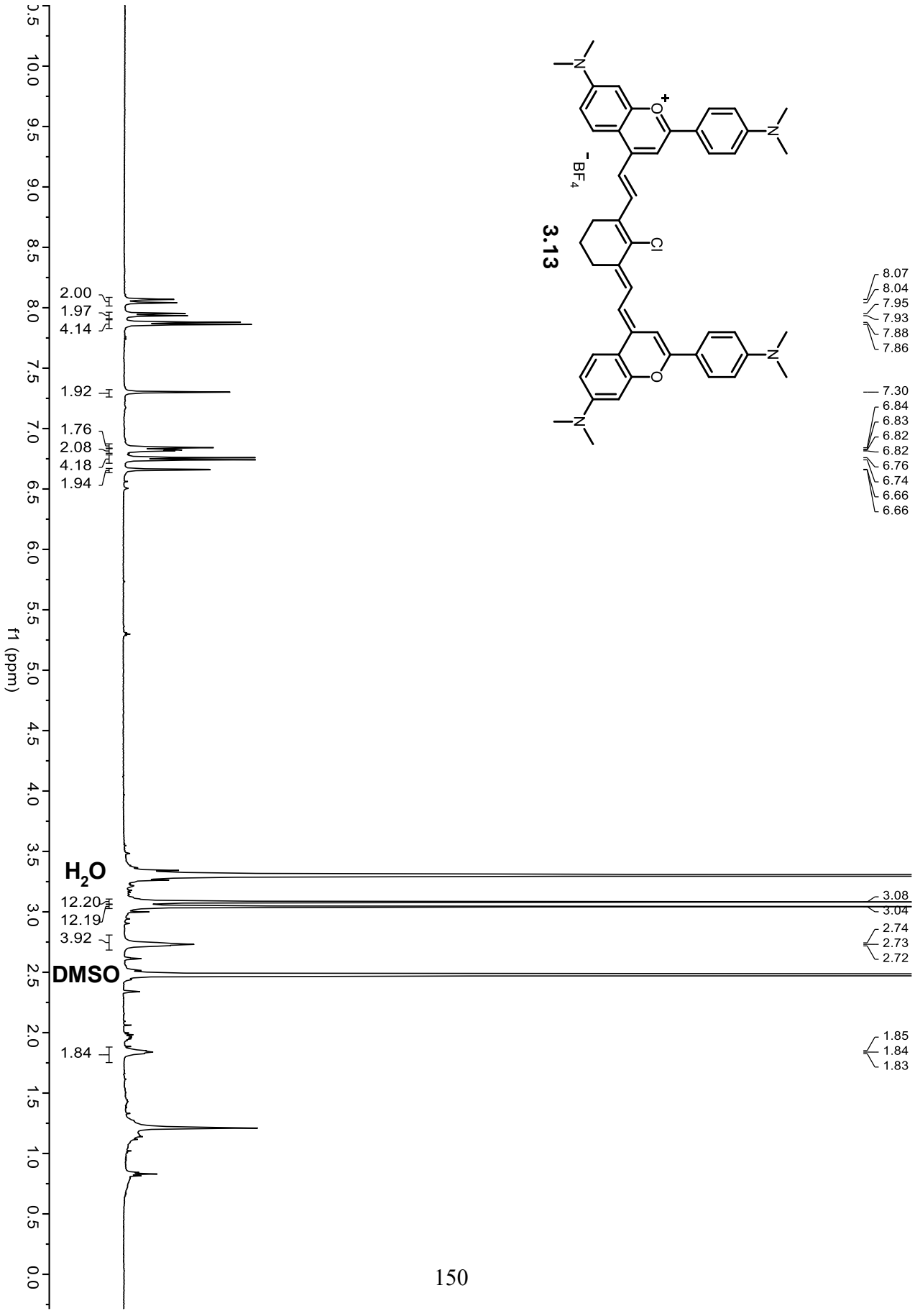
3.13
BF_4^-
Cl
O
N
f1 (ppm)
10.5
10.0
9.5
9.0
8.5
8.0
7.5
7.0
6.5
6.0
5.5
5.0
4.5
4.0
3.5
3.0
2.5
2.0
1.5
1.0
0.5
0.0
2.00
1.97
4.14
1.92
1.76
2.08
4.18
1.94
H_2O
12.20
12.19
3.92
DMSO
1.84
8.07
8.04
7.95
7.93
7.88
7.86
7.30
6.84
6.83
6.82
6.82
6.76
6.74
6.66
6.66
3.08
3.04
2.74
2.73
2.72
1.85
1.84
1.83

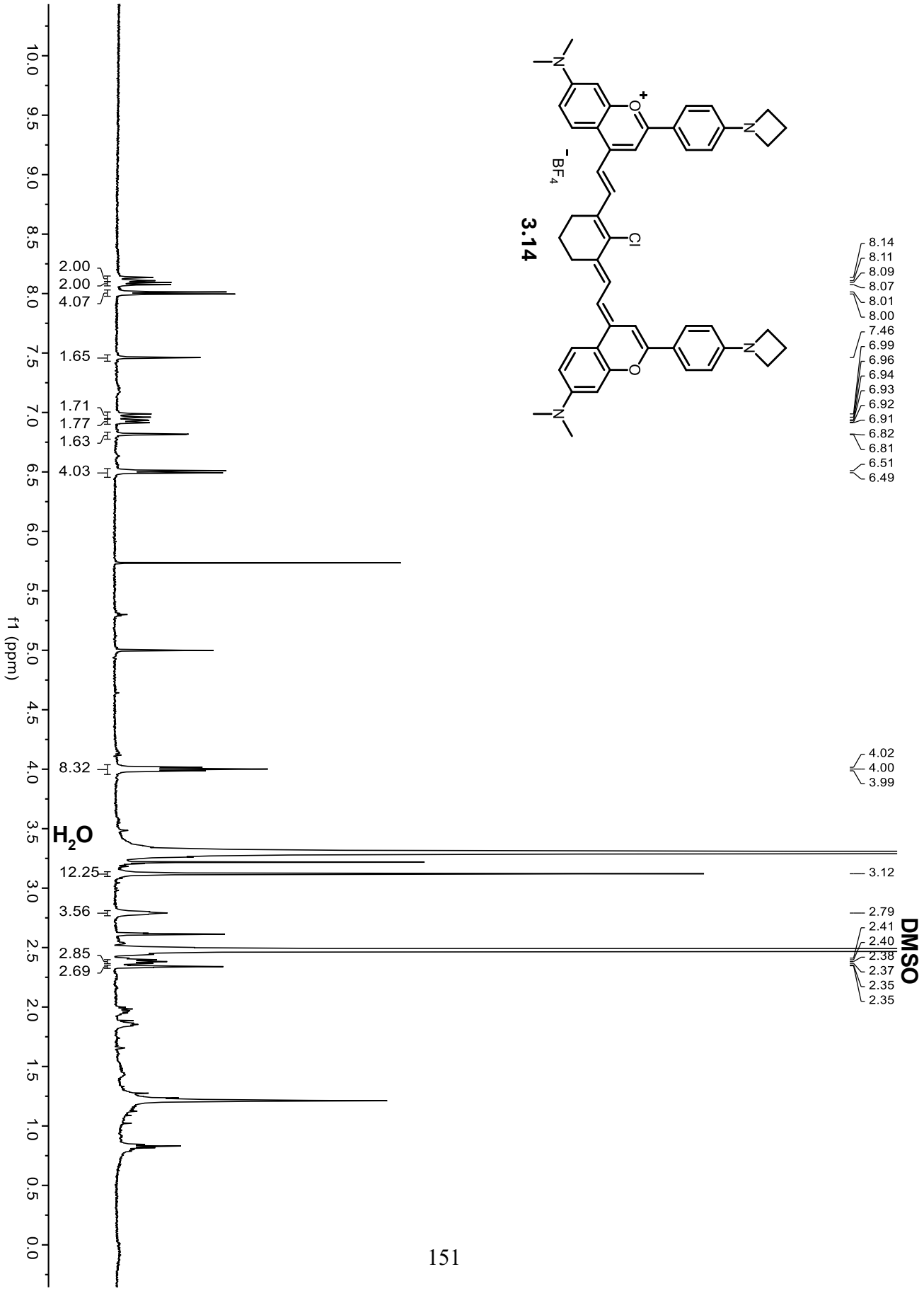
3.14
f1 (ppm)
H2O
DMSO
2.00
2.00
4.07
1.65
1.71
1.77
1.63
4.03
8.32
12.25
3.56
2.85
2.69
8.14
8.11
8.09
8.07
8.01
8.00
7.46
6.99
6.96
6.94
6.93
6.92
6.91
6.82
6.81
6.51
6.49
4.02
4.00
3.99
3.12
2.79
2.41
2.40
2.38
2.37
2.35
2.35

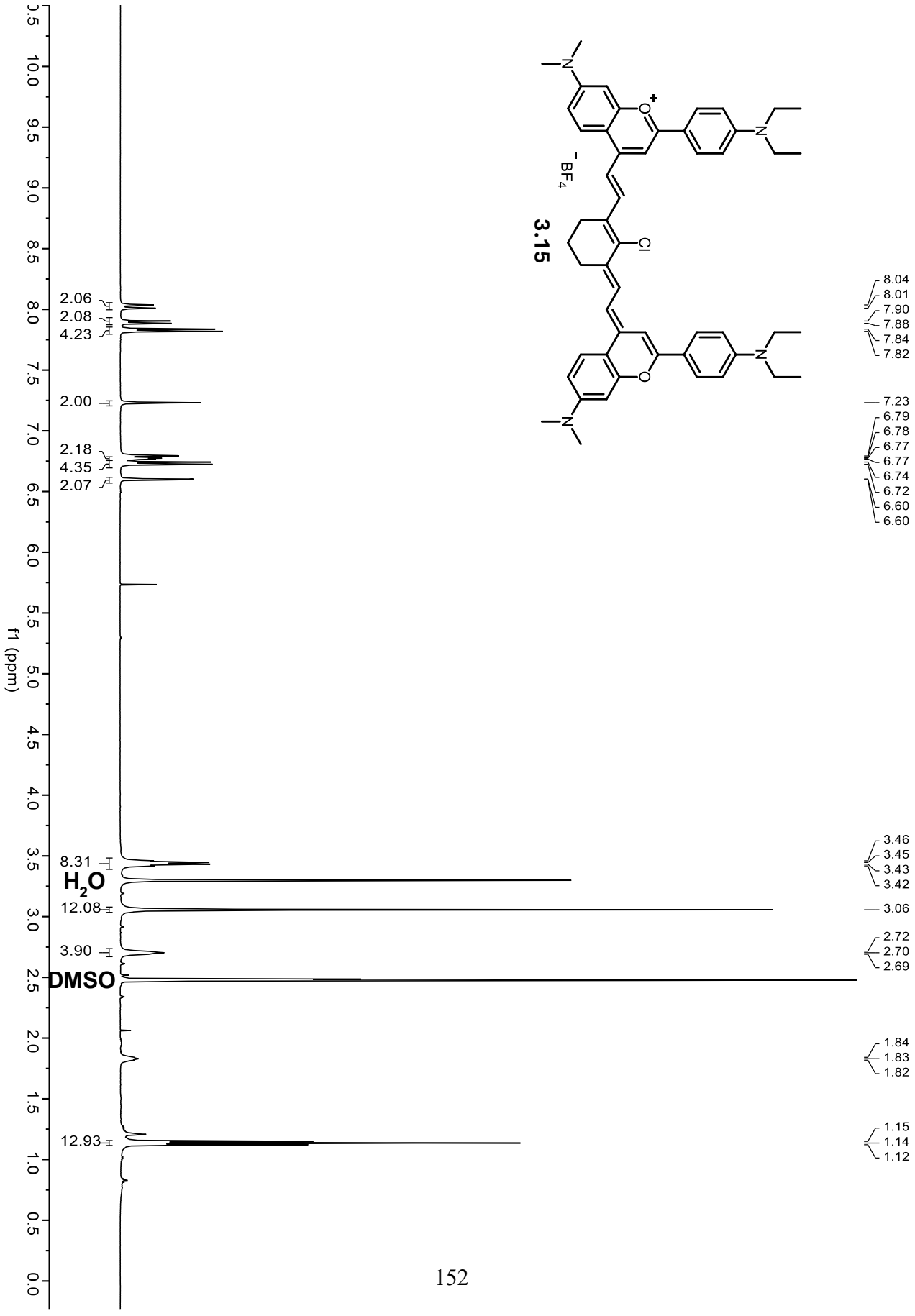
3.15
f1 (ppm)
2.06
2.08
4.23
2.00
2.18
4.35
2.07
8.31
H2O
12.08
3.90
DMSO
12.93
8.04
8.01
7.90
7.88
7.84
7.82
7.23
6.79
6.78
6.77
6.77
6.74
6.72
6.60
6.60
3.46
3.45
3.43
3.42
3.06
2.72
2.70
2.69
1.84
1.83
1.82
1.15
1.14
1.12

3.6.2 Absorbance Spectra

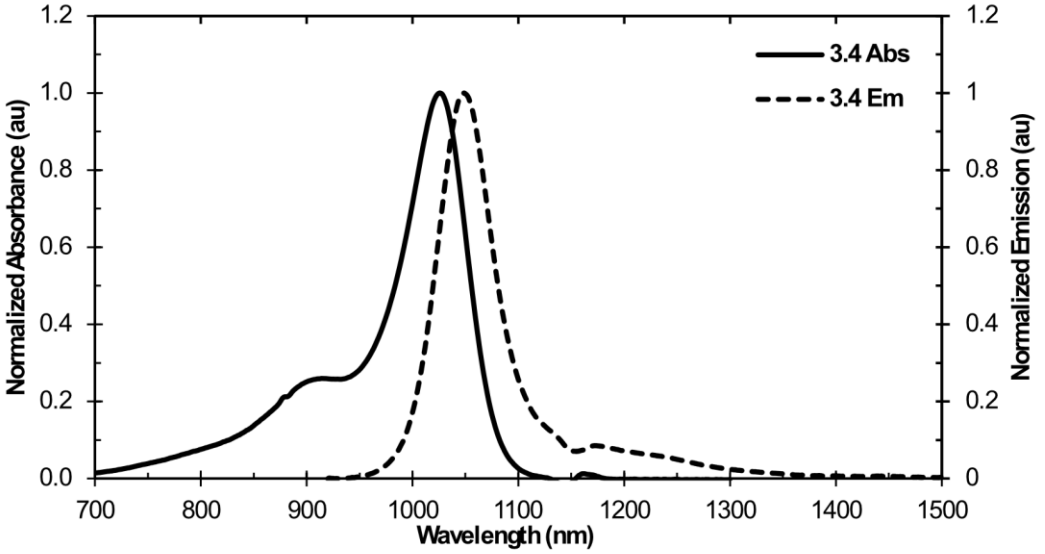

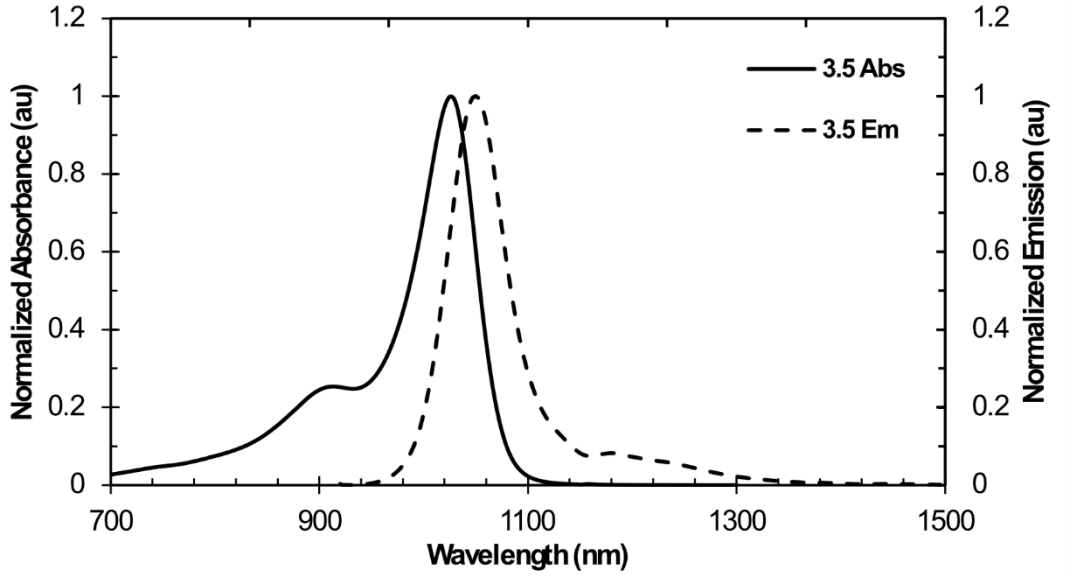

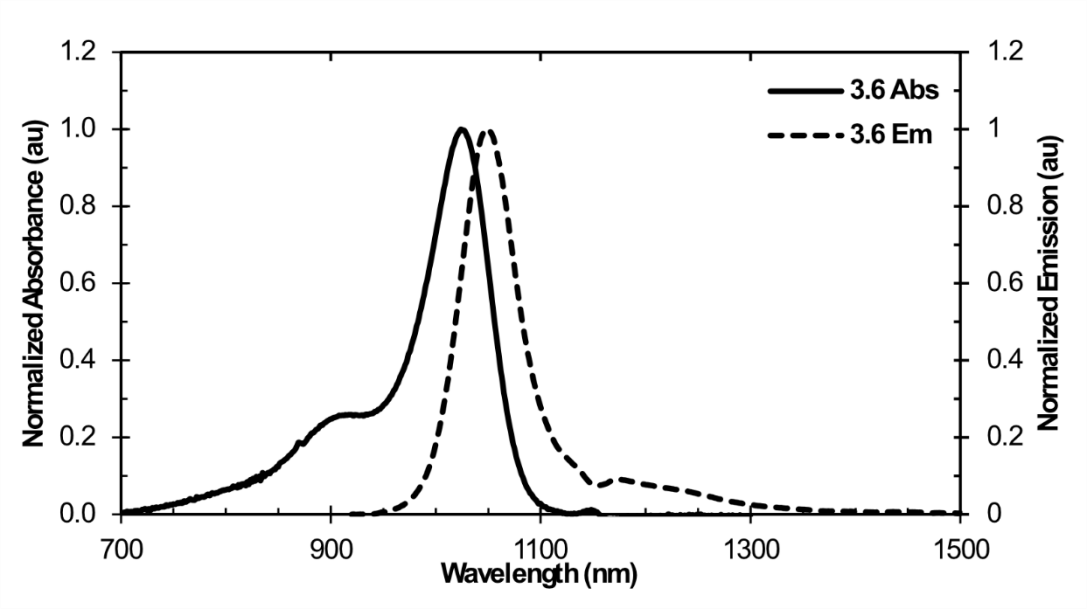
3.6 Abs
3.6 Em
Normalized Absorbance (au)
Normalized Emission (au)
Wavelength (nm)
0.0
0.2
0.4
0.6
0.8
1.0
1.2
0
1
700
900
1100
1300
1500

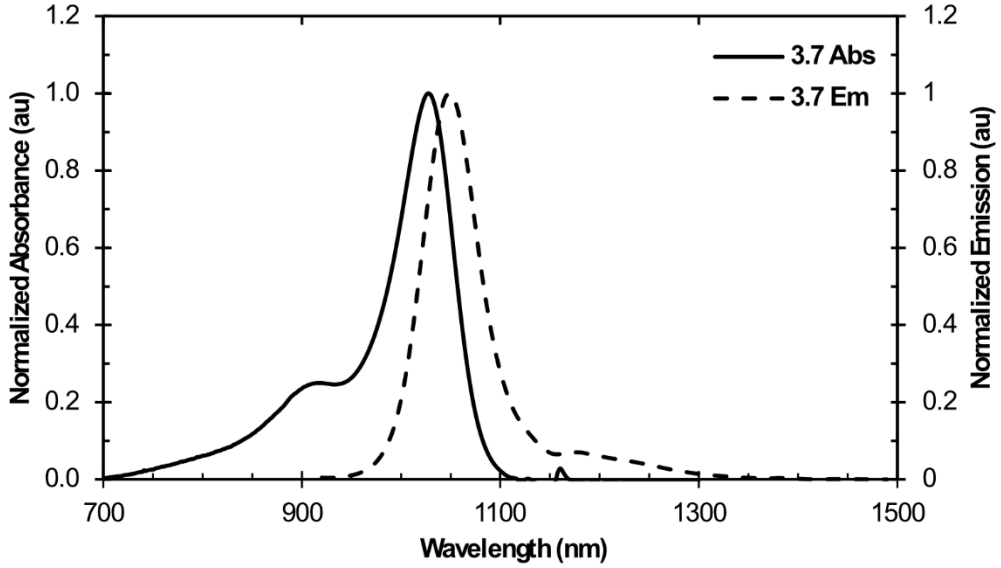
3.7 Abs
3.7 Em
Normalized Absorbance (au)
Normalized Emission (au)
Wavelength (nm)
0.0
0.2
0.4
0.6
0.8
1.0
1.2
0
1
700
900
1100
1300
1500

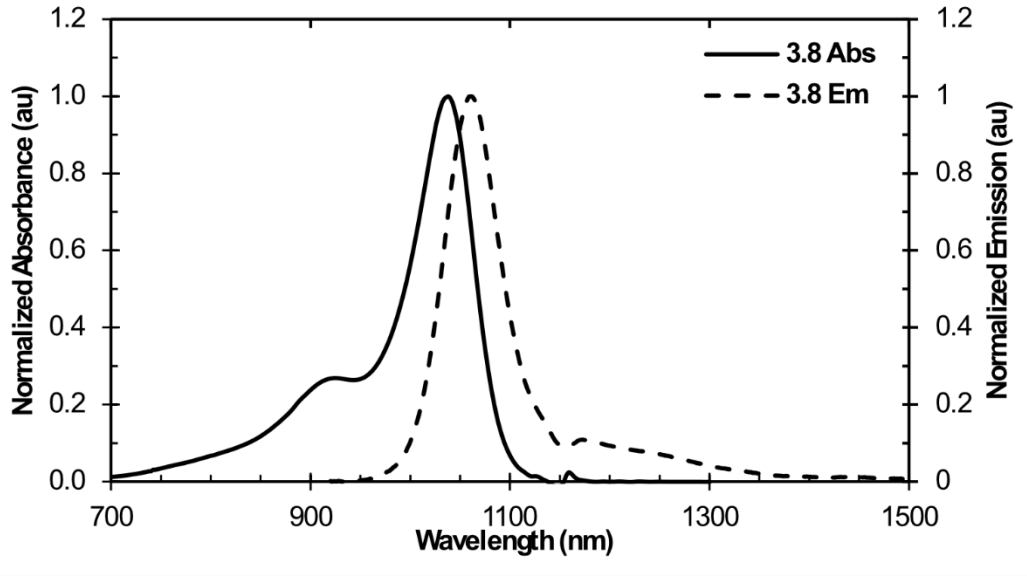
3.8 Abs
3.8 Em
Normalized Absorbance (au)
Normalized Emission (au)
Wavelength (nm)
0.0
0.2
0.4
0.6
0.8
1.0
1.2
700
900
1100
1300
1500

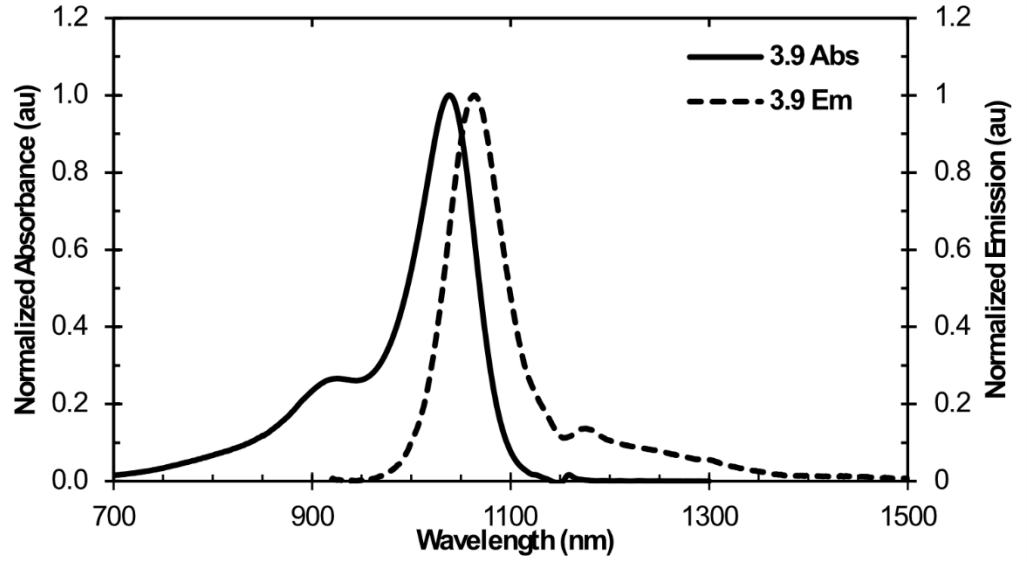
3.9 Abs
3.9 Em
Normalized Absorbance (au)
Normalized Emission (au)
Wavelength (nm)
0.0
0.2
0.4
0.6
0.8
1.0
1.2
700
900
1100
1300
1500

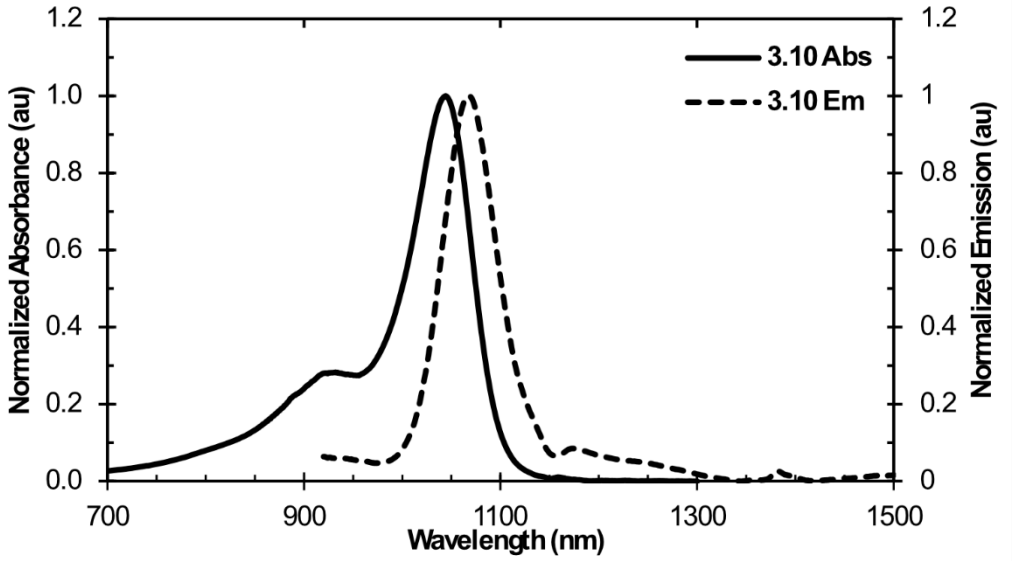
3.10 Abs
3.10 Em
Normalized Absorbance (au)
Normalized Emission (au)
Wavelength (nm)
0.0
0.2
0.4
0.6
0.8
1.0
1.2
0
1
700
900
1100
1300
1500

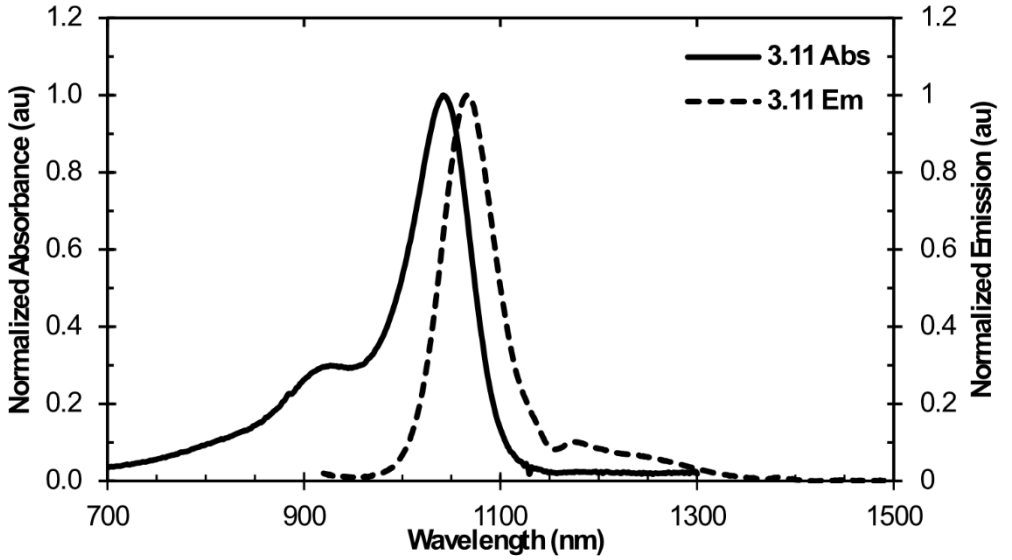
3.11 Abs
3.11 Em
Normalized Absorbance (au)
Normalized Emission (au)
Wavelength (nm)
0.0
0.2
0.4
0.6
0.8
1.0
1.2
0
1
700
900
1100
1300
1500

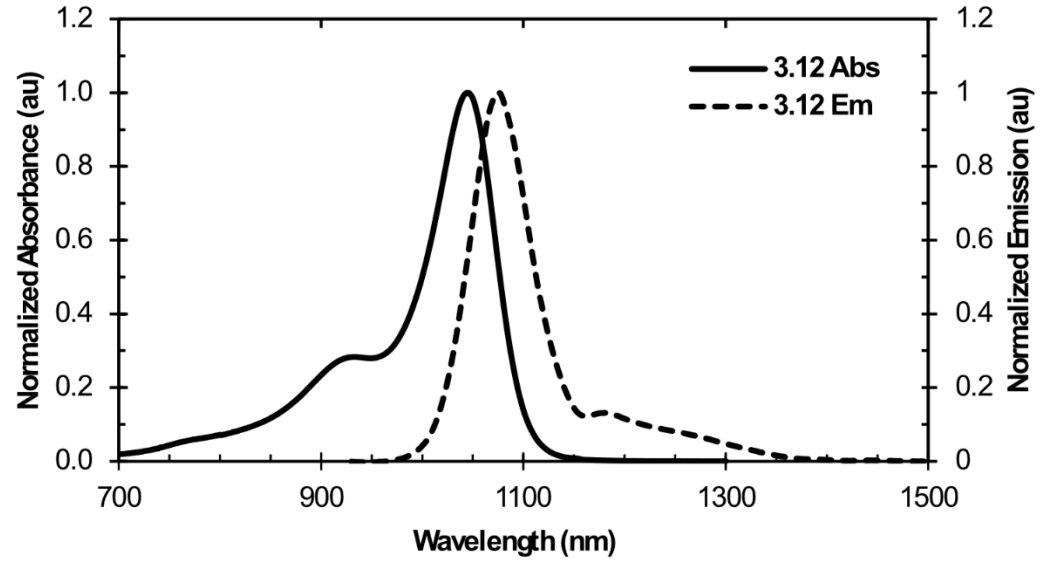
3.12 Abs
3.12 Em
Normalized Absorbance (au)
Normalized Emission (au)
Wavelength (nm)
0.0
0.2
0.4
0.6
0.8
1.0
1.2
0
700
900
1100
1300
1500

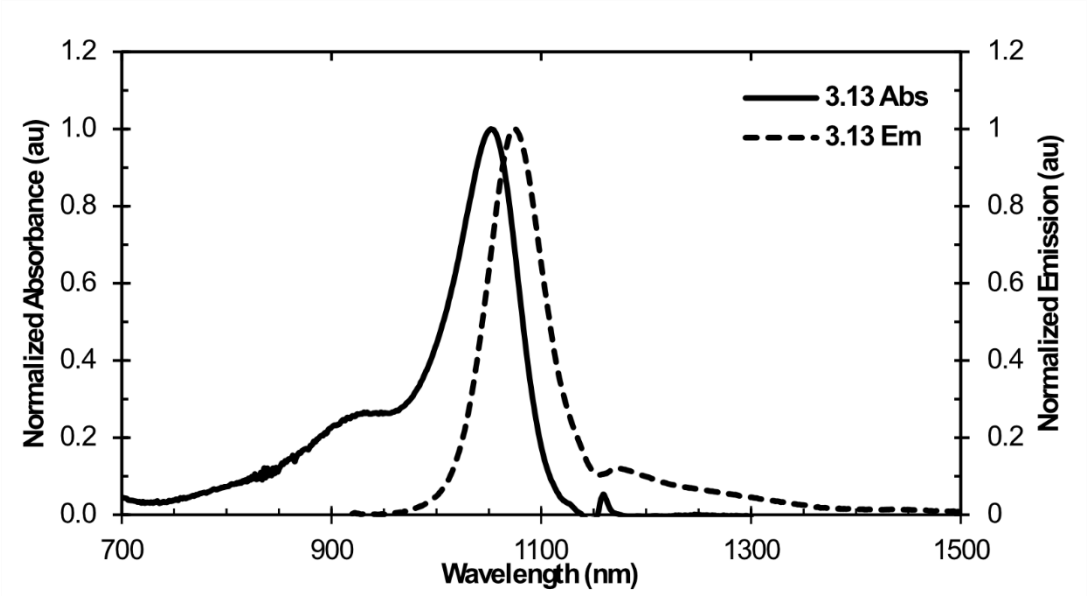
3.13 Abs
3.13 Em
Normalized Absorbance (au)
Normalized Emission (au)
Wavelength (nm)
0.0
0.2
0.4
0.6
0.8
1.0
1.2
0
700
900
1100
1300
1500

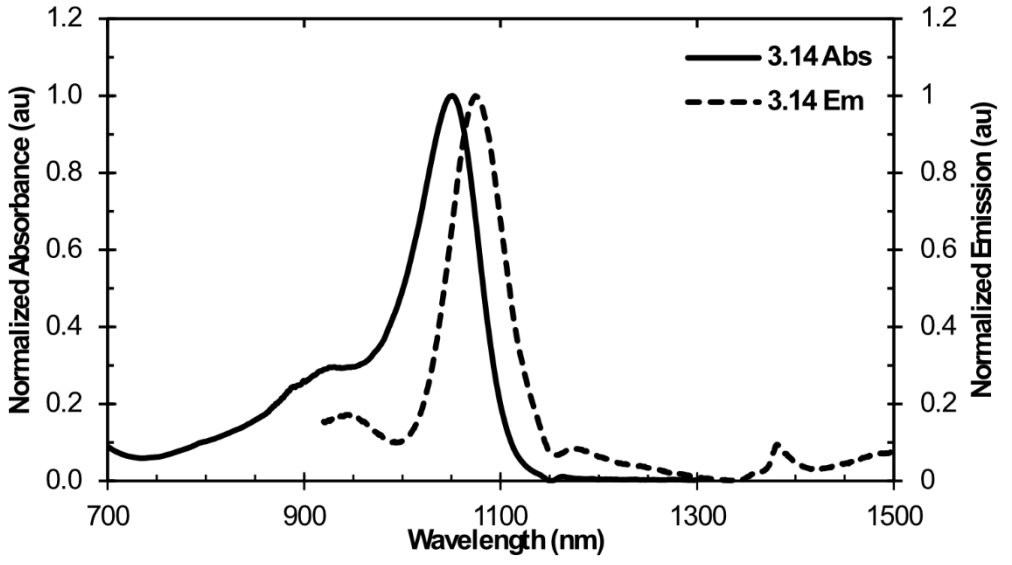
3.14 Abs
3.14 Em
Normalized Absorbance (au)
Normalized Emission (au)
Wavelength (nm)
0.0
0.2
0.4
0.6
0.8
1.0
1.2
0
700
900
1100
1300
1500

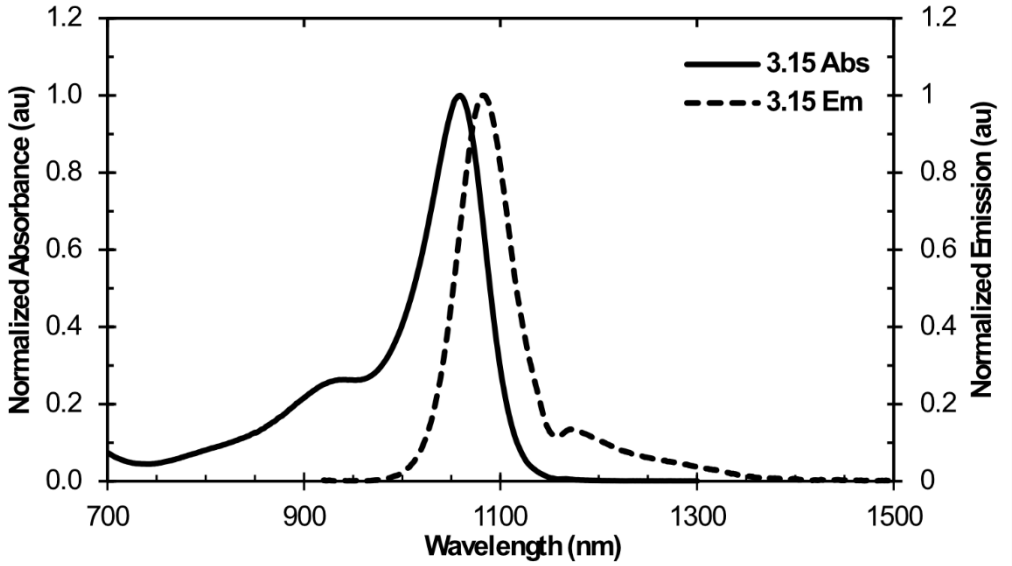
3.15 Abs
3.15 Em
Normalized Absorbance (au)
Normalized Emission (au)
Wavelength (nm)
0.0
0.2
0.4
0.6
0.8
1.0
1.2
0
700
900
1100
1300
1500

3.7 References:

(1) Lei, Z.; Zhang, F. Molecular Engineering of NIR-II Fluorophores for Improved Biomedical Detection. *Angew. Chem. Int. Ed.* **2021**, *60*, 16294–16308. https://doi.org/10.1002/anie.202007040.

(2) Ding, F.; Zhan, Y.; Lu, X.; Sun, Y. Recent Advances in Near-Infrared II Fluorophores for Multifunctional Biomedical Imaging. *Chem. Sci*. **2018**, *9*, 4370–4380. https://doi.org/10.1039/c8sc01153b.

(3) Thimsen, E.; Sadtler, B.; Berezin, M. Y. Shortwave-Infrared (SWIR) Emitters for Biological Imaging: A Review of Challenges and Opportunities. *Nanophotonics* **2017**, *6*, 1043–1054. https://doi.org/10.1515/nanoph-2017-0039.

(4) Diao, S.; Blackburn, J. L.; Hong, G.; Antaris, A. L.; Chang, J.; Wu, J. Z.; Zhang, B.; Cheng, K.; Kuo, C. J.; Dai, H. Fluorescence Imaging In Vivo at Wavelengths beyond 1500 Nm. *Angew. Chem. Int. Ed.* **2015**, *54*, 14758–14762. https://doi.org/10.1002/ANIE.201507473.

(5) Zhu, S.; Tian, R.; Antaris, A. L.; Chen, X.; Dai, H. Near-Infrared-II Molecular Dyes for Cancer Imaging and Surgery. *Advanced Materials*. **2019**, 1900321. https://doi.org/10.1002/adma.201900321.

(6) Hong, G.; Antaris, A. L.; Dai, H. Near-Infrared Fluorophores for Biomedical Imaging. *Nature Biomedical Engineering*. **2017**. https://doi.org/10.1038/s41551-016-0010.

(7) Lei, Z.; Zhang, F. Molecular Engineering of NIR-II Fluorophores for Improved Biomedical Detection. *Angew. Chem. Int. Ed.* **2021**, *60*, 16294–16308. https://doi.org/10.1002/anie.202007040.

(8) Carr, J. A.; Aellen, M.; Franke, D.; So, P. T. C.; Bruns, O. T.; Bawendi, M. G. Absorption by Water Increases Fluorescence Image Contrast of Biological Tissue in the Shortwave Infrared. *Proc. Natl. Acad. Sci. U. S. A.* **2018**, *115*, 9080–9085. https://doi.org/10.1073/pnas.1803210115.

(9) Chen, Z. H.; Wang, X.; Yang, M.; Ming, J.; Yun, B.; Zhang, L.; Wang, X.; Yu, P.; Xu, J.; Zhang, H.; Zhang, F. An Extended NIR-II Superior Imaging Window from 1500 to 1900 Nm for High-Resolution In Vivo Multiplexed Imaging Based on Lanthanide Nanocrystals.

Angew. Chemie - Int. Ed. **2023**, *62*, e202311883. https://doi.org/10.1002/anie.202311883.

(10) Hong, G.; Diao, S.; Chang, J.; Antaris, A. L.; Chen, C.; Zhang, B.; Zhao, S.; Atochin, D. N.; Huang, P. L.; Andreasson, K. I.; Kuo, C. J.; Dai, H. Through-Skull Fluorescence Imaging of the Brain in a New near-Infrared Window. *Nat. Photonics* **2014**, *8*, 723–730. https://doi.org/10.1038/nphoton.2014.166.

(11) Cosco, E. D.; Arús, B. A.; Spearman, A. L.; Atallah, T. L.; Lim, I.; Leland, O. S.; Caram, J. R.; Bischof, T. S.; Bruns, O. T.; Sletten, E. M. Bright Chromenylium Polymethine Dyes Enable Fast, Four-Color in Vivo Imaging with Shortwave Infrared Detection. *J. Am. Chem. Soc.* **2021**, *143*, 6836–6846. https://doi.org/10.1021/jacs.0c11599.

(12) Cosco, E. D.; Spearman, A. L.; Ramakrishnan, S.; Lingg, J. G. P.; Saccomano, M.; Pengshung, M.; Arús, B. A.; Wong, K. C. Y.; Glasl, S.; Ntziachristos, V.; Warmer, M.; McLaughlin, R. R.; Bruns, O. T.; Sletten, E. M. Shortwave Infrared Polymethine Fluorophores Matched to Excitation Lasers Enable Non-Invasive, Multicolour in Vivo Imaging in Real Time. *Nat. Chem.* **2020**, *12*, 1123–1130. https://doi.org/10.1038/s41557-020-00554-5.

(13) Hu, Z.; Fang, C.; Li, B.; Zhang, Z.; Cao, C.; Cai, M.; Su, S.; Sun, X.; Shi, X.; Li, C.; Zhou, T.; Zhang, Y.; Chi, C.; He, P.; Xia, X.; Chen, Y.; Gambhir, S. S.; Cheng, Z.; Tian, J. First-in-Human Liver-Tumour Surgery Guided by Multispectral Fluorescence Imaging in the Visible and near-Infrared-I/II Windows. *Nat. Biomed. Eng.* **2020**, *4*, 259–271. https://doi.org/10.1038/s41551-019-0494-0.

(14) Bricks, J. L.; Kachkovskii, A. D.; Slominskii, Y. L.; Gerasov, A. O.; Popov, S. V. Molecular Design of near Infrared Polymethine Dyes: A Review. *Dye. Pigment.* **2015**, *121*, 238–255. https://doi.org/10.1016/j.dyepig.2015.05.016.

(15) Kulinich, A. V.; Derevyanko, N. A.; Ishchenko, A. A. Electronic Structure and Solvatochromism of Merocyanines Based on N,N-Diethylthiobarbituric Acid. *J. Photochem. Photobiol. A Chem.* **2007**, *188*, 207–217. https://doi.org/10.1016/j.jphotochem.2006.12.014.

(16) Uranga-Barandiaran, O.; Casanova, D.; Castet, F. Flavylium Fluorophores as Near-Infrared Emitters. *ChemPhysChem* **2020**, *21*, 2243–2248.

https://doi.org/10.1002/cphc.202000544.

(17) Friedman, H. C.; Cosco, E. D.; Atallah, T. L.; Jia, S.; Sletten, E. M.; Caram, J. R. Establishing Design Principles for Emissive Organic SWIR Chromophores from Energy Gap Laws. *Chem* **2021**, *7*, 3359–3376. https://doi.org/10.1016/j.chempr.2021.09.001.

(18) Cosco, E. D.; Caram, J. R.; Bruns, O. T.; Franke, D.; Day, R. A.; Farr, E. P.; Bawendi, M. G.; Sletten, E. M. Flavylium Polymethine Fluorophores for Near- and Shortwave Infrared Imaging. *Angew. Chemie - Int. Ed.* **2017**, *56*, 13126–13129. https://doi.org/10.1002/anie.201706974.

(19) Pengshung, M.; Li, J.; Mukadum, F.; Lopez, S. A.; Sletten, E. M. Photophysical Tuning of Shortwave Infrared Flavylium Heptamethine Dyes via Substituent Placement. *Org. Lett.* **2020**, *22*, 6150–6154. https://doi.org/10.1021/acs.orglett.0c02213.

(20) Seijas, J. A.; Vázquez-Tato, M. P.; Carballido-Reboredo, R. Solvent-Free Synthesis of Functionalized Flavones under Microwave Irradiation. *J. Org. Chem.* **2005**, *70*, 2855–2858. https://doi.org/10.1021/JO048685Z/SUPPL_FILE/JO048685ZSI20050114_125302.PDF.

(21) Zhang, J.; Li, P.; Zeng, H.; Huang, Y.; Hong, W. Highly Efficient and Green Synthesis of 2,4-Diphenyl Substituted Thiazoles. *Synth. Commun.* **2020**, *50*, 735–741. https://doi.org/10.1080/00397911.2020.1718711.

(22) Kutateladze, D. A.; Jacobsen, E. N. Cooperative Hydrogen-Bond-Donor Catalysis with Hydrogen Chloride Enables Highly Enantioselective Prins Cyclization Reactions. *J. Am. Chem. Soc.* **2021**, *143*, 20077–20083. https://doi.org/10.1021/jacs.1c10890.

(23) Ferlin, M. G.; Chiarelotto, G.; Gasparotto, V.; Dalla Via, L.; Pezzi, V.; Barzon, L.; Palu, G.; Castagliuolo, I. Synthesis and in Vitro and in Vivo Antitumor Activity of 2-Phenylpyrroloquinolin-4-Ones. *J. Med. Chem.* **2005**, *48*, 3417–3427. https://doi.org/10.1021/jm049387x.

(24) Howard, J. L.; Nicholson, W.; Sagatov, Y.; Browne, D. L. One-Pot Multistep Mechanochemical Synthesis of Fluorinated Pyrazolones. *Beilstein J. Org. Chem.* **2017**, *13*, 1950–1956. https://doi.org/10.3762/bjoc.13.189.

(25) Knorr, G.; Hotzel, K.; Chettri, A.; Skabeev, A.; Wächtler, M.; Dietzek-Ivanšić, B.;

Peneva, K. Unlocking the Potential of Ketocoumarins: Efficient Photosensitizers for Sustainable Light Driven Hydrogen Evolution. *J. Mater. Chem. A* **2023**, *11*, 23260–23269. https://doi.org/10.1039/d3ta04450e.

(26) Wang, J. K.; Wang, C. H.; Wu, C. C.; Chang, K. H.; Wang, C. H.; Liu, Y. H.; Chen, C. T.; Chou, P. T. Hydrogen-Bonded Thiol Undergoes Unconventional Excited-State Intramolecular Proton-Transfer Reactions. *J. Am. Chem. Soc.* **2024**, *146*, 3125–3135. https://doi.org/10.1021/jacs.3c10405.

(27) Kónya, K.; Pajtás, D.; Kiss-Szikszai, A.; Patonay, T. Buchwald–Hartwig Reactions of Monohaloflavones. *European J. Org. Chem.* **2015**, *2015*, 828–839. https://doi.org/10.1002/EJOC.201403108.

(28) Pino, N. W.; Sizemore, A. R.; Cleary, L.; Liu, H.; McSwiggen, D. T.; Song, D.; Beck, H. P.; Cheng, K.; Hardy, M.; Hsiung, J.; Tang, Y.; Anugula, R.; Lakshman, S.; Merneedi, R. K.; Sinha, P. Optimized Properties and Synthesis of Photoactivatable Diazoketorhodamines Facilitate and Enhance High-Throughput Single-Molecule Tracking. *J. Org. Chem.* **2024**. https://doi.org/10.1021/ACS.JOC.4C00718/ASSET/IMAGES/LARGE/JO4C00718_0005.JPEG.

(29) Semonin, O. E.; Johnson, J. C.; Luther, J. M.; Midgett, A. G.; Nozik, A. J.; Beard, M. C. Absolute Photoluminescence Quantum Yields of IR-26 Dye, PbS, and PbSe Quantum Dots. *J. Phys. Chem. Lett.* **2010**, *1*, 2445–2450. https://doi.org/10.1021/jz100830r.

(30) Hatami, S.; Würth, C.; Kaiser, M.; Leubner, S.; Gabriel, S.; Bahrig, L.; Lesnyak, V.; Pauli, J.; Gaponik, N.; Eychmüller, A.; Resch-Genger, U. Absolute Photoluminescence Quantum Yields of IR26 and IR-Emissive Cd1−xHgxTe and PbS Quantum Dots – Method- and Material-Inherent Challenges. *Nanoscale* **2014**, *7*, 133–143. https://doi.org/10.1039/C4NR04608K.

(31) Wang, S.; Fan, Y.; Li, D.; Sun, C.; Lei, Z.; Lu, L.; Wang, T.; Zhang, F. Anti-Quenching NIR-II Molecular Fluorophores for in Vivo High-Contrast Imaging and PH Sensing. *Nat. Commun.* **2019**, *10*, 1–11. https://doi.org/10.1038/s41467-019-09043-x.

(32) He, Y.; Wang, S.; Yu, P.; Yan, K.; Ming, J.; Yao, C.; He, Z.; El-Toni, A. M.; Khan, A.;

Zhu, X.; Sun, C.; Lei, Z.; Zhang, F. NIR-II Cell Endocytosis-Activated Fluorescent Probes Forin Vivohigh-Contrast Bioimaging Diagnostics. *Chem. Sci.* **2021**, *12*, 10474–10482. https://doi.org/10.1039/d1sc02763h.

(33) Babij, C.; Poë, A. J. Deconstruction of Taft's Σ* Parameter: QSAR Meets QALE. *J. Phys. Org. Chem.* **2004**, *17*, 162–167. https://doi.org/10.1002/POC.708.

(34) Janeková, H.; Friedman, H. C.; Russo, M.; Zyberaj, M.; Ahmed, T.; Hua, A. S.; Sica, A. V.; Caram, J. R.; Štacko, P. Deuteration of Heptamethine Cyanine Dyes Enhances Their Emission Efficacy. *Chem. Commun.* **2024**, *60*, 1000–1003. https://doi.org/10.1039/D3CC05153F.

(35) Ramos, P.; Friedman, H.; Li, B. Y.; Garcia, C.; Sletten, E.; Caram, J. R.; Jang, S. J. Nonadiabatic Derivative Couplings through Multiple Franck-Condon Modes Dictate the Energy Gap Law for Near and Short-Wave Infrared Dye Molecules. *J. Phys. Chem. Lett.* **2024**, *15*, 1802–1810. https://doi.org/10.1021/ACS.JPCLETT.3C02629/SUPPL_FILE/JZ3C02629_SI_002.PDF.

(36) Dang, Z.; Liu, X.; Du, Y.; Wang, Y.; Zhou, D.; Zhang, Y.; Zhu, S. Ultra-Bright Heptamethine Dye Clusters Based on a Self-Adaptive Co-Assembly Strategy for NIR-IIb Biomedical Imaging. *Adv. Mater.* **2023**, *35*, 2306773. https://doi.org/10.1002/ADMA.202306773.

(37) Hansch, C.; Leo, A.; Taft, R. W. A Survey of Hammett Substituent Constants and Resonance and Field Parameters. *Chem. Rev.* **1991**, *91*, 165–195. https://doi.org/10.1021/cr00002a004.

CHAPTER FOUR

Red-shifted Nonamethine Chromenylium Dyes for High-Resolution Shortwave Infrared *in vivo* Imaging

Adapted from: Anthony Spearman, Eric Lin, Emily Mobley, Andriy Chmyrov, Daniel Turner, Cesar Garcia, Kyle Bui, Christopher Rowlands, Oliver Bruns, Ellen Sletten*. High-Resolution Multicolor Shortwave Infrared *In Vivo* Imaging with Chromenylium Nonamethine Dyes. *ChemRxiv.* **2024**, DOI: 10.26434/chemrxiv-2024-dxdr9.

4.1 Abstract

Imaging in the shortwave infrared (SWIR) region offers high-resolution visualization of i*n vivo* targets in a multiplexed manner. These methods require bright, bathochromically-shifted fluorescent dyes with sufficient emission at SWIR wavelengths–ideally above 1400 nm for high resolution images. Polymethine dyes are a privileged class of contrast agents due to their excellent absorption and high degree of modularity. In this work, we push flavylium and chromenylium dyes further into the SWIR region through polymethine chain extension. This panel of nonamethine dyes boasts absorbances as red as 1149 nm and tail emission beyond 1500 nm. These dyes are the brightest fluorophores at their respective bandgaps to date, with ε_{max} ~10^5 $M^{-1}cm^{-1}$ and Φ_F up to 0.5%. We showcased two nonamethine dyes for multiplexed imaging with all SWIR excitation (1060, 1150 nm) and detection at the preferred SWIR wavelengths of 1500–1700 nm, enhancing the depths and resolutions able to be obtained in multicolor SWIR imaging with small molecule contrast agents.

4.2 Introduction

Multiplexed optical imaging is a ubiquitous approach to real-time studies of dynamic biological processes in cells and transparent organisms. Considerable progress toward bringing the advantages of optical imaging to mammals has been achieved by leveraging the shortwave infrared (SWIR, 1000–2000 nm, Figure 1A) region of the electromagnetic spectrum.[1–4] The SWIR region enables non-invasive *in vivo* imaging due to decreased light scattering and minimal autofluorescence.[5,6] Some subregions within the SWIR provide exceptional resolution (*i.e.* 1350–1450 nm),[7,8] while others allow for optical imaging at depths upwards of 0.5 cm (*i.e.* > 1500 nm).[9,10] Importantly, the SWIR region increases opportunities for multiplexed imaging in mammals by greatly expanding wavelengths compatible with imaging through tissue.[11]

A major challenge for advancing non-invasive multicolor imaging in mice is developing SWIR fluorophores that can be used in combination with each other for multiplexed experiments, especially in the high-resolution and/or depth regions of the SWIR. Many SWIR fluorophores only contain a small percentage of their emission (*i.e.* tail emission) in the SWIR region and are limited to imaging below 1300 nm.[9,12] In 2020, we reported a SWIR multiplexing approach which capitalized on imaging the SWIR emissive tails of fluorophores that are excited at near- or shortwave infrared wavelengths. This approach is deemed excitation multiplexed imaging where the channels are defined by differential excitation. While excitation multiplexed imaging has enabled 3- and 4- color video rate imaging in mice, collection windows have remained in the lower resolution portion of the SWIR region. Furthermore, all excitation-based multiplexed *in vivo* experiments to date have relied on at least one fluorophore that is excited below 1000 nm.

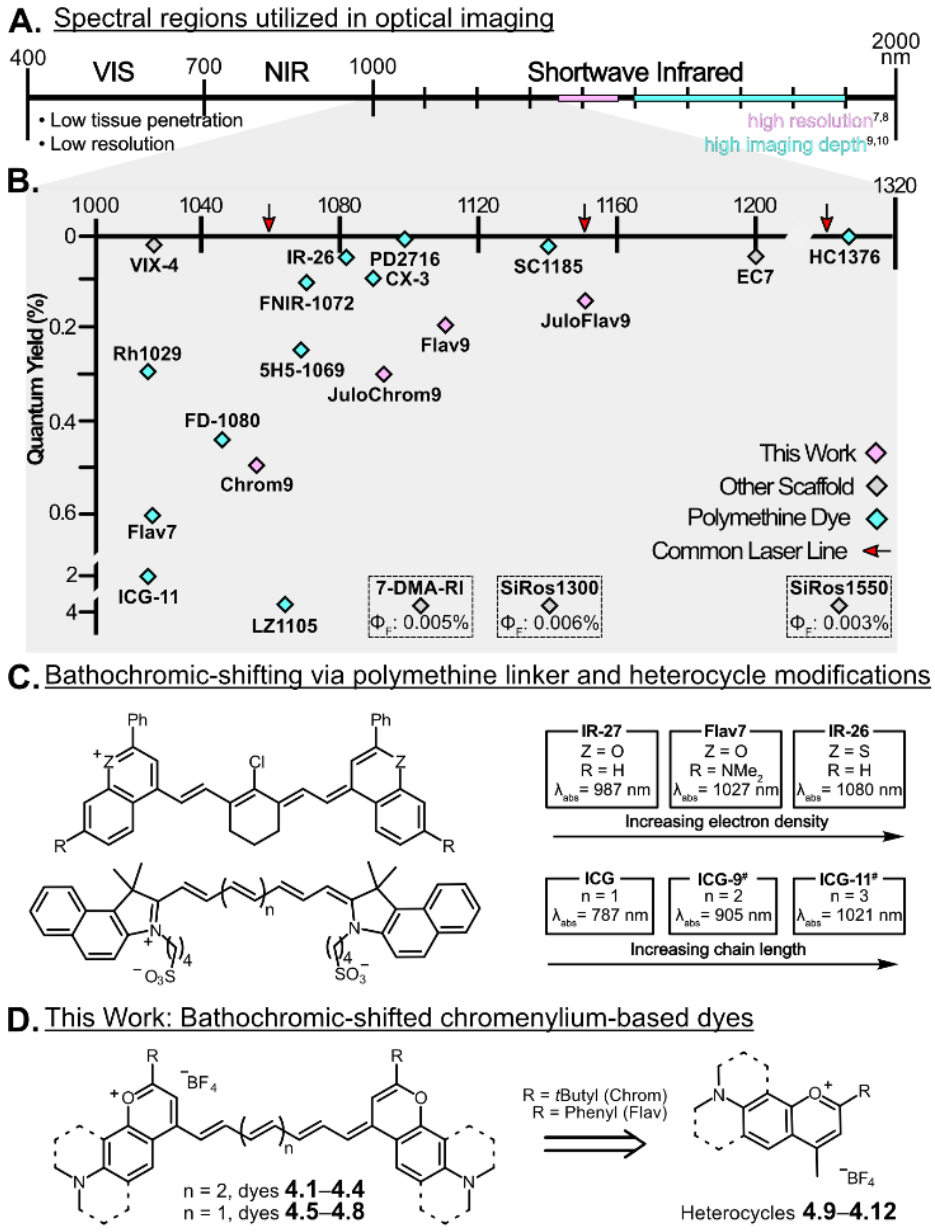

Figure 4.1. **A.** Regions of the electromagnetic spectrum utilized in optical imaging. **B.** Reported small-molecule dyes with 100% emission above 1000 nm. **C.** Strategies for red-shifting polymethine dyes. **D.** Target linear polymethine dyes in this work.

To achieve multiplexed high-resolution imaging at maximum depths with organic contrast agents, fluorophores must be spectrally separated, contain 100% SWIR emission, and be bathochromically shifted as much as possible. Surveying the small molecule fluorophores with SWIR absorbance and emission reported to date, we find that ~80% are polymethine dyes (Figure

4.1B).[4,12] Polymethine fluorophores are a popular class of biocompatible fluorophores containing two heterocycles connected by a polymethine chain. They possess excellent absorption properties and high tunability throughout the visible, near-infrared (NIR), and SWIR regions.[13,14] A marquee member is indocyanine green (**ICG**), an FDA-approved NIR heptamethine dye with benzoindolium heterocycles that has tail emission in the SWIR region.[7,15,16] Despite **ICG** being a NIR fluorophore, it remains one of the most widely used contrast agents for SWIR imaging.

Approaches to bathochromically-shift NIR polymethine dyes, such as **ICG**, into the SWIR region have included polymethine chain elongation or heterocycle modification (Figure 4.1C). Towards the former, extension of the polymethine chain by one C_2H_2 unit reliably imparts a ~100 nm wavelength red-shift.[13,17] This approach has been less frequently applied toward SWIR fluorophores as extension above seven methines (*i.e.,* heptamethine dyes) often leads to electronic ground state desymmetrization, which decreases contrast agent brightness.[18] Recently, Schnermann and coworkers have reported indolene-containing nonamethine dyes for SWIR tail imaging, and Jin and coworkers have prepared nonamethine and undecamethine variants of **ICG**, deemed **ICG-C9** and **ICG-C11**.[19,20] **ICG-C11** has an impressive fluorescence quantum yield (Φ_F) but overall moderate brightness due to its low absorption coefficient (ε_{max}), likely a result of ground state desymmetrization from chain elongation.

Heterocycle modification is a complementary strategy for bathochromic shifting. These modifications include benzannulation, tuning heterocycle electronics, heteroatom exchange or heterocycle addition.[21–26] Some initial applications of these strategies toward SWIR fluorophores include FD-1080 and **Flav7.**[21,27] Overall, these works have revealed key design strategies for bathochromically-shifting polymethine dyes that can be applied to venture further into the SWIR region.

In this work, we combine polymethine bathochromic shifting strategies to achieve four bright nonamethine dyes, **4.1**–**4.4**, with SWIR absorption and 100% SWIR emission (Figure 4.1D). These fluorophores are the brightest dyes at their bandgaps, with ε_{max} ~10^5 M^{-1} cm^{-1} and Φ_F up to 0.5%. The lowest (**4.4**, named **JuloFlav9**) and highest (**4.1**, named **Chrom9**) energy nonamethine dyes are sufficiently spectrally separated for multiplexed imaging. With these dyes, we report the first instance of biocompatible 2-color SWIR imaging utilizing exclusively SWIR excitation (1060 nm and 1150 nm) and organic contrast agents. Further, the collection window in these experiments is 1500–1700 nm, increasing the resolution/depth that can be achieved in excitation-based SWIR multiplexing. Finally, with the ability to excite at 1150 nm, we opened the door for 5-color multiplexed imaging.

4.3 Results and Discussion

4.3.1 SWIR Fluorophore Design

Our group has extensively explored chromenylium (**Chrom**) and flavylium (**Flav**) heterocycles as avenues for developing SWIR polymethine contrast agents.[28–32] Notable modifications include the addition of a julolidine moiety (Julo) to provide a ~40 nm red-shift and exchange of the 2-position phenyl group in Flav dyes for a *tert*-butyl group to give Chrom dyes that display a ~3-fold increase in quantum yield.[29] In pursuit of fluorophores with red-shifted SWIR emission, we selected four permutations of these heterocycles: Flav (**4.9**), JuloFlav (**4.10**), Chrom (**4.11**), and JuloChrom (**4.12**) to transform into nonamethine dyes **4.1**–**4.4** (Figure 4.2A).

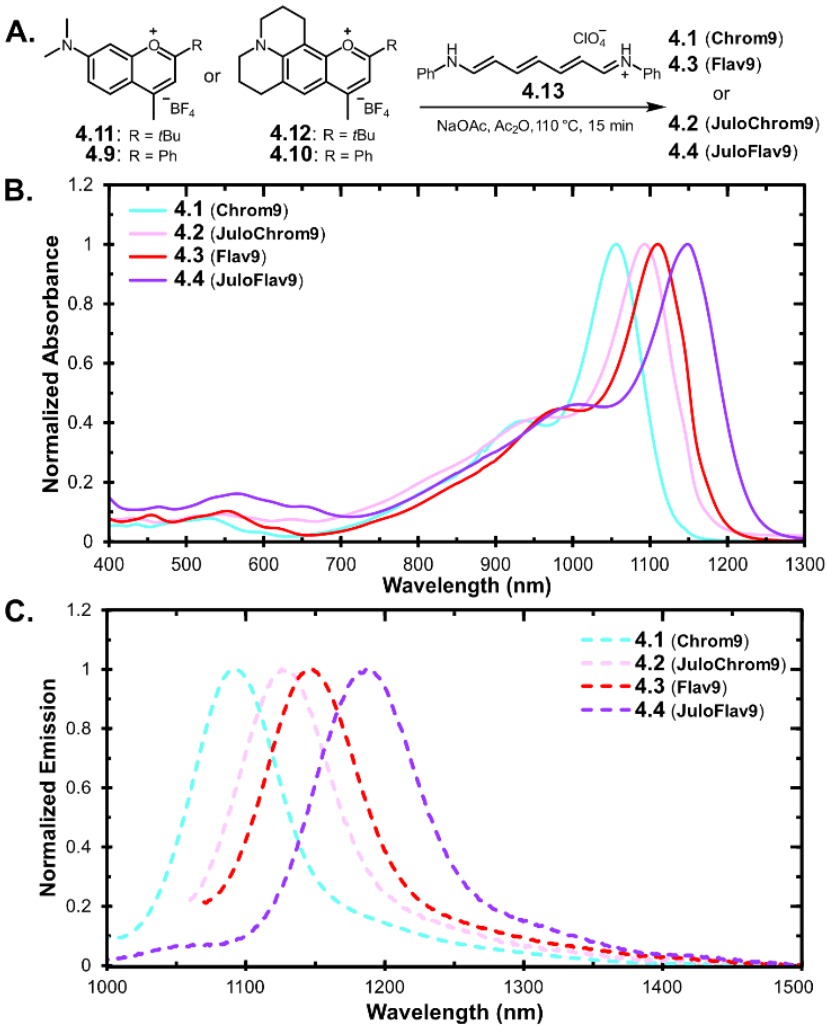

Figure 4.2. **A**. Synthetic approach towards target nonamethine dyes **4.1**–**4.4**. **B**. Normalized absorption of **4.1**–**4.4** in dichloromethane. **C**. Normalized emission of **4.1**–**4.4** in deuterated dichloromethane.

4.3.2 Synthesis of Nonamethine Dyes

Chromenylium and flavylium heterocycles **4.9**–**4.12** were synthesized according to previous reports.[29] The heptatrienylidene benzaminium perchlorate linker **4.13** was achieved through a Vilsmeier-Haack reaction with **4.22** followed by a condensation with aniline (Scheme 4.1). Finally, introduction of two equivalents of heterocycle (**4.9**, **4.10**, **4.11**, or **4.12**) with **4.13** in basic conditions afforded the nonamethine dyes **4.1**–**4.4**, with yields between 9–35% (Figure 4.2). Careful air-free technique was required in the final condensation step to avoid oxygen-mediated

degradation to shorter polymethine derivatives (Figure 4.3). This polymethine truncation has been observed in pentamethine and heptamethine cyanine dyes.[33–35]

Scheme 4.1. Synthesis of chromenylium and flavylium nonamethine dyes, **4.1**–**4.4**. Heterocycles **4.9**–**4.12** were synthesized from compounds **4.14**–**4.21** according to previous reports.

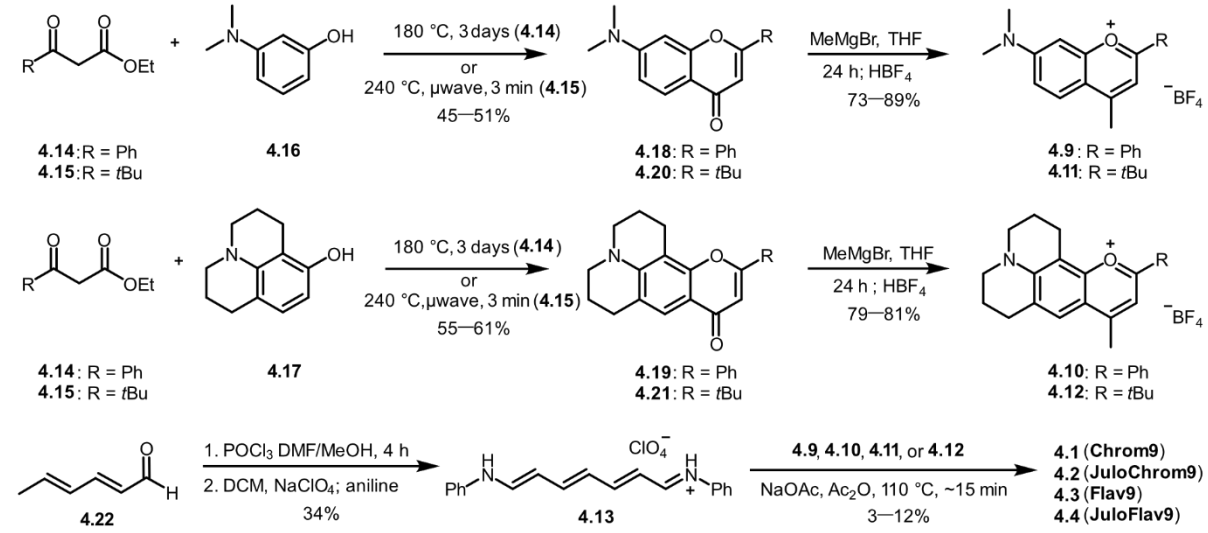

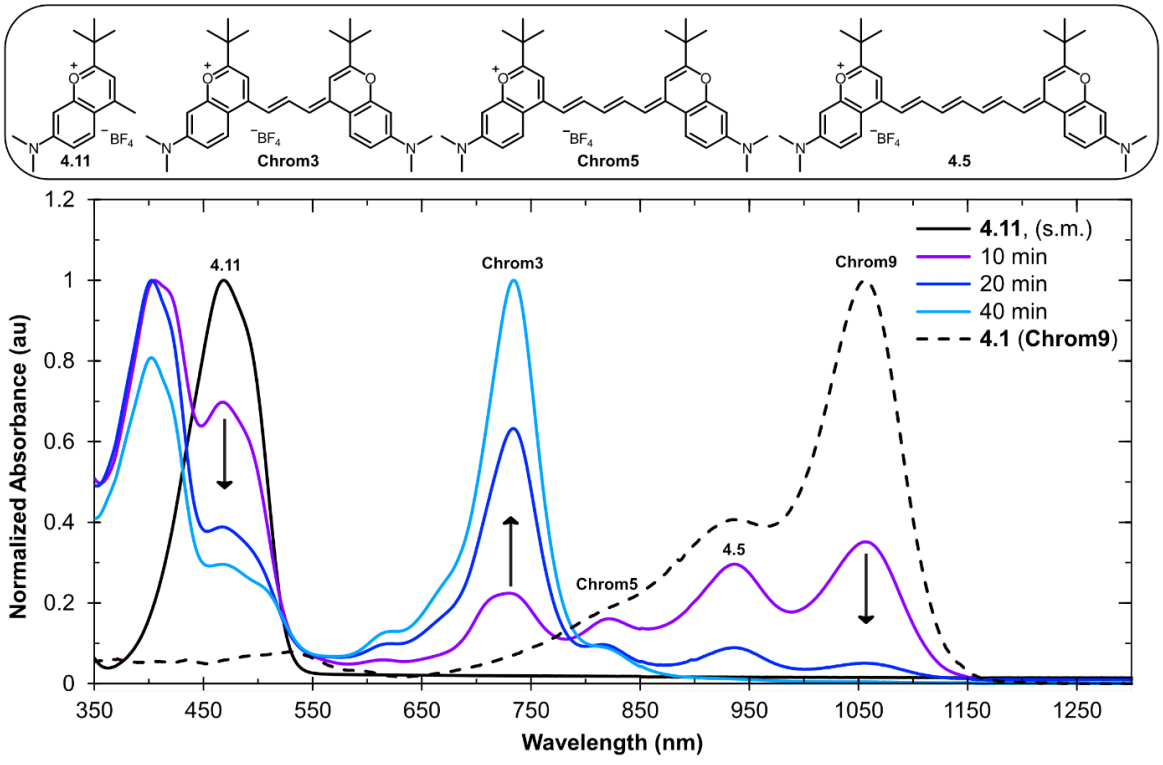

Figure 4.3. Observed degradation of nonamethine dye **4.1** (**Chrom9**) during condensation reaction

(Figure 4.2B/Scheme 4.1). Shorter chain dyes **4.5**, **Chrom5**, and **Chrom3** were generated during condensation reaction with oxygen present.

4.3.3 Photophysical Properties of Nonamethine Dyes

With dyes **4.1**–**4.4** in hand, we investigated their photophysical properties in dichloromethane (Table 4.1). The absorption spectra of these dyes all displayed $\lambda_{max,abs}$ above 1000 nm (Figure 4.2B) with $\lambda_{max,em}$ as low energy as 1188 nm (Figure 4.2C). We measured emission spectra in deuterated dichloromethane (DCM) to avoid solvent absorption. The Φ_F (DCM) of these four fluorophores ranged from 0.15% to 0.5%, with the most red-shifted **4.4** (**JuloFlav9**), displaying the lowest Φ_F, consistent with energy gap laws.[36] Notably three of the four fluorophores: **4.2** (**JuloChrom9**; $\lambda_{max,abs}$ = 1092 nm, Φ_F = 0.31%), **4.3** (**Flav9**; $\lambda_{max,abs}$ = 1110 nm, Φ_F = 0.19%), and **4.4** (**JuloFlav9**; $\lambda_{max,abs}$ = 1149, Φ_F = 0.15%), display the highest reported Φ_F at their respective wavelengths (Table 4.1, Figure 4.1B). The measured Φ_F agree with previously observed trends in that the chromenylium heterocycles result in more emissive fluorophores.

For contrast agent development, brightness is the most important comparative metric for analyzing utility for *in vivo* imaging.[11,37] Brightness is the product of ε and Φ_F, and thus a high ε can compensate for the inherently low quantum yields in the SWIR region. Fortuitously, polymethine dyes possess characteristically high ε_{max}'s, rendering them excellent SWIR imaging scaffolds.[13] The ε_{max} for the nonamethine dyes **4.1**–**4.4** spanned 105,000–159,000 $M^{-1}cm^{-1}$, leading to brightness values of 150–540 M^{-1} cm^{-1} (Table 4.1). These ε_{max} values are lower than that of shorter chain chromenylium and flavylium dyes, which we attribute to the onset of ground state desymmetrization, as has been observed with other long chain polymethine dyes.[18,38] To further characterize the extent of ground state desymmetrization, absorbance in various solvents (DMSO, MeOH, acetone, and MeCN) was investigated. As expected, the dyes display more polyene-like character in polar solvents (Figure 4.4), which is evident in their broadened absorbance profiles.

Even with some ground state desymmetrization occurring, the obtained ε values are still excellent for a small-molecule dye (~10^5 $M^{-1}cm^{-1}$) and result in brightness values that have previously been successful for real-time, multiplexed *in vivo* imaging with SWIR detection.[29]

Table 4.1. Photophysical properties of linear heptamethine and nonamethine dyes, 4.1–4.8 in dichloromethane (DCM).

Dye	$\lambda_{max,abs}$ (nm)	$\lambda_{max,em}$ (nm)	ε_{max} ($M^{-1}cm^{-1}$)	Φ_F (%)	Brightness ($M^{-1}cm^{-1}$)	SWIR Brightness ($M^{-1}cm^{-1}$) (1000–1700 nm)
4.1 (**Chrom9**)	1057	1088	107,000 ± 700	0.5 ± 0.02	540 ± 20	500
4.5	935	961	227,000 ± 1000	3.7 ± 0.2	8,400 ± 500	4,100
4.2 (**JuloChrom9**)	1092	1128	146,000 ± 200	0.31 ± 0.02	450 ± 30	440
4.6	970	1004	213,000 ± 4300	1.5 ± 0.06	3,200 ± 100	1,600
4.3 (**Flav9**)	1110	1133	159,000 ± 1000	0.19 ± 0.02	300 ± 30	290
4.7 (LFlav7)	986	1016	149,000 ± 2000	1.5 ± 0.3	2,280 ± 400	1,500
4.4 (**JuloFlav9**)	1149	1188	101,000 ± 1000	0.15 ± 0.01	150 ± 10	140
4.8	1022	1055	212,000 ± 1000	1.4 ± 0.4	3,000 ± 800	2,800

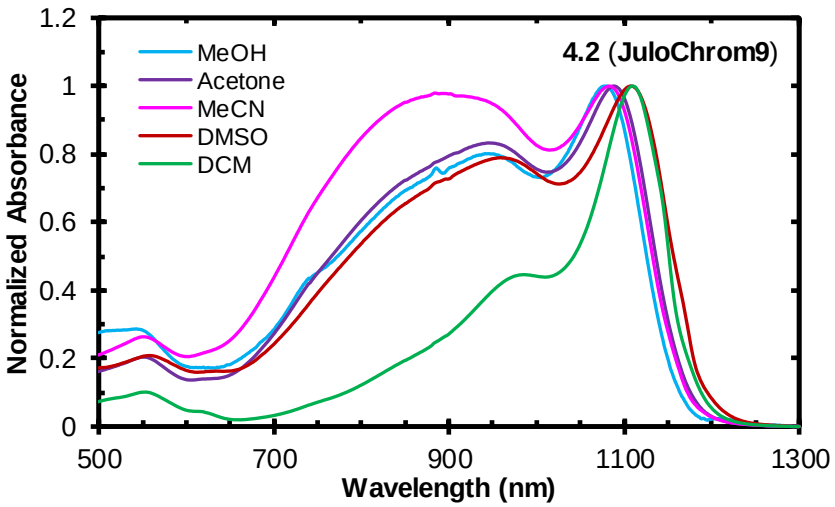

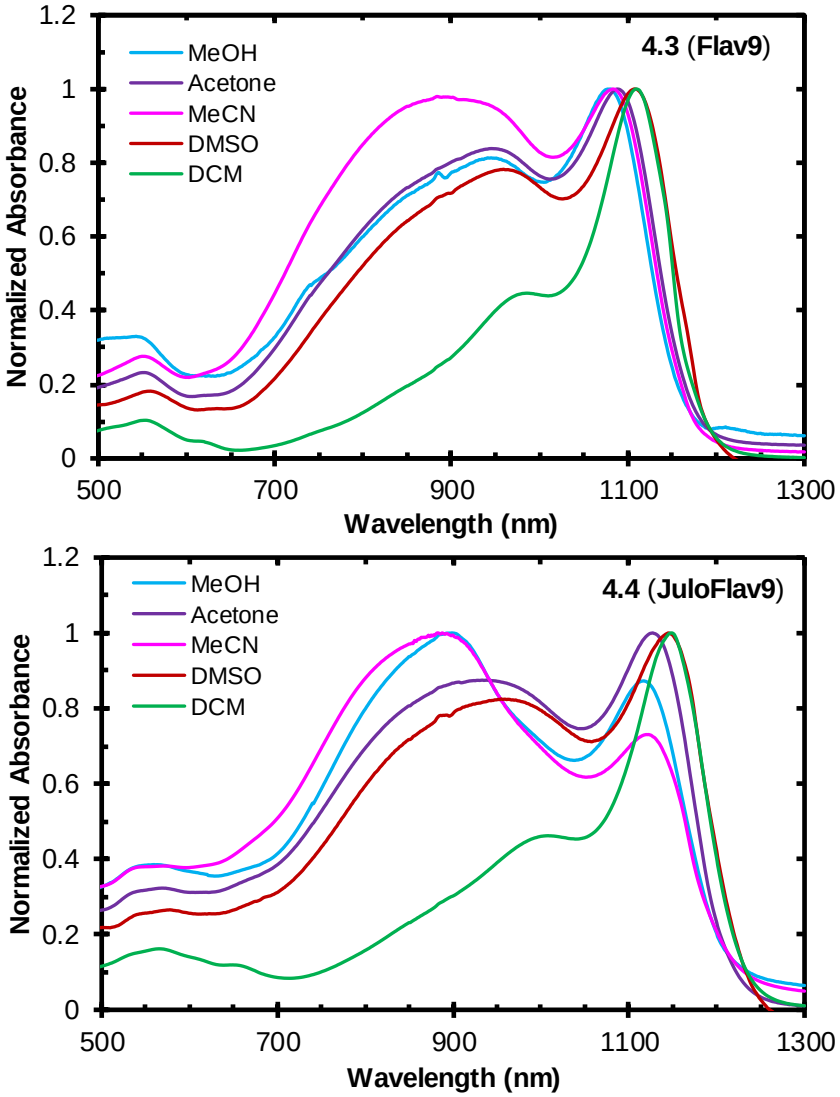

Figure 4.4. Absorbance of nonamethine dyes **4.2**–**4.4** in various solvents demonstrating stabilization of the broadened, blue-shifted polyene state. Approximately 5 μM of dyes **4.2**–**4.4** in each solvent was used.

4.3.4 Comparison of Nonamethine Dyes to Vinylene Analogues

To fully appreciate the photophysical consequences of chain extension, we directly compared the vinylene analogues derived from heterocycles **4.9**–**4.12**. Previously, we reported the direct pentamethine analogues;[27] however, our heptamethine congeners had substituted polymethine chains, precluding a direct analysis. Consequently, linear heptamethine analogues

4.5–**4.8** were synthesized with commercially available malonaldehyde bis(phenylimine) (**4.23**) using standard condensation conditions (Scheme 4.2).

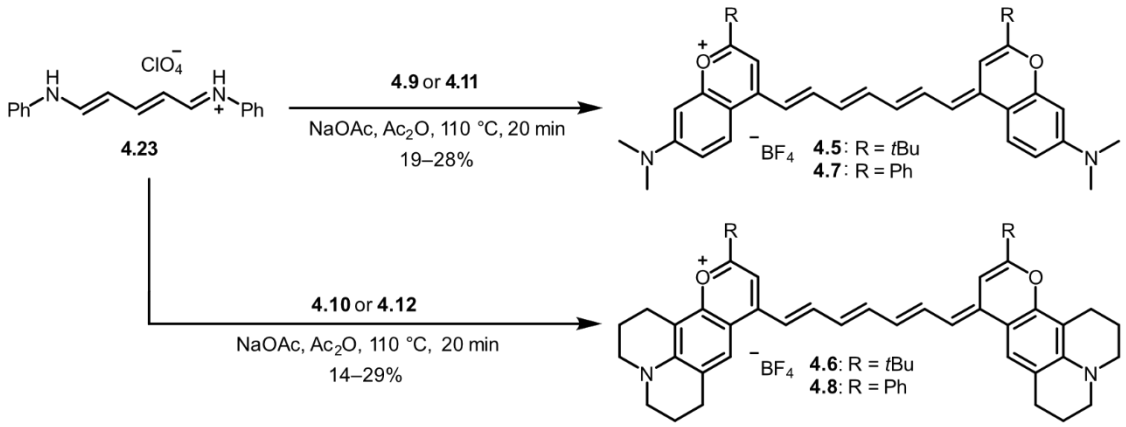

Scheme 4.2. Synthesis of linear heptamethine dyes **4.5**–**4.8** with commercial linker **4.23**.

We characterized the $\lambda_{max,abs}$, $\lambda_{max,em}$, ε_{max}, and Φ_F of heptamethine dyes **4.5**–**4.8**. (Table 4.1). These linear heptamethine dyes had $\lambda_{max,abs}$ between 935 and 1022 nm, yielding a difference in λ_{max} by about 120 nm between the 7- and 9- dyes, an observation consistent with the vinylene shift rule.[13] Interestingly, these derivatives displayed impressive Φ_F between 1.4 and 3.7%. A similar quantum yield increase has been observed with flavylium heptamethine derivatives with linear linkers.[39] These dyes had typical polymethine Stokes shifts of 26-33 nm with $\lambda_{max,ems}$ as red as 1055 nm. In tandem with previous data, we can now compare the photophysical properties of 5- 7- and 9- linear Flav/Chrom dyes (Table 4.1-4.2). The λ_{max} for the pentamethine dyes averaged 857 nm,[27,29] while heptamethines averaged 978 nm and nonamethines 1102 nm. We then calculated overall average brightness values of 52,000, 4,200, 360 $M^{-1}cm^{-1}$ for the chromenylium penta- hepta- and nonamethine dyes respectively. Notably, these chromenylium dyes show a decrease in brightness by one order of magnitude for every 2 methines added to the polymethine chain, largely due to a decrease in Φ_F as predicted by energy gap laws.[36] Apart from these total brightness values,

we looked to understanding the brightness of each of these scaffolds in the SWIR and its sub-regions.

Table 4.2 Photophysical properties of referenced pentamethine dyes in dichloromethane with errors (DCM).

Dye	$\lambda_{max,abs}$ (nm)	$\lambda_{max,em}$ (nm)	ε_{max} ($M^{-1}cm^{-1}$)	Φ_F (%)	Brightness ($M^{-1}cm^{-1}$)	SWIR Brightness ($M^{-1}cm^{-1}$) (1000–1700 nm)
Chrom5	819	836	380,000 ± 10,000	28 ± 2	106,000 ± 8000	500
JuloChrom5	852	872	389,000 ± 3,000	18.3 ± 0.4	71,000 ± 2000	4,100
Flav5	862	883	327,000 ± 7,000	6.1 ± 0.1	19,900 ± 500	440
JuloFlav5	897	925	254,000 ± 5,000	5.3 ± 0.2	13,500 ± 600	1,600

4.3.5 Considerations for SWIR Imaging.

When imaging at SWIR wavelengths, the depth and resolution achievable are highly dependent on the wavelengths collected. The highest resolution images are obtained when imaging in the 1350–1450 nm region where water absorbs stray light, leading to high signal-to-noise ratios with mm resolution.[7,8] For maximum depth penetration, recent works using inorganic particles have demonstrated the privileges of imaging at wavelengths above 1500 nm.[9] The wavelengths of light collected during *in vivo* imaging experiments are defined by a longpass (LP) filter, which allows only lower energy light to pass through. LP filters can modulate the balance of signal and resolution achieved. For SWIR dyes, using a 1000 nm LP filter results in all photons emitted being collected, resulting in maximum signal. Increasing the wavelength of LP filters generally leads to higher resolution images since lower energy light is scattered less by tissue (Figure 4.5A). Therefore, imaging with 1400 nm LP or greater is preferred in order to capitalize on the advantages of the SWIR. This approach requires red-shifted, bright SWIR fluorophores.

To assess the potential of chromenylium and flavylium polymethine dyes in SWIR imaging experiments with different LP filters, we first calculated their SWIR brightness by multiplying molecular brightness by their percentage SWIR emission (1000–1700 nm). Amongst the nonamethine dyes, **4.1** (**Chrom9**) had the highest SWIR brightness around 500 $M^{-1}cm^{-1}$ (Table 4.1).

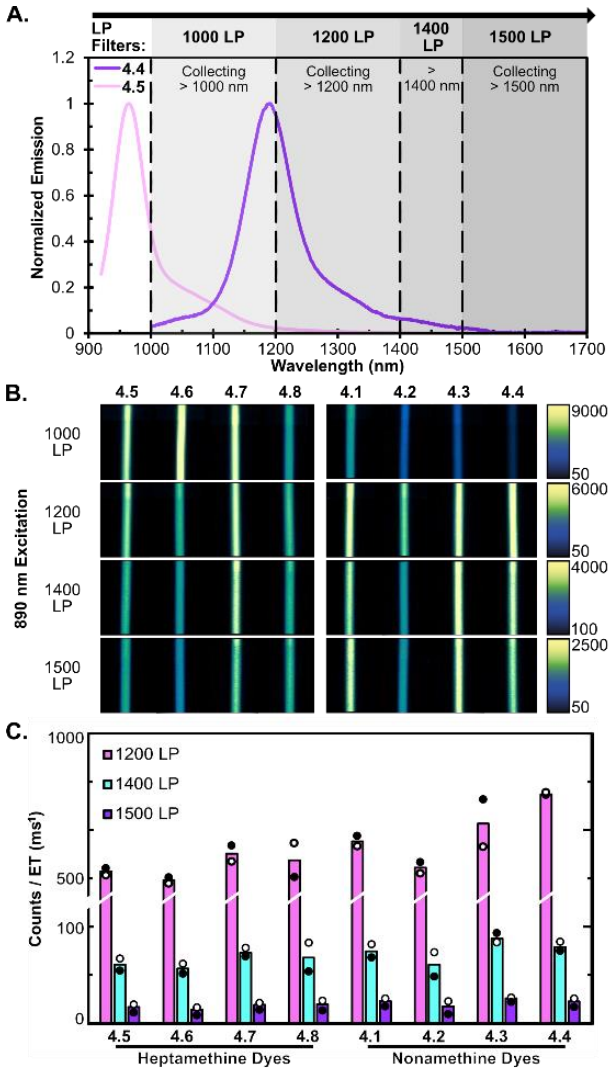

Figure 4.5. **A**. Emission collected at different SWIR LP filters for dyes **4.4** (**JuloFlav9**) and **4.5**. **B**. Capillary images of absorbance matched dyes in dichloromethane under 890 nm excitation, all with 0.7 ms ETs. **C**. Quantified results from capillaries in 4.3B, averaged over 2 trials (black and white dot denote separate trials).

We next investigated the brightness of our dyes at incrementally red-shifted LP filters, up to 1500 nm. We can determine and compare these values by preparing solutions with equal absorbance at the excitation wavelength and measuring differences in the intensity of emission as a function of LP filter. Figure 4.5B and 4.5C show raw images and quantified counts of absorbance matched **4.1**–**4.8** in capillaries under 890 nm excitation, respectively. These experiments demonstrate that despite lower Φ_F values, **4.4** (**JuloFlav9**), followed by **4.2** (**Flav9**), and **4.1** (**Chrom9**), are poised to yield the best images in high resolution SWIR imaging with $\geq$1400 nm LP filters. Notably, the high ε_{max} and Φ_F of the heptamethine dyes result in lower, but detectable, signal with LP filters at redder wavelengths.

4.3.6 Single-color, High-resolution, *in vivo* SWIR Imaging

Next, we tested the most promising nonamethine dyes in non-invasive *in vivo* imaging with SWIR excitation (1060 nm) and different LP filters. We selected **4.1** (**Chrom9**) and **4.4** (**JuloFlav9**) for single-color mouse imaging via intravenous (*i.v.*) injection. In preparation for animal experiments, we encapsulated our hydrophobic nonamethine dyes into amphiphilic poly(ethylene) glycol-phospholipid micelles (Figure 4.6A). Consistent with previous work, the Chrom dyes suffered less self-quenching aggregation in the micelles than the Flav dyes (Figure 4.7). On average, the micelles were around 17 nm in size (Figure 4.8, avg. number).

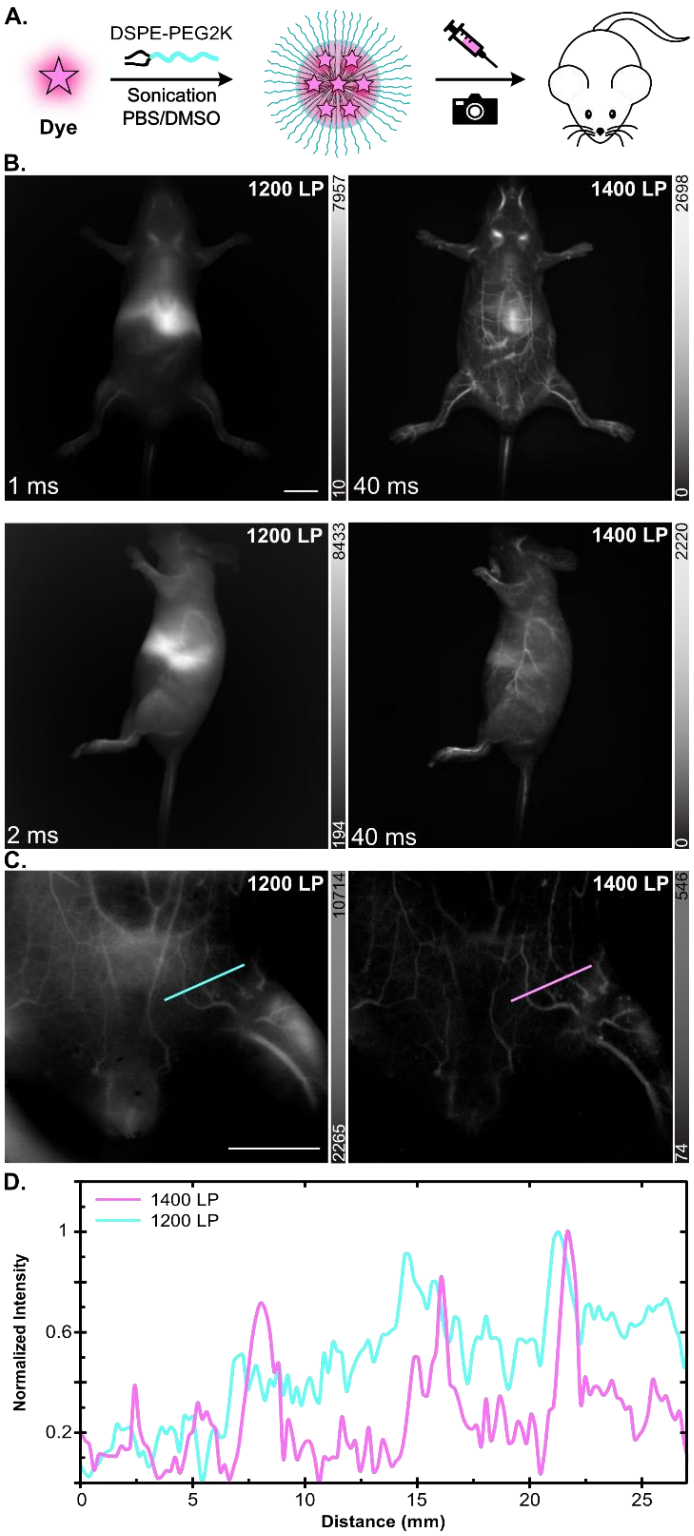

Figure 4.6. **A**. Scheme for micelle formulation and subsequent *in vivo* delivery. **B**. Vasculature imaging with **1** (**Chrom9)**. ET as listed and scale bar = 1 cm. **C**. Imaging with **1** (**Chrom9)** with zoom lens (2.5x magnification), ET = 100 ms. scale bar = 1 cm. **D**. Quantification of ROI in **C**. Power densities were 161 $mWcm^{-2}$.

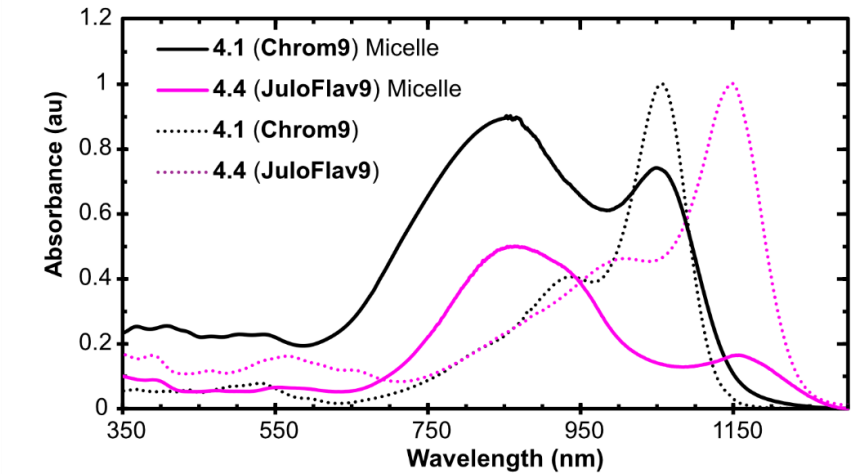

Figure 4.7. Representative micelle absorbance traces of **4.4** (**JuloFlav9**) and **4.1** (**Chrom9**). Taken in PBS (micelles diluted 1:10 in PBS). Raw micelle absorbance measured in a cuvette with a path length of 3 mm. Normalized monomer dye absorbance overlayed for reference (dotted lines).

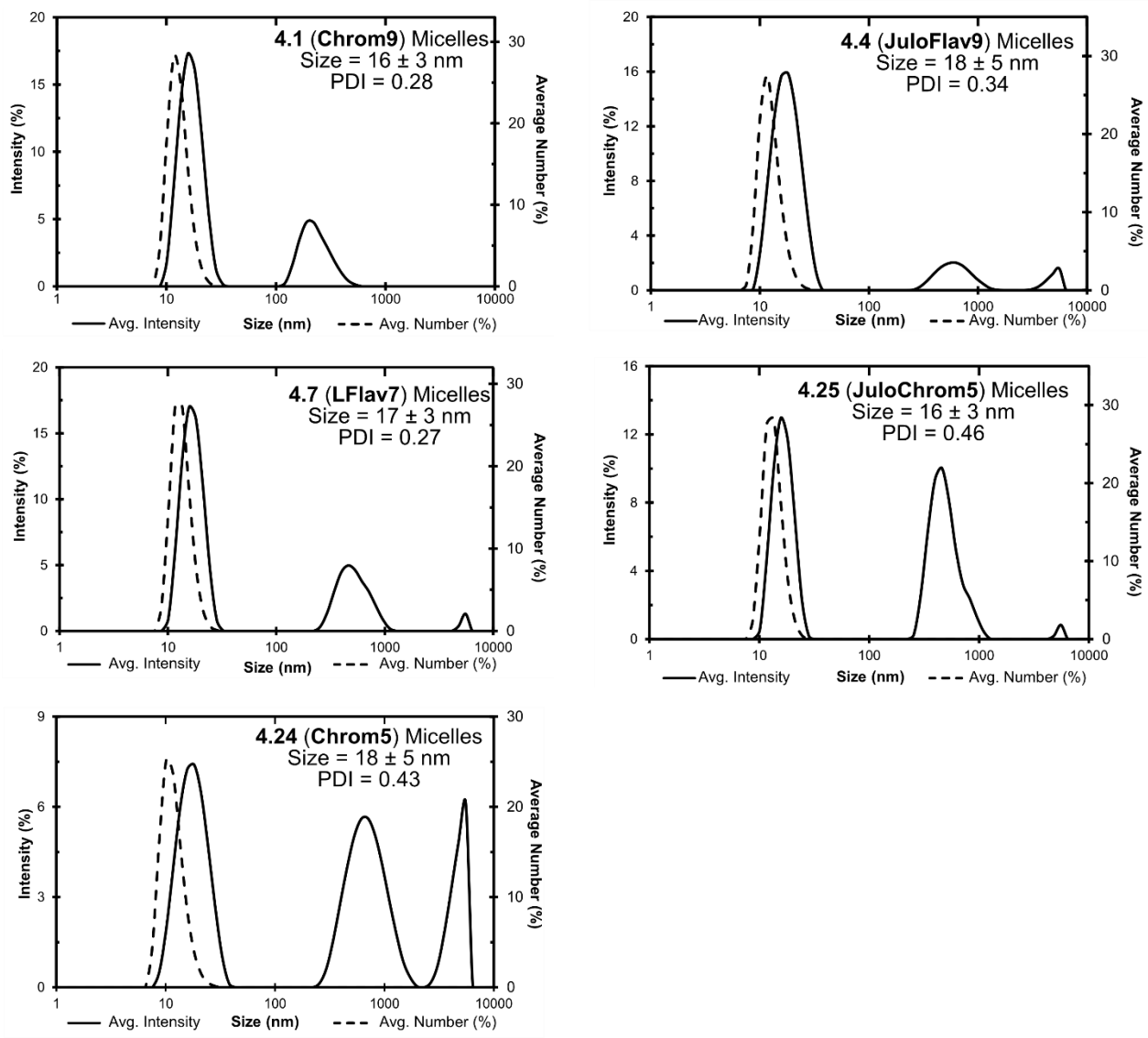

Figure 4.8. Representative DLS characterization of micelles imaged in this work. PEG-phospholipid micelles composed of 18:0 PEG2000 lipids containing dyes were used for single-color imaging (**4.1** or **4.4**), 2-color imaging (**4.1** and **4.4**), or 5-color imaging (**4.1**, **4.4**, **4.7**, **Chrom5**, and **JuloChrom5**). Data are the average of three replicate measurements. Size values and PDI values were taken and calculated from the majority peak. Size error taken as the standard deviation of the replicates.

Micelles containing **4.1** (**Chrom9**) were *i.v.* injected and vasculature images were immediately acquired with 1060 nm excitation (Figure 4.46). When using a 1300 nm LP filter, standard for imaging experiments with 1060 nm excitation, video-rate images are readily obtained.

When imaging with the 1400 nm LP filter, the enhanced resolution of this region of the SWIR is apparent, which is highlighted when the magnification is increased (Figure 4.6C–D).

After 1 h, **4.1** (**Chrom9**) was cleared from the vasculature and resided in the liver and spleen, which was confirmed at 48 h by *ex vivo* analysis (Figure 4.9). Fluorophore **4.4** (**JuloFlav9**) was also used for vasculature imaging with excitation at 1060 nm (Figure 4.10). There was lower signal achieved with **4.4** (**JuloFlav9**) than observed with **4.1** (**Chrom9**), likely due to a combination of the lower Φ_F and increased aggregation within the micelle formulation (Figure 4.7).

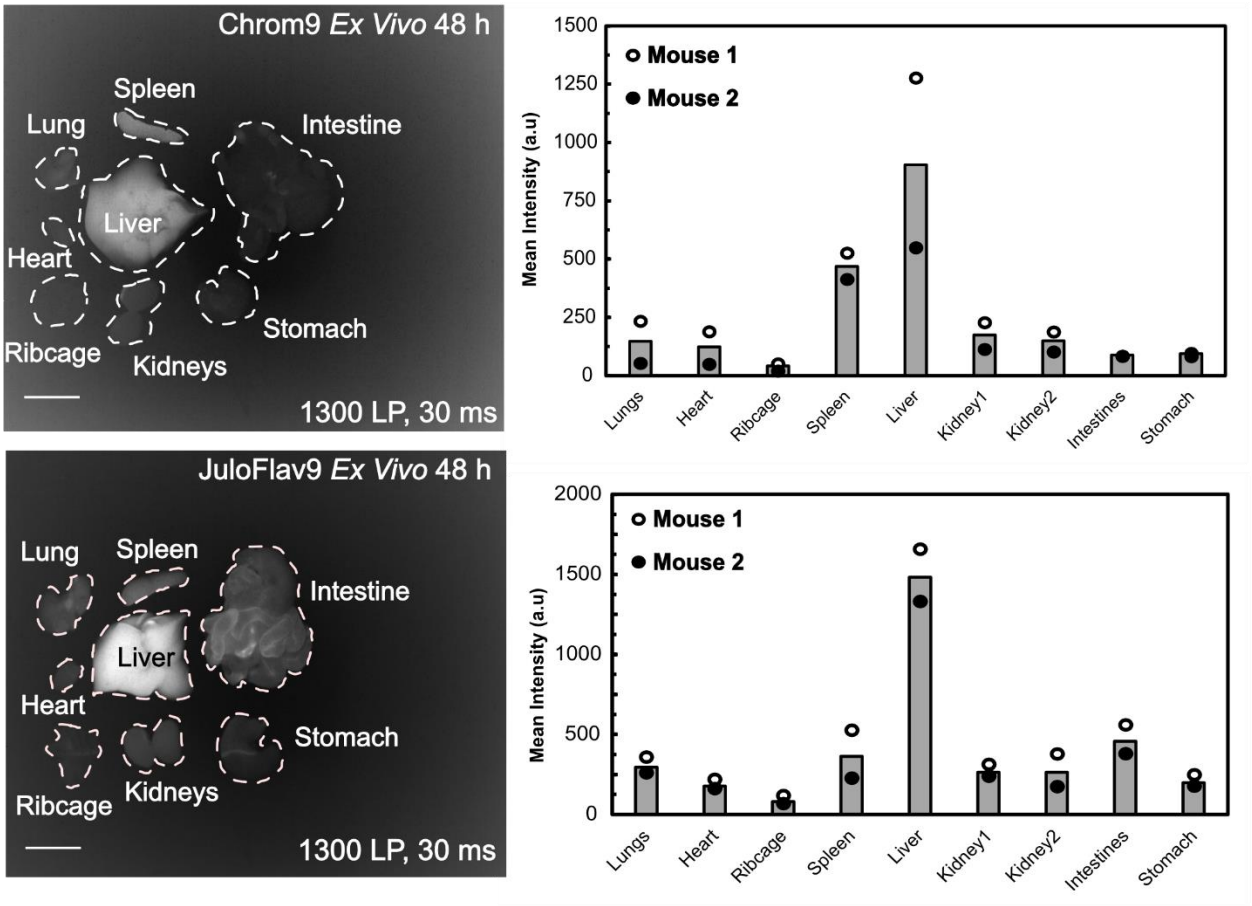

Figure 4.9. Distribution and quantification of **4.1** (**Chrom9**), and **4.4** (**JuloFlav9**), micelle emission in different organs 48 h after *i.v.* injection, estimated and normalized by the mean intensity. Intensities across ROI for each organ (dashed lines). Mean intensities plotted (points)

and then averaged (bar) for each organ; n = 2 for each dye. *Ex vivo* imaging was done with 1060 nm excitation, 1300 LP filter, and 30 ms ET. Scale bar = 10 mm.

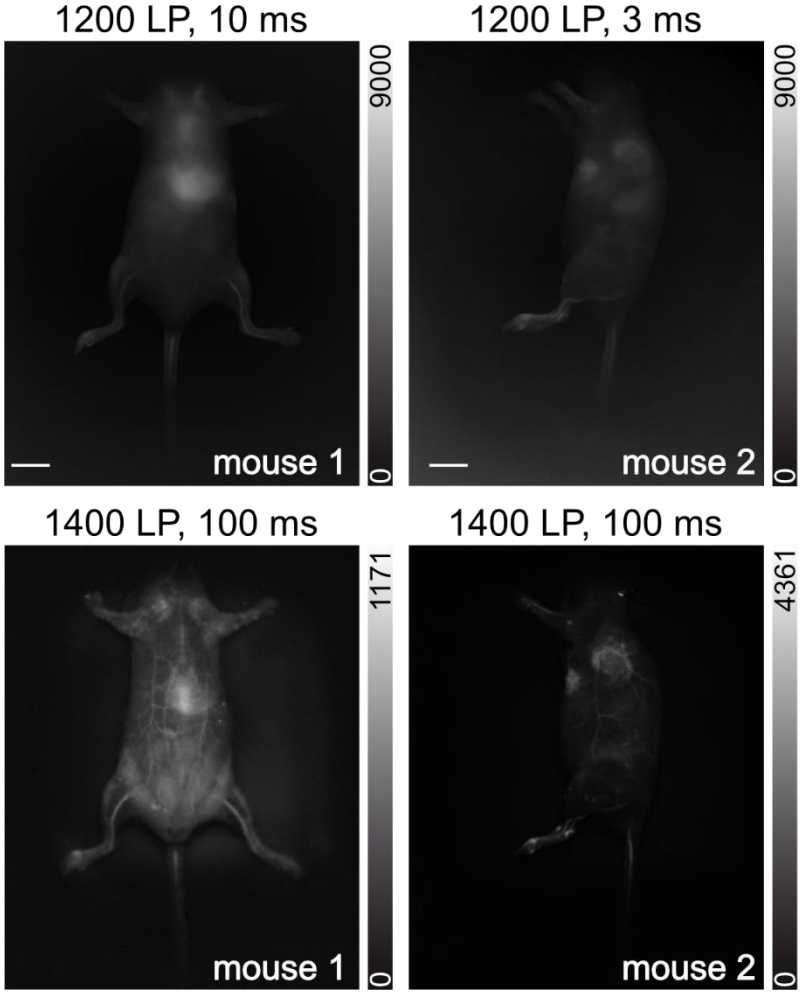

Figure 4.10. Single color imaging with **4.4** (**JuloFlav9**) (*i.v.*), 1060 nm excitation. Two replicates shown (mouse 1 = front view; mouse 2 = side view). Filters and exposure times as shown (3–100 ms). Scale bar = 10 mm. Power densities were 161 mWcm^{-2}.

4.3.7 Multicolor Experiments

Our previous approaches to excitation-based multiplexed imaging have employed excitation ranging from 785–1065 nm, with a maximum of 4 channels.[29] With the development of **4.4** (**JuloFlav9**) that has a $\lambda_{max,abs}$ = 1149 nm, we expanded our excitation capabilities through the addition of a 1150 nm laser. Although adequate signal from **4.4** (**JuloFlav9**) was seen with 1060 nm excitation (Figure 4.10), better overlap with the 1150 nm laser should allow for preferential

excitation. As a result, we focused our multiplexing efforts toward all SWIR multiplexed imaging with 1060 and 1150 nm excitation as well as 5-color multiplexing using our new set of excitation lasers.

In preparation for *in vivo* applications, we explored multiplexing experiments with dye-containing micelles in capillaries. First, we focused on multiplexing the SWIR excitation channels. After being loaded into PEG micelles, **4.1** (**Chrom9**) and **4.4** (**JuloFlav9**) showed local absorbance maxima at 1060 and 1150 nm respectively (Figure 4.11A). We found that using 15 nmol of **4.1** (**Chrom9**) and 10 nmol of **4.4** (**JuloFlav9**) provided preferential signal from **4.1** (**Chrom9**) upon 1060 nm excitation and distinct signal from **4.4** (**JuloFlav9**) with 1150 nm excitation with a 1500 nm LP filter (Figure 4.11B) Encouraged by these data, we incorporated linear heptamethine dye **4.7** (**LFlav7**) for excitation at 974 nm, along with previously reported pentamethine dyes **Chrom5** (786 nm excitation)[27] and **JuloChrom5** (890 nm excitation)[27]. Through optimization of fluorophore concentration, exposure time, and/or laser power, we were able to obtain preferential excitation of each fluorophore in capillaries at their respective wavelengths (Figure 4.11C). We commenced a similar experiment in a mouse phantom, leading to five-color imaging of different organ chambers (Figure 4.11D). Notably, imaging with the mouse phantom was more challenging than the capillary experiments due to decreased signal from light scattering.

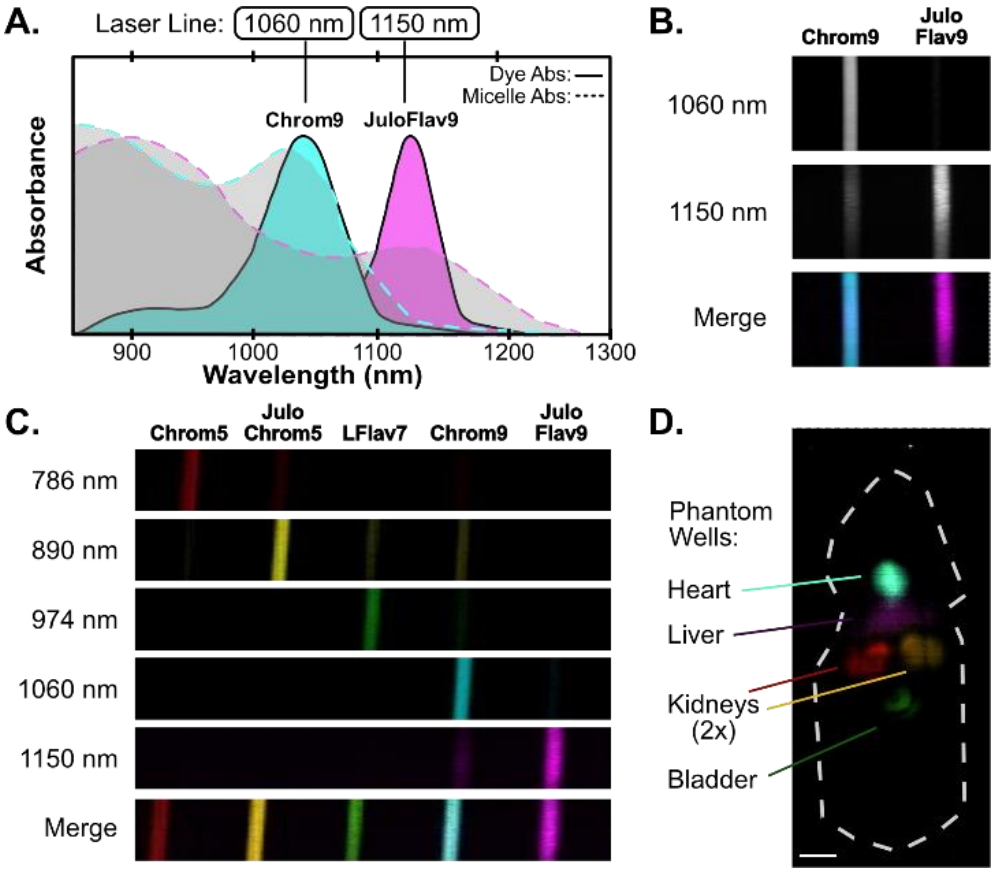

Figure 4.11. **A**. Excitation-multiplexing strategy for 2-color imaging with **4.1** (**Chrom9**) and **4.4** (**JuloFlav9**) with plotted monomer and micelle absorption. **B**. 2-color capillary imaging with **4.1** (**Chrom9**) and **4.4** (**JuloFlav9**) micelles. **C**. 5-color capillary imaging with **Chrom5** (786 nm), **JuloChrom5** (890 nm), **4.7** (**LFlav7**; 974 nm), **4.1** (**Chrom9**; 1060 nm), **4.4** (**JuloFlav9**, 1150 nm) micelles. **D**. 5-color imaging in mouse phantom, 100 ms ET, scale bar = 1 cm.

With promising initial imaging conditions for 2-color SWIR excitation multiplexing established, we injected **4.4** (**JuloFlav9**) into the intraperitoneal (*i.p.*) cavity of a mouse and obtained good signal with 1500 nm LP at 20 ms exposure time (Figure 4.12A). Next, we *i.v.* injected **4.1** (**Chrom9**) in the same mouse and performed excitation multiplexed 2-color imaging to simultaneously visualize the vasculature and *i.p.* cavity in the high-resolution region of the SWIR (Figure 4.12B). We then demonstrated the orthogonal detection (Figure 4.12C) and subsequent quantification (Figure 4.12D) of signal across a ROI for both 1060 and 1150 nm channels. This is the first time excitation-based multiplexing has been successful with small

molecule fluorophores with a 1500 nm LP filter. We accomplished these multiplexed experiments with respectable exposure times of 20-50 ms.

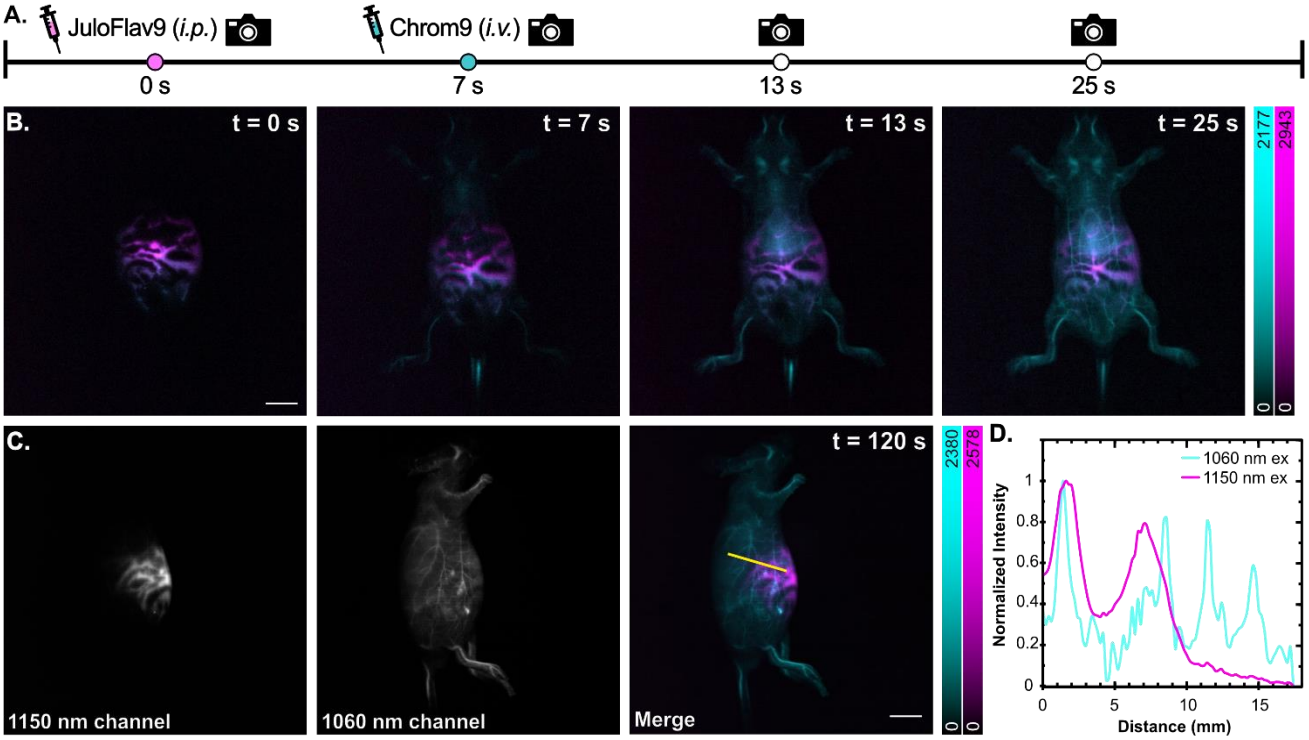

Figure 4.12. **A**. Injection timeline for 2-color excitation-multiplexed SWIR *in vivo* imaging. **B**. Representative 2-color *in vivo* imaging over the course of 25 seconds; ET = 20–50 ms, 1500 LP, scale bar = 10 mm. **C**. Side-view 1060 and 1150 nm imaging channels and ROI, scale bar = 10 mm. **D**. Plotted intensity for 1060 and 1150 nm channels from 4.6C. Power densities for each laser were as follows: 1060 nm = 161 mWcm^{-2}; 1150 nm = 160 mWcm^{-2}.

The use of nonamethine dyes facilitates excitation multiplexing without the need for NIR excitation. We also attempted a 5-color *in vivo* experiment using differential injection methods, timepoints, and an affinity probe (Figure 4.13). Unfortunately, as foreshadowed by the phantom experiments, the 5-color multiplexing was a challenge due to the balance of maximizing signal and minimizing crosstalk. As the functionality and brightness of all our SWIR-emissive fluorophores improve, we expect to be able to obtain *in vivo* 5-color imaging using **4.1** (**Chrom9**) and **4.4** (**JuloFlav9**) as contrast agents for 1060 and 1150 nm, respectively. Overall, the ability to

red-shift chromenylium and flavylium fluorophores further into the SWIR allows for the advantages of the SWIR to be extended from single color experiments to multiplexed imaging.

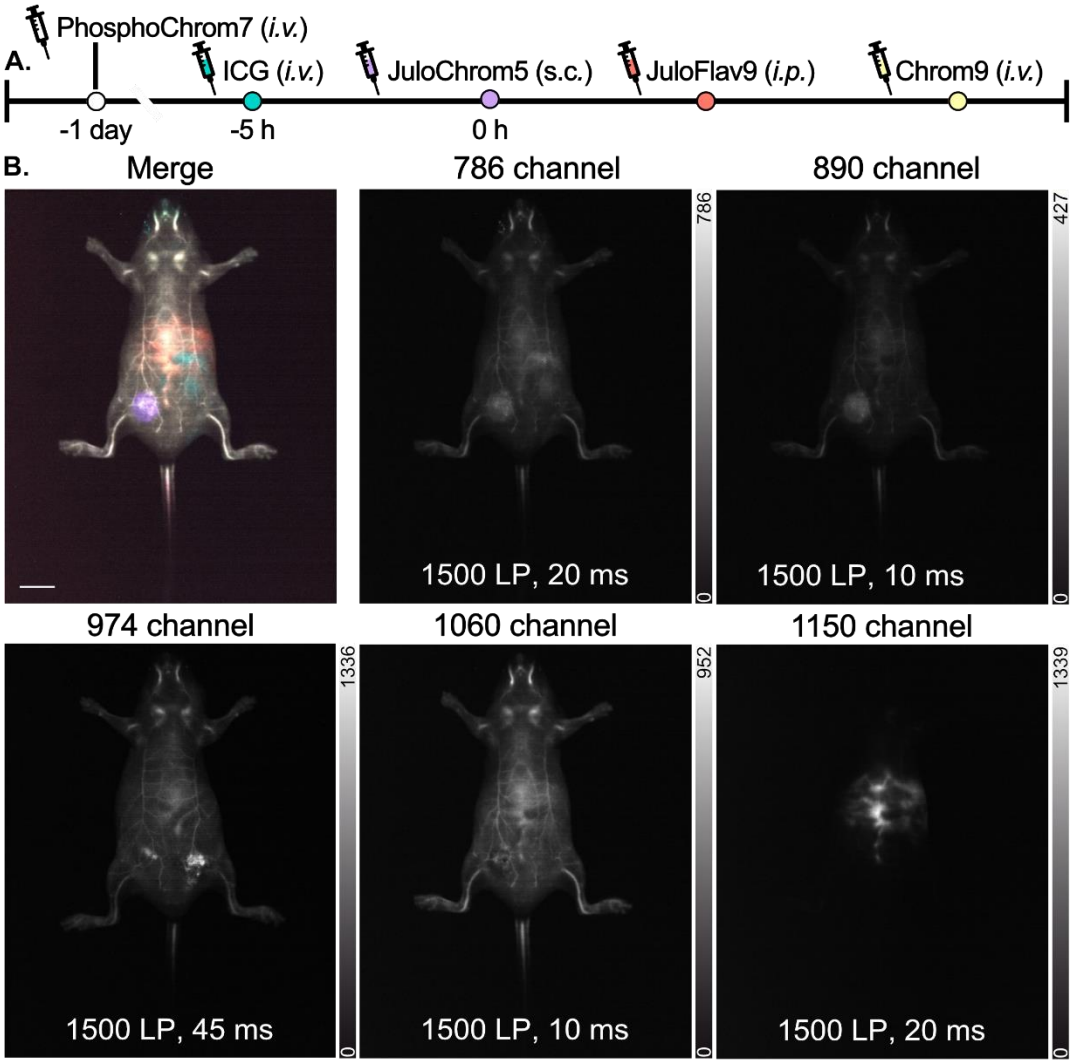

Figure 4.13. 5-color real-time *in vivo* imaging with previously reported dyes **JuloChrom5** (890 nm) and **PhosphoChrom7** (974 nm), FDA-approved indocyanine green (**ICG**; 786 nm), and nonamethine dyes **4.1** (**Chrom9**; 1060 nm) and **4.4** (**JuloFlav9**; 1150 nm). Exposure times as shown (10–45 ms). Scale bar = 10 mm. Power densities for each irradiation wavelength were as follows: 786 nm = 96.7 $mWcm^{-2}$; 890 nm = 136 $mWcm^{-2}$; 974 nm = 169 $mWcm^{-2}$; 1060 nm = 161 $mWcm^{-2}$; 1150 nm = 160 $mWcm^{-2}$.

Unfortunately, **PhosphoChrom7** could not be visualized in this experiment. When designing multiplexed experiments and optimizing to minimize crosstalk, it is often the middle excitation wavelengths that are the most challenging as increased exposure times lead to increased

crosstalk at the longer wavelengths, while increased concentration results in more significant excitation from the bluer wavelengths. Indeed, this is the scenario encountered as the signal within the 975 nm channel was insufficient and ultimately, we effectively obtained a 4-color image with distinct labeling of liver, spleen, veins, *i.p.* cavity, and flank. Note that all imaging discussed in this chapter was performed by Emily Mobley and Eric Lin.

4.4 Conclusions

The amount of bright small molecule dyes capable of imaging within the "high resolution" or "high depth penetration" subregions of the SWIR is limited. In this work, we developed red-shifted nonamethine chromenylium and flavylium fluorophores that were sufficiently bright at their bandgaps. These dyes have clinical potential for visualizing and monitoring vascularization and possibly reperfusion in real-time, without the reliance of ionizing radiation. Fluorophore **4.1** (**Chrom9**) was shown to have bright emission above 1400 nm and demonstrated excellent resolution in this window rather than higher energy regions. The most red-shifted dye in this panel, **4.4** (**JuloFlav9**), allowed for imaging with excitation at 1150 nm, paving the way for the first example of 2-color SWIR excitation-multiplexed imaging with small molecule contrast agents.

This work showcased the advantages of imaging at red-shifted, lower energy longpass filters. Moving forward, SWIR imaging efforts can improve with dyes that have better micelle photophysical properties. Additionally, developing dyes with high affinity for biologically relevant analytes or dyes with enhanced water solubility can strengthen clinical applications. However, as shown in this work, the crucial factor for imaging in these high-resolution zones with SWIR dyes is maximizing emission above 1400 nm.

4.5 Experimental Procedures

4.5.1 Abbreviations, Materials, and Instrumentation

Abbreviations: DCM = dichloromethane; DMSO =dimethylsulfoxide; EtOH = ethanol; EtOAc = ethyl acetate; MeOH = methanol; TFA = trifluoroacetic acid; DMF = dimethylformamide; THF = tetrahydrofuran; MeCN = acetonitrile; Ac_2O = acetic anhydride; PBS = phosphate buffered saline; HBF_4 = fluoroboric acid; $NaClO_4$ = sodium perchlorate; MeMgBr = methyl magnesium bromide; $POCl_3$ = phosphoryl chloride; *t*Bu = *tert*-butyl; Ph = phenyl; NaOAc = sodium acetate; rt = room temperature; h = hour; min = minutes; NMR = nuclear magnetic resonance; HRMS = high resolution mass spectrometry; DLS = dynamic light scattering; NIR = near-infrared; SWIR = shortwave infrared; ROI = region of interest; LP = longpass (filter); SP = shortpass (filter); ET = exposure time; fps = frames per second; *i.v.* = intravenous; *i.p.* = intraperitoneal; *s.c.* = subcutaneous.

Materials: Reagents were purchased from Acros Organics, Alfa Aesar, Fisher Scientific, Sigma-Aldrich, or TCI and used without additional purification. Anhydrous and deoxygenated solvents (toluene, THF, DMF) were dispensed from a Grubb's-type Phoenix Solvent Drying System constructed by the late JC Meyer. Oxygen was removed from solvents by three consecutive freeze–pump–thaw cycles in air-free glassware directly before use. For every reaction, dry Schlenk technique was used.

Instrumentation: Thin layer chromatography was performed using Silica Gel 60 F254 (EMD Millipore) plates. Flash chromatography was executed with technical grade silica gel with 60 Å pores and 40–63 μm mesh particle size (Sorbtech Technologies). Solvent was removed with a Büchi Rotovapor and further dried with a Welch DuoSeal pump. Masses for analytical measurements were taken on a Sartorius MSE6.6S-000-DM S13 Cubis Micro Balance. Bath

sonication was performed using a Branson 3800 ultrasonic cleaner. Nuclear magnetic resonance (^{1}H NMR and ^{13}C NMR) spectra were taken on Bruker AV-400, or AV-500 instruments and processed with MestReNova or TopSpin software. All ^{1}H NMR and ^{13}C NMR peaks are reported in ppm in reference to their respective solvent signals (CD_3CN δH=1.94; MeOD δH=3.31, δC=49.00; CD_2Cl_2 δH=5.32, δC=53.84; $(CD_3)_2SO$ δH=2.50). DLS measurements were performed on a Malvern Zetasizer Nano dynamic light scattering instrument. SOP parameters: 10 runs, 10 seconds/run, three measurements, no delay between measurements, 25 °C with 120 second equilibration time. Data are representative of three replicate measurements. Probe sonication for micelle preparation was performed using a QSonica (Q125) probe sonicator.

4.5.2 Photophysical Procedures and Animal Imaging Protocols

Absorbance spectra were collected on a JASCO V-770 UV-Visible/NIR spectrophotometer with a 2000 nm/min scan rate after blanking with the appropriate solvent. Photoluminescence spectra were obtained on a Horiba Fluorometer PTI QM-400. Quartz cuvettes (1 cm) were used for absorbance and photoluminescence measurements unless otherwise noted.

Absorption coefficients (taken in DCM) were calculated according to Beer Lambert's law through serial dilutions using Hamilton syringes in volumetric flasks.

$$A = \varepsilon l c$$

Where ε is the absorbance coefficient, l is the path length in cm, c is the concentration in molarity and A is the absorbance in O.D. Error was taken as the standard deviation of the triplicate experiments.

Relative quantum yields were determined in DCM with **IR-26** as the known standard (Φ_F = 0.05 ± 0.03% in DCM) and excitation at 885 nm according to the following formula:

$$\Phi_{F,x} = \Phi_{F,r}\left(\frac{m_x}{m_f}\right)\left(\frac{\eta_x^2}{\eta_r^2}\right)$$

Where m represents the slope of the line (y = mx + b) obtained from graphing integrated fluorescence intensity versus optical density across a series of samples, η is the refractive index of the solvent, and the subscripts x and r represent values of the unknown and reference (**IR-26**), respectively. To obtain a plot of integrated fluorescence intensity versus absorbance for the reference five solutions and a solvent blank was prepared and their absorbance and emission spectra acquired.

Absorption coefficients and fluorescence quantum yields with errors can be found in **Table 4.1**.

Animal imaging experiments were performed in congruence with the University of California, Los Angeles guidelines. Protocols were approved by the Animal Research Committee (Protocol number: ARC-2018-047). Non-invasive, whole mouse imaging was performed with athymic NU/J female mice (6-16 weeks old) purchased from The Jackson Laboratory. Mice were anesthetized by inhalation of 2-4% isoflurane. Tail vein injections were done with a catheter assembled by 29-gauge needle (VetriJec™) connected through plastic tubing to a syringe prefilled with isotonic saline solution. The bevel of the needle was inserted into either the dorsal, lateral left or lateral right tail vein and secured with a tissue adhesive. The tubing was then connected to a 29-

gauge needle syringe (VetriJec™ Insulin Syringe) prefilled with the desired micelle-encapsulated dye. For intravenous injections (*i.v.*) the mouse was positioned with the ventral side facing the camera. Injections were also done in the intraperitoneal (*i.p.*) space, and/or the subcutaneous (*s.c.*) space with a ventral view of the mouse. All solutions were filtered through a 0.22 μm syringe filter before injection.

For whole mouse imaging, a custom-built setup was used. Lumics laser units: LU1064D350- U30AN (35 W) "1064 nm"; LU0975DLU350-S30AN03 (35 W) "975 nm"; LU0890D280-U10AN (28 W) "890 nm"; LU0785D250-U70AN (25 W) "785 nm"; and mpbc.ca laser unit: 2RU-YFL-P-10-1160-M (10 W) "1150 nm" were used for excitation. Lumics laser outputs were coupled in a 4x1 fan-out fiber-optic bundle (Thorlabs BF46LS01) of 600 μm core diameter for each optical path. The output from the fiber was fixed in an excitation cube (Thorlabs KCB1E), reflected off of a mirror (Thorlabs BBE1- E03), and passed through a positive achromat (Thorlabs AC254-050-AB-ML), short pass (SP) filter (1100 nm, Edmund Optics #84-768) and an engineered diffuser (Thorlabs ED1-S20-MD) to provide uniform illumination over the working area. The mpbc.ca laser fiber output (collimated to a 0.7 mm gaussian beam) was fixed with a clamp (Thorlabs VC1) and reflected off of two mirrors (Thorlabs KCB1C) in sequence into a 10X AR-coated achromatic Galilean beam expander (Thorlabs GBE10-C) with an engineered diffuser (Thorlabs ED1-S20-MD) to illuminate the working area. The working area was covered by a heating mat coated with blackout fabric (Thorlabs BK5). Emitted light was detected via an InGaAs (Allied Vision Goldeye G-032 Cool TEC2) camera with a sensor temperature set point of -30 °C. The camera was placed vertically above the field of illumination, with emitted light passed through a set of longpass (LP) emission filters (defined for each experiment) and a C-mount camera lens

(Kowa LM35HC-SW). The excitation flux at the field of illumination was measured with a digital optical power sensor (Thorlabs PM100D). The assembly was partially enclosed to avoid excess light while enabling manipulation of the field of view during operation. Camera and lasers were externally controlled and synchronized by delivering trigger pulses of 5V Transistor-Transistor Logic to the laser drivers and camera using a programmable trigger controller with pulses generated with an Atmel Atmega328 micro-controller unit and programmed using Arduino Nano Rev 3 MCU (A000005) in the Arduino integrated development environment (IDE). Acquired imaging data are then transferred to the PC via either a Gigabit Ethernet (GigE), or CameraLink (CL) interface. For image acquisition, the toolbox of MATLAB programming environment was used in combination with a MATLAB script (CCDA V3, https://gitlab.com/brunslab/ccda) to preview and collect the required image data in 14-bit depth.

Images were processed using the Fiji distribution of ImageJ. All images were background corrected with a no-laser background (200 frames taken at the beginning of every imaging session) to correct for non-linearities in the detector and/or excitation. With background subtracted frames, regions of interest were then averaged using the "Z-project" feature (50+ frames) for the ventral, dorsal, and lateral views of the mouse. These averages were then compressed from the 14-bit to the 8-bit depth for display. LUT table CET-L164 was applied to all images for manuscript display in 8-bit format. For multicolor images, the brightness settings were matched before combining channels using the "merge channels" feature, with false colors assigned to each channel. Raw still images underwent no further processing. Videos were frame averaged to reduce file size, if necessary, before compression to a .AVI file. All raw and processed files can be found on BioImage Archive (https://www.ebi.ac.uk/biostudies/studies/S-BSST1383).

4.5.3 Synthetic Procedures

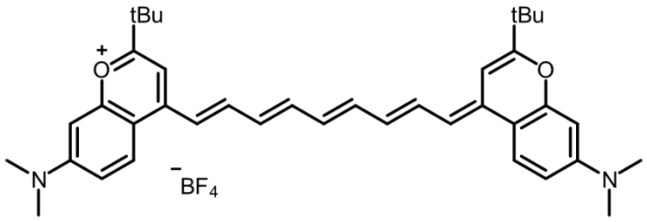

(**2-(*tert*-butyl)-4-((1*E*,3*E*,5*E*,7*E*)-9-((*E*)-2-(*tert*-butyl)-7-(dimethylamino)-4*H*-chromen-4-ylidene)nona-1,3,5,7-tetraen-1-yl)-7-(dimethylamino)chromenylium tetrafluoroborate**, **4.1**) Chromenylium, **4.11** (31 mg, 94 μmol, 1.0 equiv.), linker **4.13** (14 mg, 45 μmol, 0.48 equiv.), and sodium acetate (23 mg, 280 μmol, 3.0 equiv.) were added to a flame-dried 25 mL Schlenk tube under a N_2 atmosphere. Acetic anhydride (830 μL) was added, and the reaction mixture was immediately freeze-pump-thawed x3 before leaving the reaction to stir overnight at rt. The next day, the reaction was concentrated *in vacuo*. The product was precipitated in toluene and collected by vacuum filtration, washing with diethyl ether (1 x 20 mL) and THF (1 x 200 mL). The product was dry loaded onto silica gel and purified by column chromatography in DCM plus a gradient of 0.5–5% EtOH, resulting in a purple product (5 mg, 0.01 mmol, 7%). R_f = 0.6 in 9:1 DCM/EtOH. ^{1}H NMR (500 MHz, DMSO-d_6) δ 7.98 (d, J = 9.6 Hz, 2H), 7.82 (t, J = 12.9 Hz, 2H), 7.15 (t, J = 12.9 Hz, 2H), 7.01 – 6.98 (m, 3H), 6.97 (s, 1H), 6.90 (s, 2H), 6.69 – 6.50 (m, 5H), 3.12 (s, 12H), 1.34 (s, 18H). ^{19}F NMR (400 MHz, DMSO-d_6) δ -148.23. HRMS (ESI$^+$) calcd for $C_{39}H_{47}N_2O_2^+$ $[M]^+$: 575.3632; found 575.3662. Absorbance (CH_2Cl_2): 1057 nm. Emission (CH_2Cl_2, ex. 875 nm): 1088 nm.

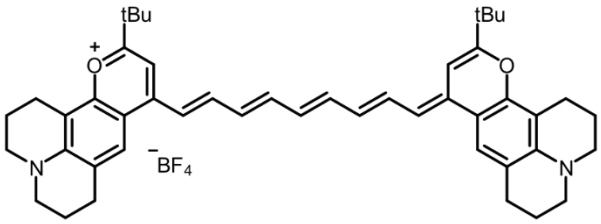

(**11-(*tert*-butyl)-9-((1*E*,3*E*,5*E*,7*E*,9*E*)-9-(11-(*tert*-butyl)-2,3,6,7-tetrahydro-1*H*,5*H*,9*H*-pyrano[2,3-f]pyrido[3,2,1-ij]quinolin-9-ylidene)nona-1,3,5,7-tetraen-1-yl)-2,3,6,7-tetrahydro-1*H*,5*H*-pyrano[2,3-f]pyrido[3,2,1-ij]quinolin-12-ium tetrafluoroborate**, **4.2**) Chromenylium **4.12** (33 mg, 86 μmol, 1.0 equiv.), linker **4.13** (13 mg, 41 mmol, 0.48 equiv.), and sodium acetate (21 mg, 260 μmol, 3.0 equiv.) were added to a flame-dried 25 mL Schlenk tube under a N_2 atmosphere. Acetic anhydride (770 μL) was added and the reaction mixture was immediately freeze-pump-thawed x3 before heating to 110 ºC for 15 min. The reaction was cooled and concentrated *in vacuo*. The product was precipitated in toluene and collected by vacuum filtration, washing with ~200 mL of diethyl ether and THF. The product was further purified by column chromatography after dry-loading onto silica in DCM plus a gradient of 0.5–5% EtOH, yielding a purple product (2.2 mg, 0.0029 mmol, 3.3%). R_f = 0.4 in 9:1 DCM/EtOH. ^{1}H NMR (500 MHz, DMSO-d_6) δ 7.73 (t, *J* = 12.9 Hz, 2H), 7.62 (s, 2H), 7.08 (t, *J* = 12.9 Hz, 2H), 6.90 (d, *J* = 13.4 Hz, 2H), 6.83 (s, 2H), 6.54 (dt, *J* = 20.7, 12.9 Hz, 3H), 3.10 (dd, *J* = 7.3, 4.8 Hz, 7H), 2.84 – 2.76 (m, 9H), 1.96 – 1.88 (m, 9H), 1.35 (s, 18H). ^{19}F NMR (400 MHz, DMSO-d_6) δ -148.32. HRMS (ESI$^+$) calcd for $C_{47}H_{55}N_2O_2^+$ [M]$^+$: 679.4258; found 679.4243 Absorbance (CH_2Cl_2): 1092 nm. Emission (CH_2Cl_2, ex. 885 nm): 1128 nm.

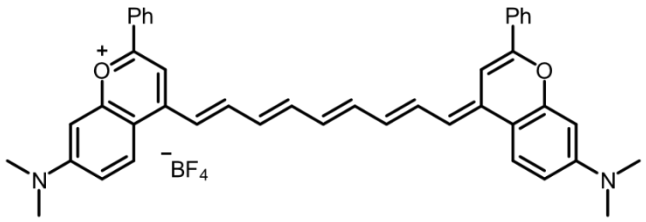

(**7-(dimethylamino)-4-((1*E*,3*E*,5*E*,7*E*)-9-((*E*)-7-(dimethylamino)-2-phenyl-4*H*-chromen-4-ylidene)nona-1,3,5,7-tetraen-1-yl)-2-phenylchromenylium tetrafluoroborate**, **4.3**) Flavylium **4.9** (22 mg, 63 μmol, 1.0 equiv.), linker **4.13** (9.4 mg, 30 μmol, 0.48 equiv.), and sodium acetate (15 mg, 190 μmol, 3.0 equiv.) were added to a flame-dried 25 mL Schlenk tube under a N_2

atmosphere. Acetic anhydride (560 μL) was added and the reaction mixture was immediately freeze-pump-thawed x3 before heating to 110 ºC for 15 min. The reaction was cooled and concentrated *in vacuo*. The product was dry loaded onto silica gel and purified by column chromatography in DCM plus a gradient of 0.5–5% EtOH, resulting in a dark purple product (5.1 mg, 0.01 mmol, 12%). R_f = 0.6 in 9:1 DCM/EtOH. ^{1}H NMR (500 MHz, DMSO-d_6) δ 8.25 – 8.14 (m, 4H), 8.04 (dd, *J* = 31.4, 11.3 Hz, 4H), 7.77 (s, 2H), 7.60 (s, 6H), 7.15 (t, *J* = 12.9 Hz, 2H), 7.08 (d, *J* = 13.2 Hz, 2H), 7.01 (dd, *J* = 9.3, 2.6 Hz, 2H), 6.87 (s, 2H), 6.68 (dd, *J* = 19.7, 12.6 Hz, 3H), 3.16 (s, 12H). ^{19}F NMR (400 MHz, DMSO-d_6) δ -148.32. HRMS (ESI$^+$) calcd for $C_{43}H_{39}N_2O_2^+$ [M]$^+$: 615.3006; found 615.3008. Absorbance (CH_2Cl_2): 1100 nm. Emission (CH_2Cl_2, ex. 885 nm): 1133 nm.

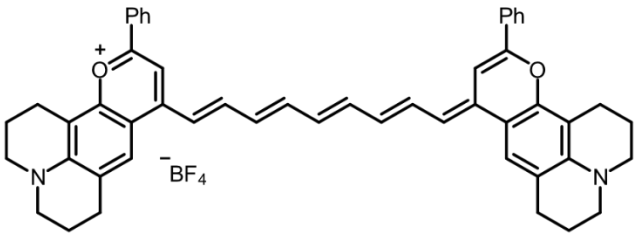

(**11-phenyl-9-((1*E*,3*E*,5*E*,7*E*,9*E*)-9-(11-phenyl-2,3,6,7-tetrahydro-1*H*,5*H*,9*H*-pyrano[2,3-f]pyrido[3,2,1-ij]quinolin-9-ylidene)nona-1,3,5,7-tetraen-1-yl)-2,3,6,7-tetrahydro-1*H*,5*H*-pyrano[2,3-f]pyrido[3,2,1-ij]quinolin-12-ium tetrafluoroborate**, **4.4**) Flavylium **4.10** (23 mg, 57 μmol, 1.0 equiv.), linker **4.13** (8.5 mg, 27 μmol, 0.48 equiv.), and sodium acetate (14 mg, 170 μmol, 3.0 equiv.) were added to a flame-dried 25 mL Schlenk tube under a N_2 atmosphere. Acetic anhydride (510 μL) was added, and the reaction mixture was immediately freeze-pump-thawed x3 before heating to 110 ºC for 20 min. The reaction was cooled on ice, extracted in approximately 25 mL of both H_2O and DCM, dried with Na_2SO_4 and then concentrated *in vacuo*. The product was precipitated in 200 mL of toluene and collected by vacuum filtration, washing with diethyl

ether (1 x 200 mL) and THF (1 x 200 mL). The product was dry loaded onto silica gel and purified by column chromatography in DCM plus a gradient of 0.5–5% EtOH, resulting in a dark purple product (3.9 mg, 0.0048 mmol, 8.5%). R_f = 0.4 in 9:1 DCM/EtOH. ^{1}H NMR (500 MHz, DCM-d_2) δ 7.99 – 7.93 (m, 4H), 7.56 (dd, *J* = 5.0, 1.8 Hz, 8H), 7.40 (s, 2H), 7.28 (s, 2H), 7.09 (t, *J* = 12.8 Hz, 2H), 6.77 (d, *J* = 13.4 Hz, 2H), 6.61 (t, *J* = 12.7 Hz, 2H), 6.55 (t, *J* = 12.9 Hz, 1H), 3.40 (d, *J* = 4.9 Hz, 8H), 2.98 (t, *J* = 6.5 Hz, 4H), 2.84 (t, *J* = 6.4 Hz, 4H), 2.08 – 2.00 (m, 9H). ^{19}F NMR (400 MHz, DMSO-d_6) δ -148.32. HRMS (ESI$^+$) calcd for $C_{51}H_{47}N_2O_2^+$ [M]$^+$: 719.3632; found 719.3671. Absorbance (CH_2Cl_2): 1149 nm. Emission (CH_2Cl_2, ex. 885 nm): 1188 nm.

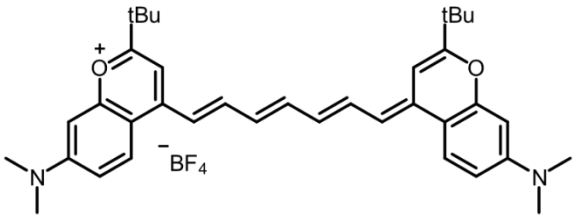

(**2-(*tert*-butyl)-4-((1*E*,3*E*,5*E*)-7-((*E*)-2-(*tert*-butyl)-7-(dimethylamino)-4*H*-chromen-4-ylidene)hepta-1,3,5-trien-1-yl)-7-(dimethylamino)chromenylium**, **4.5**) Chromenylium **4.11** (51 mg, 150 μmol, 1.0 equiv.), linker **4.23** (21 mg, 74 μmol, 0.48 equiv.), and sodium acetate (38 mg, 460 μmol, 3.0 equiv.) were added to a flame-dried 25 mL Schlenk tube under a N_2 atmosphere. Acetic anhydride (1.4 mL) was added and the reaction mixture was immediately freeze-pump-thawed x3 before heating to 110 ºC for 15 min. The reaction was cooled and concentrated *in vacuo*. The product was purified by column chromatography after dry-loading onto silica in DCM plus a gradient of 0.5–5% EtOH. This resulted in a dark violet product (28 mg, 0.044 mmol, 28%). R_f = 0.6 in 9:1 DCM/EtOH. ^{1}H NMR (500 MHz, DMSO-d_6) δ 7.99 (d, *J* = 9.5 Hz, 2H), 7.90 (t, *J* = 12.9 Hz, 2H), 7.42 (t, *J* = 12.9 Hz, 1H), 7.05 – 6.96 (m, 4H), 6.92 (s, 2H), 6.72 – 6.60 (m, 4H), 3.11 (s, 12H), 1.34 (s, 19H). HRMS (ESI$^+$) calcd for $C_{37}H_{45}N_2O_2^+$ [M]$^+$: 549.3475; found 549.3469. Absorbance (CH_2Cl_2): 935 nm. Emission (CH_2Cl_2, ex. 885 nm): 961 nm.

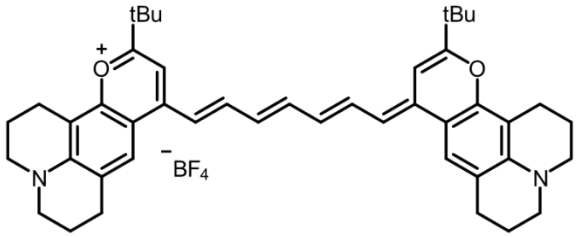

(**11-(tert-butyl)-9-((1*E*,3*E*,5*E*,7*E*)-7-(11-(tert-butyl)-2,3,6,7-tetrahydro-1*H*,5*H*,9*H*-pyrano[2,3-f]pyrido[3,2,1-ij]quinolin-9-ylidene)hepta-1,3,5-trien-1-yl)-2,3,6,7-tetrahydro-1*H*,5*H*-pyrano[2,3-f]pyrido[3,2,1-ij]quinolin-12-ium**, **4.6**) Chromenylium **4.12** (53 mg, 140 μmol, 1.0 equiv.), linker **4.23** (19 mg, 66 μmol, 0.48 equiv.), and sodium acetate (34 mg, 410 μmol, 3.0 equiv.) were added to a flame-dried 25 mL Schlenk tube under a N_2 atmosphere. Acetic anhydride (1.2 mL) was added and the reaction mixture was immediately freeze-pump-thawed x3 before heating to 110 ºC for 20 min. The reaction was cooled and concentrated *in vacuo*. The product was purified by column chromatography after dry-loading onto silica in DCM plus a gradient of 0.5–5% EtOH. This resulted in a dark purple product (15 mg, 0.020 mmol, 14%). R_f = 0.6 in 9:1 DCM/EtOH. ^{1}H NMR (500 MHz, DMSO-d_6) δ 7.79 (t, *J* = 12.9 Hz, 2H), 7.62 (s, 2H), 7.32 (t, *J* = 12.9 Hz, 1H), 6.91 (d, *J* = 13.3 Hz, 2H), 6.85 (s, 2H), 6.58 (t, *J* = 12.7 Hz, 2H), 3.34 (q, *J* = 6.9 Hz, 8H), 2.78 (t, *J* = 6.4 Hz, 8H), 1.90 (dd, *J* = 9.5, 5.9 Hz, 8H), 1.33 (s, 19H). HRMS (ESI$^+$) calcd for $C_{45}H_{53}N_2O_2^+$ [M]$^+$: 653.4101; found 653.4137. Absorbance (CH_2Cl_2): 970 nm. Emission (CH_2Cl_2, ex. 885 nm): 1004 nm.

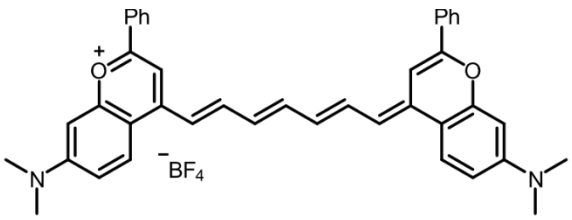

(**7-(dimethylamino)-4-((1*E*,3*E*,5*E*)-7-((*E*)-7-(dimethylamino)-2-phenyl-4*H*-chromen-4-ylidene)hepta-1,3,5-trien-1-yl)-2-phenylchromenylium tetrafluoroborate**, **4.7**) Flavylium **4.9** (52 mg, 440 μmol, 1.0 equiv.), linker **4.23** (21 mg, 72 μmol, 0.48 equiv.), and sodium acetate (36 mg, 440 μmol, 3.0 equiv.) were added to a flame-dried 25 mL Schlenk tube under a N_2 atmosphere. Acetic anhydride (1.3 mL) was added and the reaction mixture was immediately freeze-pump-thawed x3 before heating to 110 ºC for 15 min. The reaction was cooled and concentrated *in vacuo*. The product was purified by column chromatography after dry-loading onto silica in DCM plus a gradient of 0.5–5% EtOH. This resulted in a purple product (19 mg, 0.028 mmol, 19%). R_f = 0.4 in 9:1 DCM/EtOH. ^{1}H NMR (500 MHz, DMSO-d_6) δ 8.21 – 8.13 (m, 6H), 8.03 (d, *J* = 9.5 Hz, 2H), 7.83 (s, 2H), 7.59 (d, *J* = 2.7 Hz, 6H), 7.37 (t, *J* = 12.9 Hz, 1H), 7.13 (d, *J* = 13.3 Hz, 2H), 7.02 (dd, *J* = 9.3, 2.6 Hz, 2H), 6.87 (d, *J* = 2.6 Hz, 2H), 6.77 (t, *J* = 12.7 Hz, 2H), 3.15 (s, 12H). HRMS (ESI$^+$) calcd for $C_{41}H_{37}N_2O_2^+$ [M]$^+$: 589.2849; found 589.2848. Absorbance (CH_2Cl_2): 986 nm. Emission (CH_2Cl_2, ex. 885 nm): 1016 nm.

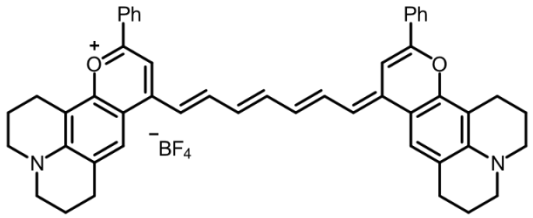

(11-phenyl-9-((1*E*,3*E*,5*E*,7*E*)-7-(11-phenyl-2,3,6,7-tetrahydro-1*H*,5*H*,9*H*-pyrano[2,3-f]pyrido[3,2,1-ij]quinolin-9-ylidene)hepta-1,3,5-trien-1-yl)-2,3,6,7-tetrahydro-1*H*,5*H*-pyrano[2,3-f]pyrido[3,2,1-ij]quinolin-12-ium tetrafluoroborate, **4.8**) Flavylium **4.10** (9.1 mg, 22 μmol, 1.0 equiv.), linker **4.23** (3.1 mg, 11 μmol, 0.48 equiv.), and sodium acetate (5.5 mg, 17 μmol, 3.0 equiv.) were added to a flame-dried 25 mL Schlenk tube under a N_2 atmosphere. Acetic anhydride (190 μL) was added and the reaction mixture was immediately freeze-pump-thawed x3 before heating to 110 ºC for 20 min. The reaction was cooled and concentrated *in vacuo*. The

product was purified by column chromatography after dry-loading onto silica in DCM plus a gradient of 0.5–5% EtOH. This resulted in a violet product (5.0 mg, 0.064 mmol, 29%). R_f = 0.5 in 9:1 DCM/EtOH. ^{1}H NMR (400 MHz, MeCN-d_3) δ 7.58 – 7.53 (m, 4H), 7.46 – 7.41 (m, 2H), 7.40 – 7.28 (m, 6H), 6.95 (t, *J* = 12.8 Hz, 1H), 6.85 (s, 2H), 6.73 (s, 2H), 6.59 (t, *J* = 12.6 Hz, 2H), 6.49 (d, *J* = 13.4 Hz, 2H), 3.21 (dt, *J* = 30.8, 5.8 Hz, 8H), 2.55 (t, *J* = 6.5 Hz, 4H), 2.32 – 2.28 (m, 4H), 1.87 (d, *J* = 5.3 Hz, 4H), 1.75 – 1.65 (m, 4H). HRMS (ESI$^+$) calcd for $C_{49}H_{45}N_2O_2^+$ $[M]^+$: 693.3475; found 693.3497. Absorbance (CH_2Cl_2): 1022 nm. Emission (CH_2Cl_2, ex. 885 nm): 1055 nm.

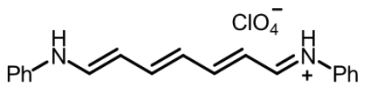

4.13

(***N*-((1*E*,2*E*,4*E*,6*E*)-7-(phenylamino)hepta-2,4,6-trien-1-ylidene)benzenaminium perchlorate**, **4.13**) Phosophoryl Oxychloride (1.4 g, 9.1 mmol, 2.0 equiv.) was added to a stirred solution of DMF (1.8 mL, 24 mmol) and MeOH (820 μL, 5.4 mmol) under N_2 gas. The reaction was then brought up to 40 °C and (2*E*,4*E*)-hexa-2,4-dienal **4.14**, (500 μL, 4.5 mmol, 1.0 equiv.) was added dropwise slowly. After 4 h, the reaction was brought down to rt and quenched with sodium perchlorate hydrate (1 g in 20 mL of H_2O). The product was then extracted in CH_2Cl_2 (2 x 25 mL) and the organic layer was dried with Na_2SO_4. Aniline (840 mg, 9.06 mmol, 2 equiv.) was then added to the organic layer at rt and left overnight for the product to precipitate out. The following day, the precipitate was filtered out and washed copiously with CH_2Cl_2. A blue solid (480 mg, 1.6 mmol, 34%) was isolated from the filtration. R_f = 0.4 in 9:1 DCM/EtOH. ^{1}H NMR (500 MHz, Methanol-d_4) δ 8.31 (d, *J* = 11.7 Hz, 2H), 7.65 (t, *J* = 12.8 Hz, 2H), 7.42 (m, *J* = 8.7, 7.4 Hz, 4H), 7.35 – 7.26 (m, 4H), 7.22 (t, *J* = 7.3 Hz, 2H), 6.50 (t, *J* = 13.0 Hz, 1H), 6.27 (t, *J* = 12.2 Hz, 2H). HRMS (ESI$^+$) calcd for $C_{17}H_{17}N_2^+$ $[M]^+$: 275.1542; found 275.1523. Absorbance

(CH_2Cl_2): 596 nm. Emission (CH_2Cl_2, ex. 530 nm): 642 nm. ^{1}H NMR shifts are in agreement with those of previous reports.

4.6 Spectra Relevant to Chapter Four

4.6.1 ^{1}H NMR Spectra

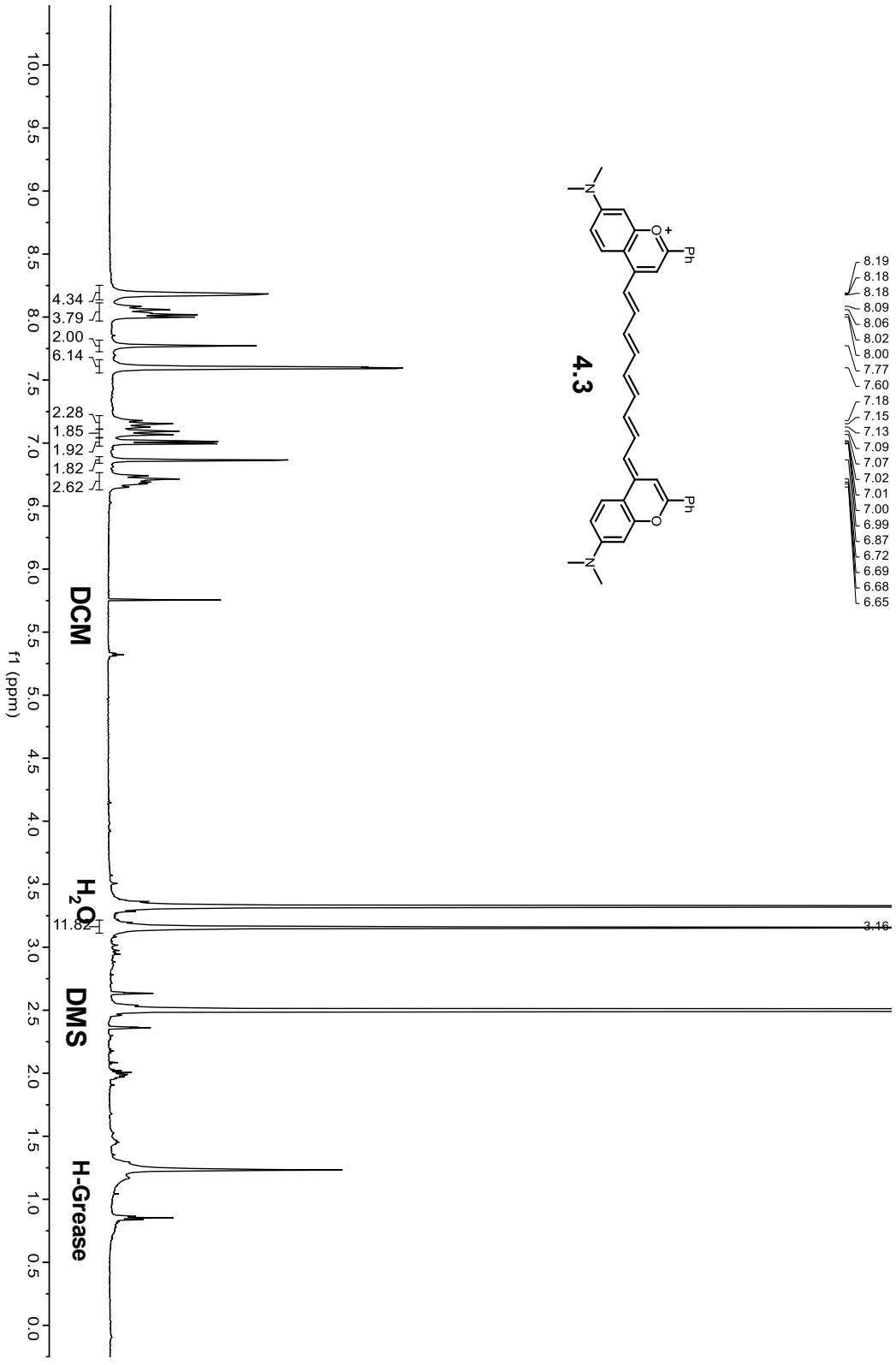

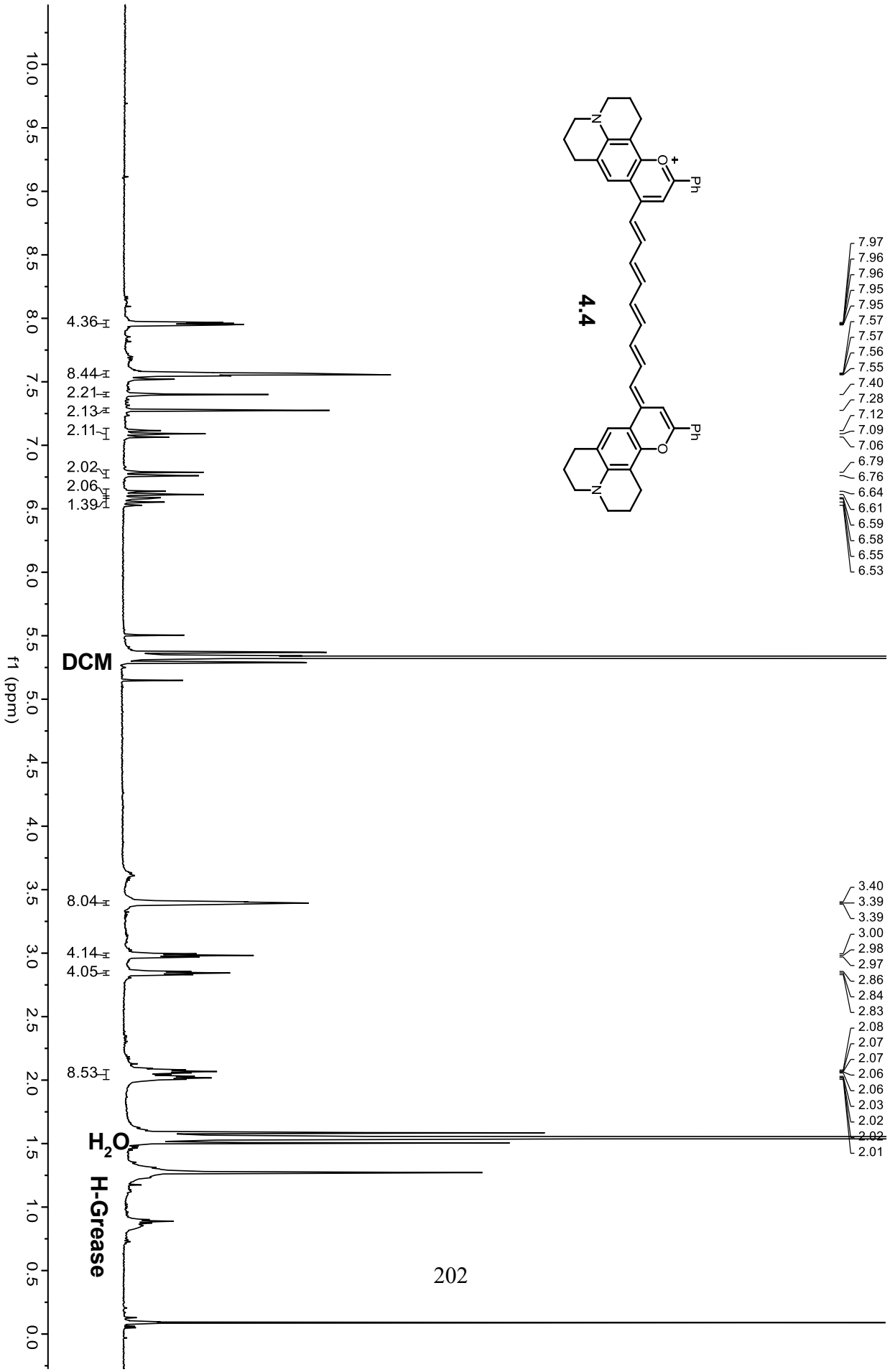
4.4
Ph
Ph
7.97
7.96
7.96
7.95
7.95
7.57
7.57
7.56
7.55
7.40
7.28
7.12
7.09
7.06
6.79
6.76
6.64
6.61
6.59
6.58
6.55
6.53
4.36
8.44
2.21
2.13
2.11
2.02
2.06
1.39
DCM
8.04
4.14
4.05
8.53
H2O
H-Grease
3.40
3.39
3.39
3.00
2.98
2.97
2.86
2.84
2.83
2.08
2.07
2.07
2.06
2.06
2.03
2.02
2.02
2.01
f1 (ppm)

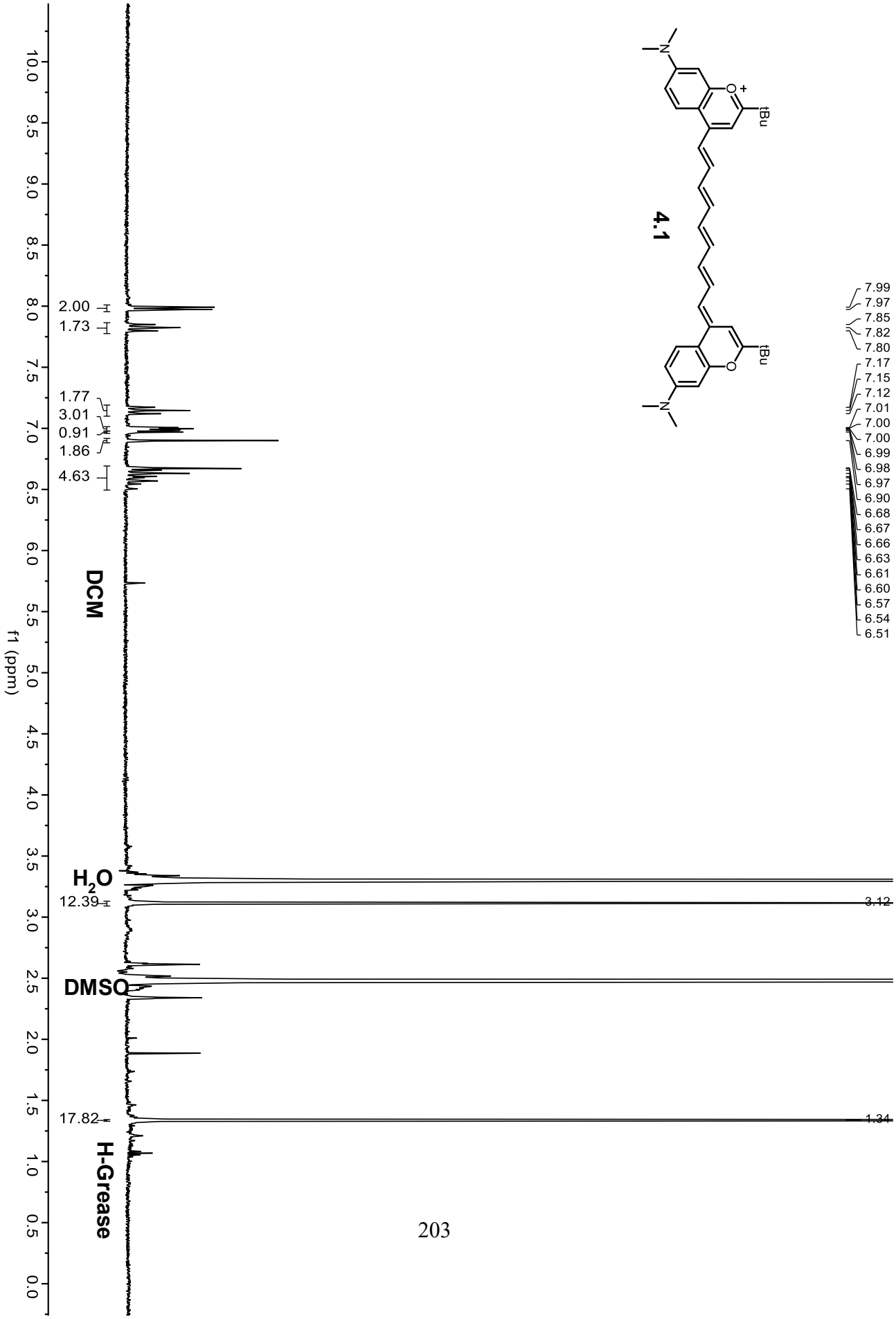
4.1
tBu
tBu
7.99
7.97
7.85
7.82
7.80
7.17
7.15
7.12
7.01
7.00
7.00
6.99
6.98
6.97
6.90
6.68
6.67
6.66
6.63
6.61
6.60
6.57
6.54
6.51
2.00
1.73
1.77
3.01
0.91
1.86
4.63
DCM
H2O
12.39
3.12
DMSO
17.82
1.34
H-Grease
f1 (ppm)

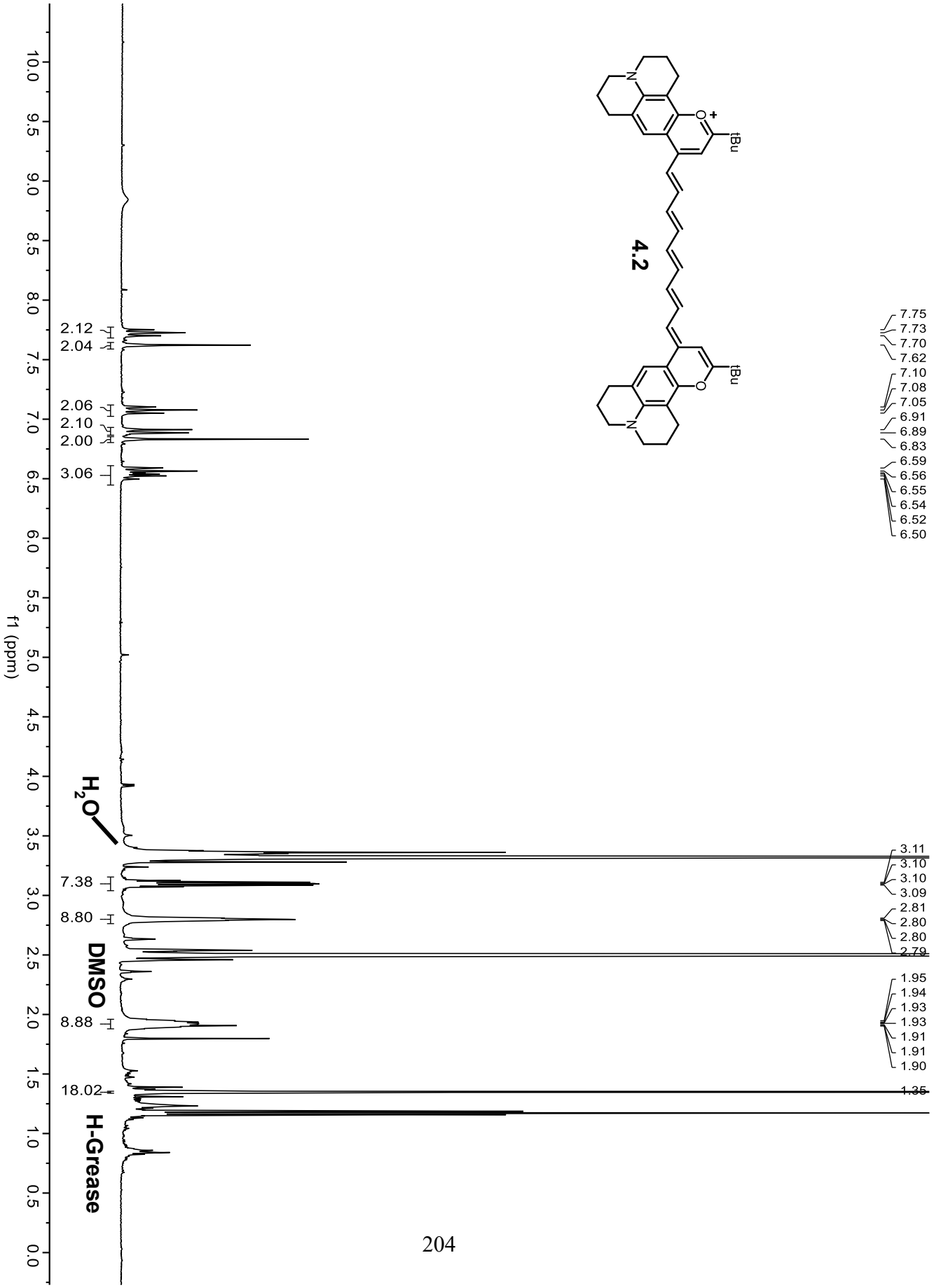
4.2
tBu
tBu
2.12
2.04
2.06
2.10
2.00
3.06
7.38
8.80
8.88
18.02
H2O
DMSO
H-Grease
7.75
7.73
7.70
7.62
7.10
7.08
7.05
6.91
6.89
6.83
6.59
6.56
6.55
6.54
6.52
6.50
3.11
3.10
3.10
3.09
2.81
2.80
2.80
2.79
1.95
1.94
1.93
1.93
1.91
1.91
1.90
1.35
f1 (ppm)

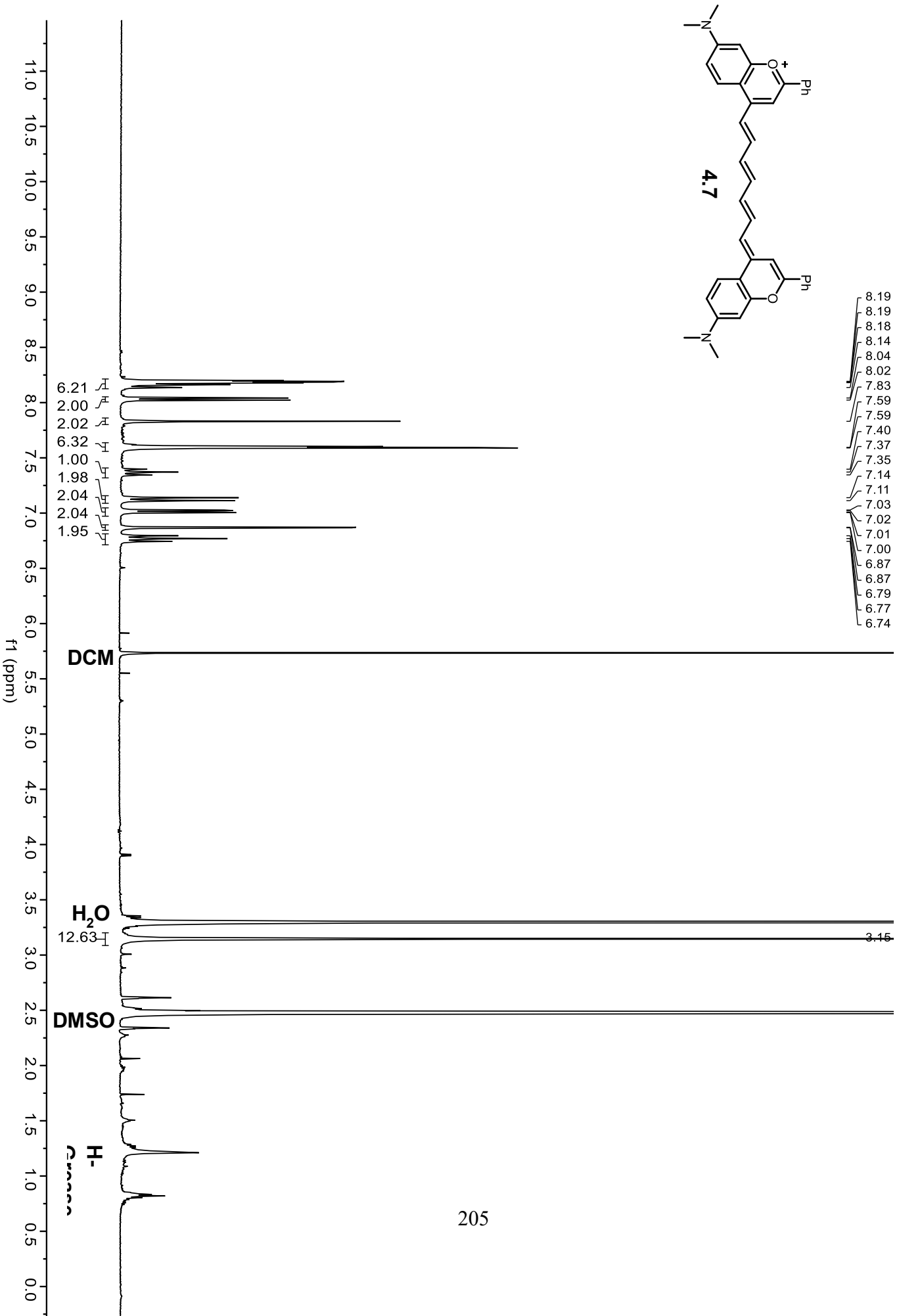
4.7
Ph
Ph
8.19
8.19
8.18
8.14
8.04
8.02
7.83
7.59
7.59
7.40
7.37
7.35
7.14
7.11
7.03
7.02
7.01
7.00
6.87
6.87
6.79
6.77
6.74
6.21
2.00
2.02
6.32
1.00
1.98
2.04
2.04
1.95
DCM
H2O
12.63
3.15
DMSO
f1 (ppm)

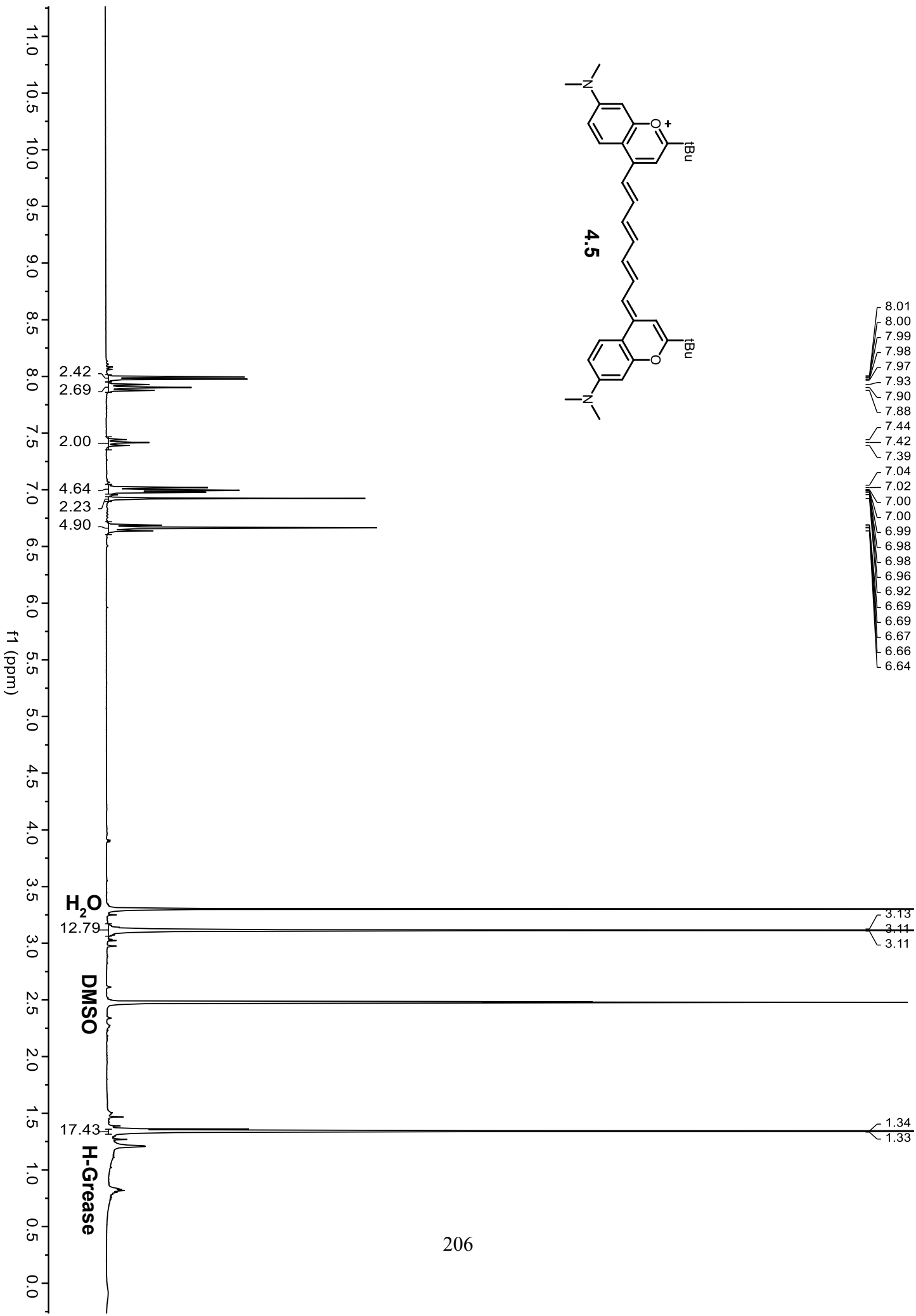
4.5
tBu
tBu
8.01
8.00
7.99
7.98
7.97
7.93
7.90
7.88
7.44
7.42
7.39
7.04
7.02
7.00
7.00
6.99
6.98
6.98
6.96
6.92
6.69
6.69
6.67
6.66
6.64
2.42
2.69
2.00
4.64
2.23
4.90
H2O
12.79
3.13
3.11
3.11
DMSO
17.43
1.34
1.33
H-Grease
f1 (ppm)

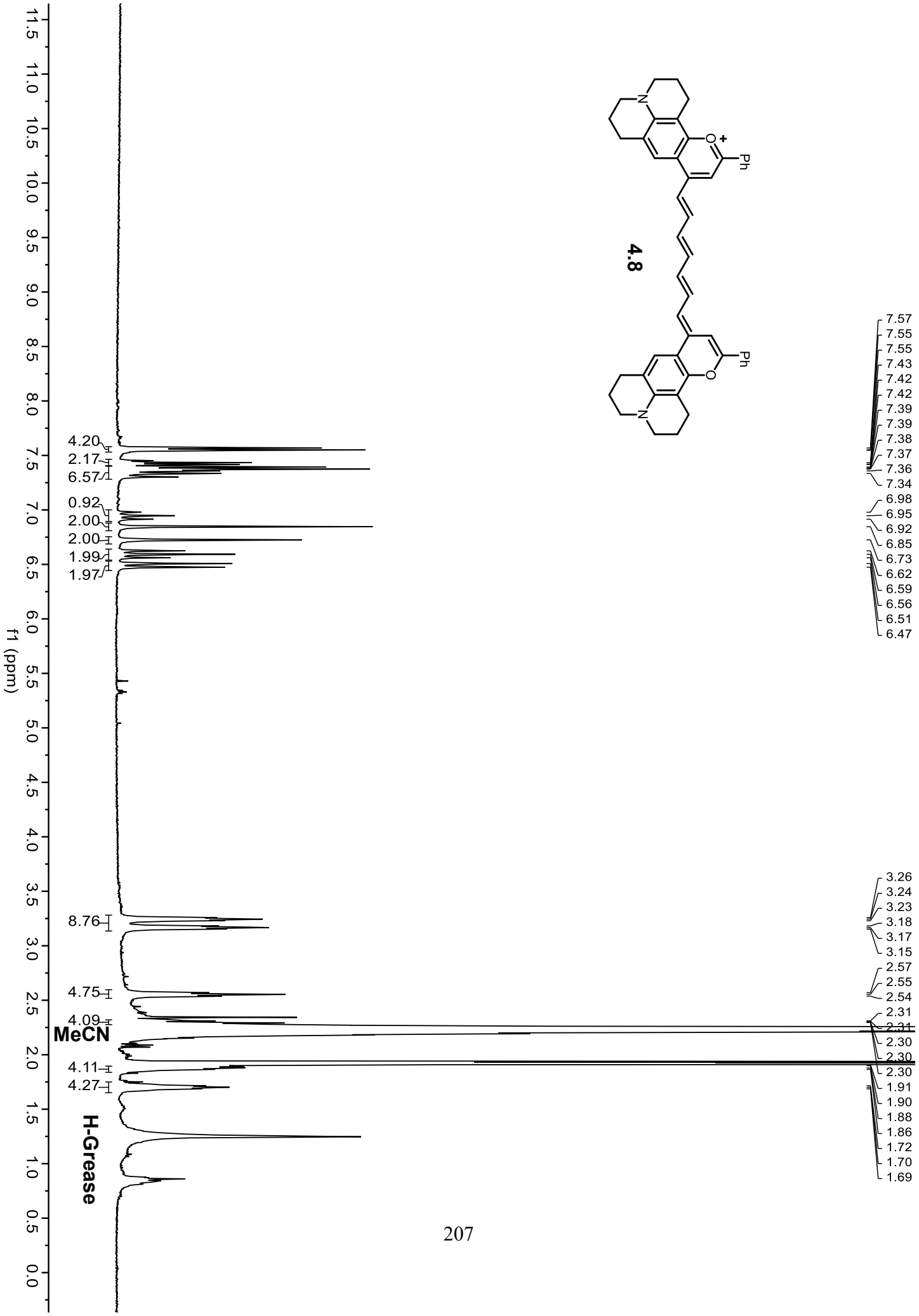
4.8
Ph
Ph
7.57
7.55
7.55
7.43
7.42
7.42
7.39
7.39
7.38
7.37
7.36
7.34
6.98
6.95
6.92
6.85
6.73
6.62
6.59
6.56
6.51
6.47
4.20
2.17
6.57
0.92
2.00
2.00
1.99
1.97
8.76
4.75
4.09
MeCN
4.11
4.27
H-Grease
3.26
3.24
3.23
3.18
3.17
3.15
2.57
2.55
2.54
2.31
2.31
2.30
2.30
2.30
1.91
1.90
1.88
1.86
1.72
1.70
1.69
f1 (ppm)

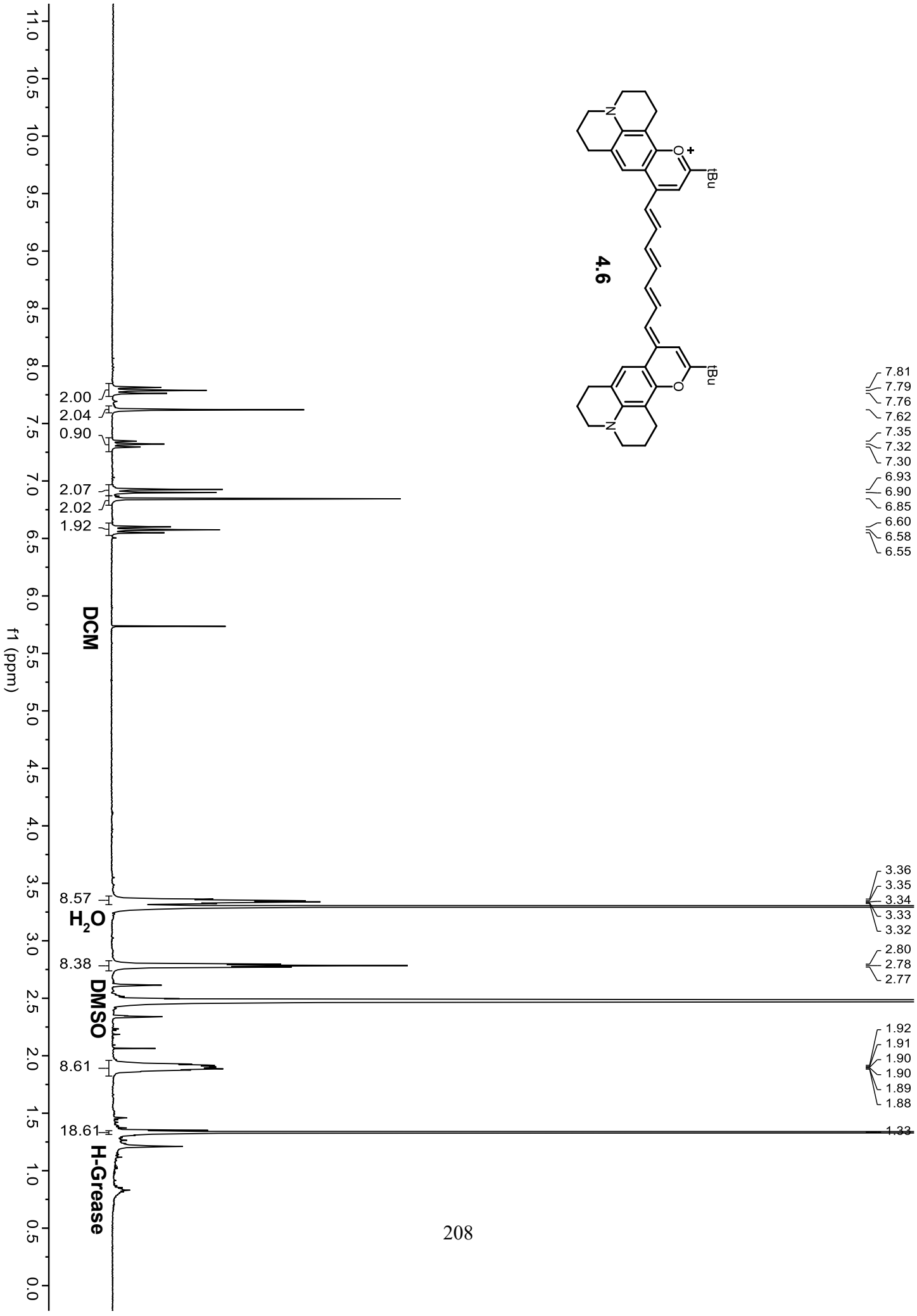
4.6
tBu
tBu
f1 (ppm)
11.0
10.5
10.0
9.5
9.0
8.5
8.0
7.5
7.0
6.5
6.0
5.5
5.0
4.5
4.0
3.5
3.0
2.5
2.0
1.5
1.0
0.5
0.0
2.00
2.04
0.90
2.07
2.02
1.92
8.57
8.38
8.61
18.61
DCM
H2O
DMSO
H-Grease
7.81
7.79
7.76
7.62
7.35
7.32
7.30
6.93
6.90
6.85
6.60
6.58
6.55
3.36
3.35
3.34
3.33
3.32
2.80
2.78
2.77
1.92
1.91
1.90
1.90
1.89
1.88
1.33

4.6.2 ^{19}F NMR Spectra

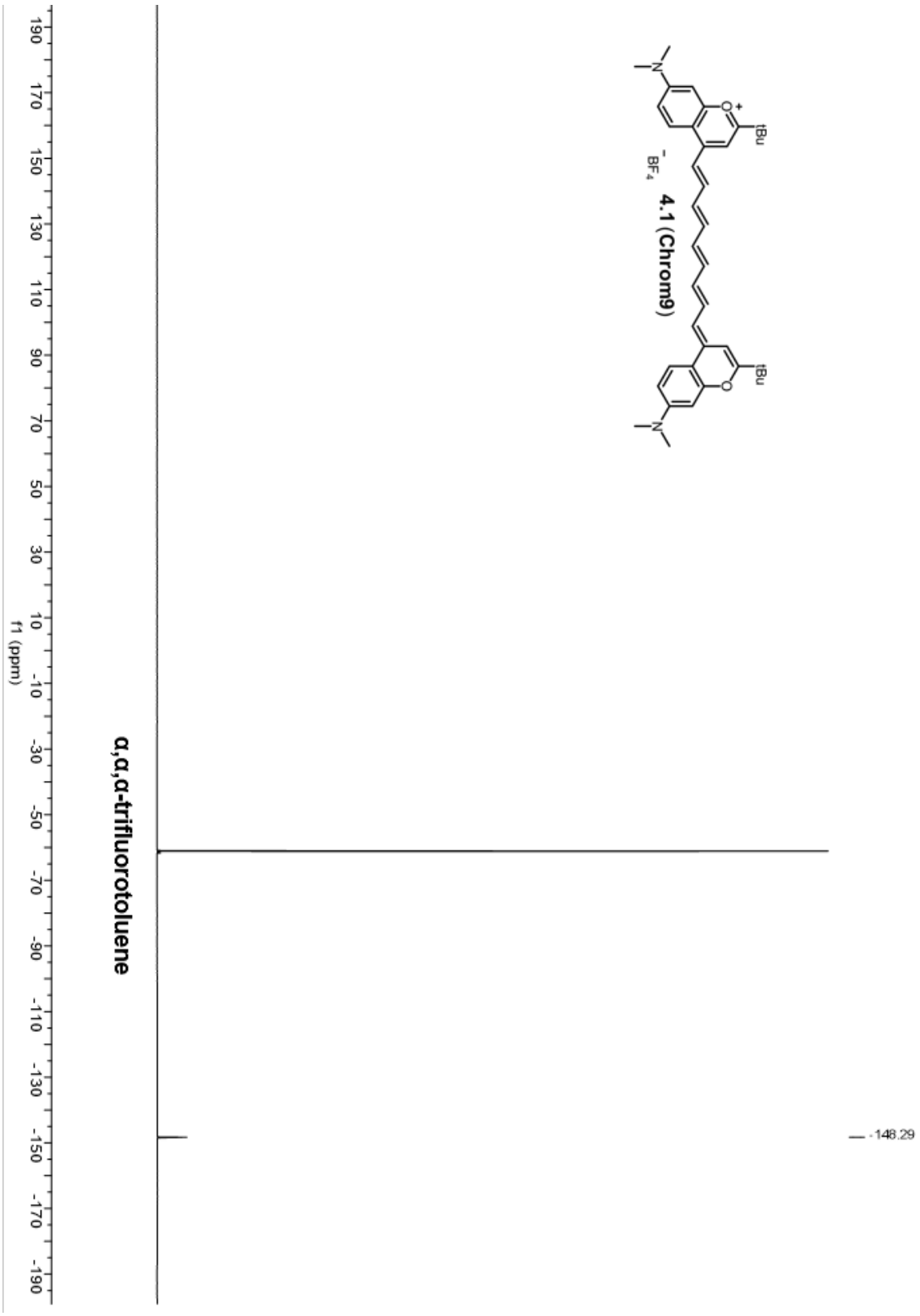

4.2 (JuloChrom9)

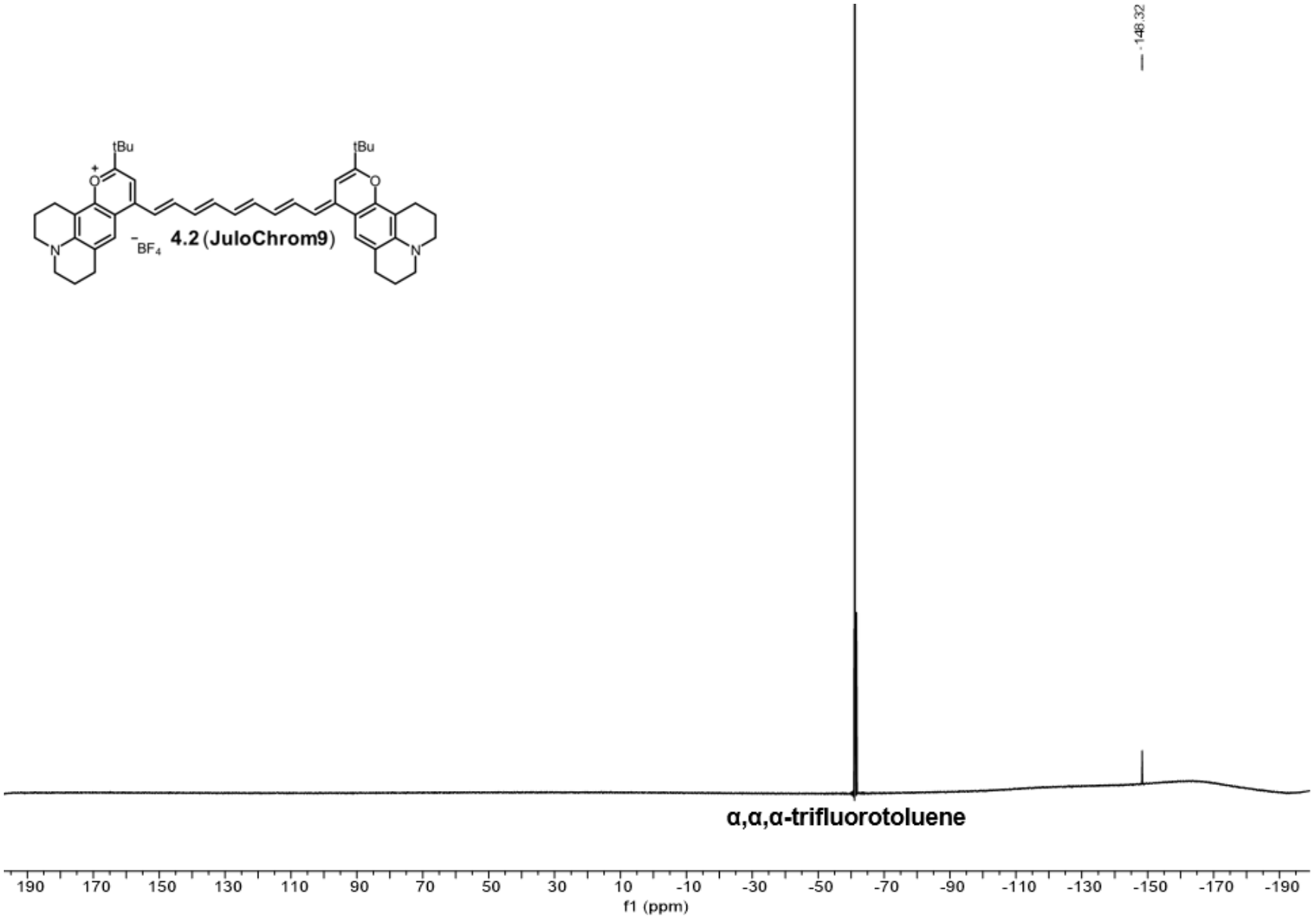

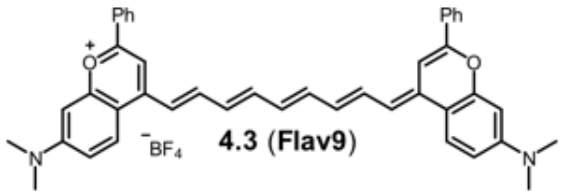

4.3 (Flav9)

-148.32

α,α,α-trifluorotoluene

190 170 150 130 110 90 70 50 30 10 -10 -30 -50 -70 -90 -110 -130 -150 -170 -190

f1 (ppm)

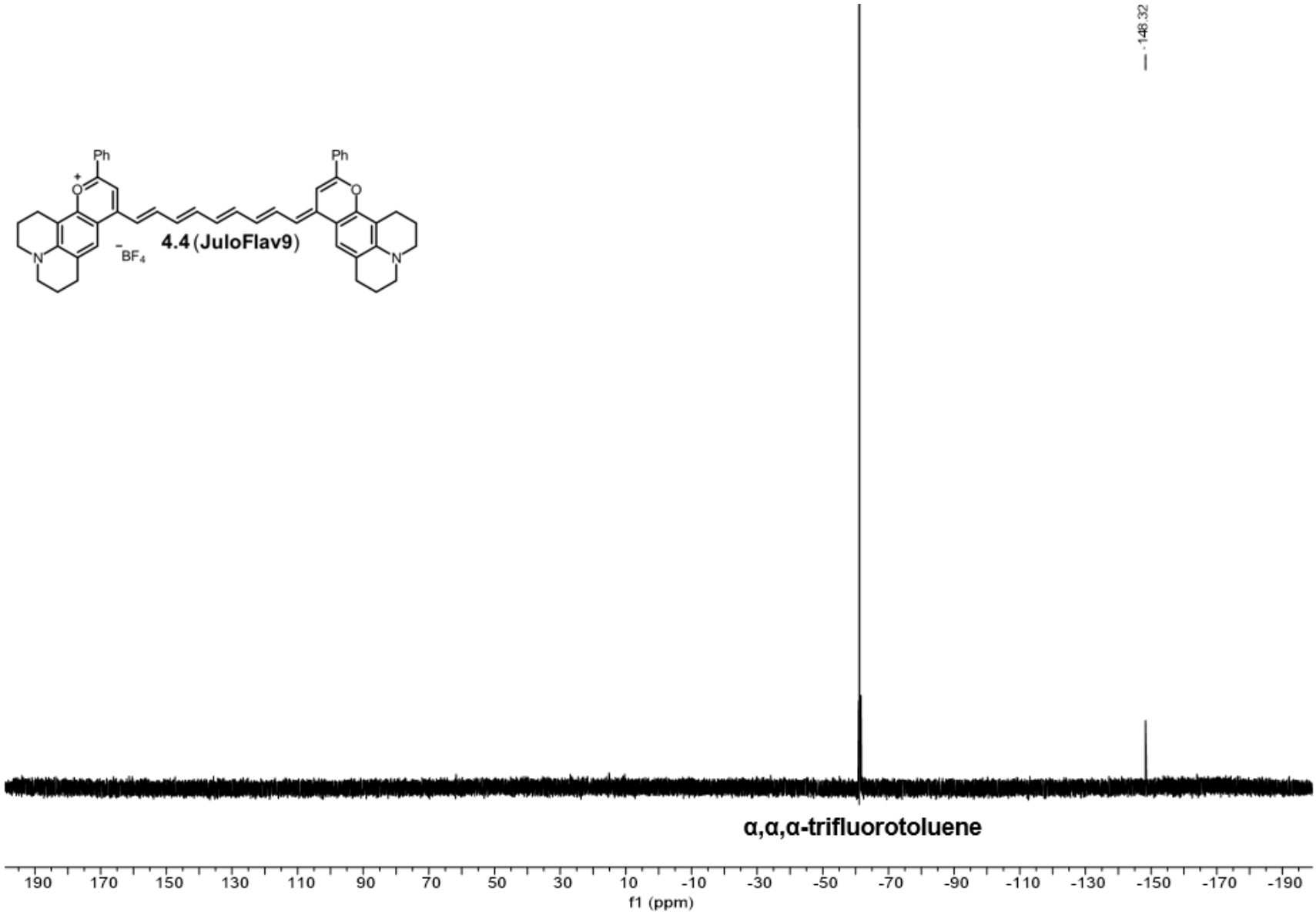
Ph
Ph
O
O
N
N
BF4
4.4 (JuloFlav9)
-148.32
α,α,α-trifluorotoluene
190 170 150 130 110 90 70 50 30 10 -10 -30 -50 -70 -90 -110 -130 -150 -170 -190
f1 (ppm)

4.7 References:

(1) Thimsen, E.; Sadtler, B.; Berezin, M. Y. Shortwave-Infrared (SWIR) Emitters for Biological Imaging: A Review of Challenges and Opportunities. *Nanophotonics*. Walter de Gruyter GmbH August 28, 2017, pp 1043–1054. https://doi.org/10.1515/nanoph-2017-0039.

(2) Li, C.; Chen, G.; Zhang, Y.; Wu, F.; Wang, Q. Advanced Fluorescence Imaging Technology in the Near-Infrared-II Window for Biomedical Applications. *J. Am. Chem. Soc.* **2020**, *142* (35), 14789–14804. https://doi.org/10.1021/jacs.0c07022.

(3) Lei, Z.; Zhang, F. Molecular Engineering of NIR-II Fluorophores for Improved Biomedical Detection. *Angewandte Chemie - International Edition*. John Wiley & Sons, Ltd July 19, 2021, pp 16294–16308. https://doi.org/10.1002/anie.202007040.

(4) Ou, Y.-F.; Ren, T.-B.; Yuan, L.; Zhang, X.-B. Molecular Design of NIR-II Polymethine Fluorophores for Bioimaging and Biosensing. *Chem. Biomed. Imaging* **2023**, *1* (3), 220–233. https://doi.org/10.1021/cbmi.3c00040.

(5) Hong, G.; Diao, S.; Antaris, A. L.; Dai, H. Carbon Nanomaterials for Biological Imaging and Nanomedicinal Therapy. *Chem. Rev.* **2015**, *115* (19), 10816–10906. https://doi.org/10.1021/acs.chemrev.5b00008.

(6) Tu, L.; Xu, Y.; Ouyang, Q.; Li, X.; Sun, Y. Recent Advances on Small-Molecule Fluorophores with Emission beyond 1000 Nm for Better Molecular Imaging in Vivo. *Chinese Chem. Lett.* **2019**, *30* (10), 1731–1737. https://doi.org/10.1016/j.cclet.2019.05.022.

(7) Carr, J. A.; Franke, D.; Caram, J. R.; Perkinson, C. F.; Saif, M.; Askoxylakis, V.; Datta, M.; Fukumura, D.; Jain, R. K.; Bawendi, M. G.; Bruns, O. T. Shortwave Infrared Fluorescence Imaging with the Clinically Approved Near-Infrared Dye Indocyanine Green. *Proc. Natl. Acad. Sci. U. S. A.* **2018**, *115* (17), 4465–4470. https://doi.org/10.1073/pnas.1718917115.

(8) Chang, B.; Chen, J.; Bao, J.; Dong, K.; Chen, S.; Cheng, Z. Design Strategies and Applications of Smart Optical Probes in the Second Near-Infrared Window. *Adv. Drug Deliv. Rev.* **2023**, *192*, 114637. https://doi.org/10.1016/j.addr.2022.114637.

(9) Chen, Z. H.; Wang, X.; Yang, M.; Ming, J.; Yun, B.; Zhang, L.; Wang, X.; Yu, P.; Xu, J.;

Zhang, H.; Zhang, F. An Extended NIR-II Superior Imaging Window from 1500 to 1900 Nm for High-Resolution In Vivo Multiplexed Imaging Based on Lanthanide Nanocrystals. *Angew. Chemie - Int. Ed.* **2023**, *62* (49), e202311883. https://doi.org/10.1002/anie.202311883.

(10) Hu, Z.; Fang, C.; Li, B.; Zhang, Z.; Cao, C.; Cai, M.; Su, S.; Sun, X.; Shi, X.; Li, C.; Zhou, T.; Zhang, Y.; Chi, C.; He, P.; Xia, X.; Chen, Y.; Gambhir, S. S.; Cheng, Z.; Tian, J. First-in-Human Liver-Tumour Surgery Guided by Multispectral Fluorescence Imaging in the Visible and near-Infrared-I/II Windows. *Nat. Biomed. Eng.* **2020**, *4* (3), 259–271. https://doi.org/10.1038/s41551-019-0494-0.

(11) Wong, K. C. Y.; Sletten, E. M. Extending Optical Chemical Tools and Technologies to Mice by Shifting to the Shortwave Infrared Region. *Current Opinion in Chemical Biology*. Elsevier Current Trends June 1, 2022, p 102131. https://doi.org/10.1016/j.cbpa.2022.102131.

(12) Zhao, X.; Zhang, F.; Lei, Z. The Pursuit of Polymethine Fluorophores with NIR-II Emission and High Brightness for in Vivo Applications. *Chem. Sci.* **2022**, *13* (38), 11280–11293. https://doi.org/10.1039/d2sc03136a.

(13) Julia L. Bricks; Alexei D.Kachkovskii; Yurii L.Slominskii; Andrii O.Gerasov; Sergei V.Popov; Bricks, J. L.; Kachkovskii, A. D.; Slominskii, Y. L.; Gerasov, A. O.; Popov, S. V. Molecular Design of near Infrared Polymethine Dyes: A Review. *Dye. Pigment.* **2015**, *121*, 238–255. https://doi.org/10.1016/J.DYEPIG.2015.05.016.

(14) Marcia Levitus; Suman Ranjit. Cyanine Dyes in Biophysical Research: The Photophysics of Polymethinefluorescent Dyes in Biomolecular Environments. *Rev. Biophys.* **2011** *44*, 123–151. https://doi.org/10.1017/S0033583510000247.

(15) Cosco, E. D.; Lim, I.; Sletten, E. M. Photophysical Properties of Indocyanine Green in the Shortwave Infrared Region. *ChemPhotoChem* **2021**, *5* (8), 727–734. https://doi.org/10.1002/cptc.202100045.

(16) Gamage, R. S.; Smith, B. D. Fluorescence Imaging Using Deep-Red Indocyanine Blue, a Complementary Partner for Near-Infrared Indocyanine Green. *Chem. Biomed. Imaging* **2024**, *2* (5), 384–397. https://doi.org/10.1021/CBMI.4C00008.

(17) Mostovnikov, V. A.; Rubinov, A. N.; Al'perovich, M. A.; Avdeeva, V. I.; Levkoev, I. I.;

Loiko, M. M. Dependence of the Luminescence and Generation Properties of Solutions of Polymethine Dyes on Their Structure. *J. Appl. Spectrosc.* **1974**, *20* (1), 31–35. https://doi.org/10.1007/BF00617286.

(18) Tolbert, L. M.; Zhao, X. Beyond the Cyanine Limit: Peierls Distortion and Symmetry Collapse in a Polymethine Dye. *J. Am. Chem. Soc.* **1997**, *119* (14), 3253–3258. https://doi.org/10.1021/ja9626953.

(19) Bandi, V. G.; Luciano, M. P.; Saccomano, M.; Patel, N. L.; Bischof, T. S.; Lingg, J. G. P.; Tsrunchev, P. T.; Nix, M. N.; Ruehle, B.; Sanders, C.; Riffle, L.; Robinson, C. M.; Difilippantonio, S.; Kalen, J. D.; Resch-Genger, U.; Ivanic, J.; Bruns, O. T.; Schnermann, M. J. Targeted Multicolor in Vivo Imaging over 1,000 Nm Enabled by Nonamethine Cyanines. *Nat. Methods* **2022**, *19* (3), 353–358. https://doi.org/10.1038/s41592-022-01394-6.

(20) Swamy, M. M. M.; Murai, Y.; Monde, K.; Tsuboi, S.; Jin, T. Shortwave-Infrared Fluorescent Molecular Imaging Probes Based on π-Conjugation Extended Indocyanine Green. *Bioconjug. Chem.* **2021**, *32* (8), 1541–1547. https://doi.org/10.1021/acs.bioconjchem.1c00253.

(21) Webster, S.; Padilha, L. A.; Hu, H.; Przhonska, O. V.; Hagan, D. J.; Van Stryland, E. W.; Bondar, M. V.; Davydenko, I. G.; Slominsky, Y. L.; Kachkovski, A. D. Structure and Linear Spectroscopic Properties of near IR Polymethine Dyes. *J. Lumin.* **2008**, *128* (12), 1927–1936. https://doi.org/10.1016/j.jlumin.2008.06.002.

(22) Li, B.; Lu, L.; Zhao, M.; Lei, Z.; Zhang, F. An Efficient 1064 Nm NIR-II Excitation Fluorescent Molecular Dye for Deep-Tissue High-Resolution Dynamic Bioimaging. *Angew. Chemie - Int. Ed.* **2018**, *57* (25), 7483–7487. https://doi.org/10.1002/anie.201801226.

(23) Pengshung, M.; Neal, P.; Atallah, T. L.; Kwon, J.; Caram, J. R.; Lopez, S. A.; Sletten, E. M. Silicon Incorporation in Polymethine Dyes. *Chem. Commun.* **2020**, *56*, 6110–6113. https://doi.org/DOI: 10.1039/c9cc09671j.

(24) Li, B.; Zhao, M.; Zhang, F. Rational Design of Near-Infrared-II Organic Molecular Dyes for Bioimaging and Biosensing. *ACS Mater. Lett.* **2020**, *2* (8), 905–917. https://doi.org/10.1021/acsmaterialslett.0c00157.

(25) Lei, Z.; Sun, C.; Pei, P.; Wang, S.; Li, D.; Zhang, X.; Zhang, F. Stable, Wavelength-Tunable Fluorescent Dyes in the NIR-II Region for In Vivo High-Contrast Bioimaging and Multiplexed Biosensing. *Angew. Chemie Int. Ed.* **2019**, *58*, 8166–9171. https://doi.org/https://doi.org/10.1002/anie.201904182.

(26) East, A. K.; Lee, M. C.; Smaga, L. P.; Jiang, C.; Mallojjala, S. C.; Hirschi, J. S.; Chan, J. Synthesis of Silicon-Substituted Hemicyanines for Multimodal SWIR Imaging. *Org. Lett.* **2022**, *24* (46), 8509–8513. https://doi.org/10.1021/ACS.ORGLETT.2C03382.

(27) Cosco, E. D.; Caram, J. R.; Bruns, O. T.; Franke, D.; Day, R. A.; Farr, E. P.; Bawendi, M. G.; Sletten, E. M. Flavylium Polymethine Fluorophores for Near- and Shortwave Infrared Imaging. *Angew. Chemie - Int. Ed.* **2017**, *56* (42), 13126–13129. https://doi.org/10.1002/anie.201706974.

(28) Cosco, E. D.; Spearman, A. L.; Ramakrishnan, S.; Lingg, J. G. P.; Saccomano, M.; Pengshung, M.; Arús, B. A.; Wong, K. C. Y.; Glasl, S.; Ntziachristos, V.; Warmer, M.; McLaughlin, R. R.; Bruns, O. T.; Sletten, E. M. Shortwave Infrared Polymethine Fluorophores Matched to Excitation Lasers Enable Non-Invasive, Multicolour in Vivo Imaging in Real Time. *Nat. Chem.* **2020**, *12* (12), 1123–1130. https://doi.org/10.1038/s41557-020-00554-5.

(29) Cosco, E. D.; Arús, B. A.; Spearman, A. L.; Atallah, T. L.; Lim, I.; Leland, O. S.; Caram, J. R.; Bischof, T. S.; Bruns, O. T.; Sletten, E. M. Bright Chromenylium Polymethine Dyes Enable Fast, Four-Color in Vivo Imaging with Shortwave Infrared Detection. *J. Am. Chem. Soc.* **2021**, *143* (18), 6836–6846. https://doi.org/10.1021/jacs.0c11599.

(30) Pengshung, M.; Li, J.; Mukadum, F.; Lopez, S. A.; Sletten, E. M. Photophysical Tuning of Shortwave Infrared Flavylium Heptamethine Dyes via Substituent Placement. *Org. Lett.* **2020**, *22* (15), 6150–6154. https://doi.org/10.1021/acs.orglett.0c02213.

(31) Pengshung, M.; Cosco, E. D.; Zhang, Z.; Sletten, E. M. Counterion Pairing Effects on a Flavylium Heptamethine Dye†. *Photochem. Photobiol.* **2022**, *98* (2), 303–310. https://doi.org/10.1111/php.13531.

(32) Jia, S.; Lin, E. Y.; Mobley, E. B.; Lim, I.; Guo, L.; Kallepu, S.; Low, P. S.; Sletten, E. M. Water-Soluble Chromenylium Dyes for Shortwave Infrared Imaging in Mice. *Chem* **2023**, *9* (12), 3648–3665. https://doi.org/10.1016/j.chempr.2023.08.021.

(33) Matikonda, S. S.; Helmerich, D. A.; Meub, M.; Beliu, G.; Kollmannsberger, P.; Greer, A.; Sauer, M.; Schnermann, M. J. Defining the Basis of Cyanine Phototruncation Enables a New Approach to Single-Molecule Localization Microscopy. *ACS Cent. Sci.* **2021**, *7* (7), 1144–1155. https://doi.org/10.1021/acscentsci.1c00483.

(34) Okoročenkova, J.; Filgas, J.; Khan, N. M.; Slavíček, P.; Klán, P. Thermal Truncation of Heptamethine Cyanine Dyes. *J. Am. Chem. Soc.* **2024**. *146*, 19768-19781. https://doi.org/10.1021/JACS.4C02116.

(35) Vahdani, A.; Moemeni, M.; Holmes, D.; Lunt, R. R.; Jackson, J. E.; Borhan, B. Mechanistic Insight into the Thermal "Blueing" of Cyanine Dyes. *J. Am. Chem. Soc.* **2024**. *146*, 19756-19767. https://doi.org/10.1021/JACS.4C02171.

(36) Friedman, H. C.; Cosco, E. D.; Atallah, T. L.; Jia, S.; Sletten, E. M.; Caram, J. R. Establishing Design Principles for Emissive Organic SWIR Chromophores from Energy Gap Laws. *Chem* **2021**, *7* (12), 3359–3376. https://doi.org/10.1016/j.chempr.2021.09.001.

(37) Roy, S.; Bag, N.; Bardhan, S.; Hasan, I.; Guo, B. Recent Progress in NIR-II Fluorescence Imaging-Guided Drug Delivery for Cancer Theranostics. *Adv. Drug Deliv. Rev.* **2023**, *197*, 114821. https://doi.org/10.1016/j.addr.2023.114821.

(38) Pascal, S.; Haefele, A.; Monnereau, C.; Charaf-Eddin, A.; Jacquemin, D.; Le Guennic, B.; Andraud, C.; Maury, O. Expanding the Polymethine Paradigm: Evidence for the Contribution of a Bis-Dipolar Electronic Structure. *J. Phys. Chem. A* **2014**, *118* (23), 4038–4047. https://doi.org/10.1021/jp501358q.

(39) Janeková, H.; Friedman, H. C.; Russo, M.; Zyberaj, M.; Ahmed, T.; Hua, A. S.; Sica, A. V.; Caram, J. R.; Štacko, P. Deuteration of Heptamethine Cyanine Dyes Enhances Their Emission Efficacy. *Chem. Commun.* **2024**, *60* (8), 1000–1003. https://doi.org/10.1039/D3CC05153F.

CHAPTER FIVE

Designer Fusion Flavylium Polymethine Dyes for Understanding Flavylium Dye Structure-Property Relationships

Adapted from: Anthony L. Spearman, Daniel W. Turner, Luigi Alde, Ellen M. Sletten* Designer Fusion Flavylium Polymethine Dyes for Understanding Flavylium Dye Structure-Property Relationships. *Manuscript in preparation*.

5.1 Abstract

Flavylium polymethine dyes are an attractive scaffold for developing near-infrared (NIR) and shortwave infrared (SWIR) contrast agents for optical imaging. Previous work in our group has looked at the photophysical impact of different sites on the flavylium heterocycle. In this work, we explore multiple modifications at both the 7 and 2-positions with a new series of flavylium polymethine dyes. Additionally, we developed pentamethine flavylium congeners. We began to understand the additive limitations of flavylium modifications and λ_{max}. Certain derivatives gave rise to new strategies for enhancing Φ_F for flavylium polymethine dyes.

5.2 Introduction

In recent years, many bright polymethine dyes have been developed for near-infrared (NIR) and shortwave infrared (SWIR) imaging.[1–6] This class of contrast agent is known for having useful imaging properties such as narrow Stokes shifts (~25 nm) and high molar absorption coefficients ($\varepsilon > 10^5$ $M^{-1}cm^{-1}$).[7–11] For a polymethine dye, both the length of the polymethine linker and heterocycle identity play an important role in determining their photophysical properties. In the past, our lab developed a panel of flavylium (Flav) polymethine dyes including a pentamethine

dye **5.1** (Flav5; $\lambda_{max,abs}$ = 862 nm) and **5.4** (Flav7**;** $\lambda_{max,abs}$ = 1027 nm) (Figure 5.1A).[12] All dyes gratifyingly displayed aforementioned properties (narrow Stokes shift, high ε) and had respectable fluorescence quantum yields (Φ_F) within their spectral regions.[13] These two parameters are integral for determining the molecular brightness (m.b.) of a dye, which is calculated as the product of Φ_F and ε_{max}.

Interested in developing flavylium dye structure-property relationships, we investigated the impact of modifying the 7-position of the heterocycle. We found that substituents with increased electron donating character at the 7-position resulted in a greater bathochromic shift.[14] The greatest effect was observed through julolidine (Julo) incorporation in **5.10** (JuloFlav7; $\lambda_{max,abs}$ = 1061 nm) giving a red-shift of ~34 nm. A similar red-shift was observed with the pentamethine analogue **5.7** (JuloFlav5; $\lambda_{max,abs}$ = 897 nm).[13] Additionally, the julolidine modification only slightly reduced Φ_F by about 1% for the pentamethine dyes and 0.1% for the heptamethine dyes, providing a reliable strategy for red-shifting without drastically reducing brightness.

The Zhang group has synthesized and characterized several flavylium and thiaflavylium (where oxygen is replaced with sulfur) pentamethine dyes, with different substituents at the 6 and 7 position.[15,16] Their works reaffirmed that 7-position amine substitution leads to a bathochromic shift. Further, this effect was intensified upon amine substitution at the 6-position of the heterocycle, albeit at the cost of decreasing Φ_F by one order of magnitude. Similar work performed by our group also identified the red-shifting effect of 6-position substitution.[17] Interestingly, a majority of the bright pentamethine dyes synthesized by the Zhang group were furnished with a *p*-methoxy phenyl group at the 2-position, though the role of the methoxy wasn't completely discussed.

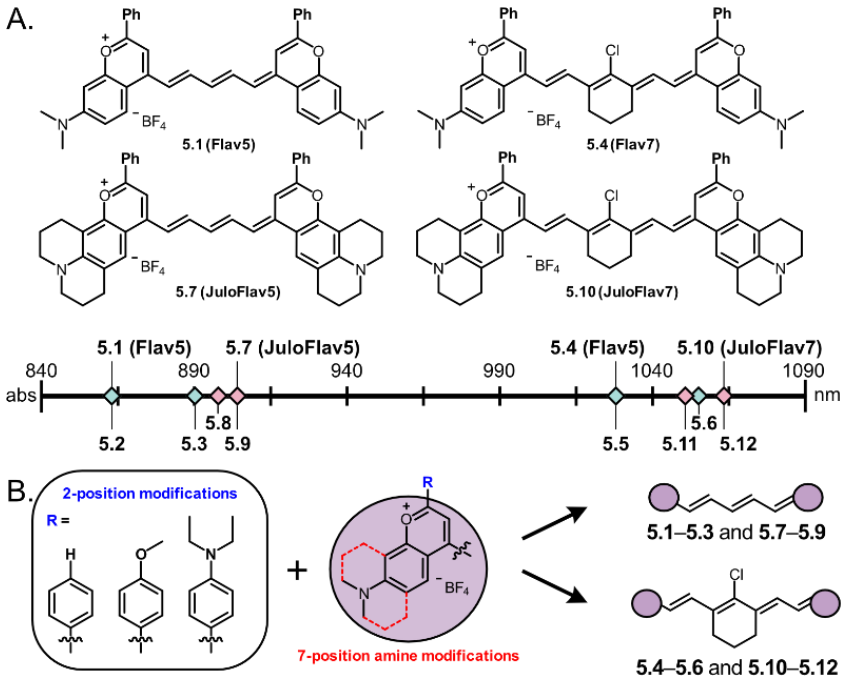

Figure 5.1. **A**. Previously explored flavylium polymethine scaffolds plotted by their absorbance maxima. **B**. Modifications leveraged in this work to understand the additive properties of 2-position and 7-position substitution.

Herein, we combine flavylium modifications at both the 2-position and the 7-position towards a series of pentamethine and heptamethine flavylium derivatives (Figure 5.1B). Four previously reported control dyes **5.1** (Flav5), **5.4** (Flav7), **5.7** (JuloFlav5), and **5.10** (JuloFlav7) serve as references for the derivatives in this work. Analogues of these reference dyes bear either a methoxy (OMe) or diethylamino (NEt_2) group at the para position of the 2-position phenyl ring. We first found that with the Flav5 and Flav7 derivatives, adding a methoxy group provided a boost to Φ_F, while diethylamino substitution led to a ~30 nm red-shift. However, the diethylamino analogues that also had a 7-position julolidine (JuloFlav dyes) only gave a red-shift of about 2 nm. Ultimately this led us to believe that regarding λ_{max}, there were additive limitations. However, more promising results were seen with brightness as the *p*-substituted JuloFlav derivatives generally had higher Φ_F's. Despite raising more questions about the additive nature of these

modifications, this work provided some initial insight towards designing flavylium polymethine dyes with enhanced Φ_F's.

5.3 Results and Discussion

5.3.1 Synthesis of Fusion Dyes

To access target Flav5 and Flav7 derivatives, standard modular routes for polymethine dye synthesis were utilized.[13] First, key heterocycles (**5.15**, **5.16**, **5.21**, and **5.22**) were prepared by treating their respective flavone precursors (**5.13**, **5.14**, **5.19**, and **5.20**) with methylmagnesium bromide and subsequently quenching with tetrafluoroboric acid. Two equivalents of each key intermediate were then condensed onto linker **5.17** or **5.18** under basic conditions, to reach the target polymethine dyes. Using linker **5.17** gave pentamethine dyes (**5.2**, **5.3**, **5.8**, and **5.9**), while linker **5.18** gave heptamethine dyes (**5.5**, **5.6**, **5.11**, and **5.12**). Despite excellent conversion, lower yields in the final dye step are attributed to difficulties in purification. With a complete panel of Flav5 and Flav7 congeners, we characterized the photophysical properties of the new phenyl-substituted derivatives against control dyes (**5.1**, **5.4**, **5.7**, and **5.10**).

Scheme 5.1. Synthetic Scheme for Flavylium Pentamethine and Heptamethine Derivatives.

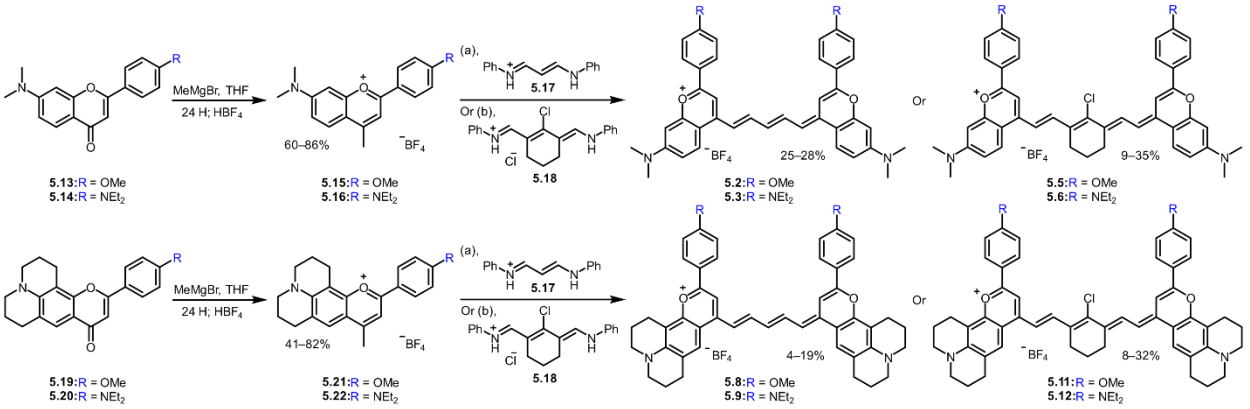

Note: (a) NaOAc, acetic anhydride, 100 °C, 20 min. (b) NaOAc, *n*-butanol/toluene, 110 °C, 20 min. See SI for synthetic procedures.

5.3.2 Photophysical Properties of Fusion Dyes

After synthesizing pentamethine dyes **5.2**, **5.3**, **5.5**, and **5.6**, as well as heptamethine dyes **5.8**, **5.9**, **5.11** and **5.12**, they were photophysically characterized in dichloromethane (Table 5.1; Figure 5.2). First, we looked at how these modifications modulated $\lambda_{max,abs}$. For the Flav5 derivatives, relative to control **5.1** ($\lambda_{max,abs}$ = 862 nm), *p*-methoxy incorporation gave no appreciable red-shift (**5.2**, $\lambda_{max,abs}$ = 862 nm). However, *p*-diethylamino substitution, led to a 28 nm red-shift (**5.3**, $\lambda_{max,abs}$ = 890 nm). These effects were also seen in the Flav7 derivatives, where relative to **5.4** ($\lambda_{max,abs}$ = 1027 nm), **5.5** had no red-shift in absorbance, while **5.6** had a 32 nm redshift ($\lambda_{max,abs}$ = 1059 nm).

As previously discussed, julolidine substitution at the 7-position reliably provided a red-shift of around ~34 nm without drastically reducing Φ_F. In pursuit of more red-shifted flavylium dyes, we sought to combine the *p*-phenyl modification with **JuloFlav5** ($\lambda_{max,abs}$ = 897 nm) and **JuloFlav7** ($\lambda_{max,abs}$ = 1061 nm) dyes. To our surprise, the pentamethine and heptamethine *p*-methoxy dyes were blue-shifted (**5.8**: $\lambda_{max,abs}$ = 889 nm and **5.11**: 1052 nm respectively). While the *p*-diethylamino JuloFlav dyes were unfortunately only red-shifted by ~2 nm (**5.9**: $\lambda_{max,abs}$ = 898 nm and **5.12**: $\lambda_{max,abs}$ = 1063 nm). These data suggest that the red-shifting nature of these modifications is not additive. We then calculated the molar absorptivity of these dyes. Generally, all dyes had characteristic ε_{max} ~10^5 $M^{-1}cm^{-1}$, though dyes with *p*-diethylamino functionality saw a 2-fold decrease. Regardless, we then measured the Φ_F of these derivatives.

Table 5.1. Photophysical properties of Fusion Flav5 and Flav7 derivatives taken in dichloromethane (DCM).

Dye	$\lambda_{max.abs}$ (nm)	$\lambda_{max.em}$ (nm)	ε_{max} ($M^{-1}cm^{-1}$)	Φ_F (%)	Brightness ($M^{-1}cm^{-1}$)	ξ
Flav5 (5.1)	862	883	330,000 ± 7,000	6.1 ± 0.1	20,000 ± 500	0
4''OMeFlav5 (5.2)	862	890	240,000 ± 100	21 ± 2	51,000 ± 5,000	2.7
4''NEt_2Flav5 (5.3)	890	916	150,000 ± 2,100	7.6 ± 0.7	11,000 ± 2,000	1.5
Flav7 (5.4)	1027	1053	240,000 ± 1,000	0.61 ± 0.02	1,500 ± 50	0
4''OMeFlav7 (5.5)	1027	1047	220,000 ± 9,000	0.74 ± 0.07	1,600 ± 170	0.15
4''NEt_2Flav7 (5.6)	1059	1081	210,000 ± 1,000	0.43 ± 0.01	920 ± 20	0.15
JuloFlav5 (5.7)	897	925	250,000 ± 5,000	5.3 ± 0.2	13,000 ± 600	0
4''OMeJuloFlav5 (5.8)	889	916	120,000 ± 150	7.3 ± 0.6	8,500 ± 700	0.15
4''NEt_2JuloFlav5 (5.9)	898	920	130,000 ± 2,000	9.8 ± 1.4	13,000 ± 3,000	0.78
JuloFlav7 (5.10)	1061	1088	240,000 ± 7,000	0.46 ± 0.01	1,100 ± 40	0
4''OMeJulo7 (5.11)	1052	1077	210,000 ± 3,000	0.53 ± 0.04	1,100 ± 1,000	0.15
4''NEt_2Julo7 (5.12)	1063	1087	220,000 ± 60	0.47 ± 0.04	1,000 ± 90	0.78

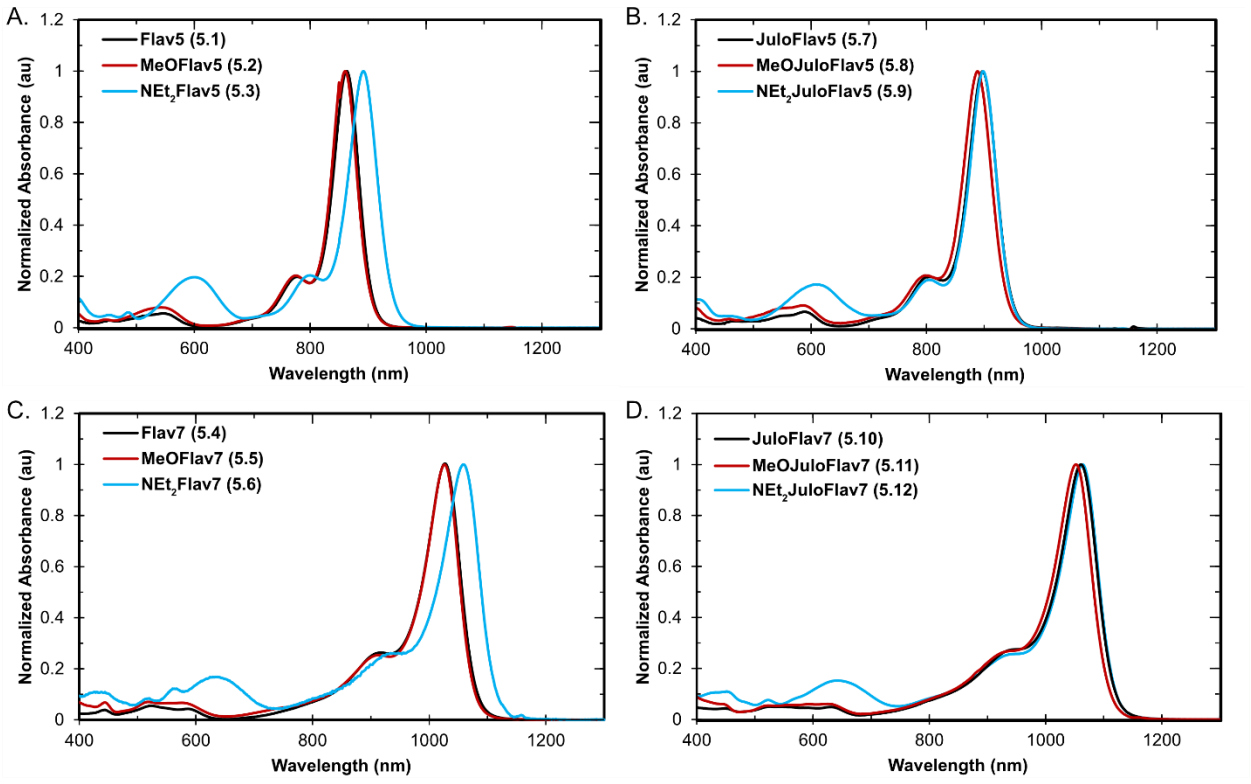

Figure 5.2. Absorbance spectra for pentamethine and heptamethine dyes **5.1**–**5.12**, taken in dichloromethane.

Absolute Φ_F's of the pentamethine dyes (Figure 5.3A) were calculated using an integrating sphere, and relative Φ_F's of the heptamethine dyes (Figure 5.3B) were done using **IR-26** as a

standard (Φ_F = 0.05% in DCM).[18,19] Within the Flav5 panel (**5.1**: Φ_F = 6.1%), **5.2** saw a dramatic increase in Φ_F (21%) while **5.3** slightly increased (Φ_F = 7.6%). Amongst the Flav7 derivatives, (compared to **5.4**: Φ_F = 0.61%), **5.5** had a slight increase in Φ_F (0.74%), while **5.6** slightly decreased (Φ_F = 0.43%). It is likely that the lower Φ_F from *p*-diethylamino derivatives **5.3** and **5.6** (relative to the p-methoxy dyes: **5.2** and **5.5**) were due to the energy-gap law effects, as only these *p*-phenyl substituted Flav dyes experienced a bathochromic shift.[3,20]

p-phenyl substitution had different effects for both **JuloFlav5** (Φ_F = 5.3%) and **JuloFlav7** (Φ_F = 0.46%) dyes. *p*-methoxy JuloFlav dyes had increased Φ_F's (**5.8**: 7.3% and **5.11**: 0.53% respectively). Next, the *p*-diethylamino JuloFlav dyes also had increased Φ_F's (**5.9**: 9.8% and **5.12**: 0.47%). To our delight, these findings outline a new strategy to increase Φ_F, by adding *p*-phenyl substituents to the Julo flavylium scaffold.

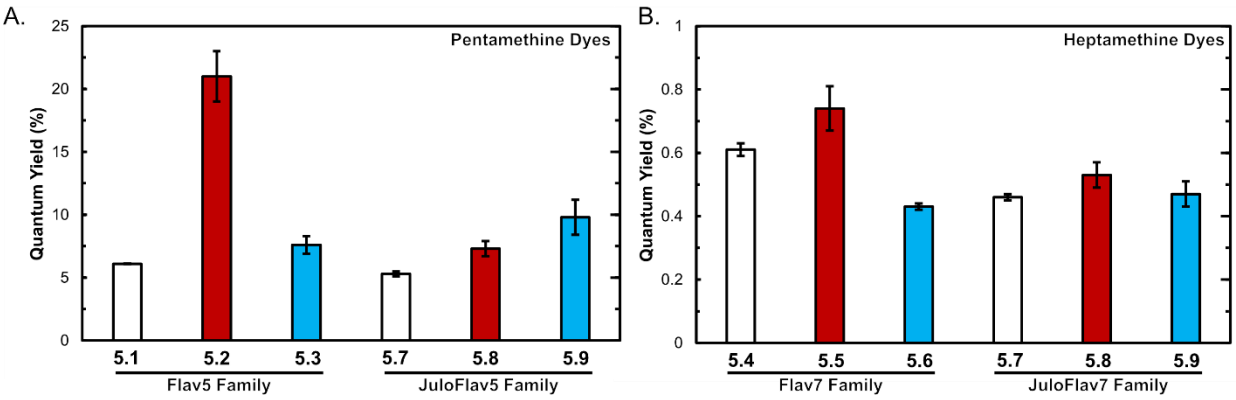

Figure 5.3. Quantum yields for flavylium dyes **5.1**–**5.12**. Calculated using either the (**a**) absolute quantum yield method (pentamethine dyes) or (**b**) relative quantum yield method (heptamethine dyes; against IR-26).

To better compare the brightness of these derivatives, we must correct for band-gap effects. Caram and coworkers developed an energy-gap improvement factor, ξ, in order to better compare quantum yields between two dyes at different band-gaps.[20] This parameter represents the improvement or worsening of the target dye Φ_F compared to a reference dye. A positive ξ is

interpreted as an improvement in Φ_F. In practice, this can demonstrate how specific structural differences can improve or worsen brightness between two dyes. Within each set (**Flav5**, **Flav7**, **JuloFlav5**, and **JuloFlav7**), ξ was calculated using the respective control dye as the reference (Figure 5.4A: pentamethine dyes; B: heptamethine dyes).

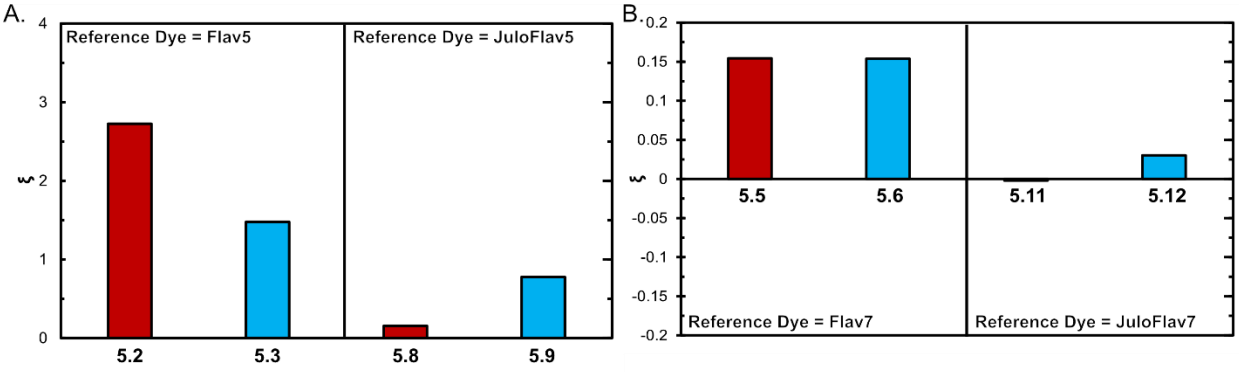

Figure 5.4. **A**. Calculated ξ values for pentamethine dyes **5.2**, **5.3** (Ref. = **Flav5**) **5.8**, and **5.9** (Ref. = **JuloFlav5**). **B**. Calculated ξ values for heptamethine dyes **5.5**, **5.6** (Ref. = **Flav7**) **5.11**, and **5.12** (Ref. = **JuloFlav7**).

After deconvoluting bandgap effects, it was observed that *p*-methoxy substitution only improved Φ_F within the Flav5 and Flav7 panels. Though the *p*-methoxy JuloFlav dyes displayed increased Φ_F's, their meager ξ values suggest that this increase is largely owed to band-gap effects. This is understandable as these dyes were blue-shifted compared to the control JuloFlav dyes. On the other hand, all *p*-diethylamino derivatives had positive ξ values, reinforcing this modification as a means to improve brightness for flavylium polymethine dyes. Lastly, it is of note that the greatest ξ values were observed within the Flav5 derivatives.

5.4 Conclusions

Flavylium polymethine dyes are an excellent non-toxic scaffold for NIR and SWIR optical imaging. Thus, elucidating new design principles for these dyes will lead to derivatives with improved photophysical properties. In this work, we combined previous flavylium modifications at both the 2- and 7-positions. Despite these modifications not leading to additive trends, this

investigation provided a new approach to red-shifting Flav scaffolds via *p*-diethylamino substitution. Additionally, this work revealed new strategies for reliably improving the Φ_F of JuloFlav scaffolds. In future work it would be interesting to see the effects of combining 2-position modifications with 6-position Flav5 and Flav7 derivatives and perhaps other sites along the heterocycle. Additionally, looking towards *in vivo* imaging applications, the photophysical performance of these derivatives within nanoparticle formulations should be assessed to see if *p*-phenyl substitution discourages aggregation (and thereby aggregate-caused quenching) within formulations.

5.5 Experimental Procedures

5.5.1 Abbreviations, Materials, and Instrumentation

Abbreviations. DCM = dichloromethane; DMSO =dimethylsulfoxide; EtOH = ethanol; EtOAc = ethyl acetate; MeOH = methanol; TFA = trifluoroacetic acid; DMF = dimethylformamide; THF = tetrahydrofuran; MeCN = acetonitrile; Ac_2O = acetic anhydride; PBS = phosphate buffered saline; HBF_4 = fluoroboric acid; $NaClO_4$ = sodium perchlorate; MeMgBr = methyl magnesium bromide; $POCl_3$ = phosphoryl chloride; *t*Bu = *tert*-butyl; Ph = phenyl; NaOAc = sodium acetate; OMe = methoxy; NEt_2 = diethylamino; m.b. = molecular brightness; rt = room temperature; h = hour; min = minutes; NMR = nuclear magnetic resonance; HRMS = high resolution mass spectrometry; DLS = dynamic light scattering; NIR = near-infrared; SWIR = shortwave infrared;

Materials. Reagents were purchased from Acros Organics, Alfa Aesar, Fisher Scientific, Sigma-Aldrich, or TCI and used without additional purification. Anhydrous and deoxygenated solvents (toluene, THF, DMF) were dispensed from a Grubb's-type Phoenix Solvent Drying System constructed by the late JC Meyer. Oxygen was removed from solvents by three consecutive freeze–

pump–thaw cycles in air-free glassware directly before use. For every reaction, dry Schlenk technique was used.

Instrumentation. Thin layer chromatography was performed using Silica Gel 60 F254 (EMD Millipore) plates. Flash chromatography was executed with technical grade silica gel with 60 Å pores and 40–63 μm mesh particle size (Sorbtech Technologies). Solvent was removed with a Büchi Rotovapor and further dried with a Welch DuoSeal pump. Masses for analytical measurements were taken on a Sartorius MSE6.6S-000-DM S13 Cubis Micro Balance. Bath sonication was performed using a Branson 3800 ultrasonic cleaner. Nuclear magnetic resonance (^{1}H NMR and ^{13}C NMR) spectra were taken on Bruker AV-400, or AV-500 instruments and processed with MestReNova or TopSpin software. All ^{1}H NMR and ^{13}C NMR peaks are reported in ppm in reference to their respective solvent signals (CD_3CN δH=1.94; MeOD δH=3.31, δC=49.00; CD_2Cl_2 δH=5.32, δC=53.84; $(CD_3)_2SO$ δH=2.50).

5.5.2 Synthetic Procedures

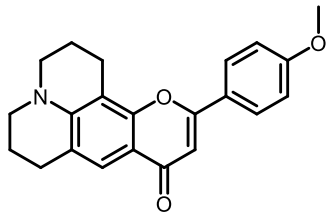

11-(4-methoxyphenyl)-2,3,6,7-tetrahydro-1*H*,5*H*,9*H*-pyrano[2,3-*f*]pyrido[3,2,1-ij]quinolin-9-one (**5.19**): Ethyl 3-(4-methoxyphenyl)-3-oxopropanoate (750 mg, 3.4 mmol, 2 equiv.), and 2,3,6,7-tetrahydro-1*H*,5*H*-pyrido[3,2,1-*ij*]quinolin-8-ol (320 mg, 1.7 mmol, 1.0 equiv.) were placed in a microwave tube and heated in a microwave at 300 W, at 240 °C for 3 minutes. The solution was cooled to rt and evaporated onto silica gel. The crude product was purified via column

chromatography, eluting with a 20:1 hexanes/EtOAc gradient to yield a yellow solid (360 mg, 1.0 mmol, 60% yield). R_f = 0.3 in 1:1 hexanes/EtOAc. ^{1}H NMR (500 MHz, Chloroform-*d*) δ 7.87 (d, *J* = 8.9 Hz, 2H), 7.62 (s, 1H), 7.00 (d, *J* = 9.0 Hz, 3H), 3.88 (s, 3H), 3.33 (d, *J* = 5.8 Hz, 4H), 3.00 (s, 2H), 2.83 (s, 2H), 2.06 (s, 2H), 2.01 – 1.95 (m, 2H). HRMS (ESI$^+$) calcd for $C_{22}H_{22}NO_3$ $[M+H]^+$: 348.1600; found 348.1670. Absorbance (CH_2Cl_2): 374 nm.

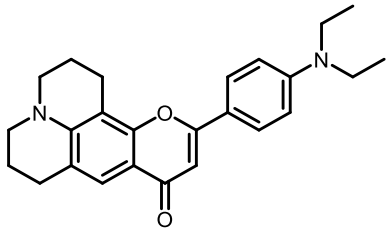

11-(4-(diethylamino)phenyl)-9-methyl-2,3,6,7-tetrahydro-1*H*,5*H*-pyrano[2,3-*f*]pyrido[3,2,1-*ij*]quinolin-12-ium (**5.20**): Ethyl 3-(4-(diethylamino)phenyl)-3-oxopropanoate (1.8 g, 6.8 mmol, 2 equiv.), and 2,3,6,7-tetrahydro-1*H*,5*H*-pyrido[3,2,1-*ij*]quinolin-8-ol (650 mg, 3.4 mmol, 1.0 equiv.) were placed in a microwave tube and heated in a microwave at 300 W, at 240 °C for 3 minutes. The solution was cooled to rt and evaporated onto silica gel. The crude product was purified via column chromatography, eluting with a 20:1 hexanes/EtOAc gradient to yield a yellow solid (480 mg, 3.4 mmol, 36% yield). R_f = 0.1 in 1:1 hexanes/EtOAc. ^{1}H NMR (500 MHz, Chloroform-*d*) δ 7.76 (d, *J* = 9.0 Hz, 2H), 7.61 (s, 1H), 6.76 (s, 2H), 6.66 (s, 1H), 3.42 (q, *J* = 7.1 Hz, 4H), 3.28 (d, *J* = 5.8 Hz, 4H), 2.99 (s, 2H), 2.81 (s, 2H), 2.04 (d, *J* = 3.1 Hz, 2H), 1.97 (d, *J* = 1.5 Hz, 2H), 1.21 (t, *J* = 7.1 Hz, 6H). HRMS (ESI$^+$) calcd for $C_{25}H_{29}N_2O_2^+$ $[M+H]^+$: 389.2229; found 389.2295. Absorbance (CH_2Cl_2): 392 nm.

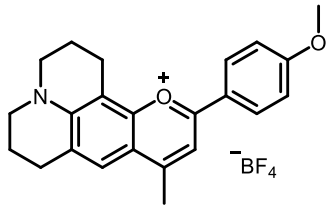

11-(4-methoxyphenyl)-9-methyl-2,3,6,7-tetrahydro-1*H*,5*H*-pyrano[2,3-*f*]pyrido[3,2,1-*ij*]quinolin-12-ium tetrafluoroborate (**5.21**): Flavone **5.19** (330 mg, 960 μmol, 1.0 equiv.) was dissolved in THF (6.2 mL) in a double-neck round bottom flask and cooled to 0 °C. Methylmagnesium bromide was added dropwise (2.9 mL, 1.0 M in THF, 3 equiv.) and the solution was warmed to rt and stirred for 24 h. The reaction was quenched by dropwise addition of 5% HBF_4 on ice, extracted with dichloromethane, dried with Na_2SO_4, filtered, and evaporated. The crude product was triturated with ethyl acetate and vacuum filtered to produce a purple solid (170 mg, 390 μmol, 41% yield). R_f = 0.5 in 9:1 DCM/EtOH. ^{1}H NMR (500 MHz, Acetonitrile-d_3) δ 8.08 (d, *J* = 9.0 Hz, 2H), 7.61 (s, 1H), 7.51 (s, 1H), 7.13 (d, *J* = 9.0 Hz, 2H), 3.91 (s, 3H), 3.53 (s, 4H), 3.02 (d, *J* = 6.5 Hz, 2H), 2.92 – 2.87 (m, 2H), 2.69 (s, 3H), 2.08 – 1.96 (m, 4H). ^{13}C NMR (126 MHz, Acetonitrile-d_3) δ 165.26, 164.35, 160.73, 154.26, 153.30, 130.41, 129.20, 124.72, 123.24, 118.01, 116.20, 110.75, 105.78, 56.68, 51.71, 51.23, 28.42, 21.02, 20.41, 19.98, 19.76. HRMS (ESI$^+$) calcd for $C_{23}H_{24}NO_2^+$ [M]$^+$: 346.1802; found 346.1874. Absorbance (CH_2Cl_2): 537 nm.

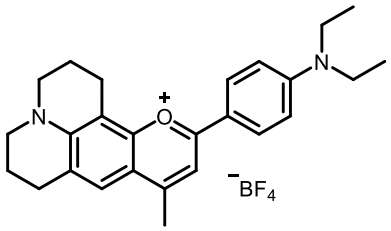

11-(4-(diethylamino)phenyl)-9-methyl-2,3,6,7-tetrahydro-1*H*,5*H*-pyrano[2,3-*f*]pyrido[3,2,1-*ij*]quinolin-12-ium tetrafluoroborate (**5.22**): Flavone **5.20** (480 mg, 1.2 mmol, 1.0 equiv.) was

dissolved in THF (9.3 mL) in a double-neck round bottom flask and cooled to 0 °C. Methylmagnesium bromide was added dropwise (3.7 mL, 1.0 M in THF, 3 equiv.) and the solution was warmed to rt and stirred for 24 h. The reaction was quenched by dropwise addition of 5% HBF_4 on ice, extracted with dichloromethane, dried with Na_2SO_4, filtered, and evaporated. The crude product was triturated with ethyl acetate and vacuum filtered to produce a purple solid (490 mg, 1.1 mmol, 84% yield). R_f = 0.6 in 9:1 DCM/EtOH. ^{1}H NMR (500 MHz, Acetonitrile-d_3) δ 7.90 (d, *J* = 9.3 Hz, 2H), 7.43 (s, 1H), 7.31 (s, 1H), 6.82 (d, *J* = 9.3 Hz, 2H), 3.50 (s, 4H), 3.46 – 3.40 (m, 4H), 2.95 (s, 2H), 2.82 (s, 2H), 2.58 (s, 3H), 2.01 (s, 4H), 1.21 (s, 6H). ^{13}C NMR (126 MHz, CD_3CN) δ 166.07, 159.30, 153.50, 153.33, 151.62, 131.06, 126.91, 124.22, 115.83, 115.80, 113.02, 109.47, 105.76, 51.28, 50.77, 45.69, 28.40, 21.21, 20.53, 20.20, 19.64, 12.85. HRMS (ESI^+) calcd for $C_{26}H_{31}N_2O^+$ $[M]^+$: 387.2431; found 387.2511. Absorbance (CH_2Cl_2): 603 nm.

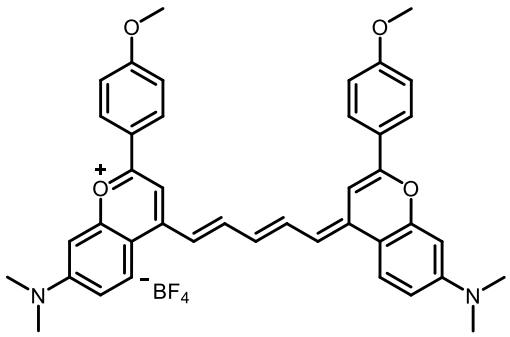

7-(dimethylamino)-4-((1*E*,3*E*)-5-((*E*)-7-(dimethylamino)-2-(4-methoxyphenyl)-4*H*-chromen-4-ylidene)penta-1,3-dien-1-yl)-2-(4-methoxyphenyl)chromenylium tetrafluoroborate (**5.2**) Flavylium **5.15** (60 mg, 160 μmol, 1.0 equiv.), linker **5.17** (17 mg, 76 μmol, 0.48 equiv.), and sodium acetate (39 mg, 420 μmol, 3.0 equiv.) were added to a flame-dried 25 mL Schlenk tube under a N_2 atmosphere. Acetic anhydride (1.4 mL) was added, and the reaction mixture was immediately freeze-pump-thawed x3 before heating to 100 ºC for 20 min. The reaction was cooled and concentrated *in vacuo*. The product was dry loaded onto silica gel and

purified by column chromatography in DCM plus a gradient of 0.5–5% EtOH, resulting in a purple product (22 mg, 27 μmol, 19%). R_f = 0.4 in 9:1 DCM/EtOH. ^{1}H NMR (500 MHz, DMSO-d_6) δ 8.22 (t, J = 12.9 Hz, 2H), 8.14 – 8.08 (m, 4H), 8.04 (d, J = 9.5 Hz, 2H), 7.64 (s, 2H), 7.19 – 7.12 (m, 4H), 7.09 (d, J = 13.4 Hz, 2H), 6.97 (dd, J = 9.3, 2.6 Hz, 2H), 6.87 – 6.76 (m, 3H), 3.88 (s, 6H), 3.14 (s, 12H). HRMS (ESI$^+$) calcd for $C_{41}H_{39}N_2O_4^+$ [M]$^+$: 623.2904; found 623.2973. Absorbance (CH_2Cl_2): 862 nm. Emission (CH_2Cl_2, ex. 740 nm): 890 nm.

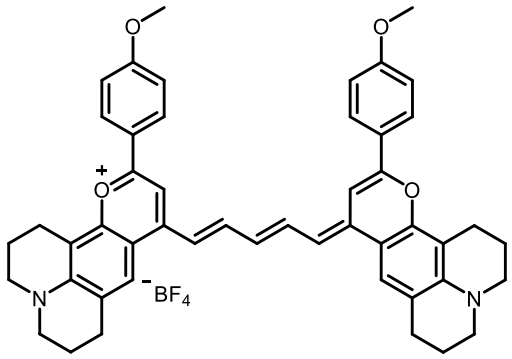

11-(4-methoxyphenyl)-9-((1*E*,3*E*,5*E*)-5-(11-(4-methoxyphenyl)-2,3,6,7-tetrahydro-1*H*,5*H*,9*H*-pyrano[2,3-*f*]pyrido[3,2,1-*ij*]quinolin-9-ylidene)penta-1,3-dien-1-yl)-2,3,6,7-tetrahydro-1H,5H-pyrano[2,3-f]pyrido[3,2,1-ij]quinolin-12-ium tetrafluoroborate (**5.8**)

Flavylium **5.21** (61 mg, 140 μmol, 1.0 equiv.), linker **5.17** (15 mg, 68 μmol, 0.48 equiv.), and sodium acetate (35 mg, 420 μmol, 3.0 equiv.) were added to a flame-dried 25 mL Schlenk tube under a N_2 atmosphere. Acetic anhydride (1.3 mL) was added, and the reaction mixture was immediately freeze-pump-thawed x3 before heating to 110 ºC for 20 min. The reaction was cooled and concentrated *in vacuo*. The product was precipitated in toluene and collected by vacuum filtration, washing with diethyl ether (1 x 20 mL) and THF (1 x 200 mL). The product was dry loaded onto silica gel and purified by column chromatography in DCM plus a gradient of 0.5–5% EtOH, resulting in a purple product (22 mg, 27 μmol, 19%). R_f = 0.5 in 9:1 DCM/EtOH. ^{1}H NMR (500 MHz, DMSO-d_6) δ 8.06 (s, 2H), 7.96 (s, 4H), 7.56 (s, 2H), 7.47 (s, 2H), 7.12 (d, J = 9.0 Hz,

4H), 6.93 (d, *J* = 13.4 Hz, 2H), 6.72 (s, 1H), 3.86 (s, 6H), 3.35 (d, *J* = 5.7 Hz, 8H), 2.85 (t, *J* = 6.5 Hz, 4H), 2.72 (t, *J* = 6.3 Hz, 4H), 1.91 (dt, *J* = 37.7, 5.9 Hz, 8H). HRMS (ESI$^+$) calcd for $C_{49}H_{47}N_2O_4^+$ [M]$^+$: 727.3530; found 727.3537. Absorbance (CH_2Cl_2): 889 nm. Emission (CH_2Cl_2, ex. 740 nm): 916 nm.

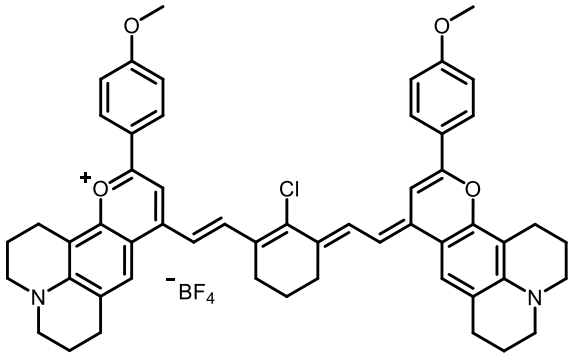

9-((*E*)-2-((*E*)-2-chloro-3-((*E*)-2-(11-(4-methoxyphenyl)-2,3,6,7-tetrahydro-1*H*,5*H*,9*H*-pyrano[2,3-*f*]pyrido[3,2,1-*ij*]quinolin-9-ylidene)ethylidene)cyclohex-1-en-1-yl)vinyl)-11-(4-methoxyphenyl)-2,3,6,7-tetrahydro-1*H*,5*H*-pyrano[2,3-*f*]pyrido[3,2,1-*ij*]quinolin-12-ium (5.11): Flavylium **5.21** (20 mg, 0.046 mmol, 1.0 equiv.), linker **5.18** (6.7 mg, 21 μmol, 0.45 equiv.), and sodium acetate (11 mg, 0.14 mmol, 3.0 equiv.) were dissolved in a mixture of *n*-butanol (290 μL) and toluene (120 μL) in a Schlenk flask and heated to 110 °C for 20 minutes. The solution was cooled to rt and evaporated onto silica gel. The product was dry loaded onto silica gel and purified by column chromatography in DCM plus a gradient of 0.5–5% EtOH, resulting in a purple product (14 mg, 15 μmol, 33%). R_f = 0.5 in 9:1 DCM/EtOH. ^{1}H NMR (500 MHz, DMSO-d_6) δ 8.08 (d, *J* = 13.7 Hz, 2H), 8.06 – 7.98 (m, 4H), 7.72 (s, 2H), 7.44 (s, 2H), 7.16 – 7.07 (m, 4H), 6.94 (d, *J* = 13.9 Hz, 2H), 3.86 (s, 6H), 3.36 (s, 7H), 2.87 (t, *J* = 6.4 Hz, 4H), 2.79 (d, *J* = 6.5 Hz, 7H), 2.01 – 1.84 (m, 12H). HRMS (ESI$^+$) Calculated for $C_{54}H_{52}ClN_2O_4^+$ [M/2]$^+$: 413.6802; found: 413.6831. Absorbance (CH_2Cl_2): 1052 nm. Emission (CH_2Cl_2, ex 885 nm): 1077 nm.

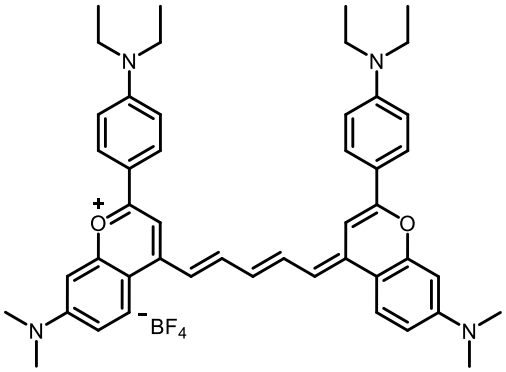

2-(4-(diethylamino)phenyl)-4-((1*E*,3*E*)-5-((*E*)-2-(4-(diethylamino)phenyl)-7-(dimethylamino)-4*H*-chromen-4-ylidene)penta-1,3-dien-1-yl)-7-(dimethylamino)chromenylium (**5.3**) Flavylium **5.16** (60 mg, 140 μmol, 1.0 equiv.), linker **5.17** (15 mg, 68 μmol, 0.48 equiv.), and sodium acetate (35 mg, 430 μmol, 3.0 equiv.) were added to a flame-dried 25 mL Schlenk tube under a N_2 atmosphere. Acetic anhydride (1.3 mL) was added, and the reaction mixture was immediately freeze-pump-thawed x3 before heating to 100 ºC for 20 min. The reaction was cooled and concentrated *in vacuo*. The product was dry loaded onto silica gel and purified by column chromatography in DCM plus a gradient of 0.5–5% EtOH, resulting in a purple product (31 mg, 39 μmol, 28%). R_f = 0.5 in 9:1 DCM/EtOH. ^{1}H NMR (500 MHz, DMSO-d_6) δ 8.16 (t, *J* = 12.9 Hz, 2H), 8.01 (d, *J* = 9.5 Hz, 2H), 7.99 – 7.95 (m, 4H), 7.51 (s, 2H), 6.98 (d, *J* = 13.4 Hz, 2H), 6.92 (dd, *J* = 9.3, 2.6 Hz, 2H), 6.84 – 6.72 (m, 7H), 3.47 (q, *J* = 7.0 Hz, 8H), 3.12 (s, 12H), 1.15 (t, *J* = 7.0 Hz, 12H). HRMS (ESI$^+$) calcd for $C_{47}H_{53}N_4O_2^+$ $[M]^+$: 705.4163; found 705.4186. Absorbance (CH_2Cl_2): 890 nm. Emission (CH_2Cl_2, ex. 740 nm): 916 nm.

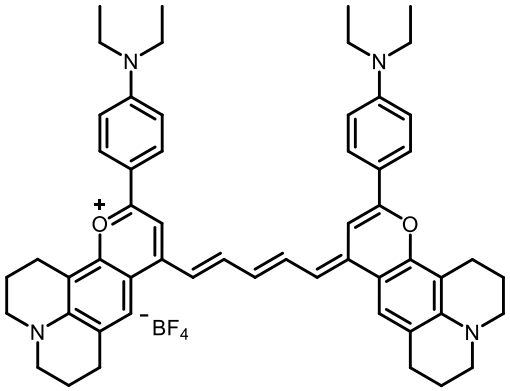

11-(4-(diethylamino)phenyl)-9-((1*E*,3*E*,5*E*)-5-(11-(4-(diethylamino)phenyl)-2,3,6,7-tetrahydro-1*H*,5*H*,9*H*-pyrano[2,3-*f*]pyrido[3,2,1-*ij*]quinolin-9-ylidene)penta-1,3-dien-1-yl)-2,3,6,7-tetrahydro-1*H*,5*H*-pyrano[2,3-*f*]pyrido[3,2,1-*ij*]quinolin-12-ium (**5.9**) Flavylium **5.22** (60 mg, 130 μmol, 1.0 equiv.), linker **5.17** (14 mg, 60 μmol, 0.48 equiv.), and sodium acetate (31 mg, 380 μmol, 3.0 equiv.) were added to a flame-dried 25 mL Schlenk tube under a N_2 atmosphere. Acetic anhydride (1.1 mL) was added, and the reaction mixture was immediately freeze-pump-thawed x3 before heating to 100 ºC for 20 min. The reaction was cooled and concentrated *in vacuo*. The product was dry loaded onto silica gel and purified by column chromatography in DCM plus a gradient of 0.5–5% EtOH, resulting in a purple product (4 mg, 5 μmol, 4%). R_f = 0.6 in 9:1 DCM/EtOH. ^{1}H NMR (500 MHz, DMSO-d_6) δ 8.03 (t, *J* = 12.9 Hz, 2H), 7.91 – 7.82 (m, 4H), 7.56 (s, 2H), 7.37 (s, 2H), 6.85 (d, *J* = 13.4 Hz, 2H), 6.82 (d, *J* = 8.8 Hz, 4H), 6.66 (t, *J* = 12.4 Hz, 1H), 3.46 (q, *J* = 7.1 Hz, 12H), 2.87 (t, *J* = 6.4 Hz, 4H), 2.74 (t, *J* = 6.3 Hz, 4H), 1.95 (p, *J* = 6.3 Hz, 4H), 1.87 (p, *J* = 7.2, 6.6 Hz, 4H), 1.15 (t, *J* = 7.0 Hz, 12H). HRMS (ESI$^+$) calcd for $C_{55}H_{61}N_4O_2^+$ [M]$^+$: 809.4789; found 809.4786. Absorbance (CH_2Cl_2): 898 nm. Emission (CH_2Cl_2, ex. 740 nm): 920 nm.

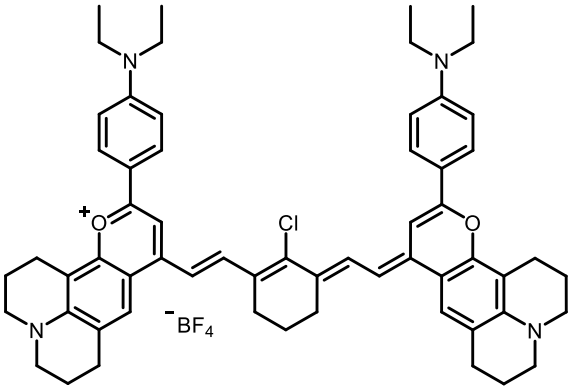

9-((*E*)-2-((*E*)-2-chloro-3-((*E*)-2-(11-(4-(diethylamino)phenyl)-2,3,6,7-tetrahydro-1*H*,5*H*,9*H*-pyrano[2,3-*f*]pyrido[3,2,1-*ij*]quinolin-9-ylidene)ethylidene)cyclohex-1-en-1-yl)vinyl)-11-(4-(diethylamino)phenyl)-2,3,6,7-tetrahydro-1*H*,5*H*-pyrano[2,3-*f*]pyrido[3,2,1-*ij*]quinolin-12-ium (5.12): Flavylium **5.22** (60 mg, 0.13 mmol, 1.0 equiv.), linker **5.18** (19 mg, 57 μmol, 0.45 equiv.), and sodium acetate (31 mg, 0.38 mmol, 3.0 equiv.) were dissolved in a mixture of *n*-butanol (800 μL) and toluene (340 μL) in a Schlenk flask and heated to 110 °C for 20 minutes. The solution was cooled to rt and evaporated onto silica gel. The product was dry loaded onto silica gel and purified by column chromatography in DCM plus a gradient of 0.5–5% EtOH, resulting in a purple product (10 mg, 10 μmol, 8%). R_f = 0.7 in 9:1 DCM/EtOH. ^{1}H NMR (500 MHz, DMSO-d_6) δ 8.01 (d, *J* = 13.7 Hz, 2H), 7.85 (d, *J* = 9.0 Hz, 4H), 7.59 (s, 2H), 7.24 (s, 2H), 6.81 (dd, *J* = 11.4, 7.1 Hz, 6H), 3.45 (q, *J* = 7.1 Hz, 9H), 3.35 – 3.32 (m, 6H), 2.81 (d, *J* = 6.7 Hz, 4H), 2.75 (d, *J* = 7.1 Hz, 8H), 1.99 – 1.80 (m, 12H), 1.14 (t, *J* = 7.1 Hz, 12H). HRMS (ESI$^+$) Calculated for $C_{60}H_{66}ClN_4O_2^+$ [M]$^+$: 909.4869; found: 909.4852. Absorbance (CH_2Cl_2): 1063 nm. Emission (CH_2Cl_2, ex 885 nm): 1087 nm.

5.6 Spectra Relevant to Chapter Five

5.6.1 ^{1}H NMR Spectra

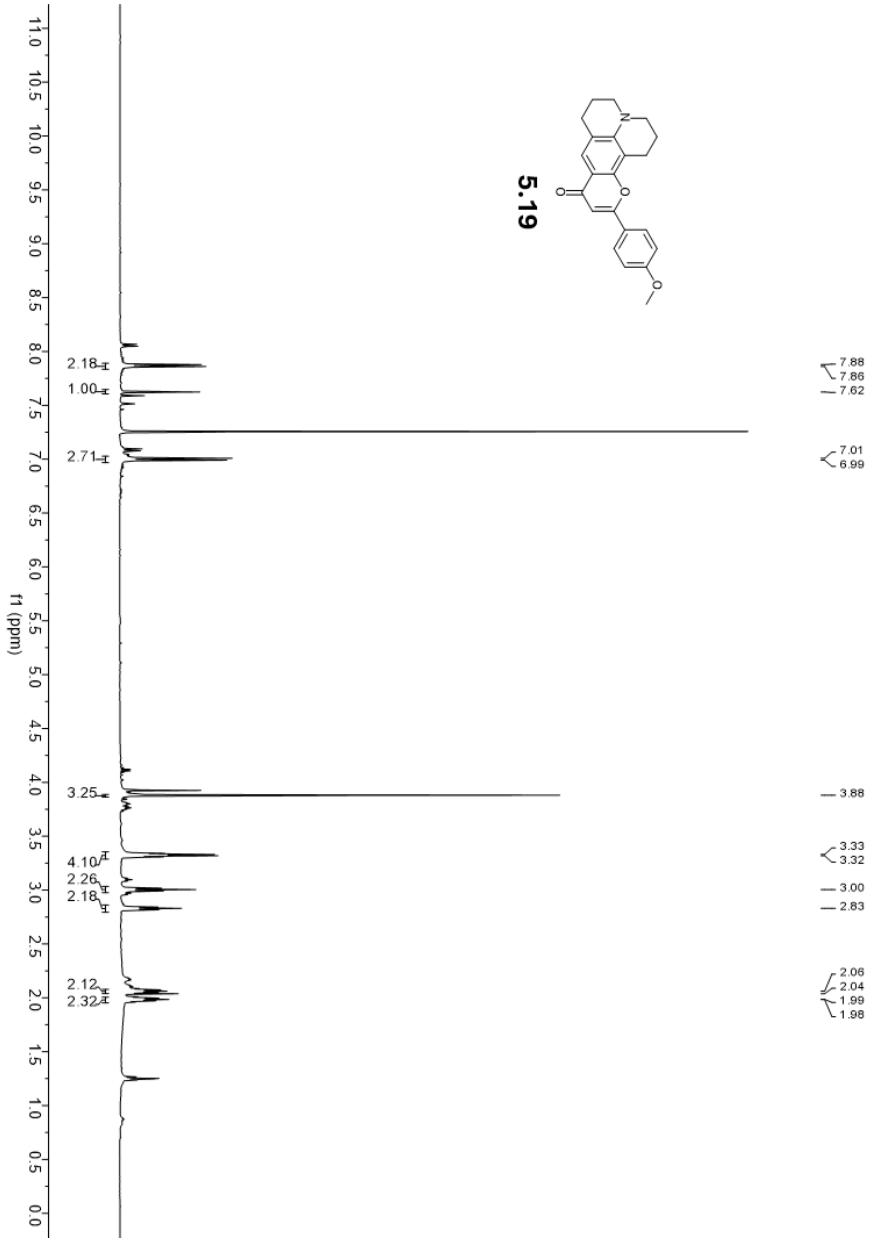

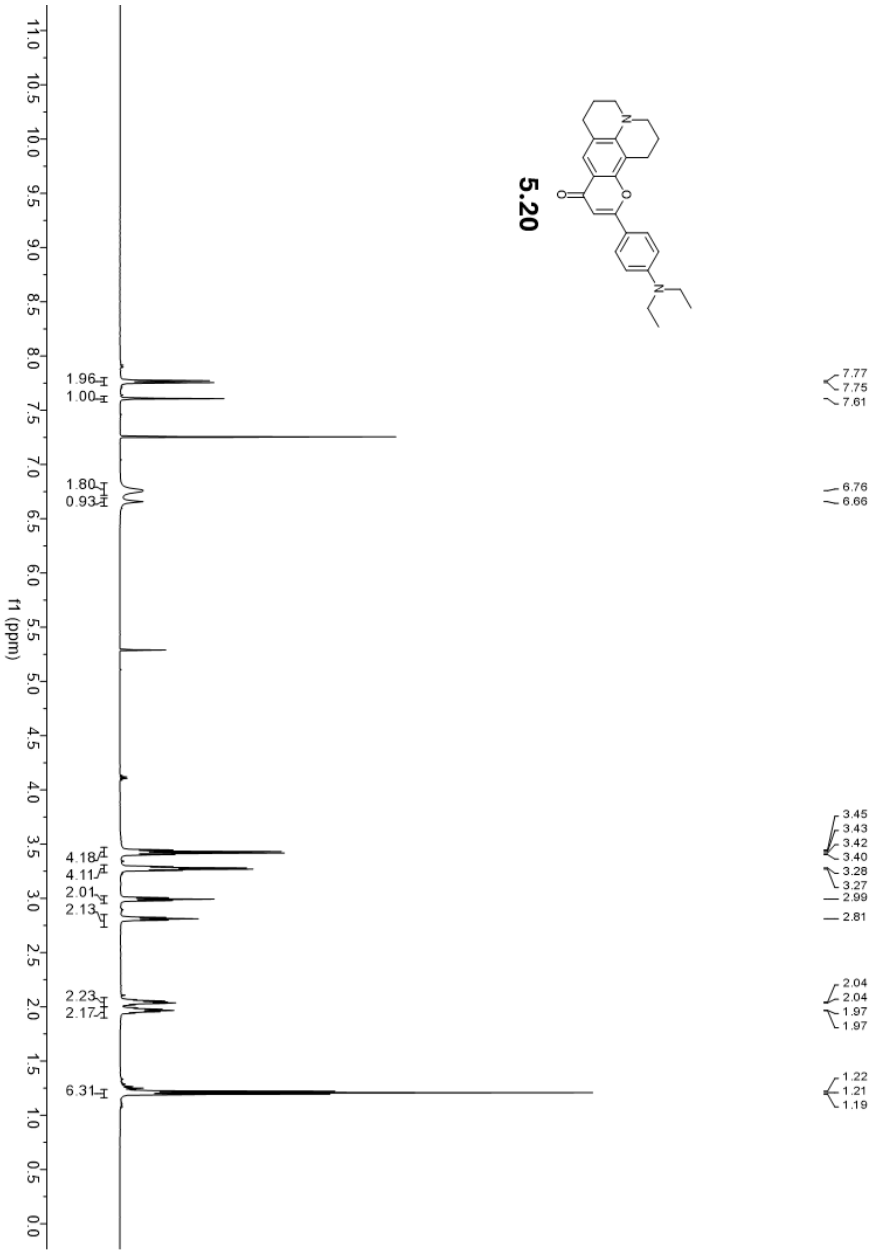
5.20
f1 (ppm)
1.96
1.00
1.80
0.93
4.18
4.11
2.01
2.13
2.23
2.17
6.31
7.77
7.75
7.61
6.76
6.66
3.45
3.43
3.42
3.40
3.28
3.27
2.99
2.81
2.04
2.04
1.97
1.97
1.22
1.21
1.19

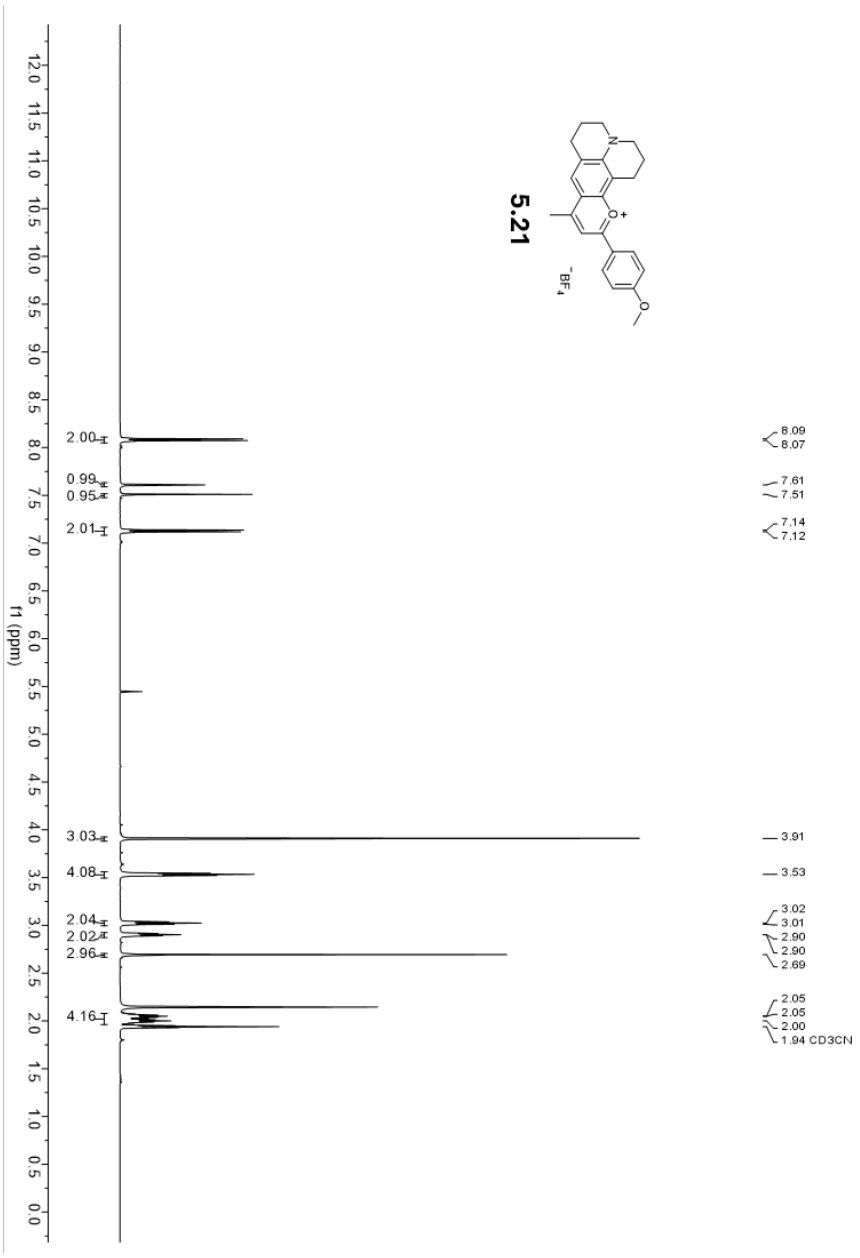
5.21
f1 (ppm)
2.00
0.99
0.95
2.01
3.03
4.08
2.04
2.02
2.96
4.16
8.09
8.07
7.61
7.51
7.14
7.12
3.91
3.53
3.02
3.01
2.90
2.90
2.69
2.05
2.05
2.00
1.94 CD3CN

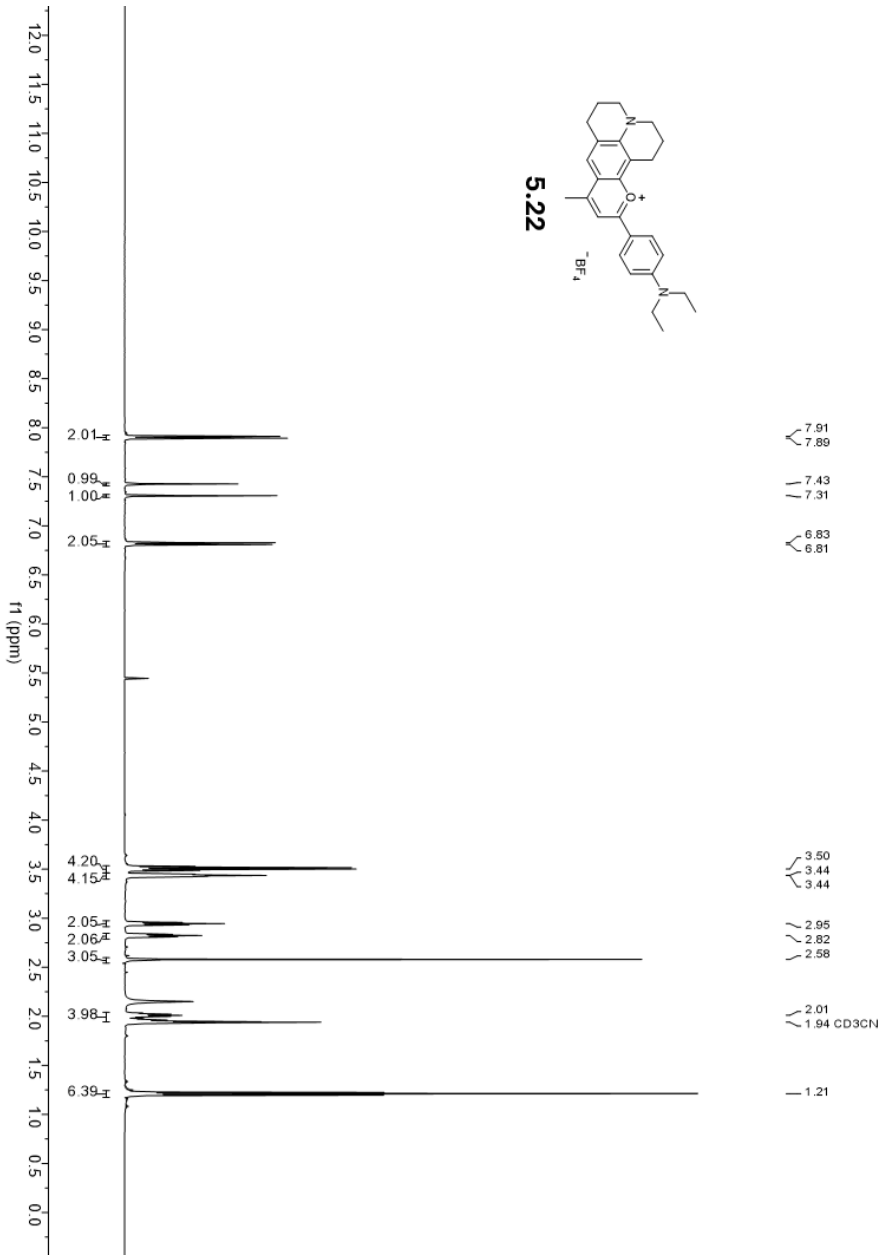
5.22
f1 (ppm)
2.01
0.99
1.00
2.05
4.20
4.15
2.05
2.06
3.05
3.98
6.39
7.91
7.89
7.43
7.31
6.83
6.81
3.50
3.44
3.44
2.95
2.82
2.58
2.01
1.94 CD3CN
1.21

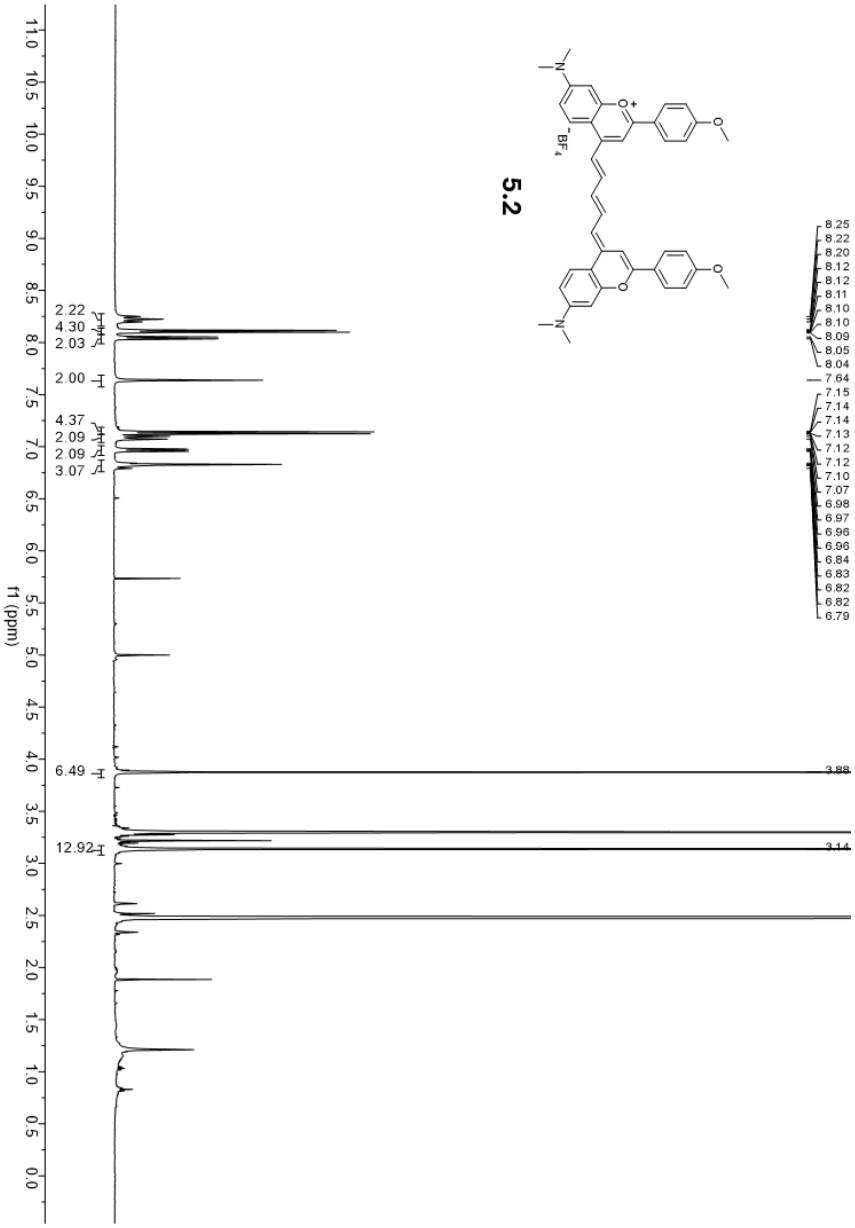
5.2
f1 (ppm)
2.22
4.30
2.03
2.00
4.37
2.09
2.09
3.07
6.49
12.92
3.88
3.14

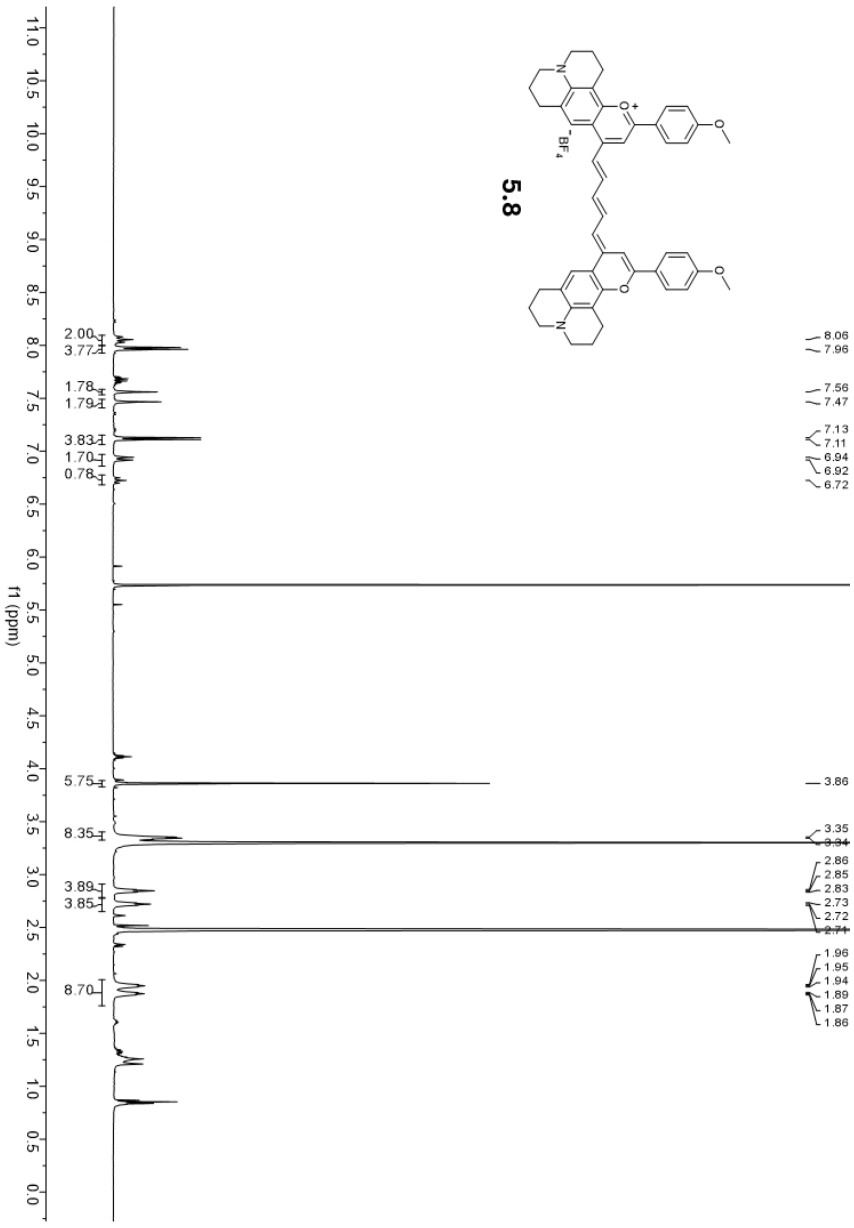
5.8
f1 (ppm)
2.00
3.77
1.78
1.79
3.83
1.70
0.78
5.75
8.35
3.89
3.85
8.70
8.06
7.96
7.56
7.47
7.13
7.11
6.94
6.92
6.72
3.86
3.35
2.86
2.85
2.83
2.73
2.72
1.96
1.95
1.94
1.89
1.87
1.86

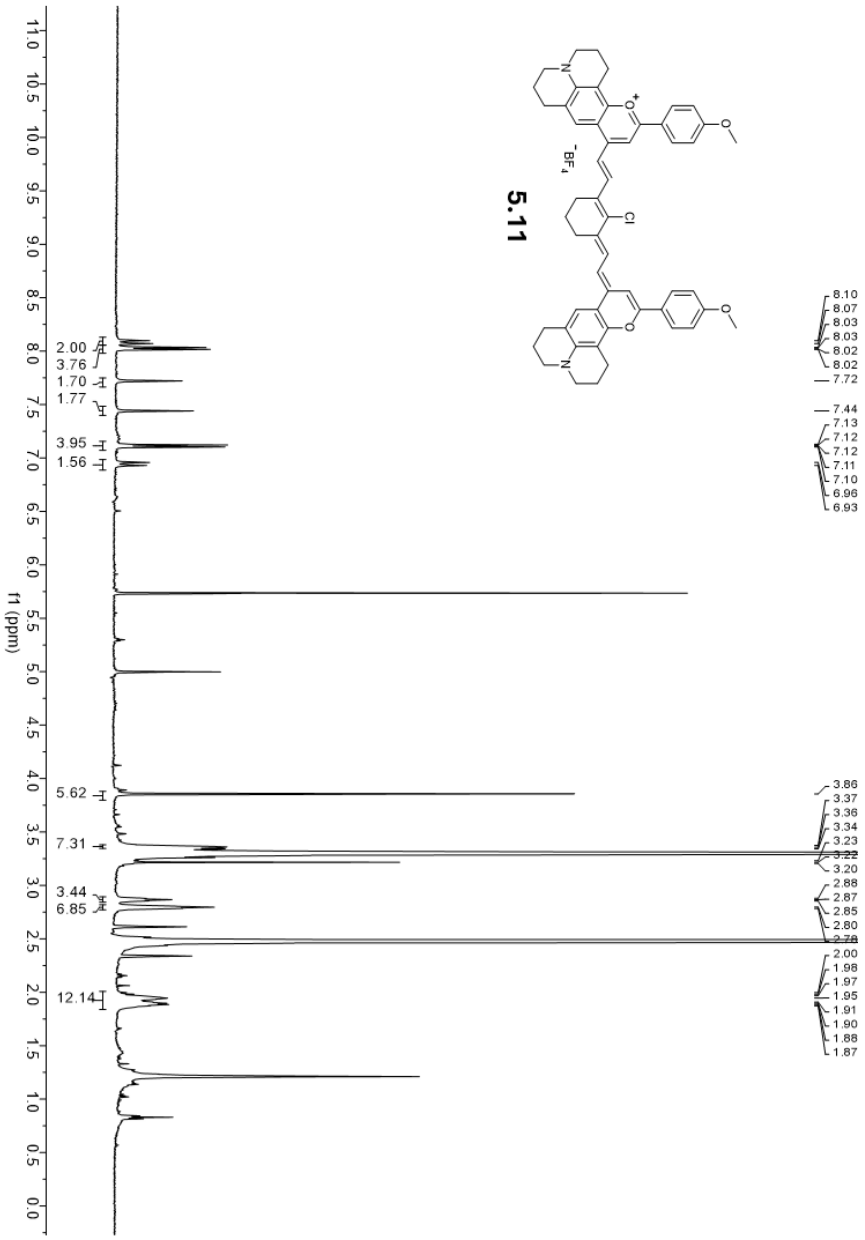
5.11
f1 (ppm)
2.00
3.76
1.70
1.77
3.95
1.56
5.62
7.31
3.44
6.85
12.14
8.10
8.07
8.03
8.03
8.02
8.02
7.72
7.44
7.13
7.12
7.12
7.11
7.10
6.96
6.93
3.86
3.37
3.36
3.34
3.23
3.22
3.20
2.88
2.87
2.85
2.80
2.78
2.00
1.98
1.97
1.95
1.91
1.90
1.88
1.87

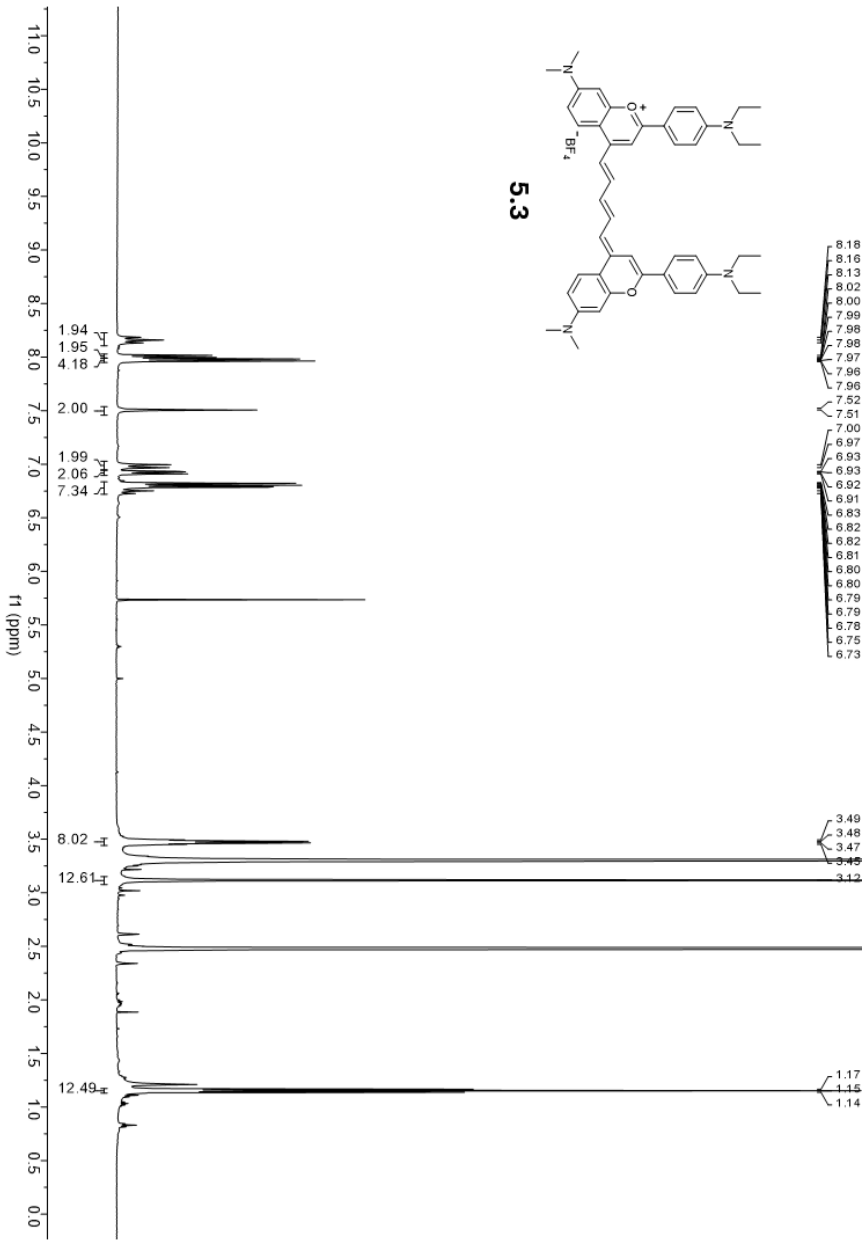
5.3
f1 (ppm)
1.94
1.95
4.18
2.00
1.99
2.06
7.34
8.02
12.61
12.49
8.18
8.16
8.13
8.02
8.00
7.99
7.98
7.98
7.97
7.96
7.96
7.52
7.51
7.00
6.97
6.93
6.93
6.92
6.91
6.83
6.82
6.82
6.81
6.80
6.80
6.79
6.79
6.78
6.75
6.73
3.49
3.48
3.47
3.12
1.17
1.15
1.14

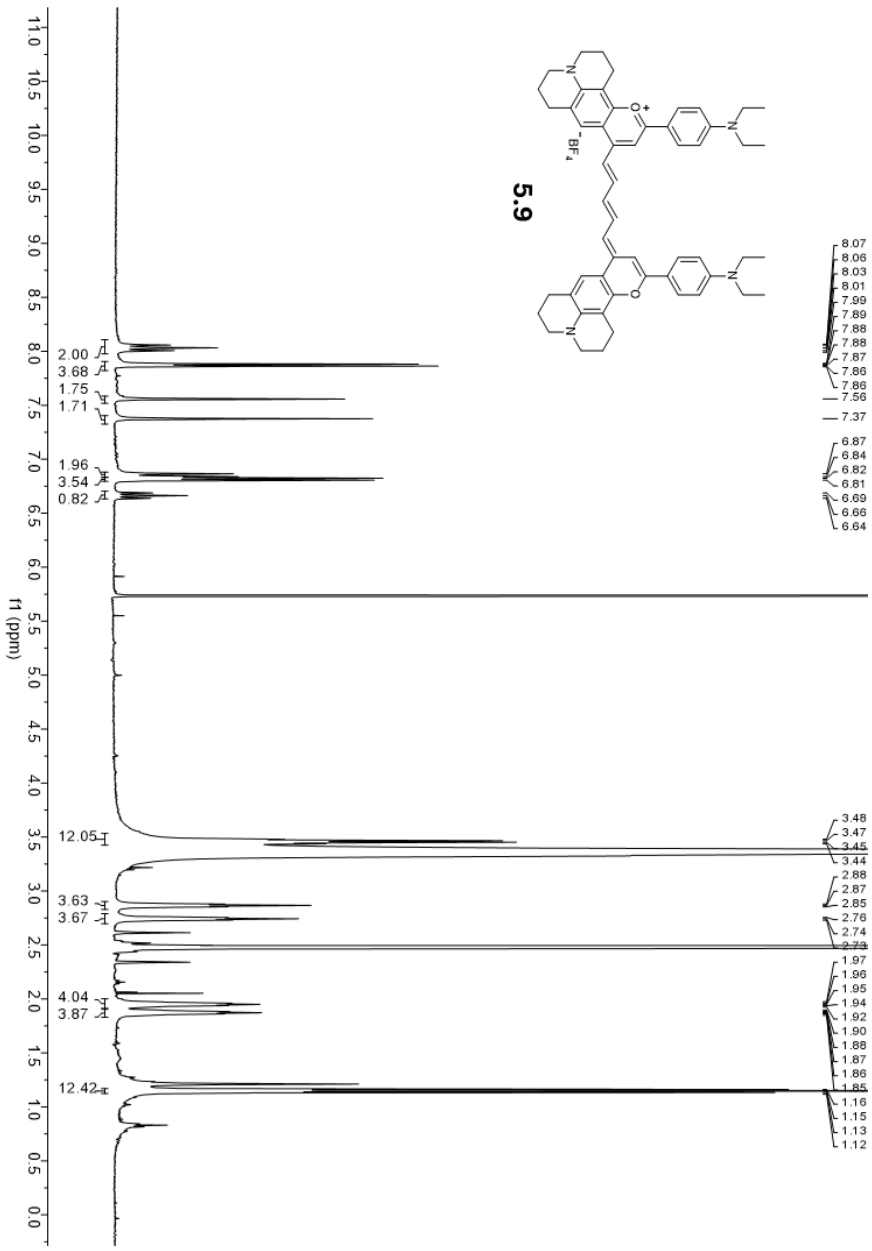
5.9
f1 (ppm)
2.00
3.68
1.75
1.71
1.96
3.54
0.82
12.05
3.63
3.67
4.04
3.87
12.42

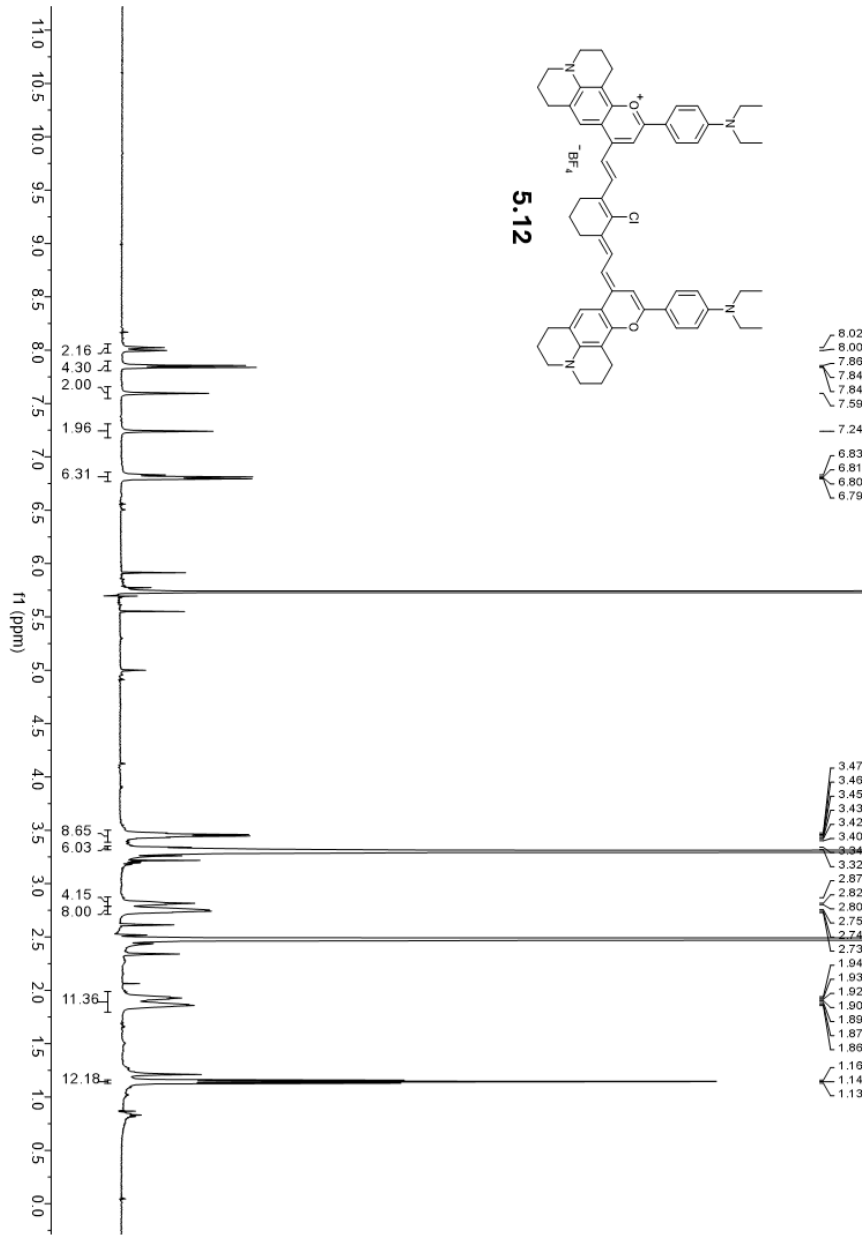
5.12
f1 (ppm)
2.16
4.30
2.00
1.96
6.31
8.65
6.03
4.15
8.00
11.36
12.18
8.02
8.00
7.86
7.84
7.84
7.59
7.24
6.83
6.81
6.80
6.79
3.47
3.46
3.45
3.43
3.42
3.40
3.32
2.87
2.82
2.80
2.75
2.73
1.94
1.93
1.92
1.90
1.89
1.87
1.86
1.16
1.14
1.13

5.6.2 ^{13}C NMR

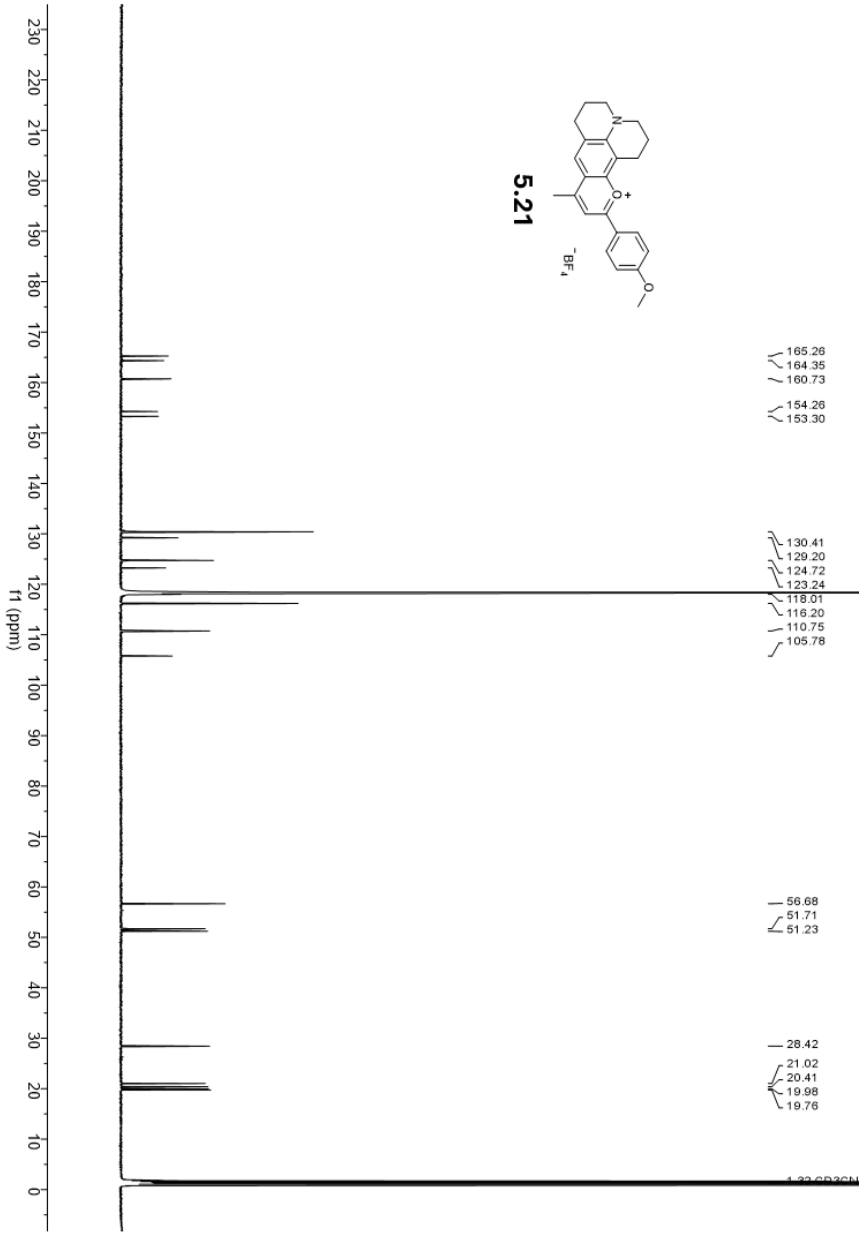
5.21
165.26
164.35
160.73
154.26
153.30
130.41
129.20
124.72
123.24
118.01
116.20
110.75
105.78
56.68
51.71
51.23
28.42
21.02
20.41
19.98
19.76
f1 (ppm)

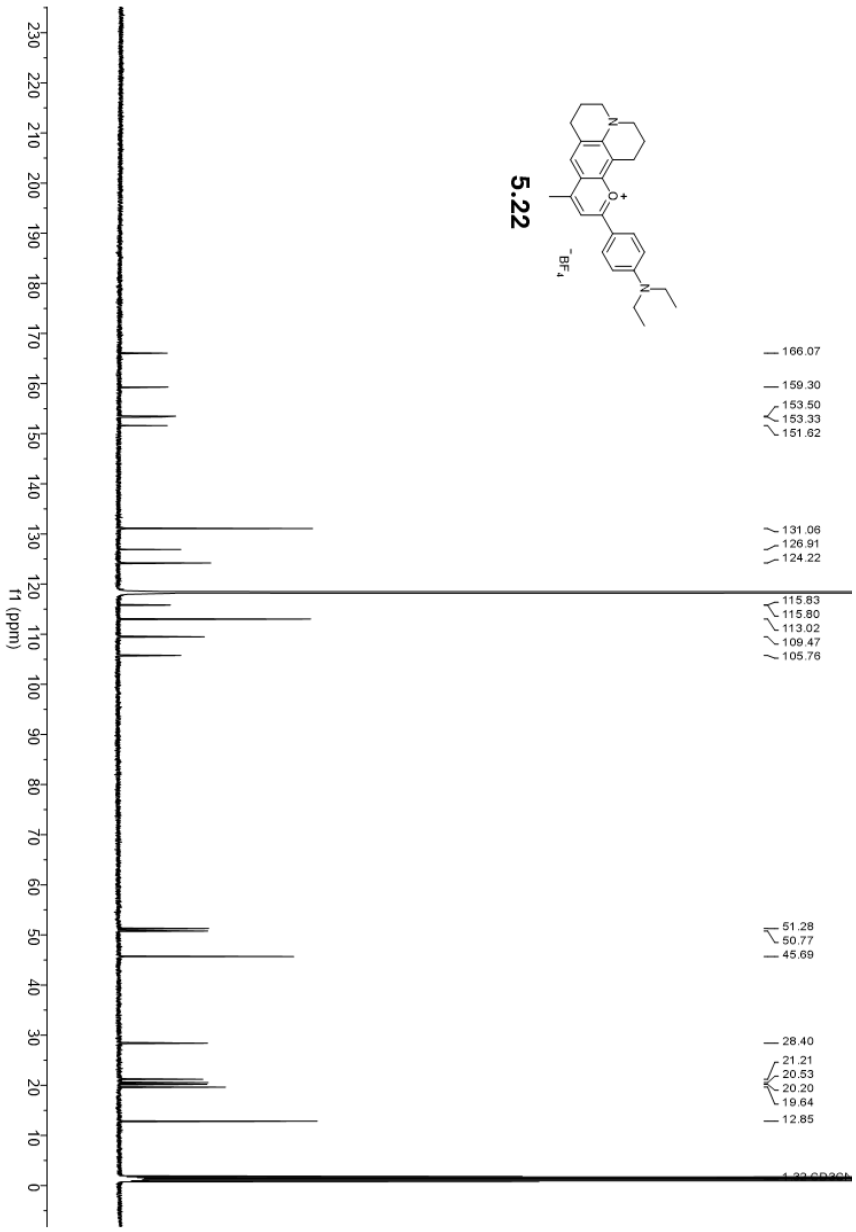
5.22
166.07
159.30
153.50
153.33
151.62
131.06
126.91
124.22
115.83
115.80
113.02
109.47
105.76
51.28
50.77
45.69
28.40
21.21
20.53
20.20
19.64
12.85
f1 (ppm)

5.6.3 Absorbance and Emission Spectra

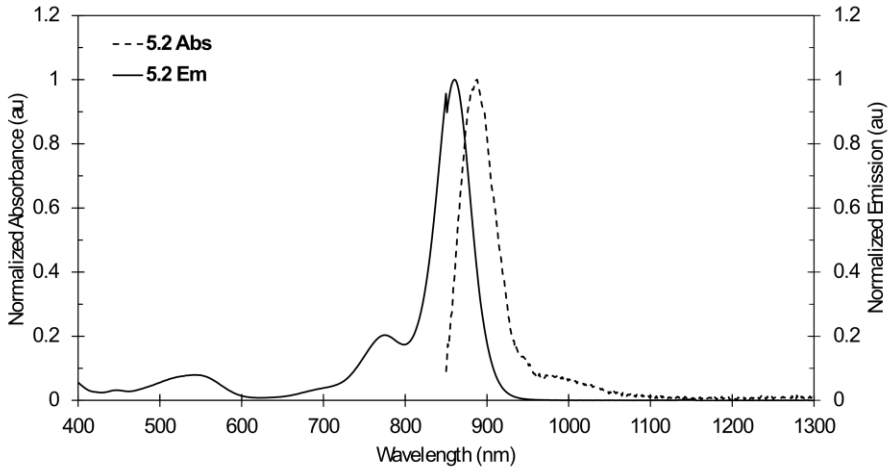

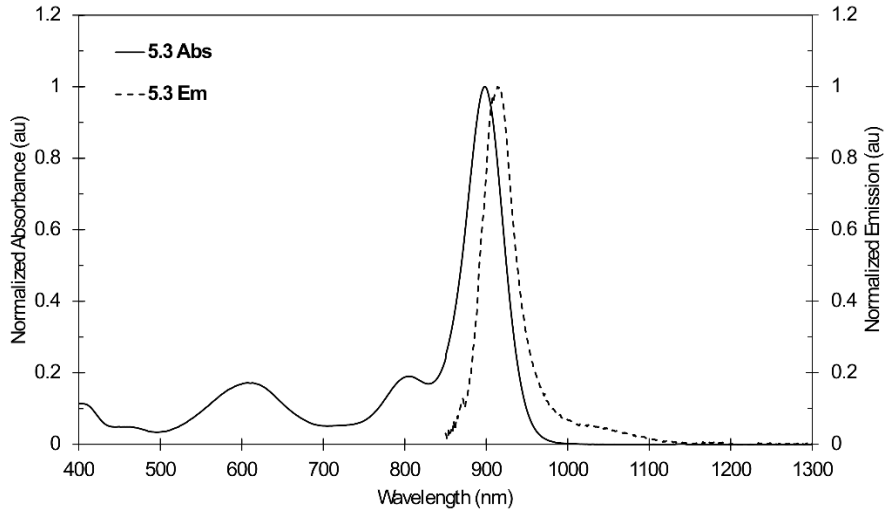

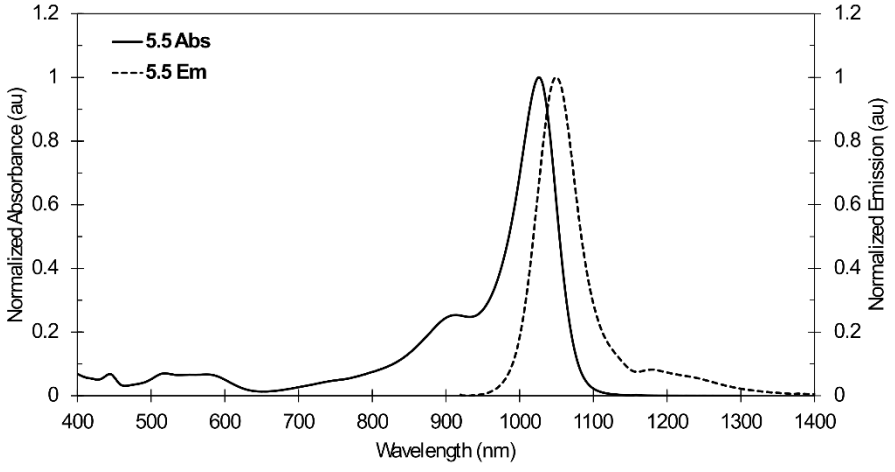

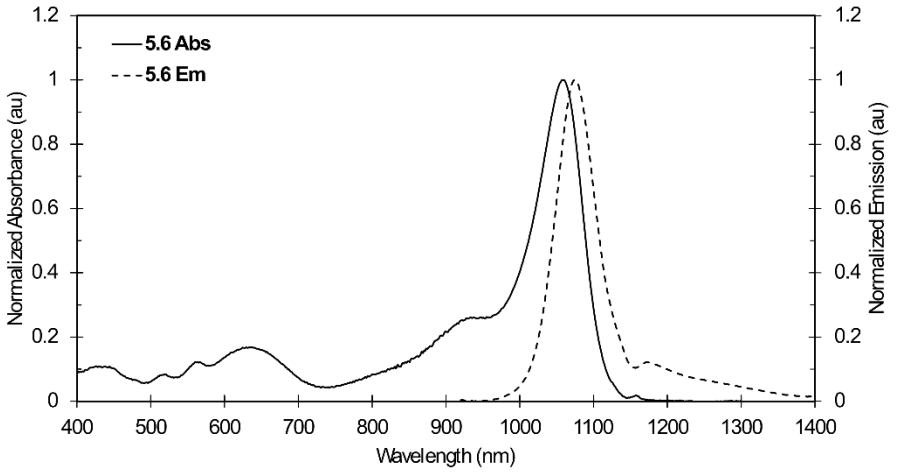
5.6 Abs
5.6 Em
Normalized Absorbance (au)
Normalized Emission (au)
Wavelength (nm)

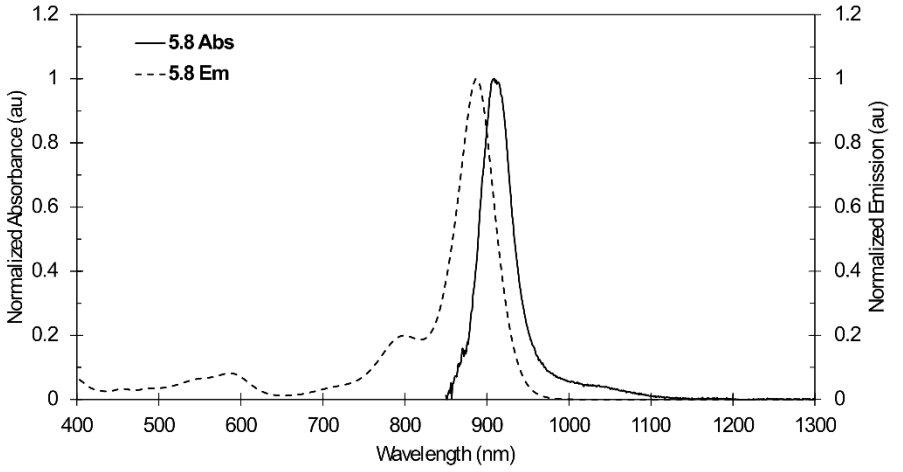
5.8 Abs
5.8 Em
Normalized Absorbance (au)
Normalized Emission (au)
Wavelength (nm)

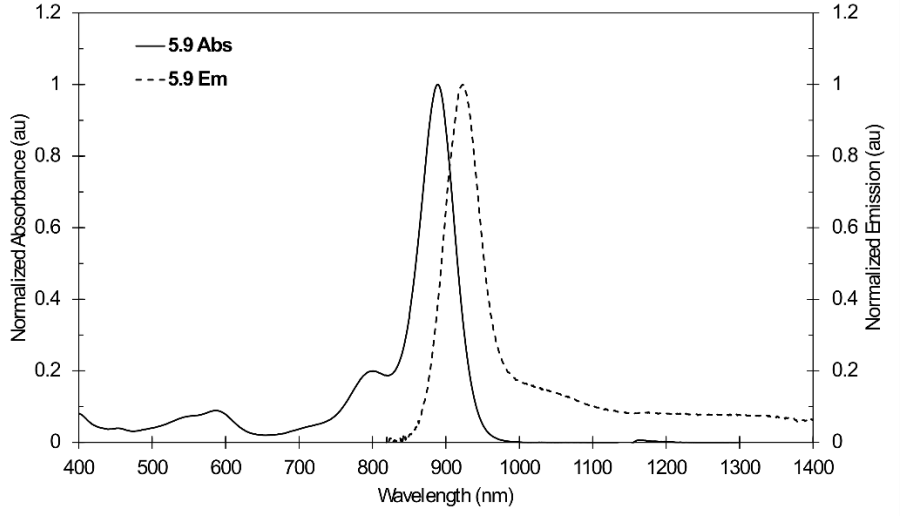
5.9 Abs
5.9 Em
Normalized Absorbance (au)
Normalized Emission (au)
Wavelength (nm)

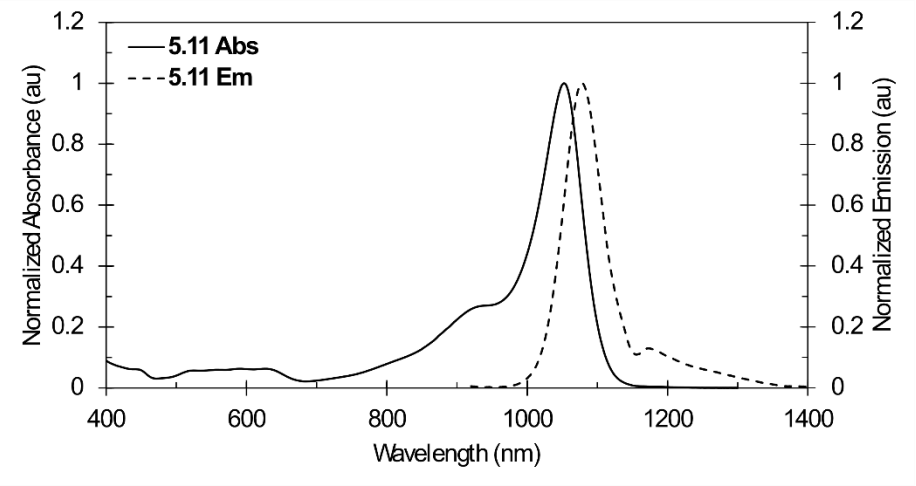
5.11 Abs
5.11 Em
Normalized Absorbance (au)
Normalized Emission (au)
Wavelength (nm)
1.2
1
0.8
0.6
0.4
0.2
0
400
600
800
1000
1200
1400

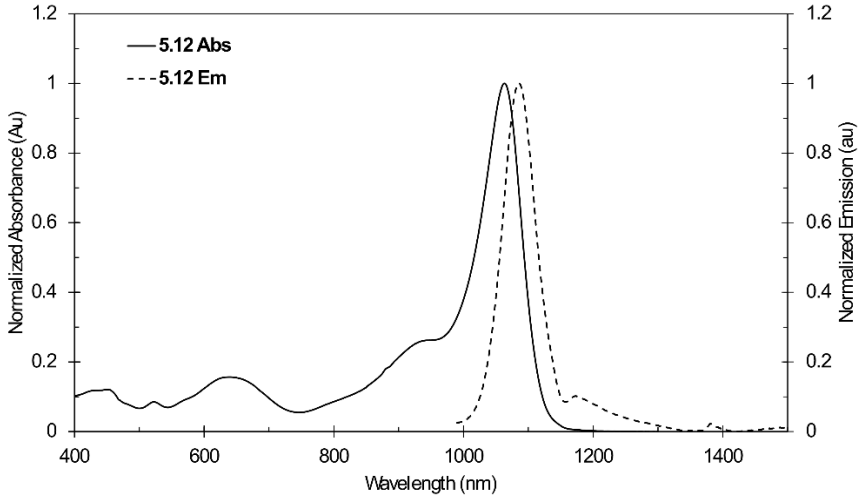
5.12 Abs
5.12 Em
Normalized Absorbance (Au)
Normalized Emission (au)
Wavelength (nm)
1.2
1
0.8
0.6
0.4
0.2
0
400
600
800
1000
1200
1400

References:

(1) Li, C.; Chen, G.; Zhang, Y.; Wu, F.; Wang, Q. Advanced Fluorescence Imaging Technology in the Near-Infrared-II Window for Biomedical Applications. *J. Am. Chem. Soc.* **2020**, *142*, 14789–14804. https://doi.org/10.1021/jacs.0c07022.

(2) Bandi, V. G.; Luciano, M. P.; Saccomano, M.; Patel, N. L.; Bischof, T. S.; Lingg, J. G. P.; Tsrunchev, P. T.; Nix, M. N.; Ruehle, B.; Sanders, C.; Riffle, L.; Robinson, C. M.; Difilippantonio, S.; Kalen, J. D.; Resch-Genger, U.; Ivanic, J.; Bruns, O. T.; Schnermann, M. J. Targeted Multicolor in Vivo Imaging over 1,000 Nm Enabled by Nonamethine Cyanines. *Nat. Methods* **2022**, *19*, 353–358. https://doi.org/10.1038/s41592-022-01394-6.

(3) Thimsen, E.; Sadtler, B.; Berezin, M. Y. Shortwave-Infrared (SWIR) Emitters for Biological Imaging: A Review of Challenges and Opportunities. *Nanophotonics* **2017**, *6*, 1043–1054. https://doi.org/10.1515/nanoph-2017-0039.

(4) Uranga-Barandiaran, O.; Casanova, D.; Castet, F. Flavylium Fluorophores as Near-Infrared Emitters. *ChemPhysChem* **2020**, *21*, 2243–2248. https://doi.org/10.1002/cphc.202000544.

(5) Lei, Z.; Zhang, F. Molecular Engineering of NIR-II Fluorophores for Improved Biomedical Detection. *Angew. Chemie - Int. Ed.* **2021**, *60*, 16294–16308. https://doi.org/10.1002/anie.202007040.

(6) Chang, B.; Chen, J.; Bao, J.; Dong, K.; Chen, S.; Cheng, Z. Design Strategies and Applications of Smart Optical Probes in the Second Near-Infrared Window. *Adv. Drug Deliv. Rev.* **2023**, *192*, 114637. https://doi.org/10.1016/j.addr.2022.114637.

(7) Webster, S.; Padilha, L. A.; Hu, H.; Przhonska, O. V.; Hagan, D. J.; Van Stryland, E. W.; Bondar, M. V.; Davydenko, I. G.; Slominsky, Y. L.; Kachkovski, A. D. Structure and Linear Spectroscopic Properties of near IR Polymethine Dyes. *J. Lumin.* **2008**, *128*, 1927–1936. https://doi.org/10.1016/j.jlumin.2008.06.002.

(8) Bricks, J. L.; Kachkovskii, A. D.; Slominskii, Y. L.; Gerasov, A. O.; Popov, S. V. Molecular Design of near Infrared Polymethine Dyes: A Review. *Dye. Pigment.* **2015**, *121*, 238–255. https://doi.org/10.1016/j.dyepig.2015.05.016.

(9) Kulinich, A. V.; Derevyanko, N. A.; Ishchenko, A. A.; Bondarev, S. L.; Knyukshto, V. N.

Structure and Fluorescence Properties of Indole Cyanine and Merocyanine Dyes with Partially Locked Polymethine Chain. *J. Photochem. Photobiol. A Chem.* **2008**, *200*, 106–113. https://doi.org/10.1016/j.jphotochem.2008.06.020.

(10) Ishchenko, A. A. Structure and Spectral-Luminescent Properties of Polymethine Dyes *Russ. Chem. Rev.* **1991**, *60*, 865.

(11) Brooker, L. G. S.; Keyes, G. H.; Sprague, R. H.; VanDyke, R. H.; VanLare, E.; VanZandt, G.; White, F. L.; Cressman, H. W. J.; Dent, S. G. Color and Constitution. X. Absorption of the Merocyanines. *J. Am. Chem. Soc.* **1951**, *73*, 5332–5350. https://doi.org/10.1021/ja01155a096.

(12) Cosco, E. D.; Caram, J. R.; Bruns, O. T.; Franke, D.; Day, R. A.; Farr, E. P.; Bawendi, M. G.; Sletten, E. M. Flavylium Polymethine Fluorophores for Near- and Shortwave Infrared Imaging. *Angew. Chemie - Int. Ed.* **2017**, *56*, 13126–13129. https://doi.org/10.1002/anie.201706974.

(13) Cosco, E. D.; Arús, B. A.; Spearman, A. L.; Atallah, T. L.; Lim, I.; Leland, O. S.; Caram, J. R.; Bischof, T. S.; Bruns, O. T.; Sletten, E. M. Bright Chromenylium Polymethine Dyes Enable Fast, Four-Color in Vivo Imaging with Shortwave Infrared Detection. *J. Am. Chem. Soc.* **2021**, *143*, 6836–6846. https://doi.org/10.1021/jacs.0c11599.

(14) Cosco, E. D.; Spearman, A. L.; Ramakrishnan, S.; Lingg, J. G. P.; Saccomano, M.; Pengshung, M.; Arús, B. A.; Wong, K. C. Y.; Glasl, S.; Ntziachristos, V.; Warmer, M.; McLaughlin, R. R.; Bruns, O. T.; Sletten, E. M. Shortwave Infrared Polymethine Fluorophores Matched to Excitation Lasers Enable Non-Invasive, Multicolour in Vivo Imaging in Real Time. *Nat. Chem.* **2020**, *12*, 1123–1130. https://doi.org/10.1038/s41557-020-00554-5.

(15) Wang, S.; Fan, Y.; Li, D.; Sun, C.; Lei, Z.; Lu, L.; Wang, T.; Zhang, F. Anti-Quenching NIR-II Molecular Fluorophores for in Vivo High-Contrast Imaging and PH Sensing. *Nat. Commun.* **2019**, *10*, 1–11. https://doi.org/10.1038/s41467-019-09043-x.

(16) He, Y.; Wang, S.; Yu, P.; Yan, K.; Ming, J.; Yao, C.; He, Z.; El-Toni, A. M.; Khan, A.; Zhu, X.; Sun, C.; Lei, Z.; Zhang, F. NIR-II Cell Endocytosis-Activated Fluorescent Probes Forin Vivohigh-Contrast Bioimaging Diagnostics. *Chem. Sci.* **2021**, *12* (31), 10474–

10482. https://doi.org/10.1039/d1sc02763h.

(17) Pengshung, M.; Li, J.; Mukadum, F.; Lopez, S. A.; Sletten, E. M. Photophysical Tuning of Shortwave Infrared Flavylium Heptamethine Dyes via Substituent Placement. *Org. Lett.* **2020**, *22*, 6150–6154. https://doi.org/10.1021/acs.orglett.0c02213.

(18) Semonin, O. E.; Johnson, J. C.; Luther, J. M.; Midgett, A. G.; Nozik, A. J.; Beard, M. C. Absolute Photoluminescence Quantum Yields of IR-26 Dye, PbS, and PbSe Quantum Dots. *J. Phys. Chem. Lett.* **2010**, *1*, 2445–2450. https://doi.org/10.1021/jz100830r.

(19) Hatami, S.; Würth, C.; Kaiser, M.; Leubner, S.; Gabriel, S.; Bahrig, L.; Lesnyak, V.; Pauli, J.; Gaponik, N.; Eychmüller, A.; Resch-Genger, U. Absolute Photoluminescence Quantum Yields of IR26 and IR-Emissive Cd1−xHgxTe and PbS Quantum Dots – Method- and Material-Inherent Challenges. *Nanoscale* **2014**, *7*, 133–143. https://doi.org/10.1039/C4NR04608K.

(20) Friedman, H. C.; Cosco, E. D.; Atallah, T. L.; Jia, S.; Sletten, E. M.; Caram, J. R. Establishing Design Principles for Emissive Organic SWIR Chromophores from Energy Gap Laws. *Chem* **2021**, *7*, 3359–3376. https://doi.org/10.1016/j.chempr.2021.09.001.